Combining Spectroscopic and Structural Probes of Molecular Dynamics

A Dissertation presented

by

Yusong Liu

to

The Graduate School

in Partial Fulfillment of the

Requirements

for the Degree of

Doctor of Philosophy

in

Chemistry

Stony Brook University

May 2021

Stony Brook University

The Graduate School

Yusong Liu

We, the dissertation committee for the above candidate for the

Doctor of Philosophy degree, hereby recommend

acceptance of this dissertation

Professor Thomas C. Weinacht - Dissertation Advisor
Department of Physics and Astronomy

Associate Professor Thomas K. Allison - Chairperson of Defense
Department of Chemistry
Department of Physics and Astronomy

Associate Professor Christopher J. Johnson - Third Person
Department of Chemistry

Professor Todd J. Martínez - External Committee Member
Department of Chemistry, Stanford University

This dissertation is accepted by the Graduate School

Eric Wertheimer
Dean of the Graduate School

Abstract of the Dissertation

Combining Spectroscopic and Structural Probes of Molecular Dynamics

by

Yusong Liu

Doctor of Philosophy

in

Chemistry

Stony Brook University

2021

Following the photoinduced excited state dynamics of polyatomic molecules in their natural time scales is the key of understanding many fundamental processes in physics, chemistry, and biology. The excitation induces coupled electron and nuclei motion, leading to either radiative processes *via* fluorescence and phosphorescence, or non-radiative manners such as internal conversion, isomerization, and dissociation. In this dissertation, I focus on the non-radiative process which are usually involve with both energy changes and structural transformations in femtosecond time scales. It is particularly interesting to follow the energy conversion from the electric part into the nuclear degrees of freedom and explore how the initial structures will affect the following reaction pathways. Thus developing different time-resolved techniques that are sensitive to energy and/or structural changes are the most effective way to view the ensuing dynamics. However, the quantum dynamics of interests are filtered by the coordinate-dependent matrix elements of the chosen experimental observable, where a single measurement observable only gives a narrow viewing of the full quantum dynamics. Therefore, it is only through a combination of experimental measurements and theoretical calculations that one can gain insights into the internal dynamics. In this

dissertation, I demonstrated a combined methodology with both spectroscopic and structural probes on coupled electronic and nuclear dynamics. I interpreted the experimental measurement from trajectory surface hopping calculations with high-level electronic structure theories, and I was able to directly compare the measured observables with the calculated observables.

The spectroscopic probe comprises time-resolved photo-electron spectroscopy and momentum-resolved photoion spectroscopy, whereas the structural probe makes use of ultrafast electron diffraction. Several systems represent different molecular families are chosen as the targets in the combined methodology. Chap. 1 provides an introduction into the molecular dynamics, time-resolved pump-probe techniques ranging from spectroscopes to diffraction methods, and theoretical treatment from quantum chemistry. In Chap. 2, the combined spectroscopic and structural probes are described with great details. The techniques as well as the treatment of the calculated measurement observables are provided. From Chap. 3 to Chap. 5, I present the experiential results with both spectroscopic and structural probes on several small organic molecules. I start with a ring-type conjugated molecular system, *cis,cis*-1,3-cyclooctadiene (C_8H_{12}) in Chap. 3, focusing on its photoisomerization dynamics with spectroscopic signatures, and extending the understanding from relatively rigid small molecules such as 1,3-cyclohexadiene (C_6H_8) into larger, more flexible systems. In this measurement, the theory calculation is used to interpret the dynamics. In Chap. 4, I turned to explore whether and how the experimental measurements can be used to benchmark theory. To do that, a TRPES measurement was carried out, and the measurement was compared with the calculations at three levels of theory, focusing on the much debated population trapping on the first bright state (S_2) of uracil. The comparison of the calculated and measured time-resolved photoelectron spectra allows to draw conclusions regarding not only the relative insights, but also the quantitative accuracy of the calculations at the different levels of theory. In Chap. 5, a comprehensive study, combining both spectroscopic and structural probes, was carried out on the dissociation dynamics of diiodomethane (CH_2I_2), including time-resolved photo-electron spectroscopy, momentum-resolved photo-ion spectroscopy, as well as ultrafast electron diffraction. Finally in Chap. 6 provides a summary of the advantages offered by the combination of spectroscopic and structural probes, and provides prospects for the future work utilizing ultrafast soft X-ray for both spectroscopy and diffraction studies.

To my family

Contents

List of Figures

List of Tables

List of Abbreviations and Symbols

BOA	Born-Oppenheimer Approximation
CI	Conical Intersection
TRPES	Time-Resolved PhotoElectron Spectroscopy
TRPIS	Time-Resolved PhotoIon Spectroscopy
rUED	Relativistic Ultrafast Electron Diffraction
WFI	Weak Field Ionization
ToF	Time-of-Flight
VMI	Velocity Map Imaging
TKE	Translational Kinetic Energy
TDSE	Time-dependent Schrödinger Equation
TSH	Trajeactory Surface Hopping
FWHM	Full-Width-Half-Maximum
IRF	Instrument Response Function
CHD	1,3-Cyclohexadiene, C_6H_8
COD	cis,cis-1,3-Cyclooctadiene, C_8H_{12}
XFEL	X-ray Free Electron Laser
e	Elementary charge
$\hbar$	Reduced Planck's constant

List of publications

This thesis is based on the following publications with author's major contribution:

Chapter 3

Pratip Chakraborty, Yusong Liu, Thomas C. Weinacht and Spiridoula Matsika. Excited State Dynamics of cis,cis-1,3-Cyclooctadiene: Non-adiabatic Trajectory Surface Hopping. *The Journal of Chemical Physics* **152**, 174302 (2020)

Yusong Liu, Chakraborty, Spiridoula Matsika and Thomas C. Weinacht. Excited State Dynamics of cis,cis-1,3-Cyclooctadiene: UV pump VUV Probe Time Resolved Photoelectron Spectroscopy. *The Journal of Chemical Physics* **153**, 074301 (2020)

Chapter 4

Pratip Chakraborty, Yusong Liu, Thomas C. Weinacht and Spiridoula Matsika. Effect of Dynamic Correlation on the Ultrafast Relaxation of Uracil in the Gas Phase. *Faraday Discussion* (2020)

Pratip Chakraborty, Yusong Liu, Samuel McClung, Thomas C. Weinacht and Spiridoula Matsika. Time resolved photoelectron spectroscopy as a test of electronic structure and nonaidabatic dynamics. *The Journal of Physical Chemistry Letter* **12**, 5099-5104 (2021)

Chapter 5

Spencer L. Horton, Yusong Liu, Ruaridh Forbes, Varun Makhija, Rune Lausten, Albert Stolow, Paul Hockett, Philipp Marquetand, Tamás Rozgonyi and Thomas C. Weinacht Excited State Dynamics of CH_2I_2 and CH_2IBr studied with UV Pump VUV Probe Photoelectron Spectroscopy. *The Journal of Chemical Physics* **150**, 174201 (2019)

Yusong Liu, Spencer L. Horton, Jie Yang, J. Pedro F. Nunes, Xiaozhe Shen, Thomas J. A. Wolf, Ruaridh Forbes, Chuan Cheng, Bryan Moore, Martin

Centurion, Kareem Hegazy, Renkai Li, Ming-Fu Lin, Albert Stolow, Paul Hockett, Tamás Rozgonyi, Philipp Marquetand, Xijie Wang and Thomas C. Weinacht. Spectroscopic and structural probing of excited state molecular dynamics with time-resolved photoelectron spectroscopy and ultrafast electron diffraction. *Physical Review X* **10**, 021016 (2020)

Yusong Liu, Tamás Rozgonyi, Philipp Marquetand and Thomas C. Weinacht. Excited-State Dynamics of CH_2I_2 and CH_2IBr Studied with UV-Pump VUV-Probe Momentum-Resolved Photoion Spectroscopy. *The Journal of Chemical Physics* **153**, 184304 (2020)

Additional work completed during the author's Ph.D career:

Spencer L. Horton, Yusong Liu, Pratip Chakraborty, Spiridoula Matsika and Thomas C. Weinacht. Ultrafast Internal Conversion of Highly Excited Pyrrole Studied with VUV/UV Pump Probe Spectroscopy. *The Journal of Chemical Physics* **146**, 064306 (2017)

Spencer L. Horton, Yusong Liu, Pratip Chakraborty, Spiridoula Matsika and Thomas C. Weinacht. Vibrationally Assisted Below-Threshold Ionization. *Physical Reviews A* **95**, 063413 (2017)

Anthony Catanese, Spencer Horton, Yusong Liu and Thomas C. Weinacht. Real-time-Adjustable, 11 μs FWHM, >5kHz, Piezo Electric Pulsed Atomic Beam Source. *Review of Scientific Instruments* **89**, 103115 (2018)

Spencer L. Horton, Yusong Liu, Pratip Chakraborty, Philipp Marquetand, Tamás Rozgonyi, Spiridoula Matsika and Thomas C. Weinacht. Strong-Field vs Weak-Field Ionization Pump-Probe Spectroscopy. *Physical Review A* **98** 053416, (2018)

J. Pedro F. Nunes, Kathryn Ledbetter, Ming-Fu Lin, Michael Kozina, Daniel P. DePonte, Elisa Biasin, Martin Centurion, Christopher J. Crissman, Michael Dunning, Serge Guillet, Keith Jobe, Yusong Liu, Mianzhen Mo, Xiaozhe Shen, Robert E. Sublett, Stephen Weathersby, Charles Yoneda, Thomas J. A. Wolf, Jie Yang, Amy A. Cordones and Xijie Wang. Liquid-phase mega-electron-volt ultrafast electron diffraction. *Structural Dynamics* **7**, 024301

(2020)

Jie Yang, Xiaolei Zhu, J. Pedro F. Nunes, Jimmy K. Yu, Robert M. Parrish, Thomas J. A. Wolf, Martin Centurion, Markus Guhr, Renkai Li, Yusong Liu, Bryan Moore, Mario Niebuhr, Suji Park, Xiaozhe Shen, Stephen Weathersby, Thomas C. Weinacht, Todd J. Martinez and Xijie Wang. Simultaneous Observation of Nuclear and Electronic Dynamics by Ultrafast Electron Diffraction. *Science* **368**, 6493, 885-889 (2020)

Acknowledgement

Looking back the years of my Ph.D in Stony Brook, there are so many people that had kindly offered help to me and it is extremely difficult to acknowledge everyone of them. This dissertation would not come true without all the support and help from all the people that I have interacted with. This dissertation is a really long, difficult, but enriched, beautiful journey at the point when I am writing it now. I would like to take this opportunity to thank all of them.

I greatly acknowledged Dr. Tom Weinacht, for being as an advisor, a mentor, and a friend with all his guidance, encouragement, and support during the time of my PhD. He is being active, willing to help on the experiments, discuss Physics and Chemistry, and brainstorm and argue ideas and thoughts all the time. In addition, he has been performing as a professional mentor with excellent language skills, clear thinking and presenting, and great patience during my time in his lab. Tom, thanks for the help in the experiments in our own lab and thanks for your generosity of supporting me reaching and working in other labs outside Stony Brook University five times, every year since 2017 till 2021, which greatly enriched my knowledge and set me up many connections with people in the field. The science, the experimental expertise, and the communication skills I learned from you will benefit for the rest of my life. Your deeds makes me understand what is called as a "gentleman and scholar". The times that we spent together on discussion and argument regarding physics and chemistry, life, and everything else, remain to be some of my most important and pleasant memories in graduate school, and I am honored to be your first student outside Department of Physics and Astronomy. I would also like to thanks to my dissertation committee members for the feedback on the thesis. Thanks to Dr. Tom Allison who offered me the opportunity of coming to Stony Brook for the Ph.D program in Department of Chemistry. He is one of the most ambitious Physicists/Chemists that I have ever seen. Thanks to Dr. Chris Johnson who has been always nice, kind, and friendly to give me advice during all the meetings of Chemistry Ph.D program. Thanks to Dr. Todd Martínez for being my external member in the committee and thank you for giving me valuable comments from the theory side.

Thanks to the group members in Weinacht Lab. Dr. Marty Cohen, who

is intelligent, energetic, experienced, and kind to provide valuable advice on laser, optics, and electronics. Dr. Spencer Horton, whom I started working with in the same project, helped me build up the skills in optics and lasers. We worked for 4 years together and made a perfect team. We struggled and progressed. I cannot remember how many late nights we stayed up in the lab tweaking up the experiments and taking data and we became great friends in life. Thanks to Sam McClung, Chuan Cheng, and Brian Kaufman. I will remember forever the times we four spent together during and after the lab work. Thanks to Anthony Catanese who has the most amazing skills in designing and machining apparatus. Thanks to Dr. Péter Sándor who had helped me on both lab work and life during the early years. Thank you for bringing me into the Physics and Math Friday afternoon soccer games. Thanks to Arthur Zhao, whom I shared with an office and has sharp thoughts in both Physics and Philosophy, and give me advice on the experimental and data analysis. Thanks to all the other people in the group that I have interacted with, Dr. Eric Jones, Dr. Vincent Tagliamonti, Gayle Gerschwind, Yi Lu, Denis Aglagul, *et al.* I do owe all of you in this group.

I would like to give my special thanks to our theory collaborators, Dr. Spiridoula Matsika and Dr. Pratip Chakraborty from Temple University, Dr. Philipp Marquetant from Universität Wien, and Dr. Tamás Rozgonyi from Wigner Research Centre for Physics, Hungary. Without their tremendous theoretical input, none of the experimental results in Chap. 3 to Chap. 5 could be interpreted properly. Dr. Matsika, Marquetant, and, Rozgonyi have been extremely active and always offered ideas between the theory and experiments. I do feel lucky working with you. Thank Pratip, and we started Ph.D around the same time and we have been closely and consistently working on the collaboration for more than five years, becoming great friends beyond research work.

I would like to thank people who were involved in the experimental data taking and analysis of the work in Chap. 5, which was built on a great collaboration with many people from several different institutes and universities. The TRPES experiments were carried out from National Research Council of Canada, and thank Dr. Paul Hockett, Dr. Rune Larsen, Dr. Albert Stolow, Dr. Varun Makhija, and Dr. Ruaridh Forbes. The UED measurements were carried out in SLAC national laboratory with the relativistic electron diffraction group including Jie Yang, Xiaozhe Shen, Thomas Wolf, Ming-Fu Lin, Renkai Li, Stephen weathersby, Kareem Hegazy, and Xijie Wang. Thanks Pedro Nunes, Bryan Moore and Martin Centurion from University of Nebraska.

The graduate student, postdocs and stuff scientists that I was working together are some of the most talented and hard working people I have ever worked with. Special thanks to Ruaridh who is always friendly, enthusiastic, careful, and kindly offering help and giving advice on all my projects of the dissertation. Special thanks are also given to Jie and Pedro who contributed tremendously time and energy in the experiments and data analysis of UED measurements. Thanks Thomas for offering me an postdoc position in Stanford PULSE institute of continuing my research in the field.

Besides research, I would like to thank my fellow AMO community, Ludwig Krinner, Bertus Jordaan, Brian and Melissa Arnold, Yuning Chen, Mehdi Namazi, Arturo Pasmino, Peng Zhao, Xinlong Li, He zhang, Joon Kwon, Alfonso Lanuza, Guodong Cui, Sonali Gera, Youngshin Kim, Yifang Fang, Xiaoyang Liu, Eli Rafkin, Ian Schwartz *et al.* The AMO community, dwelling in the basement of Physics and/or Chemistry, unitize as a productive and happy family, endlessly exchanging ideas on the research, discussing the meanings of life, and arguing politics. I also want to thank other professors in AMO groups, Dr. Hal Metcalf, Dr. Dominik Schneble, and Dr. Eden Figueroa. I would like to thank Chuan Tian, Cong Liu, Vinh Quang Tran, Ke Ma, Hang Yin, Lequan Chi, Scott Mills, Tao Zhang, Anja Röder, Xiang Li, Anbu Venkatachalam, Xinzhong Li, Oumarou Njoya, Rasmus Larsen, who are friends outside the AMO community. Thank Katharine Hughes, Jin Bently, and Vicki Grove in the Chemistry and Physics main office and your work made my life much easier. Thank Ph.D program coordinators in Chemistry, Dr. Dale Drueckhammer, Dr. Robert Grubbs, and Dr. Isaac Carrico, for the help in guidance of the Ph.D program. Thanks to Dr. Ronger Zheng in Department of Physics of my collage (OUC, China), who encouraged me pursuing Ph.D degree.

Thanks to the U.S. Department of Energy, Basic Energy Science, for funding my study and research projects. Your support is significant in pushing forward the fundamental research and experimental and theoretical techniques. Thanks all the people who help on fighting COVID-19 and your efforts really made my Ph.D time easier during this pandemic.

In the end, I would like give my greatest acknowledgements to my family. I want to thank my mom and my two older sisters, who had been taking care of me before I left my village, and support my education outside hometown. I want to thank my dad who works hard through his whole life to support the family. Thanks to my wife, Fen and her family. She has been waiting me many years in the Ph.D. Thank all the people in my village who always

gives me their best greeting and wishes every time I came back.

Chapter 1

Introduction and motivation

The photoinduced excited state dynamics of polyatomic molecules has been the central topic for understanding many fundamental process in physics, chemistry and biology, such as the basic steps involved in vision [1, 2], the photoprotetion of DNA/RNA [3, 4, 5, 6], and how energy and charge transfer facilities the light harvesting [7, 8], and energy conversion in photoabsortion [9]. While these processes can be extremely complicated, lots of insights are gained by understanding the basic dynamics steps at the single molecular level and in their natural time scales. These dynamics usually involve a complex redistribution of both electronic and nuclear energy, as well the the on going structural transformation. Due to the coupling among both electronic and nuclear degrees of freedoms, it usually gives rise to a wide vary of radiationless processes, such as internal conversion [10, 11, 12, 13, 14], isomerization [15, 16, 17, 18, 19], dissociation [20, 21, 22, 23, 24], and intersystem crossing [25, 26, 27]. The common feature of these processes is that they take place in very fast time scales from picosecond to femtosecond (10^{-12} to 10^{-15} s), and they occur in the space of molecular configuration where the electronic states or potential surfaces become close in energy or cross each other. These places are often termed as conical intersections (CIs), allowing population from one/several state(s) non-adiabatically transferring to another, leading to fast and prominent radiationless decay. A typical example is the internal conversion dynamics that the population in the excited state is allowed to evolved through one/many CI(s) back to the ground state, instead of dissociation. This has found significant importance in DNA/RNA when being exposed to UV radiations where the vast excess electronic energy can be dissipated into nuclear degrees of freedoms, enabling the often called

photoprotection.

Internal conversion gives an example of the fast charge transfer, energy flow, and structure transformation taking places in the polyatomic molecules where strong coupling of the electronic and nuclear degrees of freedom appears. Different from the adiabatic picture under the BO approximation, these non-adiabatic processes result in the breaking-down of the approximation, which induces huge amount of difficulty and challenges to follow the certain dynamics in both experimental measurements and theoretical calculations. The strong coupling between the electronic and nuclear degrees of freedoms results in the complex nuclear vibrational dynamics. Due to the larger density of the vibrational states around the space where the the electronic states are being close or crossing each other, the spectral features in energy/frequency are strongly broadened such that the conventional time-independent spectroscopic methods are no longer effectively to be implemented. Instead, more insights could be gained from the time-dependent methods, in which following the transient yield, energy changes, or directly structural transformations in the experimental perspective becomes much more attractive.

Around the space with strong coupling, the time-scale of the dynamics becomes extremely fast, and a temporal resolution with femtoscond level is needed. Besides the temporal resolution, achieving the right optical wavelength and/or wavelength tunability becomes extremely useful, but usually difficult and nontrivial. These all increase the challenge for developing ultrafast laser system as well as time-resolved techniques. Thanks to the advancement of the modern ultrafast laser systems in the past several decades, designing time-resolved techniques within below picosecond time resolution have become possible. The real breakthrough of the ultrafast time-resolved measurements were achieved in the 1980 to 1990s with the availability of femtosecond laser, particularly the ultrafast high-intensity laser systems. Subsequently development including harmonic generations as well as the large range wavelength tunable laser system enables a huge advance in both time-resolved techniques and scientific investigation of molecular dynamics. This opens a new region which is known as "Femtochemistry", awarded with Nobel Prize in Chemistry 1999 [28].

Almost all approaches for performing time-resolved measurements can be understood in terms of frame work of "pump-probe", which involves two, local in time interactions with two separate pulses: a pump pulse creates an initial, time-dependent state of the system, and a probe pulse subsequently

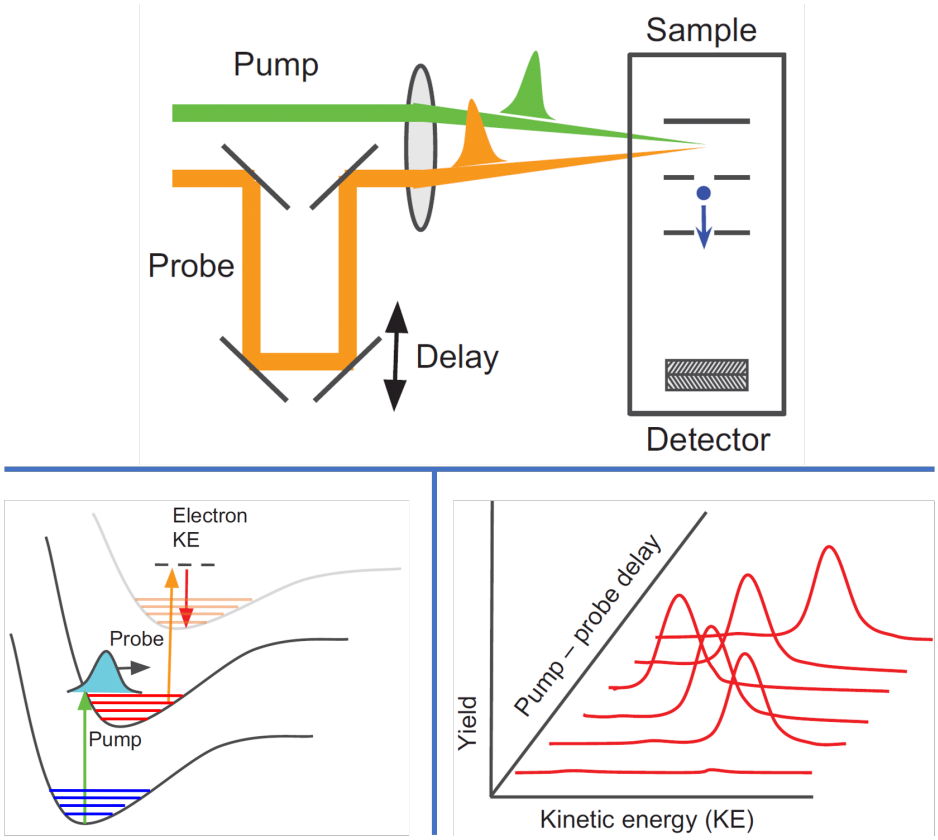

Figure 1.1: **Cartoon diagram illustrating the pump-probe frame work based on TRPES measurement.** This figure is modified from Ref. [29] with authors' permission. Top: panel shows the optical pump and probe pulse are focused into a vacuum chamber where the molecular sample is ionized. The photoelectron energy can be measured via time-of-flight or velocity-map imaging, where the time/position of the electrons encodes their energy/momentum, respectively. Bottom left: After the pump pulse excites a vibrational wavepacket on an excited state, the time-delayed probe pulse ionizes the molecule, resulting in the ejection of an electron. Bottom right: The electron yield is plotted as a function of both pump–probe delay and the KE of the emitted electron.

interacts with the evolving system. The delay between the pump and probe pulse are well-defined and-controlled, and after the probe interrogation, light and/or charged particles are collected as the measurement observable, and

variation of the yield is monitored as a function of the time delay between pump and probe interaction. Fig. 1.1 top panel depicts a cartoon example of the pump-probe framework based on time-resolved photoelectron spectroscopy (TRPES) which involves a pump-probe scheme as well as vacuum chamber for sample delivering and light/charged particle detection.

The pump pulse is almost always a short, coherent electromagnetic filed (a laser pulse) and usually has a finite spectral bandwidth, which typically covers several vibrational quantum states. As shown in Fig. 1.1 bottom left panel, the pump pulse results in a time-dependent state, formed from a linear combination of the time-independent eigenstates and this coherent superposition is called a wavepacket. As the wavepacket evolves on the electronic state potential, a probe pulse interacts with the system and produces an observable recorded with respect to the delay of the pump. Compared with the pump, the probe can be either a laser/X-ray pulse or a bunch of electrons. As shown in bottom left panel of Fig. 1.1, a second laser pulse ionizes the molecule, producing a photoelectron in the state of the cation and the kinetic energy resolved photoelectron yields are monitored as a function of pump-probe delay.

While the experimental techniques can extract information content involved in the undergoing dynamics, they do need theoretical inputs, such as accurate electronic structures and dynamics calculations, in order to interpret the measurements. Particularly, a direct comparison between the measured and calculated experimental observable usually plays a key role of understanding the undergoing dynamics. However, it is usually non-trivial to obtain high-level accurate electronic structures, and carrying out dynamics calculations with high temporal resolution is usually computationally costly. This is extremely difficult when CIs become prominent in the chosen system with many degrees of freedoms. In this dissertation, I perform measurements that are able to follow the photoinduced excited state non-adiabatic dynamics by combining multiple time-resolved techniques. My goal is to compare and contrast the information content extracted from different measured experimental observables, and interpret the results by directly comparing the measured observables with their relevant calculated observables. In the rest of this chapter, I begin with the conceptual background of excited state non-adiabatic dynamics. Next, the different time-resolved experimental techniques as well as the theoretical method are briefly explained. Finally, I will highlight the importance and advantage of combining different experimental techniques on excited state dynamics.

1.1 Molecular Hamiltonian and Born-Oppenheimer approximation

Before I step into the combined spectroscopic and structural methodology, it is useful to briefly review the basic background of the excited state dynamics. In general, following nuclear dynamics on the electronically excited state is complicated due to the coupling of the electronic and nuclear degrees of freedoms. This is most due to the Coulomb *attraction* between electrons and nuclei, and it is this effect that is responsible for molecular bonding. When taking into account all possible motions and interaction of the electrons and nuclei, the general form of the full molecular Hamiltonian operator H in atomic units can be written as

$$\hat{H} = \sum_i \frac{-\nabla_{e,i}^2}{2} + \sum_{i,j>i} \frac{1}{|\mathbf{r}_i - \mathbf{r}_j|} + \sum_j \frac{-\nabla_{N,j}^2}{2M_j} + \sum_{i,j>i} \frac{Z_i Z_j}{|\mathbf{R}_i - \mathbf{R}_j|} - \sum_{i,j} \frac{Z_j}{|\mathbf{r}_i - \mathbf{R}_j|} \tag{1.1}$$

where $\mathbf{r}_i$ represents electronic coordinates of ith electron, $\mathbf{R}_j$ the nuclear coordinate for the jth nucleus, $\nabla_{e,i}^2$ is the Laplacian operator for the ith electronic coordinate, $\nabla_{N,j}^2$ is the Laplacian operator for the jth nuclear coordinate, M_j is the mass of jth nuclei, and Z_j is the charge of the jth nuclei [1]. Each of the five terms has a simple physical meaning. The first two term are only-electronic related and represent the kinetic energy of individual electrons and potential energy between each pair, T_e and V_e. The third and fourth terms are the corresponding only-nuclear terms and represent the kinetic energy of the nuclei pairs, T_N and V_N. It is the last term, V_{eN}, that is responsible for the aforementioned Coulomb *attraction* between electrons and nuclei. The time-independent Schrödinger equation (TISE) of the total wavefunction Ψ with this molecular Hamiltonian can be write as:

$$H\Psi\left(\mathrm{r}_1, \mathrm{r}_2, \ldots, \mathrm{R}_1, \mathrm{R}_2, \ldots\right) = E\Psi\left(\mathrm{r}_1, \mathrm{r}_2, \ldots \mathrm{R}_1, \mathrm{R}_2, \ldots\right) \tag{1.2}$$

It is not possible to solve the TISE for the full molecular Hamiltonian even for the simplest molecules. In order to gain an intuitive insight, it is ex-

[1] In Equ. 1.1, the spin of the electrons are neglected for simplicity. Whereas, the spin of the electrons usually plays an important role, especially in the molecules which have atoms with larger atomic numbers. A typical example is the spin-orbit coupling effect in the CH_2IBr and CH_2I_2 in Chap. 5 of this dissertation. The spin-orbit coupling from iodine atom(s) from CH_2IBr and CH_2I_2 leads to two sets of asymptotic states along the C-I dissociation coordinate which can be seen from Fig. 5.11. The energies between the two asymptotes has a different in the order of 1 eV.

tremely useful to make approximation, such as the Born-Oppenheimer (BO) approximation, which has been treated as the cornerstone of understanding of chemical processes using quantum mechanics. [30]

It is an adiabatic picture based on the condition that the timescale for electronic motion is generally much more rapid than that for nuclear motion due to the relative masses of the electrons and nuclei, thus the electrons can instantaneously adjust to the motion of nuclei and, in return, the nuclei can be treated as moving in a time-averaged potential generated by the rapidly moving electrons, such that the total wave function $\Psi(\mathbf{r}_i,\mathbf{R}_j)$ in *an any given electronic state* can be assumed as:

$$\Psi(\mathbf{r}_i, \mathbf{R}_j) = \psi(\mathbf{r}_i; \mathbf{R}_j)\chi(\mathbf{R}_j) \tag{1.3}$$

$\psi(\mathbf{r}_i;\mathbf{R}_j)$ is the electronic portion of the wave function and $\chi(\mathbf{R}_j)$ the nuclear portion. One needs to keep in mind that $\psi(\mathbf{r}_i;\mathbf{R}_j)$ has a parametric dependence on the nuclear coordinates $\mathbf{R}_j$, since the electrons sensitive to changes in nuclear position. On the other hand, $\chi(\mathbf{R}_j)$ is only dependent to the nuclear coordinates, since we consider the nuclei as evolving in a time-averaged potential along with the nuclei repulsion generated by the rapid motion of the electrons. This time-averaged electronic potential along with the nuclei repulsion, is known potential energy surface, or PES.

Mostly, under the BO approximation of the separation of electronic and nuclear wavefunction, the mapping of the electronic energy of the system as a function of nuclear coordinates can be defined by the Schrödinger equation of the electronic part:

$$\hat{H}^e\psi\left(\mathbf{r}_i; \mathbf{R}_j\right) = E^e\left(\mathbf{R}_j\right)\psi\left(\mathbf{r}_i; \mathbf{R}_j\right) \tag{1.4}$$

Where $\hat{H}^e$ is the electronic part of the Hamiltonian and E^e the electronic energy. By solving this equation for the different nuclear configurations along, $\mathbf{R}_j$, the PES is mapped. If the nuclear configuration is varied along any particular coordinate and E^e is calculated at all these fixed configuration, then the PES of the molecule along that particular vibrational coordinate is generated. For a molecule with N ($N\geq 2$) atoms, mostly there are $3N$-6 ($3N$-5, when N=2) nuclear internal degrees of freedom regardless of the 3 (2, when N=2) rotational and 3 translational degrees of freedom. [2] And the

[2]For linear molecules, there are $3N$-5 internal degrees of freedom. For instance, CO_2 and CS_2 have 4 since they only have 2 rotational degrees of freedom.

potential energy is a function of all these nuclear internal coordinates. The motion of the nuclei under BO approximation can be treated as propagating on a PES, thus the chemical processes may be predicted if the shape of the relevant electronic PES is known. The PESs for multiple states are also available by solving the time-independent Schrödinger equation (TISE) for each electronic states. Fig. 1.1 bottom left panel shows a typical manifold of hypothetical potential energy surfaces with both ground and excited states, as well as the cationic state manifold. Conceptually, absorption of a photon (the pump process) promotes the electrons to an electronic excited state, and the nuclear wavefunction is projected on the manifold of vibrational states of that excited PES, result in a wavepacket which moves on the excited PES. In this manner, the PES becomes a very useful tool when understanding the chemical processes or the nuclear motions along with the excited states.

1.2 Non-adiabatic dynamics and conical intersection in polyatomic molecules

The validity of the adiabatic picture under BO approximation is typically excellent, since the electronic dynamics are generally much more rapid then any nuclear motion. Another way of thinking is that the timescales for quantum dynamics are generally dictated by the inverse of the energy-level spacing, and the BO approximation is valid whenever the spacing between the PESs (electronic spacing) are much larger than the spacing between the vibrational levels (nuclear spacing). However, there are cases where the different PESs come close together, and the timescales for electronic dynamics in the vicinity of this near-degeneracy can be comparable to, or even longer than, the timescales for nuclear dynamics. Thus these adiabatic PESs are coupled by vibrational motions and the BO approximation breaks down, in which it is no longer possible to separate electronic and nuclear motions, leading to the non-adiabatic processes. The different electronic states become strongly mixed in level crossings, implying there is a large change in electronic-state character (i.e., the shape of the electronic wave functions) with respect to any change in nuclear coordinate. The coupling between PESs become quite large exactly when electronic states come close together in energy.

For a diatomic molecule with only one internal degree of freedom (vibration between the two nuclei), two potential energy curves corresponding to

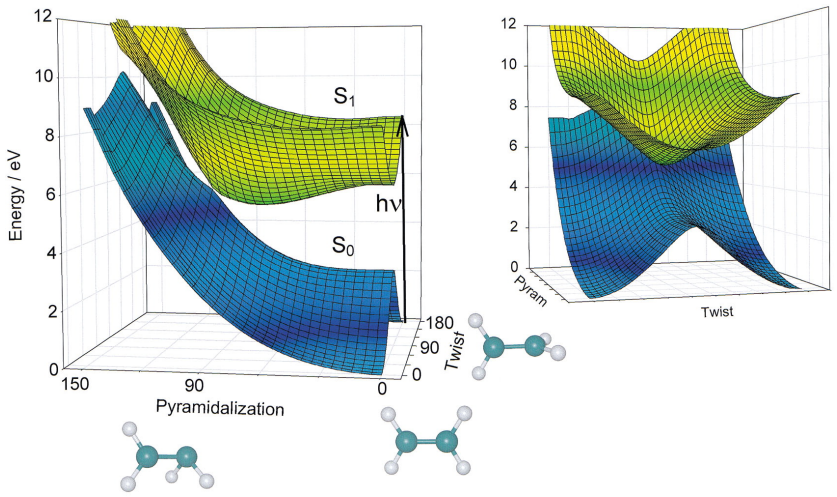

Figure 1.2: **A conical intersection between ground (S_0) and first excited (S_1) state of ethylene molecule (C_2H_4), as a function of the pyramidalization and twist angles** A photo excitation projects a wavepacket from S_0 minimum to S_1 and the nuclear wavepacket quickly evolves towards to the CI, followed with the transition to S_0. The figure is reused from Ref. [31]

electronic states of the same symmetry in general are not degenerate from all the atomic distances, and the positions along the curves come close are called *avoided crossing*. For polyatomic molecules which have more than two internal degrees of freedom, there are a set of isolated points where two PES can touch, forming the so called "conical intersections (CIs)" [32, 33, 30]. Fig. 1.2 shows a conical intersection between two electronic PESs of the ethylene molecule along the twist angle and pyramidalization coordinates. At these avoided crossing and CIs, and the vicinity around them, the timescales of the electronic and nuclear motions are comparable, and the BO approximation breaks down. Non-adiabatic transitions between different electronic states occur. An importance example in polyatomic molecules is the internal conversion of the electronic excitation into nuclear motion facilitate by the CIs, and it plays a crucial role in physical, chemical and biological processes, such as the photoprotection of DNA/RNA bases under internal conversion through CIs [3]. Although the BO approximation is not valid under these crossings, this picture is still useful provided that the surface is well described by it in all other areas of configuration space.

1.3 Combining spectroscopic and structural probes on excited state dynamics

Though the excited state dynamics undergoes both energetic and structural changes with rich information content, the quantum dynamics of interest are filtered by the coordinate-dependent matrix elements of the chosen experimental observable. Thus, it may be only through a combination of experimental measurements and theoretical calculations that one can gain insight into the internal dynamics, and a more complete picture of the reaction dynamics, such like a "molecular movie" may be able to built up. A typical example is the photoinduced ring-opening of 1,3-cyclohexadiene (CHD) to 1,3,5-hexatriene (HT), which represents the prototypical electrocyclic reaction with the conjugated system. This ring-opening reaction proceeds by a non-radiative relaxation through one or more CIs to the ground state and it has been studied extensively in the gas phase by optical and X-ray spectroscopies [34, 35, 36, 19, 37, 38, 39, 40]. Due to the preferential sensitivity to the electronic wavefunction in different electronic states, these studies mapped out the relaxation pathways from the excited state to the ground state through CIs and reveal the relevant time scales. However, the ring-opening picture has not been able to be viewed directly in the structural changes on atomic space at their timescales [41, 42, 43, 44, 45]. Intrinsically, this can be resolved by structural probe with enough spatial and temporal resolutions. With the recent advancement of the seminal relativistic ultrafast electron diffraction (rUED) [46, 47], which provide sub-*å*ngström and femtosecond resolution in space and time, Wolf and co-authors were able to resolve the atomic motion on femtosecond timesscales for the photochemistry [48].

The electron diffraction measurement of the CHD ring-opening dynamics provided a direct view of the structural transformation to HT, providing very useful complementary information content to the previous spectroscopic studies. Thus it is necessary to combine both techniques to follow the undergoing dynamics with both spectroscopic and structural signatures. In this dissertation, my goal is to combine two different time-resolved techniques, time-resolved ionization spectroscopy and relativistic ultrafast electron diffraction to follow the coupled electronic and nuclear dynamics.

In order to illustrate the combined methodology, I make use of CH_2I_2 as an example and show multiple probes in Fig. 1.3. In the figure, the simplified

state potentials from the calculation are plotted in different colors indication the ground (black), excited (red-dissociative and cyan-bound), and cationic (dark yellow). The dynamics starts from the initial population in the excited state after the UV excitation, as the wavepacket evolves along the potentials, the molecule is probed with several processes as shown with cartoons and arrow in the figure:

- Upon the initial excitation, an optical VUV pulse ionizes the molecule to the continuum, performing a TRPES measurement as the molecule dissociating, in which the photoelectrons are recorded as function of kinetic energy and pump-probe delay as shown with number 1.

- As the wavepacket is moving away from the FC region and relax on the dissociative potentials, the electronic potential energy is converted into nuclear kinetic energy, and upon the ionization to the cationic state, the translational momentum of the fragment ions (CH_2I^+) are recorded, performing a time-and momentum-resolved photoion spectroscopy, indicated as number 2.

- Instead of using an optical pulse as the probe, a MeV ultrashort electron bunch interrogates with the excited molecules, and the diffraction patterns that contain the structural information in the far field are recorded, performing an UED measurement labeled as number 3.

In time-resolved photoelectron spectroscopy, the quantity is no doubt the electronic energies. The final state, the cationic state plays an important role such that the different neutral states can be correlated with different cationic states with a simple picture of the Koopmans' correlation [49, 50, 51]. Thus the wavepacket undergoing different electronic excited states can be viewed from the deferentially measured electron kinetic energies, which makes it useful due to the sensitivity to both *electronic* and *nuclear* degrees of freedom. On the other hand, one can also track time-resolved momentum of a fragment ion, in which the nuclear kinetic energy as a function a time can be directly measured. In this way, one is able to map out the energy flow from the electronic into nuclear degrees of freedoms. In contrast, diffraction techniques do not usually observe exact state(s), but rather the structures that may be related to all states, which makes several main differences compared with the ionization spectroscopies in both experimental measurements and theoretical modeling.

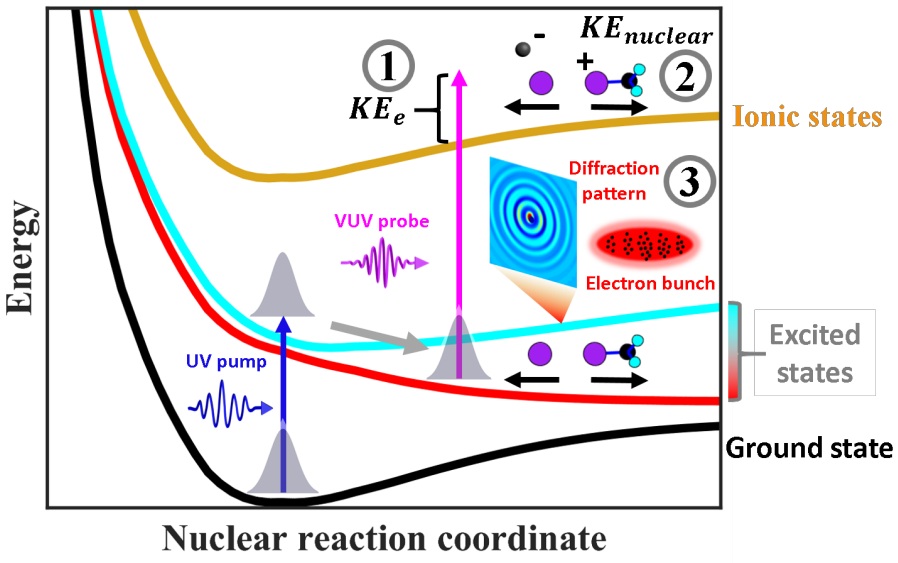

Figure 1.3: **A example schematic illustration of combining spectroscopic and structural probes on CH_2I_2 photodissociaton dynamics.** The simplified of state potentials from the calculation are plotted in different colors indication the ground (black), excited (red-dissociative and cyan-bond), and cationic (dark yellow). Multiple cartoons and arrows depicts the multiple probing processing after the initial UV initial excitation, including: ① photoelectron spectroscopy (photoelectron kinetic energy release) and ② momentum results ion spectroscopy (TKE of photoion) with the optical VUV photon probing, and ③ the structural probe of the diffraction technique with an ultrashort electron bunch.

One of the significant differences between them is the type of information contents obtained. Diffraction experiments ideally provides atomic pair distance as a function of time in the molecule and the basic principle of the diffraction method takes advantage of the much smaller de Broglie wavelength (in Ångström) of energetic electrons (between several KeV to MeV) or X-rays (several KeV) as compare to the wavelength of optical light (hundreds of nm), and at least in principle, can determine the molecular structure. Whereas spectroscopic measurements tend to yield energies as a function of time (e.g. $E_n(t)$). It is also possible to retrieve the structural information from the time-dependent energies, but the experimental data must be in-

ferred to a molecular model. It is typically possible to perform calculations that switch between the two methods. If position of all atoms are known as a function of time, one can calculate the energies of the states as well. Conversely, one can use energetic information to infer structure. However, both kinds of calculations involved significant effort and lead to additional uncertainties, especially when the system employs many degrees of freedom.

In both techniques, charged particles are experimentally detected, whereas, the signal levels between the ionization and the diffraction method are quite different and need to be considered. The signal of the experiment, S may be expressed by a simple equation as,

$$S \propto N_m \cdot V \cdot \varepsilon_{pump} \cdot \varepsilon_{probe} \cdot \varepsilon_{detect} \tag{1.5}$$

where N_m and V represent the number density of the sample and the focal volume around the integration region, respectively. ε_{pump} and ε_{probe} are for the excitation and probing fractions, assuming both the pump and probe processes are linear to the intensities. ε_{detect} reflects the detection efficiency from the detector. In ionization spectroscopy, the photoelectrons/photoions usually allow for very high detection efficiency and single electron/ion can be detected in which ion/electron coincidence measurement has been possible [52]. Whereas, in the diffraction experiment, such as electron diffraction, the detection efficiency is orders of magnitude lower than the ionization spectroscope [3] Assuming the measurements are preformed in the same conditions and the pump and probe fractions are roughly the same, the signal level can be order or magnitude lower in the electron diffraction measurement. Often, to improve the signal levels, a very high number of density gas source (using a pulsed molecular nozzle and putting the pump laser and probe electron beam very close to the top of the nozzle to increase the number of density) and higher pump intensity are needed. Meanwhile, the ionization usually takes place when the molecules are populated in the excited state(s), such that the ionization from the ground state are usually avoided, i.e., the signal

[3]The detector for charged particles in a photoionization experiment often consists of one or several electron multiplier, such as micro-channel-plate which gives a gain of $\sim 10^3$ from a single plate. Whereas, this is usually not possible in the detector of high kinetic energy electron in an electron diffraction measurement due to potential damages from the electron, but rather high kinetic energy electrons hit on phosphor screen directly and generate the fluorescence. Thus the amount of light generated from a shower of electrons in the ionization experiment is much more than that from a single electron in the case of an electron diffraction measurement.

to background ratio is high. With ultrafast electron diffraction, in order to obtain better time-resolution, usually the number of electrons is limited to few tens of thousand per bunch in order to avoid space-charge issue. Only a few hundred electrons are scattered from the molecules ($\sim$1%), and these scattering electrons are contributed from molecules that are populated in both ground and excited states. However, in order to avoid ionization from the optical pump, the UV intensity is usually attenuated and only a few percent (<5%) of the molecules are excited. This makes a high signal to background ratio of UED measurement very challenging compared with the ionization spectroscopy.

1.4 Calculated measurement observables

The ultimate goal is to compare the time-resolved experimental measurement observbles with the theoretical simulated ones, and the ideal method to simulate the non-adiabatic dynamics is performing calculations fully in quantum mechanical manner, i.e., numerically solving the time-dependent Schrödinger equation for both electronic and nuclear degrees of freedom. This requires the establishment of the multidimensional PESs in order to propagate the nuclear wavepacket. It is already very expensive to generate the multi-dimensional PESs, and in addition, calculating the nuclear wavefunction induces an exponential scaling. For polyatomic molecules, one needs to generate a map with particular number of sampling points, N, for each nuclear degree of freedom. If the system has M nuclear internal degrees of freedom along a PES, solving the Schrödinger equation will scales to N^{3M}. Thus, the whole process is very expensive and limited to a very few nuclear degrees of freedom.

Due to the extremely expensive calculation cost, another semi-classical time-dependent treatment of the non-adiabatic dynamics, trajectory surface hopping technique, is widely used for studying excites state dynamics [53, 54]. Different from the quantum wavepacket simulation, the electronic and nuclear degrees of freedom are treated differently, where the electronic degrees of freedom are treated quantum mechanically, and the nuclear degrees of freedom are treated classically. Fig 1.4 showcase two cartoon schematics of the quantum wavepacket simulation and trajectories surface hopping calculation between two states when CI is involved. For the TSH calculation in panel (b) the wavepacket is approximated as a bunch of classical nuclear trajectories, whereas the multi-dimensional PESs are still calculated quantum

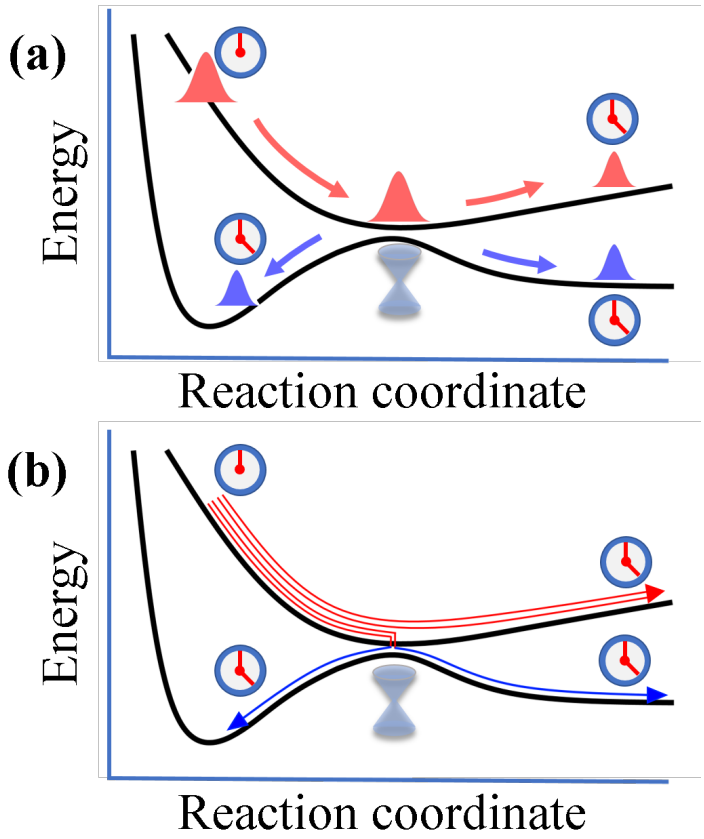

Figure 1.4: **Cartoon schematics of quantum wavepacket and trajectory surface hopping propagation along hypothetical molecular potential energy surface.** Panel (a) depicts an initial wavepacket on the excited state propagating along the potential energy surface followed with a population splitting to the ground state *via* a conical intersection. Whereas in panel (b), shows the trajectory surface hopping, in which the propagating wavepacket is approximated as a bunch of classical nuclear trajectories.

mechanically. The trajectories are sampled at different regions of the potential and each individual trajectory propagates independently using Newton's equation of motion. During its propagation, the energies, gradients/forces, and non-adiabatic couplings are calculated on-the-fly at every time step for the nuclear geometry and the transition probability between states are evaluated. Whether a hop takes place between the current electronic state to

others is determined by a stochastic algorithm which uses these transition probabilities. At each time step, the PESs are regenerated on-the-fly with the propagation of the nuclear trajectories [55].

Although TSH is not fully quantum mechanical, there are several significant advantages that make it as one of the most effective and popular semi-classical time-dependent methods. First, the trajectories are propagated independently and each individual trajectory is only propagated on one BO electronic state at any time. In this way, the trajectories are allowed to be propagated with all nuclear degrees of freedom unlike quantum wavepacket simulation. This makes it possible to study much larger molecular system with many nuclear degrees of freedom. Second, the non-adiabatic processes, i.e., electronic transitions across different electronic states, can be simulated in a proper manner. In this way, the dynamics path ways, excited state lifetime, electronic state populations and branching ratio, energy and charge transfer rates, quantum yield can be evaluated by estimating a number of trajectories. This is extremely useful to mimic the non-local wavepacket dynamics which is very rich in the coupled electronic and nuclear dynamics.

Third, the trajectories contains both time-dependent energetic and structural information which could be used to directly simulate the measurement observables. This makes the combining of different experimental techniques more favorable since the same TSH calculation can be used to simulate multiple measurement obserables and directly compare with the measurements. For example, all the measurement observables shown in Fig. 1.3, including photoelectron kinetic energy, time-resolved photoion kinetic energy, and electron diffraction patterns, can be calculated. Fig. 1.5 showcases a example of the available information content from trajectories. Panel (a) shows two example trajectories, with state potential and indices as a function of time, whereas panel (b), (c) and (d) indicate the different calculated observables. These simulated observables include:

- Photoelectron spectrum, in panel (b), can be obtained by evaluating the Dyson correlation between the neutral state and the cationic states.
- In panel (c), the translation kinetic energy of the dissociating fragment CH_2I can be estimated classically with the time-dependent geometries in the trajectories.
- Panel (d) shows two line plots of the pair distribution functions (PDFs) respect to two different molecular structures, the ground state CH_2I_2,

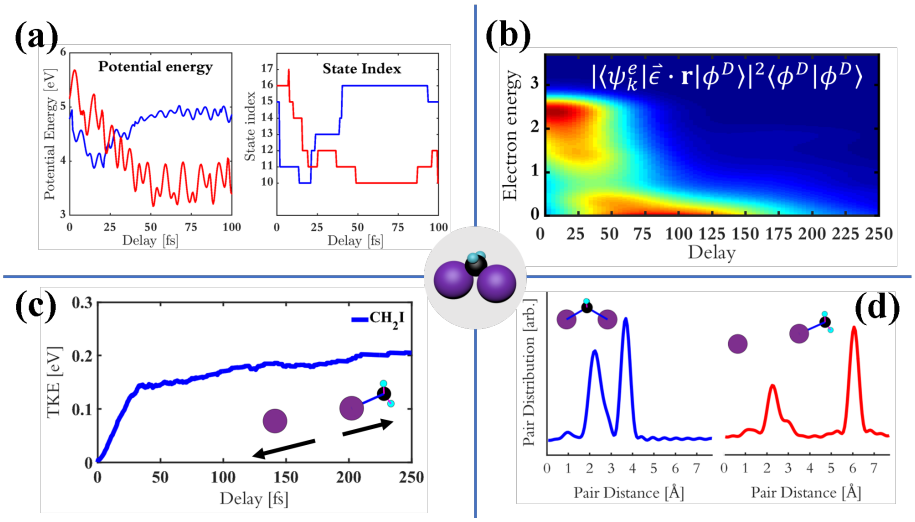

Figure 1.5: **A example schematic illustration of combining spectroscopic and structural probes on CH_2I_2 photodissociaton dynamics.** In this figure, 4 panels are showing the relevant calculated opbservables respect to the measurements in 1.3. Panel (a) depicts two example trajectories for the TSH calculation in the views of time-dpendent potential energy and state indices, whereas panels (b), (c) and (d) indicate the different calculated measurement observables, including, the photoelectron spectrum, the fragment (CH_2I) translational kinetic energy, and pair distribution functions, respectively. The calculations were carried out by Dr. Philipp Marquetand and Dr. Tamás Rozgonyi.

and the dissciative CH_2I and I.

1.5 Contents of this dissertation

In Chap. 2, experimental methods including time-resolved photoelectron spectroscopy, momentum-resolved photoion spectroscopy, and ultrafast electron diffraction are discussed in detail. The ultrafast laser system, the optical harmonic generation, the experimental apparatus, data analysis protocols, and simulation of the measurement observables will be presented.

Chap. 3 to Chap. 5 present the major experimental results. A series of molecular systems are examined, and different non-adiabatic dynamics are

studied. In Chap. 3 and Chap. 4, two important organic chromophores, *cis,cis*-1,3-cyclooctadiene (cc-COD) and uracil, are experimentally studied, focusing on their internal conversion and isomerization back to the ground state *via* CIs. TRPES measurements are carried out with UV/VUV pump/probe scheme for both molecular systems. The measurements of cc-COD in Chap. 3 are interpreted by comparing the measured TRPES with the calculated one, and some discrepancies between them leave the question that whether the theory is good enough to predict the measurements. In order to test the theory, especially the effect of the dynamics correlation, in Chap. 4, a TRPS experiment of uracil is preformed and the results are used to compared with calculated signals from three levels (CASSCF, MRCIS, amd XMS-CASPT2) of theory, focused on the much debated population trapping in the first optical bright state, S_2. In Chap. 3 and Chap. 4, the measurements are focused on TRPES. However, TRPES may only provide a narrow view of the electronic energy probe. So in Chap. 5, I developed a combination of both energetic and structural probes on internal conversion and dissociation dynamics of CH_2I_2 and CH_2IBr. Multiple observeables, including time-resolved photoelectron, momentum-resolved photofragment ion, and electron diffraction pattern, are experimentally measured and the signatures in the observables are well captured by the calculated measurement observables from high level theory TSH calculations. Particularly, a non-local quantum wavepacket dynamics of the dissociation of CH_2I_2 can be well reflected by different groups of classical nuclear trajectories and the combined spectroscopic and structural probes showcases surprisingly high sensitivity on following the coupled electronic and nuclear non-adiabatic dynamics.

Finally, Chap. 6 provides a general conclusion and describe an outlook for the future work utilizing novel ultrafast soft X-ray for spectroscopy, and ultrafast hard X-ray for diffraction.

Chapter 2

Gaseous time-resolved ionization spectroscopy and ultrfast electron diffraction

2.1 Introduction

Chap. 1 provided a basic physical and/or chemical pictures of molecular dynamics, the different experimental time-resolved spectroscopic and diffraction methods, as well as the theoretical treatment of the calculated measurement observables. As per the interests of the coupled electronic and nuclear dynamics in this dissertation, the pump process in all the measurements comes with an ultrashort optical pulse in the deep UV regime ($\sim$260 nm), which generates a wavepacket in the neutral excited state(s), initiating the dynamics. Due to different probe process, either an optical VUV pulse or an short bunched of electron, the experimental setup, the data analysis, and the interpretation with the aid of theoretical measurement observables vary dramatically between the different approaches. In this chapter, I discuss in detail of time-resolved photoelectron spectroscopy (TRPES) and its variant, time-and momentum-resolved photoion spectroscopy (TRPIS), as energetic probes, and ultrafast electron diffraction (UED) as a structural probe. I describe experimental constructions, data analysis, as well as how to simulate relevant measurement observables with the aid of computer simulations.

The rest of the chapter is arranged as follows: TRPES as well as its variant, TRPIS, are introduced with in great details, including the pump and

probe light harmonic generations, photoelectron and photoion spectrometer, data acquisition and analysis. These two techniques own a similar experimental setup, and both of then can give an energetic probe, and can be switched between each other fairly straightforwardly. I then switch gears to ultrafast electron diffraction. The gaseous diffraction theory will be reviewed at the beginning, followed with a brief description of the SLAC ultrafast electron beam line and experimental data analysis methods. The last section in this chapter covers the simulation of the measurement observables according to the trajectory surface hopping calculations.

2.2 Time-resolved photoelectron spectroscopy

In Chap. 1, I used TRPES as an example to illustrate the pump-probe framework. Before I step into the details of the experimental setup, it is useful to review some mathematical description of the TPPES method. TRPES makes use of photoionization to the continuum as the probe in order to track the wavepacket evolving in the neutral state(s). In a TRPES experiment, the quantity of observable is no doubt the time and kinetic energy resolved photoelectrons. Fig. 2.1 illustrates the basic idea of a TRPES with three Born-Oppenheimer (BO) electronic state, a, b, and c. A photon in the pump laser pulse excited a molecule from state a (ground state) to the intermediate excited state b, creating a wave packet. From the intermediate state, the molecule absorbs an amount of energy corresponding to the photon energy of the probe pulse, leaving an excess energy equal to the probe photon energy minus the difference in the energy between the states c and b. The excess energy, ε_i, is carried away by the outgoing photoelectrons as kinetic energy, and this energy is monitored as a function of the pump-probe delay.

As shown in the figure, while the wave packet evolves at different position of the PES of state b, the photoelectron kinetic energy remaining correlates to the potential energy different between state b and c. If the different between the two states is monotonic as a function of the nuclear coordinate, R, the position of the wave packet on the intermediate state has a one-to-one relationship with the kinetic energy of the photoelectron. This makes TPRES to be a useful tool such that the wave packet motion in the intermediate state may be mapped out if making a series of snapshots of monitoring the kinetic energy of photoelectron. Thus TRPES can be treated as a wave placket methodology.

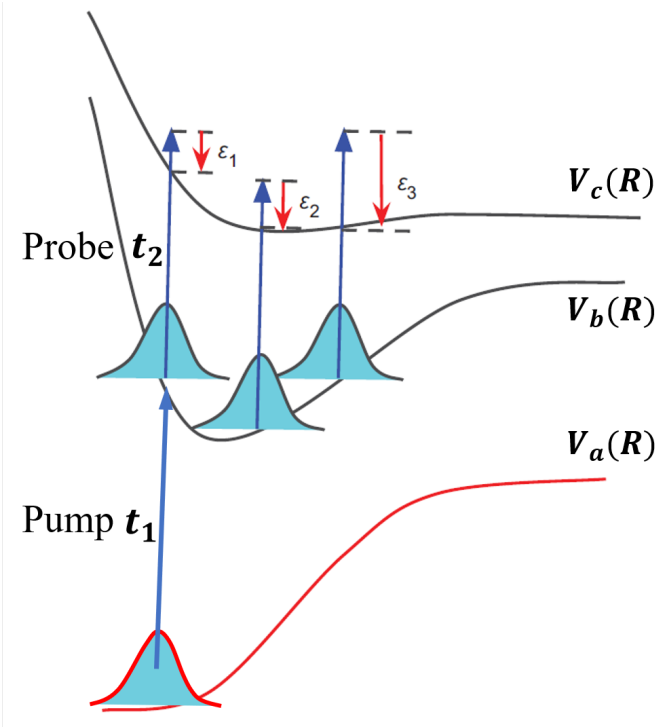

Figure 2.1: **Illustration of how TRPES can be used to follow the evolution of wave packet on an excited state potential.** Three Born-Oppenheimer electronic state potential energy surfaces represents the ground state $V_a(R)$, intermediate excited state $V_b(R)$, and final ionic state $V_c(R)$. At each each nuclear coordinate R, the photoelectron kinetic energy ε_i depends on the difference between the two potentials, b and c. This figure is modified from Ref. [29] with authors' permission.

Experimentally, a TRPES measurement yield a time and energy resolved spectrum map, i.e., the numbers of photoelectron as a function of pump-probe delay and photoelectron kinetic energy. In connection to the wave-function picture in the PESs of b and c, the spectrum at a particular pump-probe delay τ is given by the probability of finding photoelectrons with a kinetic energy with ε in the final cationic state. It is useful to consider from a perturbation and analytic picture of the pump and probe processes with external fields on the system behind the measurement observables. Assume a nuclear vibrational wavefunction $\chi_a(R, t = 0)$ in the ground state a. State a and b are resonantly coupled by the pump field $E_1(t)$ centered at time, t_1.

With first-order time-dependent perturbation theory, the wave function on the excited b state can be expressed as,

$$\chi_b^{(1)}(R,t) = \frac{1}{i}\int_0^t dt_1 e^{-iH_b(t-t_1)}\left(-\mu_{ba}E_1\left(t_1\right)\right)e^{-iH_a t_1}\chi_a(R,0), \tag{2.1}$$

where H_a and H_b are nuclear Hamiltonian of the vibrational wave function on the potential energy surface (PES) corresponding to the the electronic states a and b. μ_{ba} and μ_{cb} (next equation) are the transition dipole moment between state a and b and between state b and c, respectively. Incorporating the subsequent interaction with the probe pulse, $E_2(t_2)$, the wave function in the final state c can be express by the second order perturbation theory as

$$\chi_c^{(2)}(R,t) = \frac{1}{i}\int_0^t dt_2 e^{-iH_c(t-t_2)}\left(-\mu_{cb}E_2\left(t_2\right)\right)\chi_b^{(1)}\left(R,t_2\right), \tag{2.2}$$

By assuming the pump pulse is localized in time around $t_1 = 0$, so that the initial wave function on state b will be $\chi_b^{(1)}(R,0)$ and Equ. 2.2 can be rewritten as

$$\chi_c^{(2)}(R,t) = \frac{1}{i}\int_0^t dt_2 e^{-iH_c(t-t_2)}\left(-\mu_{cb}E_2\left(t_2\right)\right)e^{-iH_b t_2}\chi_b^{(1)}(R,0). \tag{2.3}$$

Due to the fact that the final state is ionic, thus the nuclear Hamiltonian $H_c = H_I + \varepsilon = T + V_1(R) + \varepsilon$, where T is the nuclear kinetic energy operator, H_I is the Hamiltonian for the ionic state, and ε is the electron kinetic energy. One can also write H_b as $T + V_b(R)$ and the probe field as $E_2\left(t_2\right) = \frac{1}{2}E_{02}\left(t_2\right)\left(e^{+i\omega_2 t} + e^{-i\omega_2 t}\right)$ where $E_{02}(t_2)$ is the amplitude envelope of the function on the ionic state associated with a photoelectron energy ε. ω_2 is the laser frequency of the probe pulse. By plugging $E_2\left(t_2\right)$ and H_b and H_c into Equ. 2.3, the wavefunction on the cation ionic state then can be rewritten as,

$$\begin{aligned}\chi_{c,\varepsilon}^{(2)}(R,t) =& \frac{-1}{2i}e^{-i(H_I+\varepsilon)t}\int_0^t dt_2 e^{i(T+V_I(R)+\varepsilon)t_2}\mu_{cb}E_{02}\left(t_2\right) \\ &\times\left(e^{+i\omega_2 t} + e^{-i\omega_2 t}\right)e^{-i(T+V_b(R))t_2}\chi_b^{(1)}(R,0).\end{aligned} \tag{2.4}$$

This equation becomes useful since the wave function in the state of the cation can be associated with the state potential between the excited state b and cation state c, and the kinetic energy ε of the outgoing photoelectron. To

assume a case of an idealized experiment in which the evolution of the wave function during the probe pulse is neglected. This allows one to neglect the commutators between the T and V for both H_I and H_b inside the integral. We again make the rotation-wave approximation, where we keep only the on-resonance $e^{-i\omega_2 t}$ term from the applied filed. The above equation then can be rewritten as,

$$\begin{aligned}\chi^{(2)}_{c,\varepsilon}(R,t) =& \frac{-1}{2i} e^{-i(H_I+\varepsilon)t} \\ & \times \int_0^t dt_2 e^{i(V_I(R)-V_b(R)-\omega_2+\varepsilon)t_2} \mu_{cb} E_{02}\left(t_2\right) \chi^{(1)}_b(R,0)\end{aligned} \tag{2.5}$$

The probability of finding an electron in the cation state then can be obtained by the norm in the cation state wavefunction which can be expressed as,

$$P(\varepsilon,t) = \left\langle \chi^{(2)}_{c,\varepsilon}(R,t) \mid \chi^{(2)}_{c,\varepsilon}(R,t) \right\rangle \tag{2.6}$$

By doing the integral, one will find that the probability will be only profound when the values $V_i(R) - V_i(R) - \omega_2 + \varepsilon$ approaching zero, i.e., the energy of the photoelectron produced, ε roughly follows the different between the potentials where the wave packet is located in the nuclear coordinate:

$$\varepsilon = \omega_2 - \left(V_c(R) - V_b(R)\right). \tag{2.7}$$

This will be experimental reflected in the photoelectron kinetic energy yield in which the kinetic energy of the photoelectron is equivalent to the probe photon energy minus the ionization potential between the intermediate state, and the probability is relevant to the integral of the nuclear wavefunctions.

2.2.1 TRPES experimental setup

Figure 2.2 showcases a schematic diagram of the gas phase TRPES experiment. The experiment has to be conducted in a vacuum chamber with a baseline pressure in the order of 10^{-7} to 10^{-6} Torr of pressure. The molecules are delivered either by a diffusive or pulse nozzle into the vacuum chamber. In conjunction with a velocity map imaging (VMI) spectrometer (can be other type of electron spectrometers, such like a time-of-flight magnetic bottle), and a position sensitive detector, the kinetic energy and angular distribution of the photoelectron is obtained. The setup involves a pump-probe frame

work as shown in Fig. 2.2, the electrons generated by the probe pulse then are projected onto a two-dimensional detector with the aid of an external electromagnetic field, and the information content is preserved by the momentum distribution of the photoelectrons.

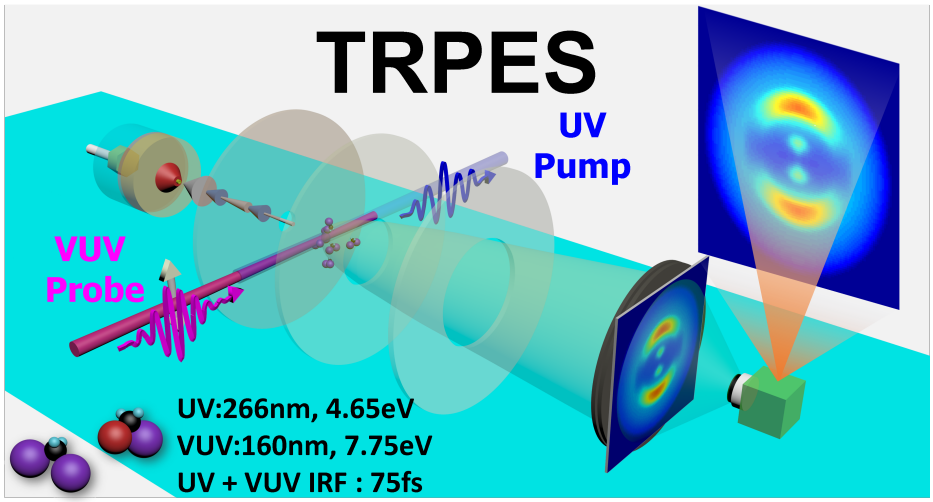

Figure 2.2: **A schematic cartoon diagram of time-resolved photoelectron spectroscopy.**

The probing laser pulse lies in the region of vacuum UV (VUV) regime and the advantage of using the VUV light being as the probe is the ability of ionizing from everywhere in the excited states, avoiding the "windowing effect", but without having the background from the ionization of the ground state. Both pump and probe beams can employ a weak field single photon excitation and ionization, making the so called 1+1' configuration. [56, 57] The weak field 1+1' pump and probe configuration is also in great favor to the theoretical modeling, such that both the pump and probe processes can be calculated in great accuracy. A typical examples can be seen from Ref. [58]. The intensity of the pump pulse is usually below 10^{12}W/cm^2 and the probe pulse intensity is more than an order of magnitudes lower than the pump.

2.2.2 VUV light generation and UV-VUV pump-probe setup

A commercial ultrafast Ti:sapphire laser systems (KMLab) was applied to the time-resolved photoelectron spectroscopy. The laser consists of an oscillator and an amplifier setup, outputting a ∼30 fs, ∼1.2 mJ pulse at central wavelength of 780 nm (ω) with a repitition rate of 1 kHz. Fig. 2.3 shows the optical layout of the VUV pulse generation together with the UV-VUV pump-probe setup and a velocity-map-imaging (VMI) spectrometer. This configuration was used for the photoelectron and/or photoion experiments in Chap. 3 ,4 and 5. [1] The total IR (fundamental, ω) output is split into two components from a beam splitter with 80/20 reflection/transmission. The main portion from the reflection is sent into a frequency tripling stage, generating the 3^{rd} harmonic generation at central wavelength of 260 nm (THG, 3ω, 4.75 eV). The tripling stage consists of a series of crystals along the beam path. The generated 3ω is then split into two arms, in which the main component is mixed with the small portion of the transmitted IR beam in a gas cell for fifth-harmonic-generation (5ω, 7.94 eV) at the vacuum-UV (VUV) regime. The VUV and the small portion of the UV are then sent into the interaction chamber, forming a pump-probe geometry.

One can see a detailed configuration of the UV generation in the frequency tripling state from the sub-panel inside Fig. 2.3. The UV generation is facilitated with two Beta Barium Borate (β-BaB_2O_4, BBO) plates successively along the propagating of the fundamental. The first BBO plate generates the second harmonic generation (SHG, $\omega + \omega$) and the second crystal generates the third harmonic generation (THG, UV) by mixing the collinearly propagated SHG with the residual fundamental (2ω+ω). Both generations are under Type I phase matching condition and it requires that the two pump and seed beams are in same polarization direction, whereas, the generated signal beam is 90° polarized with respect to the incoming beams. In order to fulfill the right polarization in the second BBO crystal, a zero-order dual-band waveplate (WP) is applied in order to rotate the ω ($\lambda/2$ @ 780nm) for 90°, and 180° for 2ω (λ @ 390nm). As shown in Fig. 2.3, the outgoing UV beam is in same polarization with the incoming IR beam (P-Polarization). As the ω and generated 2ω propagating thought the crystals, one needs to

[1] The TRPES at Chap. 3 was first performed at National Research Council (NRC) of Canada, and then was reproduced in Stony Brook. Whereas, the TRPIS in Chap. 3 and TRPES in Chap. 4 and Chap. 5 were conducted in Stony Brook.

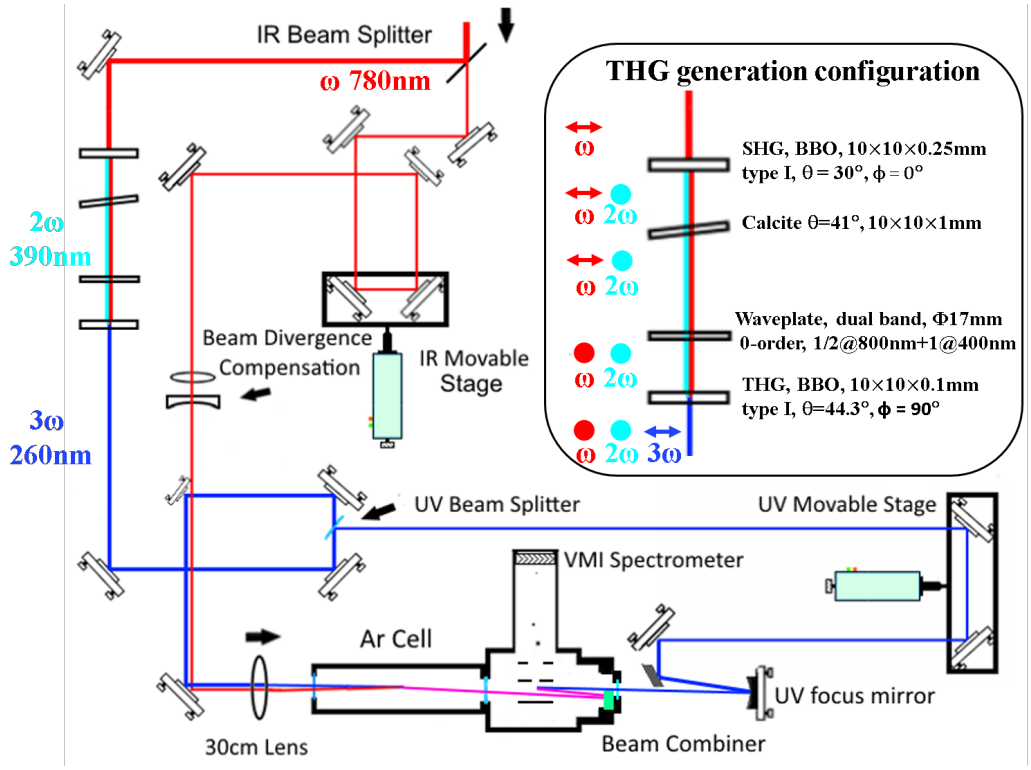

Figure 2.3: **Optical layout of the UV/VUV pump/probe setup used in the TRPES and TRIIS experiments.** The color-coded lines represent different harmonic generations: red is for IR (ω), cyan SHG (2ω), blue THG (3ω) and, purple for VUV (5ω), respectively. One movable stage is used to temporally overlap the IR and UV pulses for VUV generation, and a second one is used to perform the UV-VUV pump-probe measurement. A sub-panel displays the details of the UV frequency tripling stage with the optical components and the relevant polarizations directions. The UV and VUV beams are combined and loosely focused to a molecular beam in a VMI spectrometer under vacuum, and photoelectron or photoion are projected to a 2D position-sensitive charged particle detector.

take into account the effect of the group-velocity-mismatch (GVM) in order to make the THG efficiently. Generally, different colors of light transmit through the materials with different group velocities, and the limited thickness of the SHG crystal and the waveplate induce a temporal "walk-off" between the foundamental and second harmonics. Usually, a negative dis-

persion compensator made of calcite (c-cut, 41°) is used to delay the residual IR with respect to the SHG, bringing them back together in the THG crystal. This setup gives about 30 μJ of UV output, and several UV dielectric mirrors are used to clean the residual IR and SHG before sending into the vacuum chamber. A 15/85 reflection/transmission 2mm-thick UVFS beam splitter is inserted into the beam with 45° incidence angle to separate the UV into two arms, with the reflected beam (<5μJ) being used as the pump and the transmitted beam (~25 μJ) for generating the VUV pulse.

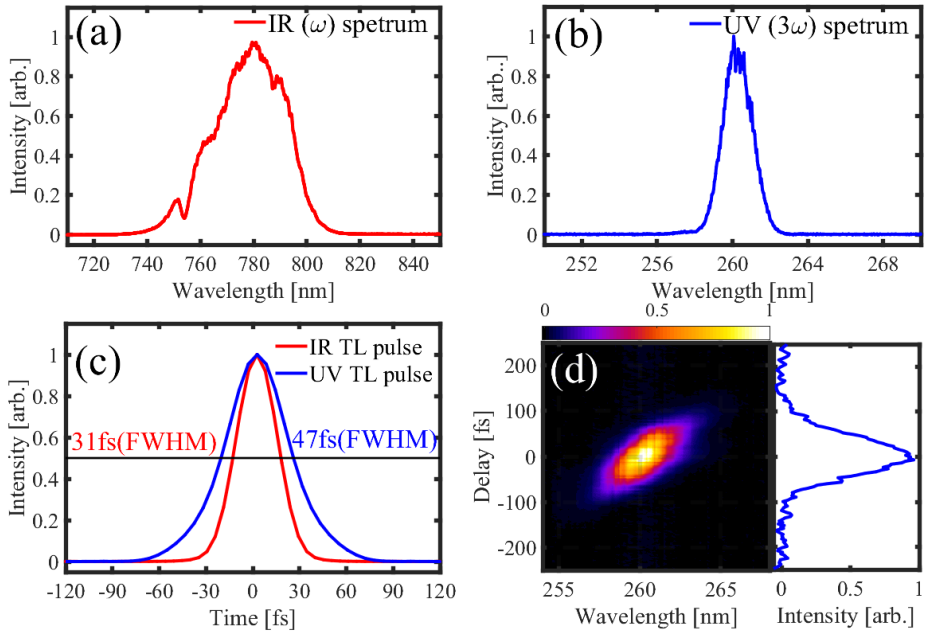

Figure 2.4: **Spectrum and pulse characterization of the UV generation.** In this figure, panels (a) and (b) show the spectra of the fundamental IR and generated UV. Panel (c) shows the pulse shapes according to the measured spectra by assuming a transform limited (TL) Gaussian shaped pulse, whereas panel (d) displays a measured 2D SD-FROG trace and 1D cross-correlation line-out. The IR spectrum is taken with a Ocean Optics HR4000 spectrometer, the UV spectra was taken with the high-resolution AvaSpec-2048L UV spectrometer, and the FROG traces was collected with a home-built SD-FROG setup in conjunction with a Ocean Optics USB2000 spectrometer.

Figure 2.4 illustrates some characteristics of the UV pulse generation.

Panels (a) and (b) shows the spectra from the fundamental IR and UV. The bandwidth of the UV is measured as 1.8 nm FWHM (∼50 millielectronvolt (meV)) centered at 261 nm, corresponding to a transform limited (TL) pulse duration of ∼ 45 fs FWHM. In order to better estimate the pulse shape of UV, a proper characterization with the self-diffraction frequency-resolved-optical-gating (SD-FROG) technique is necessary. [59] The result of the UV SD-FROG trace can be found in Fig. 2.4 panel (d). There is still a chirp to the UV pulse indicated by the tilted shape in the contour plot of the 2D FROG trace. The spectrum integrated line-out gives a cross-correlation width of ∼90 fs FWHM and a FROG reconstruction yields a pulse duration of < 60 fs.

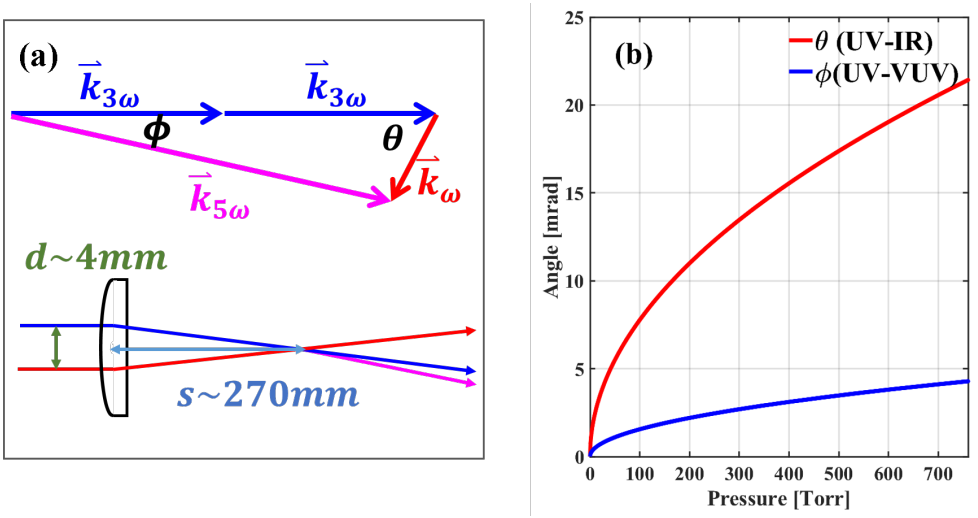

Figure 2.5: **VUV generation phase matching configuration.** Panel (a) shows the phase matching condition of the 5ω in the non-collinear four-wave-mixing configuration. The angle, θ, between the IR and UV is controlled by the transverse separation (d). In panel (b), the phase matching angle between the IR and UV is calculated from the Sellmeier equation as a function of argon gas pressure.

Let us switch gears to the VUV light generation. It is nontrivial to make the fifth harmonic generation VUV compared with the third harmonic generation of UV in crystal. Different from the harmonic generation in crystal, the VUV has reached the transmission cut-off edge of most condensed matter materials with few exceptions [60, 61, 62]. Besides the generation, the

VUV spectrum lies in the region with strong absorption in the atmosphere (mostly corresponding to the absorption from oxygen), therefore the fifth and higher order harmonics need to be generated and propagated under vacuum conditions. In our experiment, the VUV is made from the UV and IR beam in the gaseous of argon, under the phase matching condition of a non-collinear four-wave-mixing ($3\omega + 3\omega$ - $\omega = 5\omega$) scheme [63, 64, 65]. Compared with the collinear geometry, this phase matching angle can be fulfilled under relatively much higher gas pressure [66]. A cartoon diagram of the phase matching geometry can be viewed from Fig. 2.5 panel (a). Panel (b) showcases the calculated phasing matching angle between the incoming IR and UV beams, according to a Sellmeier-type equation as a function of the gas pressure [63, 67]. The UV and IR beams are focused into an argon gas cell by using a plano-concave CaF_2 lens of 30 cm focal length and the phase-matching angle is controlled by the transverse distance between the UV and IR beams, as shown in Fig. 2.5 panel (b). In the residual IR arm, a telescope is applied to adjust the focus position of the IR such that the focuses of the UV and IR can be longitudinally overlap. Approximately 100 nJ of the VUV is generated in the setup.

A schematic diagram of the vacuum chamber and the VMI spectrometer is shown in Fig. 2.6. Once generating the VUV light, IR, UV as well as VUV beams are propagating divergently from up-stream to the interaction chamber through a thin window (CaF_2, 500 μm). [68, 69, 70] Upon reaching the down-stream VUV dichroic mirror, the beams travel between the middle and bottom plates of the VMI setup through a pair of special designed baffles. In the down-stream, the VUV beam is reflected and loosely focused by the dichroic mirror (Layertech GmbH) inside the vacuum chamber back to the VMI plates. The mirror has a high reflectively coating of $> 90\%$ at 0° for 156 - 160 nm light and $< 5\%$ reflectivity for 260 nm and 780 nm, allowing us to get rid of the residual IR and UV. The mirror sits in a movable mirror mount, in order to physically align the VUV beam back into the middle of the VMI plates. On the other hand, the pump UV is loosely focused by a curved mirror into the vacuum chamber and overlapped with the VUV beam in the molecular beam. If the beam travels through the dichroic mirror (6 mm thickness) at the same spot from where the VUV reflected, the temporal smearing between the two beams is minimized. However, any material to the ultrashort pulse will induce dispersion, hence stretching the pulse. In order to avoid the unnecessary dispersion, a custom designed mirror holder is employed in which allows a dichroic mirror and a thin (500μm) CaF_2 window

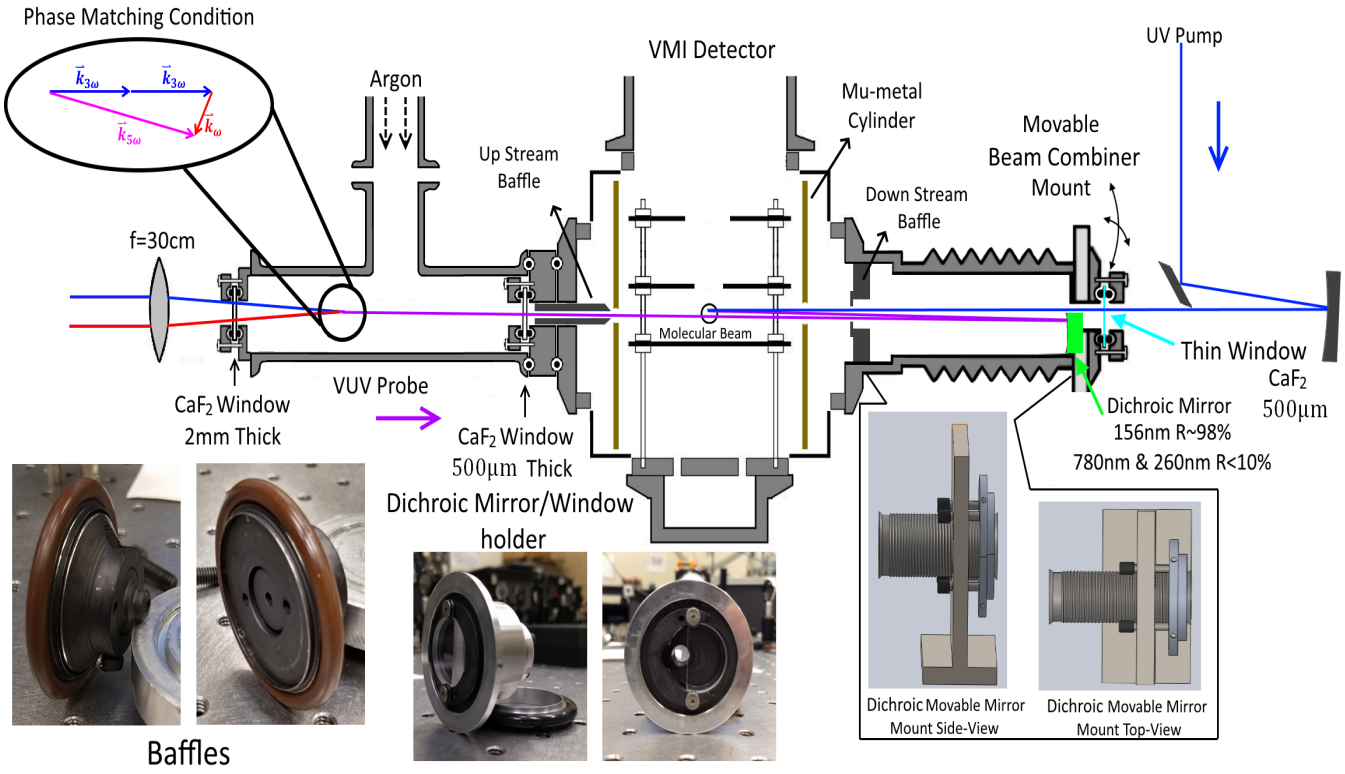

Figure 2.6: **A schematic diagram of VUV generation and velocity mapping imaging spectrometer.** The UV/VUV beams are combined in a velocity-map-imaging spectrometer and the apparatus consists of two main vacuum chambers that are connected each other, the argon gas cell and the interaction chamber. The VMI spectrometer is set in the interaction chamber, including an electrostatic lens and a home-made two-dimension charged-particle detector. Several images and 3D drawings show the baffles, the VUV dichroic mirror holder, and the movable mount which holds the dichroic mirror.

both sitting on the holder which is shown in in two pictures of Fig. 2.6.

2.2.3 Photoelectron and photoion coincidence velocity map imaging spectrometer

The VMI spectrometer employs a continuous molecular beam, an electrostatic lens and a micro-channel-plate (MCP) and phosphor based position-sensitive detector. Fig. 2.7 depicts a cartoon drawing of the VMI spectrometer together with a fast time-stamping camera, TimePix3 camera. The electrostatic lens consists of a standard repeller-extractor-ground electrode lens sitting inside a μ-metal sheet cylinder for magnetic shielding. [71] The pump and probe beams propagate parallel through the plates perpendicular to the molecular nozzle. Above the VMI plates is a $\sim$20 cm long time-of-flight (ToF) tube and at the end of the tube, there is a home-built charged particle position-sensitive 2D detector and the fluorescence light from the phosphor is collected by the TimePix3 camera. [72] Both the pump and probe pulses are linearly polarized with the polarization direction perpendicular to the ToF direction, such that there is symmetry about the laser polarization allowing for an Abel inverse transforming the data.

Fig. 2.8 left panel showcases the VMI static lens assembly. The repeller, extractor and the ground plates are made of thin titanium, sitting on a four-alumina-rod frame held by a KF40 flange. Two Kapton wrapped wires connect to the plates are used to add voltages to the repeller and extractor, respectively, and the ground plate is connected to the chamber body. The plates are relative small (1.25", 38mm, diameter) which makes the whole setup compact. The generated photoelectrons and/or photoions are projected to a home-built charged particle position sensitive detector which consists of two MCPs and a phosphor screen. The MCPs and phosphor screens are sitting on a 6" conflact flange which can be seen in Fig. 2.8 right panel. The MCPs (Photonis, 40 mm active diameter) are orientated in the Chevron configuration for higher electron avalanche efficiency. A P47 type phosphor (Beam Imaging Solution) screen is fixed to the back side of the MCPs. The fluorescence light from the phosphor screen transmit through a window and is focused to the camera. In order to detect both photoelectrons and photoions with a single detector, the VMI voltages are initially negative for collecting photoelectrons. The polarity then is rapidly switched after detection of the

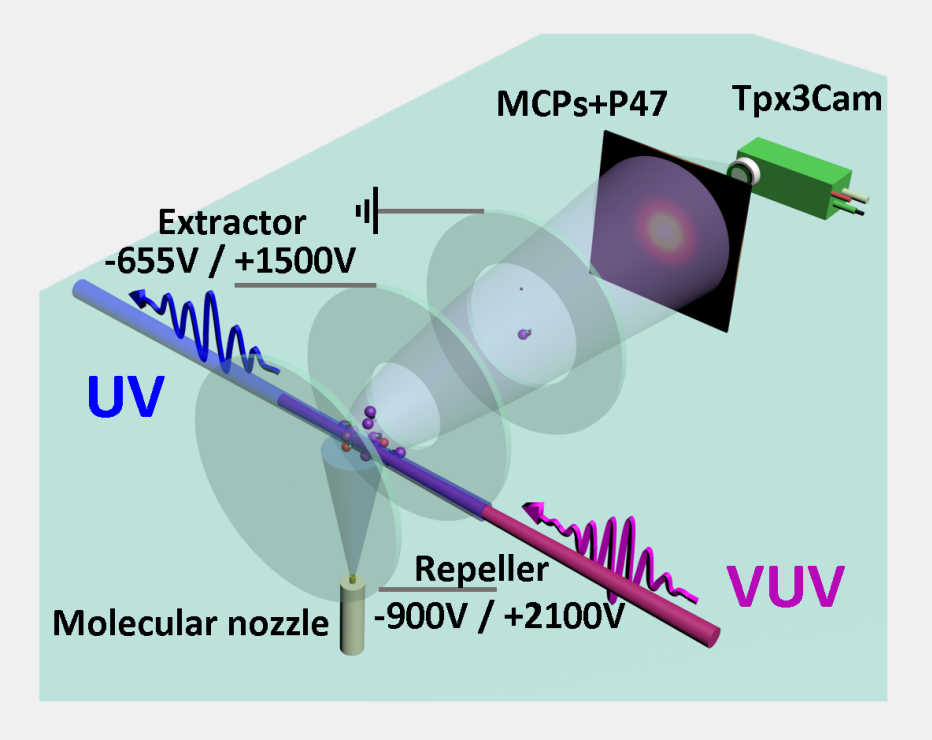

Figure 2.7: **A schematic of momentum-resoled photoion spectroscopy using TimePix3 camera.** This figure lays out the UV-pump VUV-probe apparatus with VMI detection of ions and/or electrons. The main difference from Fig. 2.2 is the ability of the fast high-voltage switches on the VMI plates, and the implementation of TimePix3 camera, which allows both detection of electrons and ions for each laser shot. The TimePix3 camera is able to record the hit position (x, y) as well as the time-of-arrival (t) for each charged particle with ns time resolution.

electrons. [2] Since the time between ionization and detection of the electrons is small (less than 100 ns), we can neglect the motion of the ions before the voltages on the VMI plates are switched.

TimePix3 camera has excellent spatial and temporal resolution, and can simultaneously measure the time and position for each hit, allowing us to

[2]The voltage flipping usually takes plate 10 ns after the electrons arrive the detector. The flight time of the electron is less than 100 ns.

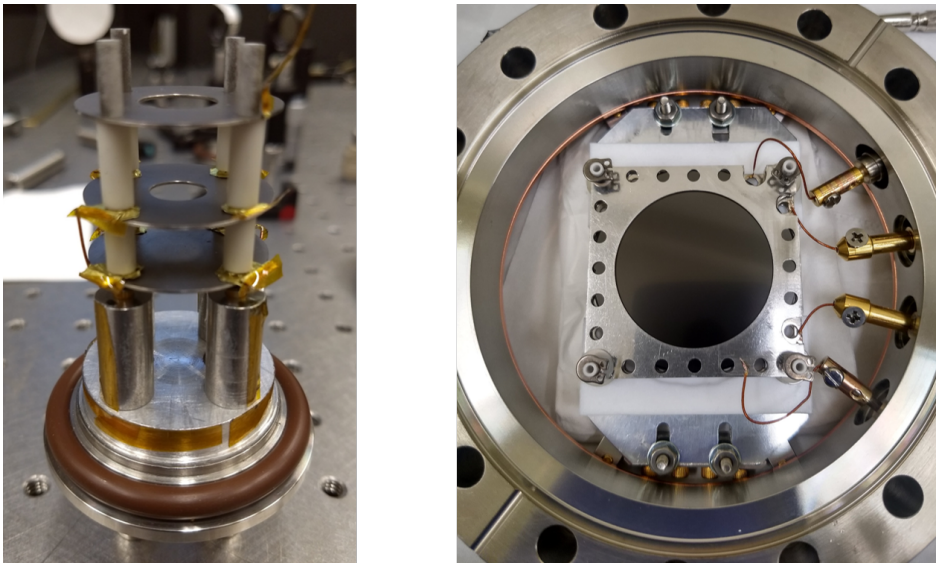

Figure 2.8: **Pictures of VMI electrostatic lens and 2D charged particle detector.** The panel in the left shows repeller-extractor type electrostatic lens for velocity mapping of the electrons and/or ions. Panel in the right shows an inside view of the home-built position sensitive charged particle detector, consists of two chavron type configuration MCPs and a P47 phosphor screen (∼70 ns emission lifetime [73]). The whole detector is sitting in a 6" conflact flange.

determine the mass and velocity, *V(x)*, *V(y)*, and *V(z)*. [3] We note that with the current ∼1 ns time resolution, the 3D momentum measurement for ions is possible without requiring an inverse Abel transform, while for electrons we rely on cylindrical symmetry about the pump and probe laser polarization axis to invert the two dimensional data since the electrons all arrive within a few ns and its V(z) cannot be determined from time. In contrast with a conventional frame-based camera, the TimePix3 camera records the position (x and y) and time (t) for each electron or ion incident on the detector, and the pump-probe delay information for each electron or ion incident is encoded into the data set by a systematic variation in the trigger signal to the camera. The camera's large throughput enables a straightforward switch between

[3] x direction is along the laser propagation, and y is perpendicular to x, forming a plane that is parallel to the VMI plates. z is the direction from the plates towards to the detector.

low-rate coincidence and high-rate non-coincidence detection modes. In addition, as a standalone piece of equipment outside the vacuum chamber, it allows for easy exchanges, upgrades and maintenance.

A common issue involved with VUV light a so called "stray electron" problem. As the VUV beam propagates through the apparatus, the VUV photons can be scattered on the surface of the titanium plates. The energy of these photons are high enough to generated electrons from the photoelectric effect. These stray electrons are directed to the detector together with the photoelectron from the ionization of the sample molecules. Due to the lower work function (< 5 eV) of the metal as well as higher density compared with the gaseous molecular sample, the stray electrons generation is efficient and the number of the stray electrons can be several order of magnitude higher than those from the molecules. [74] This mainly results two consequences. First, the large number of stray electrons may either saturate the detector or induce a huge background in the signal, lowering the signal to noise ratio. Second, the large number of stray electrons reaching to the detector increases the possibility of overlapping hits, which ruins the centroiding algorithm during the data acquisition.

Any direct incident or scattered VUV photon from other surfaces can possibly generate stray electrons at the VMI plates. In order to avoid the stray electrons, a pair of baffles were installed on both side of the VMI plates along the laser beam propagation direction. A baffle consists of cylinder and a holder that hold the cylinder. According to the dimension of the chamber and the VMI geometry, the position, length, and the inner diameter of the cylinder were determined with care, such that VUV photons were prevent to reaching at any areas of the the repeller and extractor plates. A baffle design can be found from the pictures in Fig. 2.6.

The reaction chamber base pressure is $\sim 10^{-7}$ Torr, and the running pressure is kept at $\sim 10^{-6}$ Torr. A multi-functioning sample manifold is integrated into the VMI chamber, which allows delivering gas, liquid, as well as solid phase samples. Two sets of molecular nozzles are installed onto the vacuum chamber, facing each other on the opposite side of the VMI set up. A schematic drawing of the sample manifold is depicted in Fig. 2.9. A nozzle with a diameter of 30 μm is set parallel to the surface of repeller and extractor plates from one side, which is used for delivering gas and liquid samples with relatively higher vapor pressure. The nozzle is connected to a sample manifold. Liquid samples are loaded into the sample cell, pumped on while frozen ("freeze pumped") in order to remove air from the sample, and

then regulated with a precision leak valve (also for gas samples) between the sample cell and the nozzle. The pressure behind the nozzle is kept at several Torr, which generates a continuous molecular beam through the nozzle to the VMI chamber.

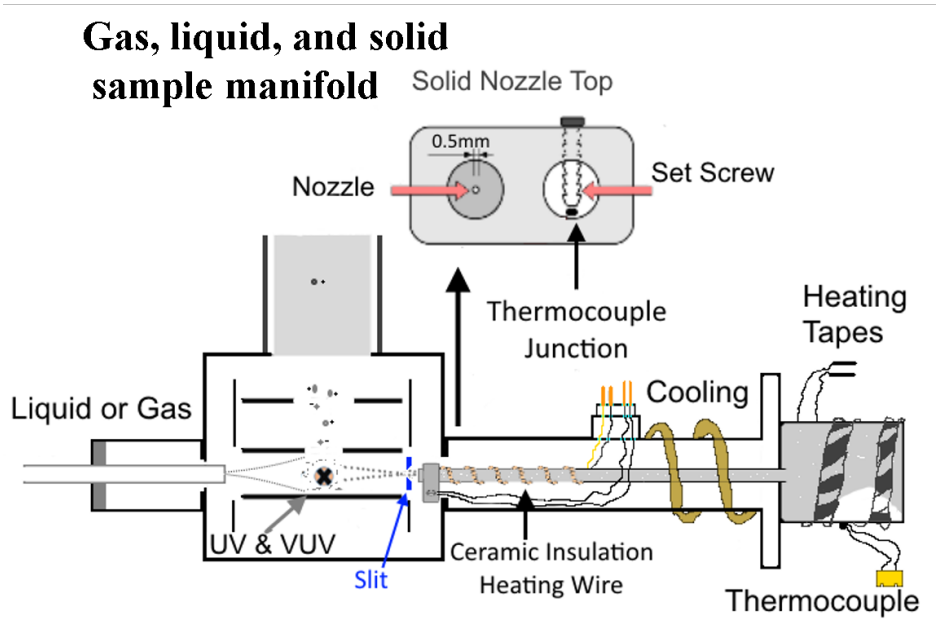

Figure 2.9: **Multi-sample manifold configuration in the photoelectron and photoion spectrometer.** The apparatus is integrated with two sets of molecular nozzles. The nozzle on the left hand side of the figure is for delivering gas and liquid sample. The assembly in the right hand side plays the role of delivering solid samples with capabilities of heating and temperature controls. Solid samples are enclosed in an oven, connected with a pipe to the molecular nozzle.

In order to deliver solid samples, another custom designed sample manifold with heating and temperature controlling ability is installed onto the opposite direction of the gas and liquid nozzle. The manifold is composed of a sample oven, a delivering pipe, and a molecular nozzle. Several sets of heating tapes and thermal-couples are wrapped on the oven in the outside, as well as the pipe and the nozzle in the vacuum, for heating and temperature measuring. The temperatures of different components are carefully controlled such that a gradient from the oven to the nozzle can be formed: i.e., the tem-

perature is slightly increasing from the oven towards to the nozzle, preventing potential clogging. One of the issues related to the solid sample experiment is the sample coating onto the VMI plates, leading to a distorted VMI focusing condition. This is essential for solid sample experiment. Therefore, we make use of a pair of blades forming a slit opening and mounted it in front of the nozzle, in order to limit the molecule beam vertical spreading angle. The opening size and the distance to the nozzle are carefully decided in order to deliver more sample but preventing coating the whole area of the plates.

2.2.4 VMI pump-probe data acquisition and analysis

Here we describe the experimental data acquisition and analysis of the photoelectron and photoion measurements. The TRPES measurement in chap. 3 and Chap. 4 were carried out in Stony Brook, whereas the experiments presented in Chap. 5 were performed at National Research Council of Canada (NRC) and reproduced afterwords in Stony Brook. In these experiments, the data were taken with a conventional fast frame-based camera (From Basler, acA2000-340 km, used in Stony Brook), whereas, the momentum-resolved photoion measurement was taken by Timepix3 camera in Stony Brook [75]. In all these measurements, the photoelectron VMI images or photoions are recorded as a function of pump-probe delay. Each sequence of pump-probe delays, i.e., a single experimental scan, is kept relatively short (integrating several hundreds of laser shots) in order to mitigate the impact of low frequency signal fluctuations on the pump-probe measurement. These slow fluctuations are usually induced by the temperature changes which will drive the changing of the UV and VUV pulse energy from the laser and the harmonic generations.

Typically, the UV/VUV pulse energy are set sufficiently low in order to avoid any single color multiphoton ionization with either pulse. In addition, an image off time-zero of the pump and probe pulse, often far negative pump-probe delay, is taken which accounts for any possible ionization from individual pump and probe alone as well as other backgrounds signal. A multi-step-size delay axis is often implemented in order to efficiently scan both the short (near time-zero with small step-size) and long (far away time-zero with larger step-size) time scale dynamics. The VMI image at each pump-probe delay step is usually an integration of several hundred to a thousand laser shots, and a typical dataset contains approximate 100 delay steps in each scan and 80-100 scans are averaged.

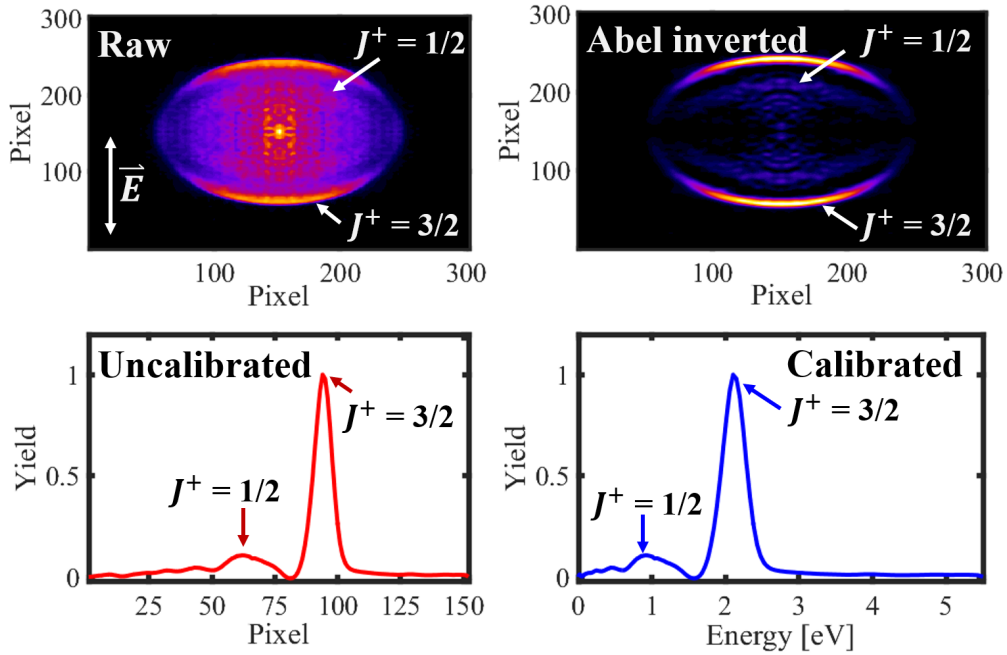

Figure 2.10: **Xe photoelectron VMI image and kinetic energy line-out through non-resonance 3 UV photon ionization.** This image was recorded using the VMI spectrometer discussed in Sec. 2.2.3. 3 UV photon ionizes Xe into the lowest cation state, with two spin-orbit coupling split energy of 1.34 eV. Top left panels is the raw photoelectron image after center finding, imaging rotation, and symmetrization. Top right panel shows the Abel inverted image and two features (rings) are corresponding to the spin-orbit coupling state, $J^+ = 1/2$, and $J^+ = 3/2$. Bottom panels showcase the kinetic energy line out (photoelectron spectrum) after the polar and azimuthal interaction of the inverted data, left for energy uncalibratied and right for energy calibrated. The pump and probe laser polarization is indicated by a white arrow in the raw image.

For a TRPES dataset, the recorded photoelectron VMI images are processed through several procedures. First, a reference image taken at large negative delay is subtracted from each image in the pump-probe scan, obtaining a "background free" image for each delay. These images are then averaged from all the scans. The center of the VMI image need to be located, either manually set or defined by the center of gravity or other fitting algorithms.

The images is then rotated in order to align with the polarization correctly, followed by a imaging symmetrization of the four quadrants. [4] An inverse Abel transform is then applied in order to reconstruct the 3D momentum distribution, which relies on the condition that the generated photoelectron or photoion has the cylindrical symmetry about laser polarization axis. The photoelectron spectrum is then obtained *via* polar and azimuthal integration of the 3D distribution. Fig. 2.10 showcases an example of the TRPES analysis and data is recorded with non-resonance 3 UV photon ionization of Xe. Top panels show a raw (left) and Abel inverted (right) VMI image and bottom panels show the kinetic energy line-out after the inverse Abel transform. The main features of the inverted VMI images are two kinetic energy rings labeled as $J^+ = 1/2$, and $J^+ = 3/2$ and these features can be also seen from the photoelectron lineout (bottom left) where two peak located at different pixel numbers.

If a known photoelectron kinetic energy distribution can be recorded, then under the same focusing conditions (voltages in the plates) utilized in the experimental measurement on the molecules of interest, and the absolute energy calibration as well as the detector energy resolution can be obtained. This can be accomplished by the Xe measurement. As I mentioned, the two features in the Xe photoelectron spectra are corresponding to two state (spin-orbit coupling) with well defined IPs: $J^+ = 3/2$, $Xe^+(^2P_{3/2})$ with an IP of 12.13 eV, and $J^+ = 1/2$, $Xe^+(^2P_{1/2})$ with an IP of 13.43 eV [76, 77]. Thus these features can be also used to calibrate the energy axis of the measured photoelectron lineout. For a VMI spectrometer, the relationship between the kinetic energy of a photoelectron and the radius (pixel of the camera image) in the detector can be described with an simple equation,

$$E_{\mathrm{ke}} = \frac{m_{\mathrm{e}} v^2}{2} = \alpha R^2 \tag{2.8}$$

where E_{ke} is the kinetic energy, m_e and v are the mass and speed of an electron, and R is the radius from the center of the VMI image. α is the calibration factor which is only related to the running condition of the ex-

[4] The polarization axis is usually checked by looking at the image in the spatial imaging mode. In the spatial imaging mode, the VMI plates voltages are tuned such that the positions (in stead of kinetic energy) of the photoelectrons/photoions generated along the laser beams are imaged to the detector. In this way, the laser polarization of the beams can be accurately determined according to the beam propagation, in which the polarization direction is perpendicular to the laser beams.

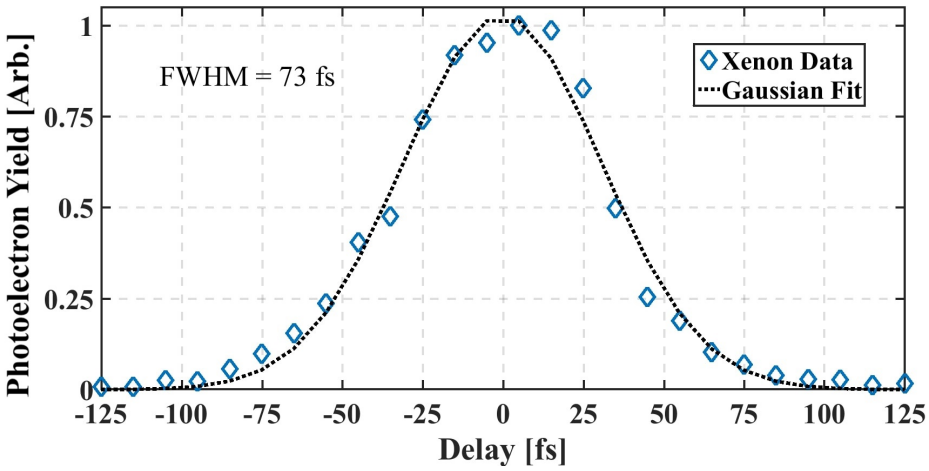

Figure 2.11: **Energy integrated TRPES signal of Xe used to determine IRF.** This figure shows the photoelectron spectra of the UV-VUV pump-probe on Xe gas. Fitting the integrated spectra of this data give the IRF of 73 fs in this experiment.

periment.[5] With 3 UV (∼261 nm) photon , the totally energy is $4.75 \times 3 = 14.25$ eV, thus the kinetic energies of the two peaks in the Xe photoelectron spectrum are 2.12 ($J^+ = 3/2$) and 0.82 ($J^+ = 1/2$) eV, respectively. These energies can be used to calibration the photoelectron spectra and the kinetic energy calibrated spectrum is shown in the bottom right panel of Fig. 2.10. Besides the energy calibration, the Xe measurement can also give an approximated upper limit of the energy resolution of apparatus. According to the kinetic energy peak for $J^+ = 3/2$, a 400 meV in FWHM is treated as the energy resolution.

Generally, in any pump-probe measurement, it is essential to locate the pump-probe time-zero (T0) and extract the instrument response function (IRF) in great accuracy, which is the key to follow the dynamics of the measurement correctly. In our experiments, the pump-probe T0 can be determined in a relatively convenient way, by performing a TRPES (or ToF mass spectroscopy) measurement with either Xe or ethylene under the same

[5] α can be also expressed by a simple equation as $\alpha = \frac{eU}{L^2}$, where eU is the gained kinetic energy from the external field in the VMI plates and L is the distance between the top plate (ground) and the detector. This equation assumes that the free flight distance of after the electron leaving the VMI region is much larger than the VMI setup.

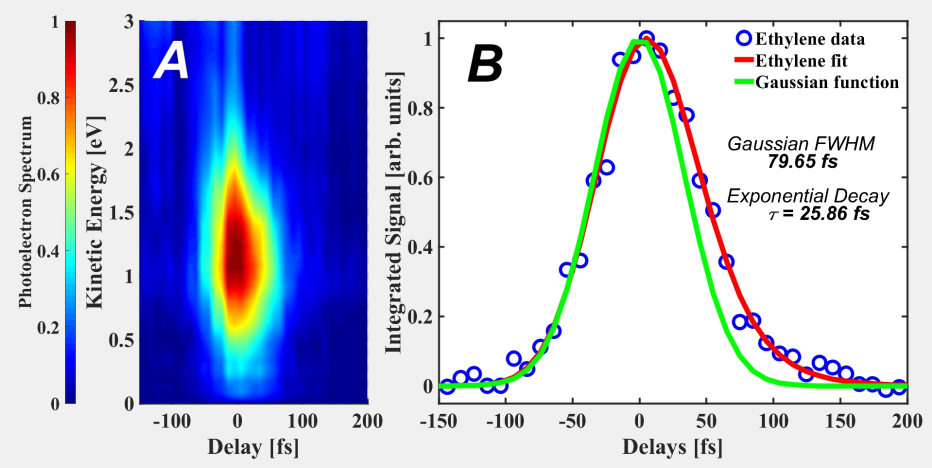

Figure 2.12: **Ethylene TRPES signal and fitting results used to define time-zero and the impulse response function determination.** A TRPES measurement of ethylene can be seen in panel A. Positive delay corresponds to VUV-pump and UV probe. Panel B shows the energy integrated photoelectron yield and fitting results.

experimental condition with the samples of interest. For Xe, a non-resonance UV + VUV (1+1') ionization experiment can be performed. The total energy of the UV+VUV is 4.75+7.95=12.70 eV, which can reach to the state of J^+ = 3/2. Presented in Fig. 2.11 is a energy-integrated photoelectron yield of Xe with UV+VUV, yielding a cross-correlation of 73 fs FWHM from a single Gaussian fitting, which can be treated as the IRF and directly related to the UV and VUV pulse duration through $\sigma_{cross-correlation} = \sqrt{\sigma_{UV}^2 + \sigma_{VUV}^2}$. The TRPES measurement in Chap. 5 use Xe measurement to located T0.

Different from Xe, ethylene has strong absorption around VUV region and ethylene undergoes rapid relaxation through conical intersection down to ground state, such that the ionization yield as a function of time roughly maps out the IRF of the apparatus [78, 79, 13]. With our pump-probe setup, the ethylene molecules are excited with the VUV pulse, followed by the ionization of the UV pulse, and the TRPES of ethylene can be found in Fig. 2.12 panel (a). [6] By fitting the ethylene signal with a Gaussian and an exponential function, we acquired the time-zero and IRF of the UV-VUV

[6]Pay attention that the positive delay in Fig. 2.12 corresponds to VUV light pumping and UV light probing, i.e., VUV pulse comes before the UV pulse.

cross correlation, which is $\sim$ 80 fs. The TRPES measurements from Chap. 3 and Chap. 4 use ethylene measurement to locate T0.

While the TRPES measurements can be accomplished using a conventional frame based camera, the momentum-resolved photoion measurement is more challenging, because there are multiple species in the ToF mass spectrum. With a conventional camera, previous measurements were usually accomplished by gating the voltage on MCPs within the ToF window that correspondents to the fragment of interests (e.g., parent ion or dissociated fragment) [72]. In the photoion measurement of CH_2I_2 and CH_2IBr in Chap. 5, I implemented the Timepix3 camera which was able to capture all the ion species without gating the detector. TimePix3 is designed to be able to acquire the ToF information of photons into the detector. The camera's main function units consist of a specialized silicon sensor [80], a Timepix3 chip [81] and a SPIDR readout system [82], in which it allows each individual pixel unit functioning independently with a fast pixel refreshing rate ($\sim$640MHz). The light generated on the phosphor from each individual ion can be recorded separately according to the different arrival time and it also records the position information, providing both position and time which allows for 3D momentum, P_x, P_y, and P_z for each hit detected [75].

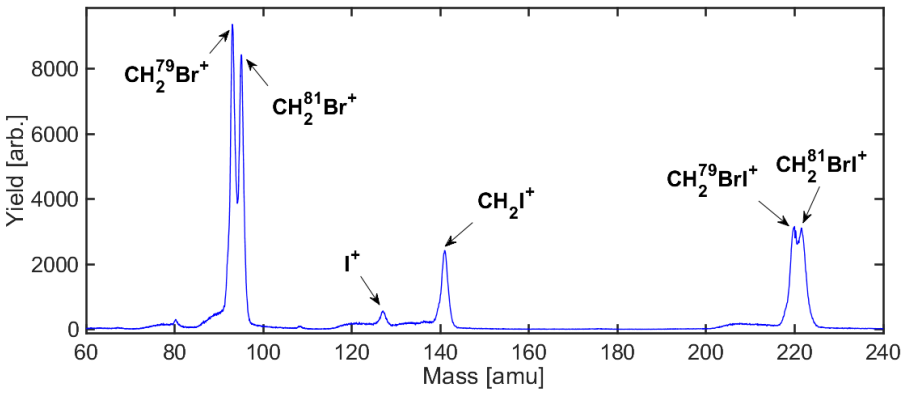

Figure 2.13: **ToF mass spectrum of CH_2IBr obtained from Timepix3 camera.** Note that the bromine isotopes are clearly separated in this measurement.

Figure 2.13 shows a histogram plot of the ToF mass spectrum recorded by TimePix3 camera in the TRPIS experiment of CH_2IBr. One can see the clear discriminated different ion peaks corresponding to the bromine isotopes.

In the pump-probe measurement with TimePix3 camera, each ion event, instead of VMI image, is encoded with the pump-probe delay information and the momentum or kinetic energy can be then calculated according to both the position on the detector and the time of arrival, $X \rightarrow P_x$, $Y \rightarrow P_y$, and $Z \rightarrow P_z$. I note that with the current $\sim$1 ns time resolution, the 3D momentum measurement for ions is possible without requiring an inverse Abel transform, while for electrons we rely on cylindrical symmetry about the pump and probe laser polarization axes to invert the two dimensional data since the electrons all arrive within a few ns. On the other hand, the VMI image for a single ion species can be also generated such that the analysis procedures of the photoelectron VMI image aforementioned is applicable.

2.3 Gaseous ultrafast electron diffraction

In this dissertation, we made use of electron diffraction being as a structural probe. Compared with X-ray diffraction, UED allows for a much larger range in the momentum transfer space ($\geq$10 Å^{-1}) which is favorable for higher spatial resolution. The temporal resolution of gas phase UED experiments using KeV (sub-relativistic) electrons is dominated by two main factors due to the electron bunches. Due to the space-charge induced bunch broadening, the distance between the electron gun and the sample has to be kept in very small, usually in the order of several centimeters and the number of electrons in each bunch is also kept low (few tens of thousand). The second main challenge arises from the the velocity mismatch between the pump laser pulse and the probe electron bunch associated with a typical gas target thickness much larger than a few micrometers.

In order to accomplish higher temporal resolution in the face of space-charged and velocity mismatch, one solution is to bring the electron up to relativistic regime, i.e., Mega-electron-volt (MeV) electron kinetic energy. Thus we make use of electron diffraction beamline at SLAC national lab, in which the electron beam energy is $\sim$ 3.7 MeV. Compared with conventional UED setup with KeV electron beam, the space-charge repulse effect is much smaller and the velocity mismatch us negligible. Fig. 2.14 depicts a cartoon diagram of a gas-phase UED experiment with the example of CH_2I_2 which will be described in Chap. 3. Similar with other time-resolved spectroscopies, in UED experiment, a basic pump-probe scheme is established using an optical ultrashort laser pulse and an electron bunch being as the pump and

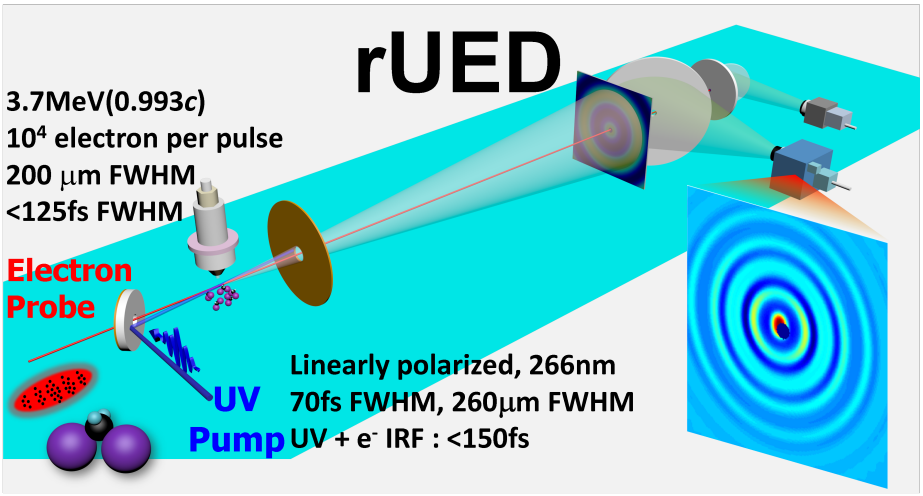

Figure 2.14: **A schematic of gas-phase UED setup.** An ultrashort 266 nm pump laser (in blue color) excites the CH_2I_2 molecules in the molecular beam from a pulsed nozzle, while a 3.7 MeV electron pulse probes the transient structural changes after the initial excitation. The electrons are scattering from the molecules and projected to a two dimensional detector in far field. The time-dependent scattering intensity map are recorded with a camera.

the probe, respectively. Both pulses originated from a Ti:sapphire ultrafast laser system. In the CH_2I_2 experiment, a deep UV pulse which is the 3^{rd} harmonic, initiates the dynamics by launching a wave packet on the excited states. A gas phase molecular beam is introduced from either a diffusive nozzle or pulse valve, to interact with the pump and probe pulses. The optical pulse and the electron bunches are combined using a "holey" mirror in which the electron going though the hole and the UV beam is reflected by the mirror near the hole, restricting the angle between the electron beam and laser pulse in a very small angle. The main beam and the diffracted electrons are projected to a two dimensional detector in the far field and diffraction patterns are recorded by a camera. The beams are usually kept close to the nozzle in order to obtain higher gas density.

As I will discuss in Sec. 2.3.2, we are able to achieve with a spatial-and-temporal resolutions at 0.63 Å and 150 fs FWHM, respectively. This makes it possible to capture the dynamics at the very beginning after the

initial excitation, effectively making a "molecular movie" as the chemical process taking place from reactants all the way to the products. In the rest of the section, I will introduced the elastic scattering theory of gas-phase UED, relativistic UED setup in SLAC National Laboratory, as well as the experimental data acquisition and analysis.

2.3.1 Gas phase electron diffraction theory

Electron diffraction is widely used for structure determination. We consider an energetic electron beam scattering off a molecule and the contribution only from the nuclear charge density, i.e., elastic scattering model. Assume that $\mathbf{k_o}$ is the wave-vector of the incident electrons which can be represented by a plane wave of the form $e^{ik_0 z}$ for the electron beam propagating along z-direction, the primary quantity of interest is the scatting vector (wave-vector change) $\mathbf{s} \equiv \mathbf{k_o}$ - $\mathbf{k}$, where $\mathbf{k}$ is the wave-vector for the scattered electrons. The diffraction pattern is usually expressed as a function of $\mathbf{s}$ in momentum-transfer space (unit of Å^{-1}), and geometrically its magnitudes can be written as:

$$\begin{aligned} s &= |\mathbf{k} - \mathbf{k}_0| \\ &= 2k_o \sin(\theta/2) \\ &= \frac{4\pi}{\lambda_o} \sin(\theta/2) \end{aligned} \tag{2.9}$$

where λ_0 is the de Broglie wavelength of the electrons, and θ is the scattering angle between $\mathbf{k_o}$ and $\mathbf{k}$. We consider the widely-used independent atomic model (IAM), based on the approximation that the scattering amplitude and phase from each atom is dominated by spherical potential atoms at specific locations within the molecules, i.e., the each atom in the molecule is treated as an isolated atom and the the scattering from the bonding electrons is neglected [83, 84]. [7] We note that recent experiments and calculations proved that both the elastic (dominated by nuclear charge density) and the inelastic (dominated by bonding electrons) scattering signatures can be captured simultaneously, whereas the inelastic scattering signals is located in very small s, typically smaller than 1 Å^{-1} [85]. This is because the binding electrons usually have very weak influence on the scattering cross-section when the electron energy is higher than a few hundred eV [86, 84].

[7] IAM can break down and diffraction signal can have contribution from delocalized bonding electrons. These contribution are dominated by inelastic scattering.

Under the assumption that the incoming electrons are plane waves, the scattering amplitude may be best modeled as outgoing spherical waves from individual atoms from a molecule of the form:

$$\psi(R,\theta) = f(\theta)\frac{e^{ikR}}{R} \tag{2.10}$$

where $f(\theta)$ is the complex-valued angular-dependent scattering amplitude and R the distance from the atom. Equ. 2.10 describe the scattering from an individual atomic center. In general, one needs to *coherently* add the scattering amplitude from all atoms in the sample, with the detected scattering intensity being the square of this coherent sum. For a molecule with N total atoms, Equ. 2.10 results in the following expression as a function of $\mathbf{s}$:

$$I_{\text{sample}}(\theta) \propto \left|\sum_{n=1}^{N} f_n(\theta)\frac{e^{i\mathbf{s}\cdot\mathbf{r}_n}}{R}\right|^2 \tag{2.11}$$

where $\mathbf{r}_n$ is the vector connecting the n^{th} atom to the detector, and R the average distance from the atoms in the sample to the detector. Due to the large ratio between the distance R and the spatial extent of the sample, the $1/R$ amplitude dependence is same for all atoms. Equ. 2.11 is true for individual molecules in any case. However, its usefulness very much depends on the type of molecular sample. For instance, in gas-phase samples that we are interested, the different molecules are randomly positioned (nonspatially uniform) and orientated throughout the sample, and transverse spatial coherence of the indecent scattering wave is often small compared with the intermolecular space and sample size. This leads to Equ. 2.11 becoming impractical, and the contribution of the scattering intensity of each molecule to the total diffraction signal adds with a random overall phase. [8] In other words, for intramolecularthe scattering signal is *coherently* added up whereas, for intermolecular, the contribution is added up *incoherently*, implying they add as the sum of squares as opposed to the square of a sum.

Ideally, gas-phase diffraction measurement would use *perfectly* aligned molecular sample where the projection of the aligned bond lengths on to the detector plane is same for all molecules in the sample. However, experimentally, the molecular ensemble can never be perfectly aligned. Even with

[8] Impractical here means Equ. 2.11 is only relevant for atoms in a given molecule, and one has to make a incoherent sum for a molecular ensemble.

aligned gas-phase molecules, it is nontrivial to directly retrieve the molecular structure from the diffraction pattern. This is simply because one could only measure *intensity* by counting the number of electrons incident on a spatially resolved detector, instead of *field* of the scattering electrons, where in the latter case, a Fourier transform of the signals yields the molecular structure. The Fourier transform of the *intensity* distribution gives the autocorrelaton of the molecular structure without the phase information among the atoms, thus one need to use iterative phase-retrieval algorithms to recover the molecular structure, even for a perfectly-aligned sample [87, 88, 89]. In this dissertation, instead of focusing on the scenario with aligned (or partial aligned) molecular samples, we turn to more general picture assuming the two spatial coherent conditions aforementioned are *not* simultaneously satisfied. In the single molecule, the measured signal is the total elastic scattering intensity from all the atoms, thus Equ. 2.11 can be rewritten as by assuming the molecule contains N atoms:

$$\begin{aligned} I_{\text{molecule}}(\theta) &= \frac{I_0}{R^2}\left|\sum_{n=1}^{N} f_n(\theta) e^{i\mathbf{s}\cdot\mathbf{r}_n}\right|^2 \\ &= \frac{I_0}{R^2}\sum_{i=1}^{N}\sum_{j=1}^{N} f_i(\theta) f_j^*(\theta) e^{i\mathbf{s}\cdot\mathbf{r}_{ij}} \end{aligned} \tag{2.12}$$

where $\mathbf{r}_n$ is the position of the n_{th} atom (relative to the detector), I_0 a constant, and R the distance from the center of mass to the detector. The quantity $\mathbf{r}_{ij} = \mathbf{r}_i$ - $\mathbf{r}_j$ represents the vector pointing from the i_{th} to j_{th} atom. Here we consider an unaligned sample and taking account the randomly orientation of each molecule with respect to the scattering vector, each $\mathbf{r}_{ij}$ in Equ. 2.12 needs to be averaged uniformly overall possible orientations relative to the scattering vector $\mathbf{s}$. It is more convenient to introduce a polar, α, and azimuthal angle, β, representing the relative orientation between the vector $\mathbf{r}_{ij}$ and $\mathbf{s}$, and the angular averaging for the term, $e^{i\mathbf{s}\cdot\mathbf{r}_{ij}}$, can be accomplished by a double integral as:

$$\frac{1}{4\pi}\int_0^{2\pi} d\beta \int_0^{\pi} e^{is\cdot\mathbf{r}_{ij}} \sin\alpha d\alpha = \frac{1}{2}\int_0^{\pi} e^{isr_{ij}\cos\alpha}\sin\alpha d\alpha \tag{2.13}$$

And evaluating the integral yields

$$\frac{-e^{-isr_{ij}} + e^{+isr_{ij}}}{2isr_{ij}} = \frac{\sin(sr_{ij})}{sr_{ij}} \tag{2.14}$$

As showed in Equ. 2.9 where $s = 2k_0\sin(\theta/2)$, it is more convenient to write everything as a function of s. Plugging Equ. 2.13 and 2.14 back to Equ. 2.12, the averaged scattering intensity of Equ. 2.12 transforms to

$$I_{\text{averaged}}(s) = \frac{I_0}{R^2}\sum_{i=1}^{N}\sum_{j=1}^{N} f_i(s)f_j^*(s)\frac{\sin(sr_{ij})}{sr_{ij}} \tag{2.15}$$

and it could be naturally separated into two parts with $i{=}j$, or $i{\neq}j$, which represents the atomic and molecular contribution to the total scattering intensity, respectively and they can be written as:

$$I_{\text{averaged}}(s) \equiv I_A(s) + I_M(s) \tag{2.16}$$

$$I_A(s) = \frac{I_0}{R^2}\sum_{i=1}^{N} f_i(s)f_i^*(s) = \frac{I_0}{R^2}\sum_{i=1}^{N} |f_i(s)|^2 \tag{2.17}$$

$$I_M(s) = \frac{I_0}{R^2}\sum_{i=1}^{N}\sum_{j\neq i}^{N} f_i(s)f_j^*(s)\frac{\sin(sr_{ij})}{sr_{ij}} \tag{2.18}$$

where I_A contains the (incoherent) sum of scattering from all the constituent atoms in a molecule, i.e., I_A has no dependence on the $\mathbf{r}_i$ and therefor no information about molecular structure is included in it. Thus, the atomic scattering is independent at the excitation process since structural changes do not affect the contribution of the atomic scattering. Usually, in the experimental measurement, one cares about the scattering difference with respect to the excitation process, and the atomic scattering then can be cancelled by subtracting the signal before the excited process. I_M represents the interference due to the coherent scattering from the different nuclei in a given molecule and the information of the time varying pair distances is included. In contrast with the atomic scattering, the molecular contribution is different before and after the excitation and contain information about time varying pair distances. As an example, consider the case of randomly-aligned, gas-phase CH_2I_2. Fig. 2.15 showcases the simulated diffraction intensity as a function of momentum transfer, s, for both randomly-aligned molecular sample ($I_A(s) + I_M(s)$) and only the atomic scattering component ($I_A(s)$). Due to the random alignment of the molecules, the coherent interference between scattering amplitudes from different atomic centers in a given molecule is a

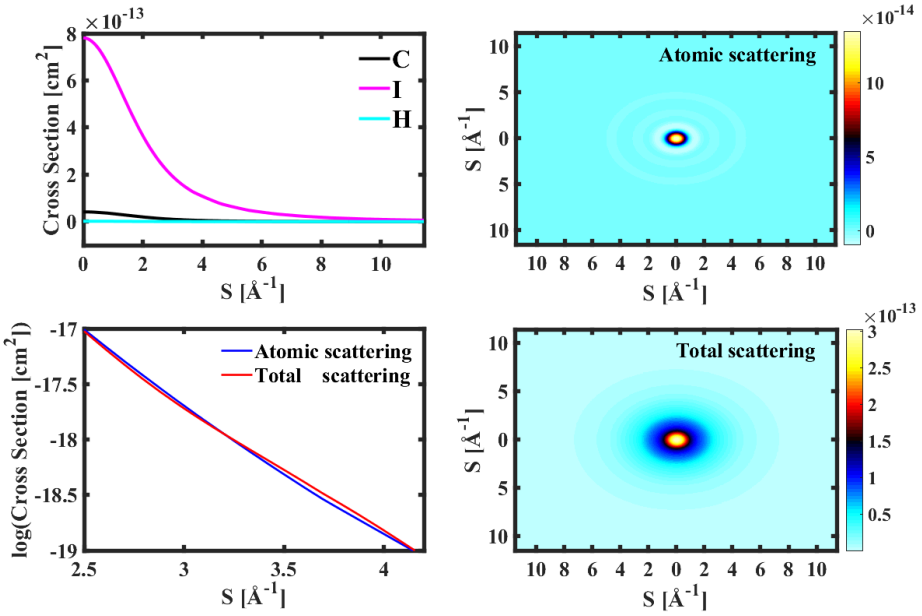

Figure 2.15: **Simulated static electron diffraction signal from gas phase CH_2I_2 molecule with an electron beam energy of 3.7 MeV: atomic and molecular scattering.** Top left panel panels shows the elastic differential scattering cross of carbon, iodine, and hydrogen atoms-$I_A(s)$. Bottom left panel shows the calculated atomic scattering versus the total scattering intensity assuming the random orientation of the molecules-$I_{average(s)}$. Compared with the $I_A(s)$, one can observe a modulation in $I_{average}(s)$ which arises from the interference intensity of the pairs of atoms. Top and bottom right panels shows the two-dimensional atomic and total diffraction pattern.

small perturbation ($I_M(s)$) on the atomic scattering background, but it is this small oscillation that contains molecular structural information.

Equ. 2.18 is true when assuming the randomly-orientated molecular ensemble contains static molecules with well-defined atomic positions, and early works in the gas-phase electron diffraction neglect the effect of the vibration of the atoms, which induced a smearing of the signal in the real space. In order to account for this effect, a correction term with an Gaussian shape can be applied to the molecular part by inducing a vibrational amplitude between the atomic pair ij, R_{ij}, and Equation 2.18 becomes:

$$I_M(s) = \frac{I_0}{R^2} \sum_{i=1}^{N} \sum_{j \neq i}^{N} f_i(s) f_j^*(s) e^{-\frac{1}{2} R_{ij}^2 s^2} \frac{\sin(sr_{ij})}{sr_{ij}} \tag{2.19}$$

The Gaussian shape function preforms as an damping in the momentum transfer space, leading to a slight smaller range of the available range of the s. This is equivalent to a reduced spatial resolution in the R space as the described smearing. As far as we have discussed, for all the formula given above only elastic scattering is considered. In an electron diffraction experiment, both elastic and inelastic scattering are covered in the signal. Whereas, the inelastic scattering is usually incoherent for electron kinetic energy in the KeV or higher energy range, thus it does not carry structural information, but rather remains as the background in the experimental measurement. [90] Similar to the atomic scattering, the inelastic scattering signal behaves the same before and after the excitation, and can be removed by simply a subtraction in the data analysis.

It is useful to estimate the signal level of the atomic and molecular scattering signal. $f(s)$ approximately scales as Z/s^2 according to Rutherford scattering model where Z denotes the atomic number [90]. As Equation 2.17 and 2.18, I_A is a falling with a dependence of s^{-4}, whereas I_M has an s^{-5}. Thus the signal level of both I_A and I_M drop fast with s increasing. It useful to remove the s^{-5} dependence in the molecular scattering, I_M, by inducing a fraction between the atomic and molecular scattering together with the multiplying of s, defined as a "modified molecular scattering intensity," sM,

$$sM(s) \equiv s \frac{I_{\text{averaged}}(s) - I_A(s)}{I_A(s)} = s \frac{I_M(s)}{I_A(s)}. \tag{2.20}$$

The scattering signal, I_A, I_A, and sM, are all in reciprocal space (momentum transfer), whereas, one cares more about the structure information, i.e., atomic pair distances, in the real space. Each atomic pair will give rise to a sinusoidal modulation in sM with amplitude inversely proportional to their distance. Thus an inverse sine transform can be used to calculate a radial distribution function as

$$f(r) = \int_0^\infty \mathrm{sM}(s) \sin(sr) e^{-ks^2} ds, \tag{2.21}$$

where k is a damping factor, and the inclusion of the damping term is widely applied method in the experiment in order to remove the sharp edge at s_{max}

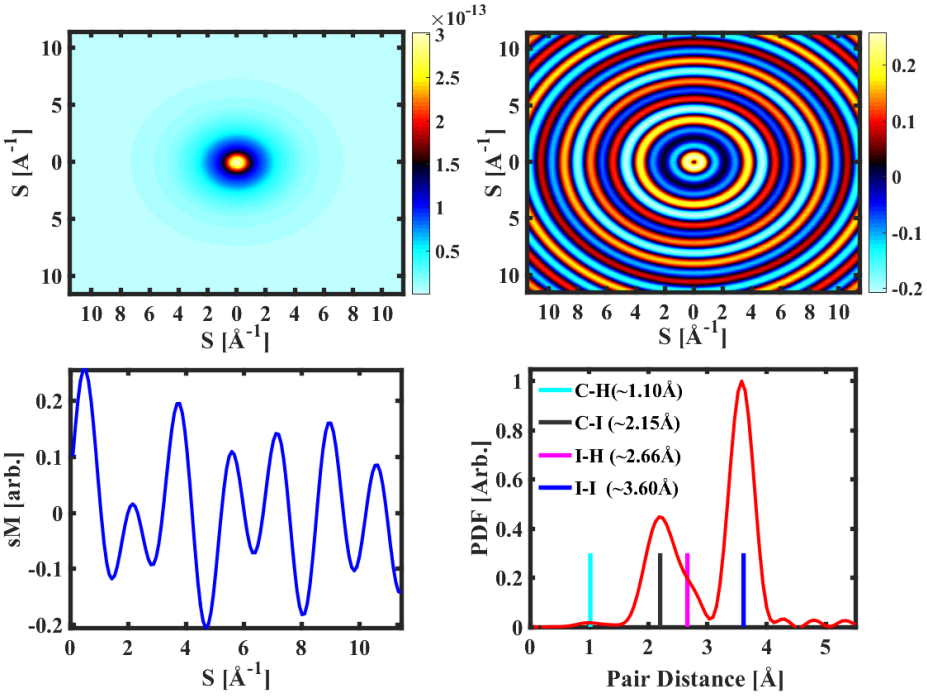

Figure 2.16: **Simulation of electron diffraction from CH_2I_2 ground state geometry with an electron beam energy of 3.7 MeV.** Panel (a) is the raw diffraction data, while panel (b) shows the modified molecular scattering intensity, $sM(s)$. Panel (c) plots the azimuthal average of $sM(s)$, and panel (d) shows the radial distribution function, $f(R)$.

which give rise to high frequency noise in $f(r)$. In the case of randomly-orientated molecules, the structural information of the interatomic distances is included in the 1-D radial distribution function.

2.3.2 SLAC relativistic UED experimental apparatus

The first experimental demonstration of gas phase UED with a few-picosecond temporal resolution was achieved by Zewail's group, and several benchmarking experiments have been carried out in the early years of this century, as well as the novel data analysis methods being introduced [41, 42, 91, 92]. An example among these experiments is following the photoinduced dissociation pathways of diiodotetrafluoroethane ($C_2F_4I_2$), in which Ihee and co-works

were able to determine the intermediate structure during the dissociation and the transient signal ruled out a previous hypothetical bridged structure [42]. With a conventional DC field of electron acceleration, the experiment apparatus offer a temporal resolution of several picosecond which allows one to access the interaction with slow intermediate state, however, the information content related to the fast dynamics is not available due to the limited temporal resolution with the conventional electron gun. It is very necessary to improve the temporal resolution such that the fast nuclear motion in various photoinduced processes can be captured.

In the CH_2I_2 experiment described in Chap. 5, the focus is on photoinduced dissociation dynamics takes place in the order of ∼100 fs time scales. Using a conventional UED setup (KeV electron beams) is unlikely to resolve the fast transient structural change after the initial excitation. However, using a higher energy electron beam in MeV, the two major effects, Coulomb repulsion and velocity mismatch, will be strongly suppressed. This is simply because the Coulomb induced forces scales as $1/(\beta^2\gamma^3)$, where $\beta = v/c$, v is the velocity of the charged particle, and c is the speed of light, and $\gamma = 1/\sqrt{1-\beta^2}$. On the other hand, larger electron velocity will induce less velocity mismatch respect to the optical pulse. For instance, the Coulomb repulsion of an electron beam with 3.7 MeV kinetic energy in SLAC UED facility is more than three order of magnitude smaller than that of a 100-keV counterpart, and the speed of the electron is 0.993 c, in which the time smearing across a 500 um gas sample is in the order of <10 fs. [9] The FWHM of the UV pump pulse is 70 fs according to the SD-FROG measurement, and the cross-correlation of the UV and the electron bunch is about 150 fs according to the experimental measurement, taking into account the possible jittering between the electron and the UV beam [47].

Figure 2.17 panel (a) shows a 3D drawing of the MeV UED beamline. Different from a conventional electron gun, this apparatus makes use of a S-band 1.6-cell photocathode RF gun to generate high-fluence 3.7 MeV electron beams [93]. Downstream of the gun, several diagnostics stations, including the beam profile monitor, movable Faraday cup (to estimate bunch charge), and a motorized collimator, allowing to control and manipulation of the electron beam and measurements of the parameters. Following the

[9] For a beam that electron energy is 3.7 MeV, the speed is $0.993c$ and this factor of Coulomb induced forces, $1/(\beta^2\gamma^3)$ is 0.6×10^{-4}, whereas, for an electron beam with energy of 100 KeV, the electron speed is $0.548c$ and this this factor increases to ∼1.

diagnostic stations and the differential pumping sections, are the laser and electron beam incoupling cube and the main gas sample chamber, where the laser and electron beam are combined and interact with the sample, as is shown in panel (b) of Fig. 2.17. A 3-dimensional translation stage holds the molecular nozzle inside the sample chamber, enabling the accurate positioning with respect to the laser and electron beam overlap region. The scattering electrons are then recorded 3.1 meters away from the sample chamber downstream with the detector, which is composed of a 4-cm-diameter P47 type phosphor screen positioned perpendicular to the electron beam and a 45° oriented high-reflection folding mirror. The plane of the phosphor is imaged to an electron-multiplying charge-coupled device (EMCCD, Andor iXon Ultra 888) camera. The undiffracted electron beam is directed to a second detector (another sets of phosphor screen, folding mirror, and camera) through a small hole (∼3 mm diameter) in both of the phosphor screen and the folding mirror, allowing for the monitoring the intensity and possible steering of the main electron beam.

The whole system is driven by a Ti:sapphire laser (25 mJ, ∼50fs pulse duration, 180 Hz repetition rate) with the fundamental wavelength at 800 nm, where a small amount of pulse energy (∼1 mJ) is frequency tripled to 266 nm for electron beam generation in the gun. The main portion of the fundamental is used to generate the pump pulses at various spectral ranges, either with harmonic generation (2ω, 3ω and 4ω at 400 nm, 266 nm, and 200 nm, respectively) or tunable wavelength through an optical parametric amplifier. Several experimental protocols are essential in a successful gas phase UED experiment in order to improve the signal level:

- Sample delivery: To increase the number of scattered electron, a high density molecular beam is needed, which can be accomplished by using a pulse nozzle (for lower vapor pressure gas, <100 Torr) with carrier gas or a continuous flow cell (higher vapor pressure gas, >100 Torr). The pressure of the sample chamber pressure is kept below 10^{-5} Torr. To avoid the contamination of the gas sample into the mirror in the incoupling cube, a 2-mm-diameter movable capillary, protruding into the sample chamber, ensures two orders-of-magnitude pressure difference by differential pumping between the incoupling mirror cube and the sample chamber. A schematic representation of the incoupling mirror and differential pumped capillary assembly is shown in Fig. 2.17 panel (b).

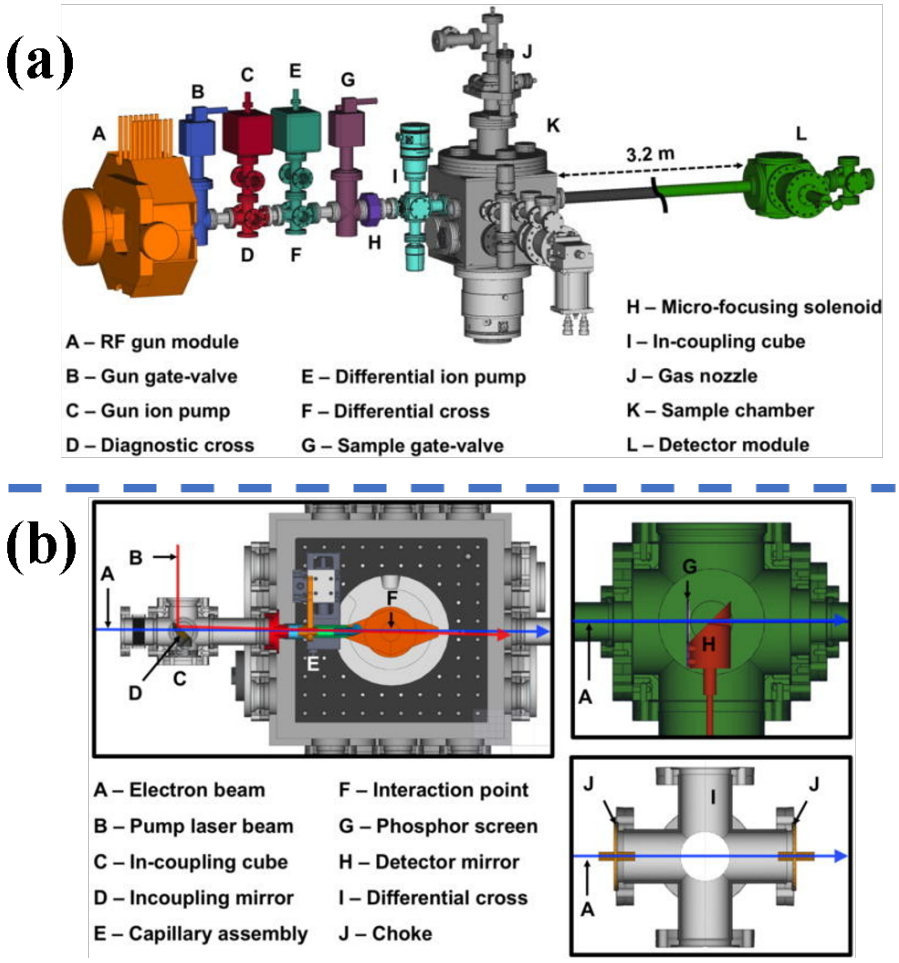

Figure 2.17: **A Schematic drawing of gas-phase MeV UED apparatus at SLAC.** Panel (a) in the top lays out a 3D drawing of the beam line, from the upper stream RF gun towards to the lower stream with the gas phase experimental chamber and the detector. Panel (b) in the bottom shows a zoomed in view of the gas chamber (top left), the invaccuum electron detector module (top right), and the diffraction pumping (bottom right). The figure is reproduced from ref [47] with the authors permission.

- Spatial overlap and UV power: the spot size of the UV pump which is set around 350 μm FWHM, and the electron beam size is focused smaller (~300 μm in FWHM) than the UV beam size, ensuring that the electron beam sees all the possible excited molecules. The UV pulse

energy is carefully attenuated to avoid the possible ionization. A pump power scan is usually carried out to ensure the experiment is in the regime that is linearly proportional to the UV fluence.

- Low S data: While the hole in the center of the phosphor avoids the unnecessary damage of the detector, the signal is lost in the center. According to the calibration from the position on the detector to momentum transfer (s), about 1 $Å^{-1}$ is missing if one sets the electron beam in the center. To access more information in the low s data, it is useful to position the main electron beam close to the edge of the hole in which the smaller S signal could be partially reached. More discussion is included in the later section.

2.3.3 Diffraction pattern analysis

The measured diffraction signal consists of contribution from all populated quantum states, i.e., both ground and excited state, which is quite different from the optical spectroscopies which are usually state-specific. Thus, it is useful to access diffraction difference signal by subtracting out the contribution from the unexcited molecules. In a typical UED measurement, this step could be simply accomplished by subtracting the static diffraction pattern in which the probe electron bunch comes before the optical pump pulse, i.e., $\tau < 0$. As discribed in Sec. 2.3, the subtraction simply removes all the molecule unrelated backgrounds, the contribution from the ground state molecules, as well as the atomic scattering of the excited molecules, and this difference signal is the excited state molecular scattering signal. [10]

Figure 2.18 shows an averaged diffraction pattern at far negative time delay (<-10 ps), i.e., the molecules are populated in ground state. This image is obtained from an averaging of 180 diffraction patterns after a diffraction pre-analysis with several so called "clean-up" steps in order to remove the artifact. After the "clean up", an azimuthally averaged (1D) diffraction analysis is usually applied if one is not interested in the angular distribution/anisotropy. However, the diffraction signal from the excited molecules intrinsically displays the angular distribution, and this property simply originates from the preferential excitation along the linear polarized pump UV.

[10] For a more precise description, the subtraction results in a signal which represents the molecular scattering component from the molecules in the excited state(s) geometries with respect to themselves in the ground state.

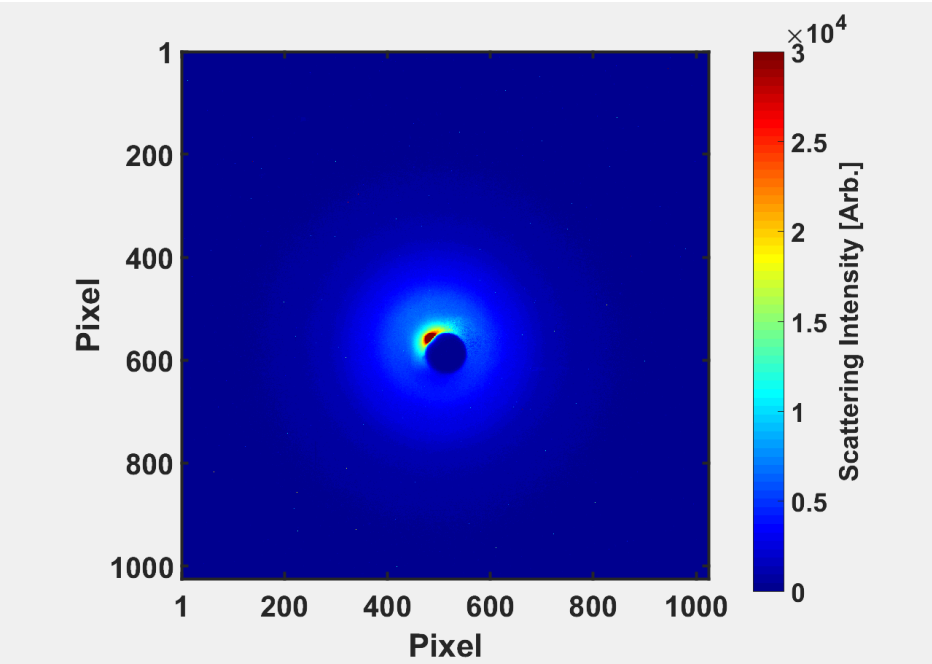

Figure 2.18: **Measured diffraction pattern from averaging 180 images at a same delay.** This figure gives an example of the total diffraction signal at a single delay after averaging images. This pattern is from far negative pump-probe delay (<-10 ps).

Similar with the circumstance of TRPES that was discussed in Sec. 2.2.4, the polarization of pump UV is set parallel to the detector plain (perpendicular to the electron beam) and the linear polarization induces a $\cos^2\theta$ distribution, where θ is the transition dipole moment (TDM) direction respect to the laser polarization. The total diffraction signal does not usually display obvious anisotropy and it is more visible from the difference diffraction signal. The angular distribution often delivers important information content of the structure especially for polyatomic molecules which have more than one atomic pairs. More details of the mathematics description involving TDM and atomic pair orientations is included in Sec. 2.4.3 of computer simulation of the 2D diffraction signal.

Here I focus on the 2D data analysis of the measured diffraction pattern, and the details of diffraction pre-analysis as well as the 1D azimuthally averaging analysis are included in Appendix C.2. The linearly polarized

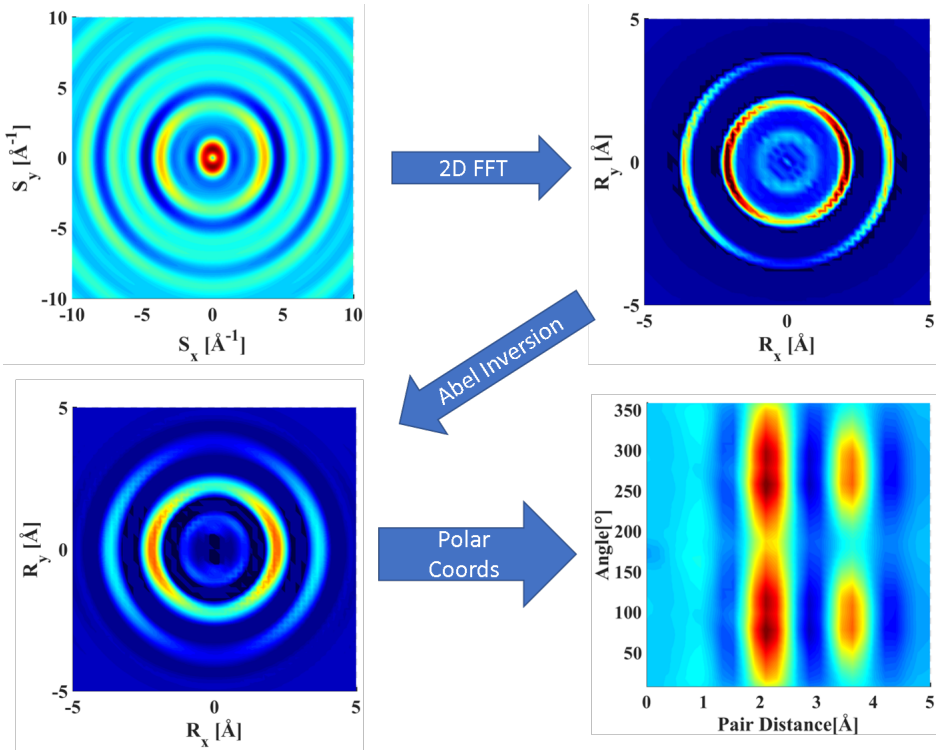

Figure 2.19: **3D analysis of electron diffraction patterns procedure.** This figure depicts an example of the data analysis procedures with the implementation of inverse Abel transform for the angular dependence. Top left panel shows a simulated diffraction signal (sM) with a $\cos^2\theta$ distribution between the laser polarization and the TDM direction. We used a geometry of ground state CH_2I_2 and assume the TDM direction is perpendicular to the I-C-I plane. Top right panel is the 2D pair distribution function (PDF) after a 2D fast Fourier transform in the real space. The PDF is then inverse Abel transformed, generating a 3D distribution PDF in a spherical coordinate. Bottom left panel shows the Abel inverted PDF and bottom right panel plots PDF as a function of pair distance (r) and polar angle (θ), where θ is the angle respect to the laser polarization.

UV induces a cylindrical symmetry of the three-dimensional (3D) scattering electron distribution, projected onto a 2D detector, forming the diffraction pattern. In order to reconstruct the 3D nature of diffraction signal, an inverse Abel transform [94] or pBASEX [95] methods are employed. Fig. 2.19

shows the 3D diffraction pattern analysis based on a simulated diffraction signal of CH_2I_2 with ground state geometry, by assuming the TDM direction is perpendicular to the I-C-I formed plain. Following the arrows, the calculated sM (top left panel) is Fourier transformed from momentum transfer space to real space obtaining the pair distribution function (top right panel). Followed by an inverse Abel transform, the 3D distribution of the PDF in spherical coordinates is reconstructed, and by integrating along the ϕ axis (azimuth), the PDF then can be plotted as a function of pair distance (r) and polar angle(θ). Fig. 2.19 bottom right panel delivers useful information, such that the two C-I bond ($\sim$ 2.15Å) and the I-I bond ($\sim$ 3.60Å) are both along the perpendicular direction respect to the laser polarization with a $\cos^2\theta$ distribution, which agrees with the initial assumption that the TDM direction is perpendicular to the I-C-I plane.

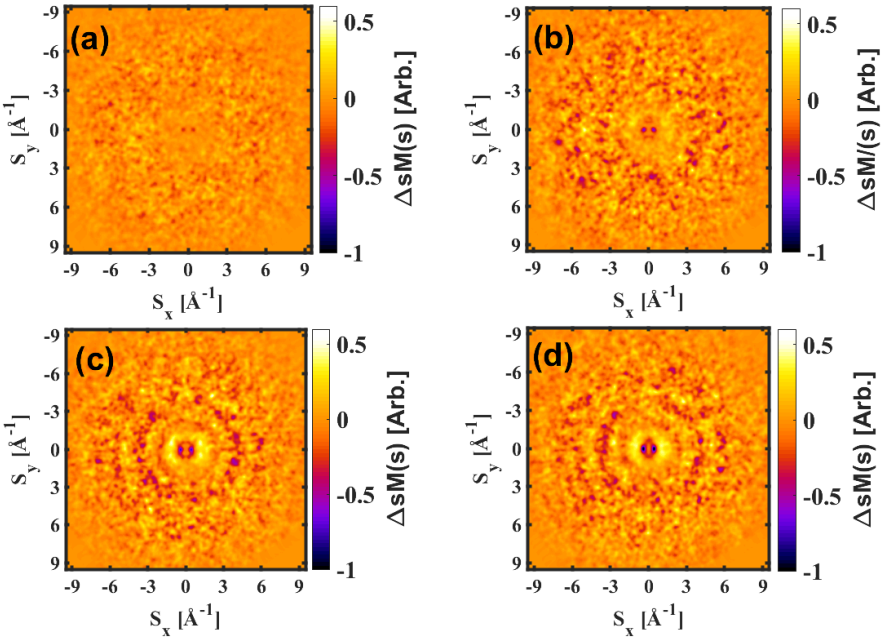

Figure 2.20: **Experimental 2D diffraction difference pattern, ΔsM(s), at different pump-probe delays. (A)** Pattern averaged over delays from -250 to -150 fs. **(B)** Pattern averaged over delays from -50 to 50 fs. **(C)** Pattern averaged over delays from 200 to 300 fs. **(D)** Pattern averaged over delays from 500 to 600 fs.

The 3D diffraction pattern analysis is also applicable to the diffraction

difference data and Fig. 2.20 showcases an example of the 2D diffraction pattern difference signal obtained by subtracting the far negative delay signal. These is quite obvious anisotropy from the 2D ΔsM(s). One of the main issue for 2D diffraction pattern analysis is how to deal with the detector hole region. As I discussed of the 1D diffraction pattern analysis in Appendix C.2the azimuthally integrated analysis takes the advantage of the off-center beam, allowing to reach to the lower diffraction signal (often as low as 0.4 $Å^{-1}$), whereas, the 2D diffraction pattern needs more care before doing the Fourier transform. Previous experiments made use of a simulated signal according to a simple model of the dynamics to fill up the missing data in the hole region, in order to reduce the artifacts [21, 96, 48]. According to the symmetry of the diffraction pattern respect to the laser polarization, I switch to an alternative route, by mirroring the partially available data at the quadrant close to the main electron beam into the other three quadrants that are far away from the main beam. In this way, the 2D diffraction signal can be made available down to 0.4 $Å^{-1}$, without the aid of simulation. The rest of the area can be filled by interpolating the signal along the slope of the edge down to zero point.

2.4 From trajectory surface hopping calculation to measurement observables

In the sections above, I have discussed both the energetic and structural probes in the experimental perspectives with detail. However, it is usually not straightforward to establish a connection between the measurements and the dynamics without theory input. Often, with the aid of dynamics calculations the experimental signals are interpreted and the underlying dynamics can be mapped out. In the measurement, the quantum dynamics of interests are filtered by the coordinated-dependent matrix element of the chosen experimental observable, therefore, in this dissertation, one of the main contents is to simulate the observables and directly compare these calculated observables with the experiments [11]

[11] For all the TRPES signals in this dissertation, our theory collaborators calculated the photoionization rate by evaluating the Dyson norms at each time step of individual trajectories and the TRPES signal is an average of all the trajectories.

2.4.1 Nuclear trajectories from the trajectory surface hopping calculation

Trajectory surface hopping (TSH) calculation is one of the most frequently used methods to deal with the coupled electronic and nuclear dynamics, in which the electronic degrees of freedom are treated quantum mechanically, and the nuclear degrees of freedom are treated classically. Instead of propagating a time-dependent wavepacket, an ensemble of independent classical nuclear trajectories are initiated, each of which samples different regions of the multidimensional potential energy surface (PES) upon the excitation process. For each trajectory, energies, gradients/forces, and nonadiabatic coupling are evaluated at each time step for the nuclear geometry on-the-fly, together with the transition probabilities of hopping event from on electronic state to another. The propagation of the trajectory along the potential is governed by Newton's equation of motion.

Each individual trajectory provides rich information from multiple aspects, such as time-dependent energy, active electronic state index, hopping events, and molecular geometries (atomic centers) etc. However, single trajectories cannot represent the overall picture of the underlying dynamics, and only an ensemble of trajectories is meaningful. A simple example is to statistically track the time-dependent state indices of neutral electronic state, such that the excited state population is obtained, and the dynamics pathways, state lifetimes, reaction products may be inferred. Obviously, this state population cannot be directly measured, but may be rather extracted with fitting algorithm as well as dynamics models. One step beyond this, is to generate the measurement observables, such as the energy integrated/differentiated photoelectron or photoion yield, or simulated the time-dependent diffraction signal from the classical trajectories. One thing to note here is that the calculation is complete and there is not much meaning interpreting the calculation itself. One can judge the accuracy of the calculation, such like a higher level of theory used in the dynamics calculation may yield better results. Or one may be able to gain insight with proper manipulation of the trajectories. As the hopping being as a manifestation of the nonadiabatic transition, one is able to evaluate the significance of the non-adiabatic effects by simply **"turning on"** or **"turning off"** the hopping during the trajectories propagation and compare the calculated observables with the measurements. According to the behaviors of the trajectories, one may be able to examine the local versus non-local wavepacket dynamics by sorting

the trajectories into sub-groups.

In this dissertation, all of the dynamics calculations are based on trajectory surface hopping method that are carried out from our theory collaborators, and the calculations are used to simulated the measurement observables, indlcuding photoelectron spectra, momentum-resolved photofragment kinetic energy distribution, and diffraction pattern and pair distribution function. In brief,in Chap. 3 and 4, the calculation of cc-COD and uracil dynamics were carried by *Pratip Charkraborty* and *Spiridoula Matsika*. Whereas, in Chap. 5, the calculation of the CH_2I_2 and CH_2IBr were carried by *Philipp Marquetand* and *Tamás Rozgonyi*.par

2.4.2 From trajectories to time-resolved photoelectron and momentum-resolved photoion spectra

The values that one measures in the time-resolved ionization spectroscopy is photoion and/or photoelectron yields. In order to calculate the TPRES signal, the ionization probability along the time-dependent trajectories are obtained and naturally, one or more ionic states need to be considered. The ionization process can be assumed as a vertical transition, i.e., the nuclear wave function of the initial neutral state and the final target ionic state are identical, and the ionization probability along the time-dependent trajectories is obtained in an approximate manner from calculation of the Dyson orbital norms. Dyson orbital is treated as an one-electron quantity that represents a projection between a N-electron wavefunction (neutral) and a (N-1)-electron wavefunction (cationic) which can be described as [97]

$$\psi_{IF}^{d} = \sqrt{N} \int \Psi_I^N(1,\ldots,n)\Psi_F^{N-1}(2,\ldots,n)d2\ldots dn \tag{2.22}$$

Ψ_I^N, usually, refer to the initial ground or electronically excited state, whereas Ψ_F^{N-1} refers to the final cationic state of the system. The integral is over N-1 electrons. If the initial state is the ground state, the Dyson orbitals are similar to the corresponding Hartree-Fock molecular orbitals from which the ionization takes place. For the ionization from the electronically excited states, extra care is needed since the excited state usually include contribution from more than one molecular orbitals (configurations) and Dyson orbitals have to be evaluated [55].

With the Dyson orbital, the transition dipole matrix elements from the neutral state to the cationic state is given by:

$$D_{IF} = \left\langle \psi^d_{IF} | \boldsymbol{\mu} \cdot \mathbf{u} | \psi^k_F \right\rangle . \tag{2.23}$$

where $\boldsymbol{\mu} \cdot \mathbf{u}$ is the scalar product of the dipole operator and the unit vector along the laser polarization axis. ψ^k_F is the wavefucntion of the outgoing electron, and ψ^d_{IF} is the Dyson orbital defined as the overlap between the initial neutral electronic state and the final cation state after an electron is ejected. By assuming the photoelectron ejection is fast without interaction with the cation in the final state (cationic), the wavefunction of the ejected electron may be ignored and one can approximate $|D_{IF}|^2$ with the square of the Dyson norm and it has been widely used in the literature without significant influence on the photoelectron spectrum. [13, 98, 99]

For an individual trajectory j, generally, the TRPES signal at time step t can be expressed by the following equation: [55]

$$S_j\left(t;\epsilon_k\right) = \sum_F^{\text{ion.states}} \frac{4\pi^2 k\hbar\omega}{c} \left|D_{IF}\right|^2 \delta\left(\hbar\omega - \Delta V_{IF} - \epsilon_k\right) \tag{2.24}$$

where $\Delta V_{IF} = V_F - V_I$ represents the difference of the vertical electronic energies of the initial neutral state I and the final ionic states F, and ϵ_k and k are kinetic energy and momentum of the ejected electron, respectively. $\hbar$ is the probe photon energy and c is the speed of light.

The calculated TRPES signal then can be obtained by adding up the energy differentiated ionization probability from all the trajectories, and with the convolution of the instrument response function as follows,

$$S\left(t;\epsilon_k\right) = \eta(\epsilon) \otimes G(t) \otimes \sum_j S_j\left(t;\epsilon_k\right) \tag{2.25}$$

where $\eta(\epsilon)$ and G(t) represent the energy and temporal resolution functions which can be estimated from the experimental measurement.

Besides the photoelectron signal, one is able to simulate the photoion signals as well. The total ion (including parent and fragment ions) yield can be obtained from the calculated energy resolved photoelectron spectra, by integrating the ionization probability from all energies. Moreover, the time-and-momentum resolved photo-fragment ion signal may be partially available

by classically calculating the kinetic energy from the time-dependent molecular geometries. The trajectories contain the three dimensional geometries of all the atoms at each time step, which can be plugged into the equation of motion with Newton's law,

$$E_T = \frac{1}{2} m_c v^2 \tag{2.26}$$

where E_T is the translation kinetic energy. m_c and v represent the center of mass and the instantaneous velocity which can be calculated from the relative positions of each atoms between two time steps. The trajectories propagate in the neutral states, thus these calculations neglect the influence of the cationic state, i.e., calculation do not include changes to the kinetic energies from the ionic states potential. In principle, the kinetic energy of the fragment ions should be calculated from the trajectories propagating in the cationic states. This requires a TSH calculation for each pump-probe delay and each state of the cation. However, such calculations are extremely computational expensive and obtaining accurate potential energy surfaces of the cation is very challenging.

2.4.3 From trajectories to electron diffraction pattern and pair distribution function

Similar with the TRPES or TRPIS, the electron diffraction signal can be simulated from the nuclear trajectories. We make use of the independent atom approximation (IAM) in the scattering process, where the scattering amplitude and phase of each individual atom in the molecule are approximated to be the same as an isolated atom, i.e., the electrons that participate in chemical bonds are neglected. The time-dependent atomic centers are needed. Each trajectory has the positions for each atomic center as a function of time, as well as the TDM direction with respect to the relative positions of the atoms. Experimental conditions, such as electron beam energy, are applied to the simulation in order to compare with the experimental measurements. Only the elastic scattering effect is considered and the scattering amplitudes (phases) for different atoms and H, etc, are calculated using the Dirac partial-wave method (ELSEPA sofeware) [84]. The simulation can be accomplished either with or without considering the angular distribution/anisotropy of the diffraction pattern induced by the linearly

polarized UV excitation. Without considering that, the diffraction simulation can be followed the equations in Sec. 2.3.1, by assuming the molecules in different orientations are evenly excited by the pump UV, i.e., the TDM direction is not related. Here we consider the latter case and introduce the relative novel TDM direction related 3D diffraction pattern simulation.

We start from a single molecule with an single orientation in the molecular ensemble. The molecular scattering intensity for this single molecule with orientation $\vec{a}$ at time t can be written as,

$$I^{\vec{a}}(t;\vec{s}) = \sum_{i=1}^{N}\sum_{j\neq i}^{N} f_i(s)f_j^*(s)Re[e^{(i\vec{s}\cdot\vec{r}_{ij}(\vec{a};t))}], \tag{2.27}$$

where, N is the number of atoms in the molecule, $f_i(s)$ is the complex-valued elastic scattering amplitude for the i^{th} atom, $\vec{r}_{ij}(\vec{a},t)$ is the vector pointing from the i^{th} to the j^{th} atom. $\vec{s}$ is the momentum transfer vector between the initial and final wave factor ($\vec{s} = \vec{k} - \vec{k_0}$) with magnitude $\frac{4\pi}{\lambda}\sin(\Theta/2)$, Θ (use Θ in order to differentiate the θ as indicated below) here denotes the electron scattering angle.

In the experiments, the linearly polarized UV light preferentially excites molecules whose TDM direction is along the laser polarization, leading to a $\cos^2(\theta)$ dependence, in which θ is the angle between laser polarization and TDM directions. This angle was taken into account by weighing the scattering magnitude with $\cos^2(\theta)$.Therefore, the total scattering intensity for the molecular ensemble with considerration of the can be written as an incoherent sum of the single-molecule scattering intensities,

$$I(t;\vec{s}) = \sum_{\vec{a}} I^{\vec{a}}(t;\vec{s})\cos^2\theta^{(\vec{a})}, \tag{2.28}$$

In order to capture the angular distribution of the molecule during the excitation, we simulated an ensemble of diffraction patterns from an ensemble of different orientations of the molecule [100, 101]. Practically, a molecular frame, [X, Y, Z] is defined, in which all the atoms in the molecule are located into the frame under its given structure. A lab frame, [x, y, z] is defined by the laser polarization direction being along the y axis and electron beam traveling along the z axis. Different orientations of the molecules in the lab frame are generated by starting with the lab and molecular frames being the overlapped and rotating the molecular frame along the proper Euler angles,

α, β, γ, in which α represents a rotation around the z axis, β represents a rotation around the rotated x axis, and γ represents the rotation around the rotated z axis. The diffraction pattern of the total scattering intensity is then a sum from all the rotated geometries, which can be written as,

$$I(t;\vec{s}) = \sum_{\alpha}\sum_{\beta}\sum_{\gamma} I^{(\alpha,\beta,\gamma)}(t;\vec{s})\cos^2\theta^{(\alpha,\beta,\gamma)}, \tag{2.29}$$

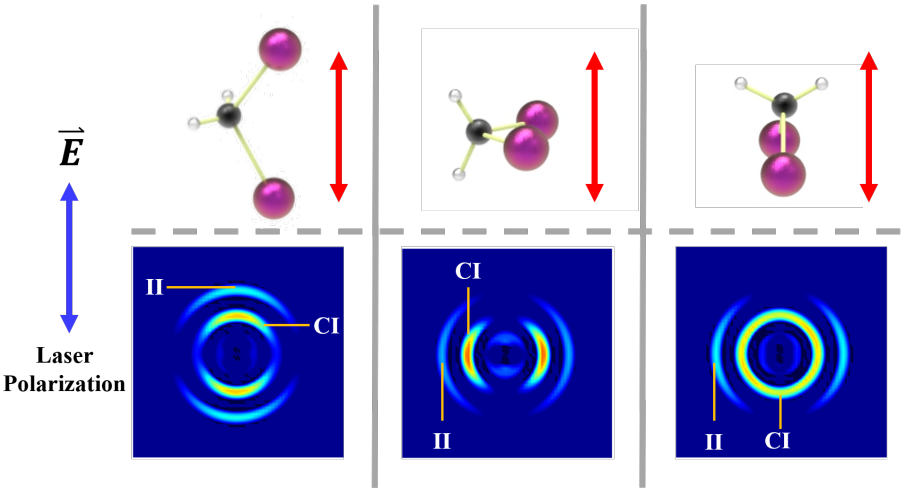

Figure 2.21: **3D diffraction pattern simulation: considering the TDM direction and laser polarization.** A CH_2I_2 molecule is used to describe simulation. Black, gray and purple represent carbon hydrogen and iodine, respectively. Three scenarios of the TMD direction with respect to the atomic positions are assumed as shown in the top panels from left to the right. The diffraction patterns are calculated according to Equ. 2.29, followed with a 2D Fourier analysis and Abel inverse transform. The 2D pair distribution function for each scenario is displayed in the bottom panels and the C-I and I-I pairs are indicated.

The diffraction patterns are then calculated for the geometry at each time delay of each individual trajectories, and the same diffraction pattern analysis routine used for the experimental data (described in Fig. 2.19) is applied to the simulated diffraction patterns to generate the angular dependent PDF. An example of the TDM direction dependent simulation is described in Fig. 2.21. The pump UV polarization is indicated with the arrow in the

left side of the figure. In top panels, three different orientations of a CH_2I_2 molecule are displayed, as well as the TDM directions indicated by the red arrows. The diffraction patterns from these different configurations are then simulated based on Equ. 2.29. By implementing a 2D Fourier transform followed by an inverse Abel transform, the 3D PDFs are plotted in the bottom panels. From these simulations, there is obvious angular dependence with considering the TDM direction with respect to the laser polarization. Different pairs, C-I, I-I, indicate different angular distribution with respect to the laser polarization.

2.5 Conclusion

In this chapter, I described the experimental details of TPRES/TRPIS and UED methods with great details for doing spectroscopic and structural measurement. Along the spectroscopic side, a detailed description of the fifth harmonic VUV light generation, the UV-VUV pump-probe optical geometry, the photoelectron and photoion VMI spectrometer are provided. The characterization of the instrument response function as well as the data analysis methods are reviewed. For structural probe, a review of the gaseous electron elastic scattering theory and signal processing protocol are provided, followed with a brief description of the relativistic UED beamline in SLAC, in which the space-charge and velocity mismatch issues are greatly improved compared with a conventional KeV UED setup. A two-dimensional diffraction pattern analysis method is introduced. Finally, simulating the measurement observables from trajectory surface hopping calculations are instructed, which is essential for the interpretation of the experimental measurements from Chap 3 to Chap. 5.

Chapter 3

Excited state dynamics of *cis,cis*-1,3-cyclooctadiene: UV pump VUV probe time-resolved photoelectron spectroscopy

3.1 Introduction and motivation

As I have alluded in Chap. 1, understanding the dynamics of photoexcited molecules is of great importance to many areas of chemistry, physics and biology. The coupled electron-nucleus dynamics initiated by photoabsorption can lead to internal conversion, isomerization and dissociation. While these dynamics can be quite complicated and difficult to follow, particularly for larger molecules with many degrees of freedom, systematic studies of similar molecules can be very much helpful in elucidating essential features in the dynamics and a deeper understanding of the connection between structure and dynamics. From this chapter, I start to describe experimental measurements in several specific molecular systems. In this chapter, I extend earlier work on simple organic molecules, in an effort to understand isomerization and internal conversion in systems with a few C-C double bonds. The most basic unit to examine photoisomerization is the smallest molecule with a single double bond: ethylene, which has been studied ex-

tensively [78, 102, 103, 104, 105, 106]. Beyond ethylene, many biological chromophores however, such as retinal, include a more extended linear or circular conjugated system with several double bonds [107].

Two such systems which have drawn considerable interest in past decades are *trans*-1,3-butadiene (BD, C_4H_6) [108, 109, 110, 111, 52, 112], and 1,3-cyclohe-xadiene (CHD, C_6H_8) [34, 19, 113, 114, 115, 38, 40]. Several measurements and calculations have extended our understanding of the isomerization dynamics in small conjugated organic molecules. However, these studies have focused on relatively rigid small molecules, and we aim to extend our understanding to larger, more flexible systems, where we might expect qualitative differences in the internal conversion and isomerization dynamics. A natural choice that I chose which extends the previous studies is *cis,cis*-1,3-cyclooctadiene (cc-COD, C_8H_{12}). cc-COD is similar to CHD, but larger and more flexible. In both CHD and cc-COD there are two alternating double bonds, but the remaining cyclic system imposes different constraints on the dynamics. In CHD, the dynamics are controlled by conical intersections (CIs) with the ground state that can lead to either relaxation, or photochemistry to produce hexatriene, which has been studied extensively with both time-resolved spectroscopies and diffraction measurements [39, 40, 48]. In cc-COD on the other hand, there can be cis-trans isomerization, as well as photochemistry to other products [116, 117, 69]. Compared with CHD, the isomerization dynamics of cc-COD have not been well studied by either spectroscopic or structural probes. Fuß *et al.* performed UV pump - IR probe ionization measurements on cc-COD and established basic timescales for the dynamics and possible photochecmical products, but did not provide a detailed picture of the dynamics [116].

Time-resolved photoelectron spectroscopy (TRPES), with measuring photoelectron kinetic energy, is sensitive to both electronic and nuclear dynamics, therefore, a TRPES experiment can be used to follow the internal conversion and isomerization dynamics after UV excitation. Compared with IR and/or UV, it is essential to use VUV as the probe in the TRPES measurement, since the higher photon energy of VUV photon allows ionization from everywhere in the excited state with one photon, but ionization from the ground state of cc-COD is avoided (IP: 8.62 eV) [118]. Fig. 3.1 shows our UV pump pulse spectrum together with the calculated absorption spectrum of cc-COD from our theory collaborator, Pratip Chakraborty and Spiridoula Matsika, together with which the electronic structures as well as a dynamics calculations using trajectory surface hopping (TSH) calculation were also carried

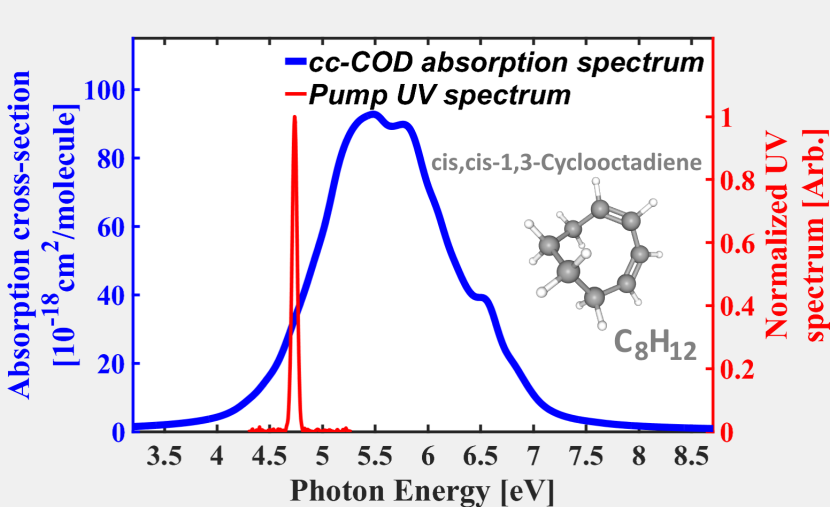

Figure 3.1: **Calculated cc-COD absorption spectrum in the deep UV.** A cartoon of cc-COD (C_8H_{12}) is shown next to the spectra. The calculated spectrum is obtained at the XMS-CASPT2(4,4)/cc-pVDZ level of theory and agrees well with the measured absorption spectrum as reported in Ref. [117]. The details about the calculation of the absorption spectrum are provided in Appendix A.

out. As shown in Fig. 3.1, the absorption peak of cc-COD is around ∼5.5 eV, in which the pump UV spectrum sits at the lower energy tail of the absorption spectrum. This is an essential point in the data interpretation. In order to make a meaningful comparison between the experiment and simulations, only those trajectories at the lower edge of the absorption spectrum (corresponding to the 4.75 eV pump pulse) are selected to calculate the TRPES signal [119].

The TRPES experiment I performed utilized the UV/VUV pump/probe coincidence VMI apparatus, which has been described in Chap. 2 with great details. The sample is purchased from Sigma-Aldrich (98%) and used without further purification. The sample is delivered to the vacuum chamber with the liquid-gas nozzle under room temperature. A 4.75 eV deep UV pump pulse launches a vibrational wave packet on the first electronically excited state, S_1, and the ensuing dynamics are probed *via* ionization using the 7.92 eV probe pulse. After the molecules ionized by the probe pulse, the photoelectrons VMI images are recorded as a function of the pump and probe delays. An

Abel inversion algorithm is used to recover the full 3D vector momentum distribution of the photoelectrons based on the measured 2D projection with cylindrical symmetry about the laser polarization axis. The photoelectron spectrum (yield as a function of energy) is then calculated from the 3D momentum distribution. In the rest of this chapter, I present the detailed data analysis on the measured photoelectron spectra and the interpretation with the aid of the calculated TRPES from dynamics calculations.

3.2 2D global analysis of measured photoelectron spectra

Before I step into the measured and calculated TRPES of cc-COD, I first describe the data analysis protocols of the the experimental TRPES. Fig. 3.2 panel A showcases the measured TRPES with a linear intensity scale, including both negative and positive delays. The pump-probe time-zero (T0) is located according to a TRPES measurement of ethylene, and this measurement also provides an instrument response function of UV-VUV cross-correlation as a Gaussian with FWHM $\sim$ 80fs. The details of the ethylene TRPES measurement can be found in Sec. 2.2.4. In general, identification the right T0 is useful and applicable to any time-resolved measurements involved with a pump-probe frame work. For cc-COD, this is particularly essential. In Fig. 3.2 panel A, positive delays reflects that UV pulse comes before VUV pulse (UV pumps and VUV probes) and one can see that the measured TRPES signals showcases on both side of the the T0 indicating that the signal contains both UV and VUV induced dynamics. Since what we are interested in are the UV driven dynamics in the positive delays, the VUV driven dynamics complicates the interpretation for small positive delays, given the finite pump and probe pulse duration. In the TRPES siganl, the photoelectron yield is higher for negative delays than for positive and this is a common feature for these pump and probe wavelengths, since many molecules have stronger absorption in the VUV (at $\sim$ 160 nm) than in the deep UV (at $\sim$ 260 nm).

In order to decompose the UV/VUV induced signal, a 2D bilateral global least-squares fitting analysis is implemented with the identified right time-zero from ethylene measurement, allowing to extract information for the positive delays despite the larger signal for negative delays which can bleed

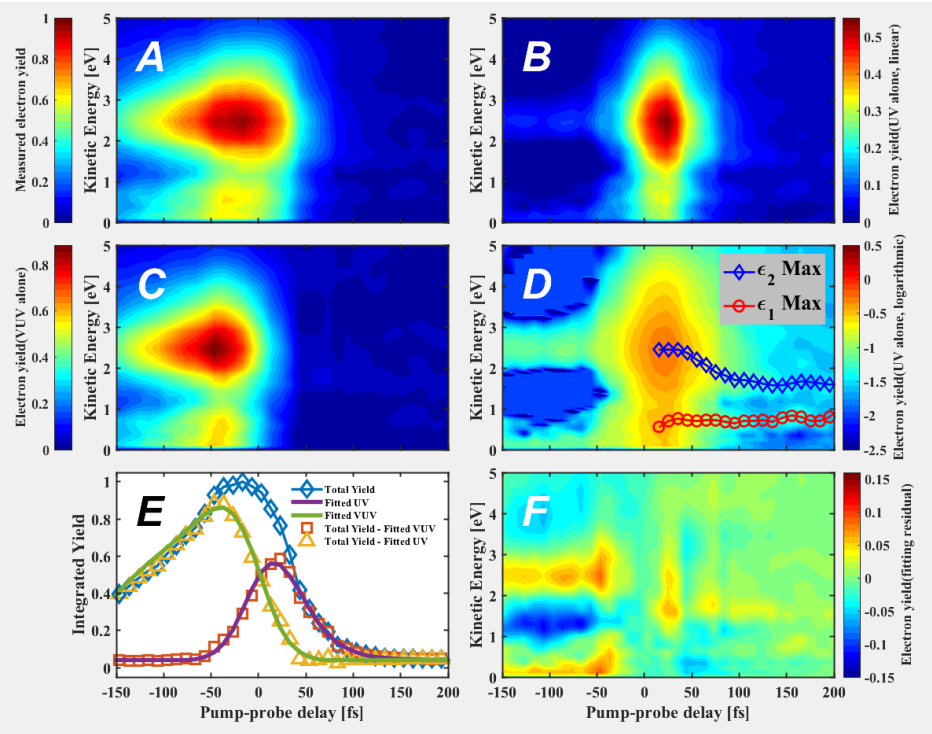

Figure 3.2: **Photoelectron spectra of cc-COD and 2D global fitting analysis.Photoelectron spectra of cc-COD and 2D global fitting analysis.** Panels **A** through **F** share the same pump-probe delay axis. Panel **A** shows the measured time-resolved photoelectron spectrum for both positive and negative delays. Panels **B** and **C** plot the spectra with fitted VUV and UV driven dynamics subtracted respectively. In panel **D**, the spectrum in panel **B** is shown with a logarithmic intensity scale as shown in panel **D**. Panel **E** shows the energy integrated photoelectron yield of the measurements and fits. Panel **F** shows the residuals from the fitting procedure.

into the positive delay signal because of the finite IRF [52, 120]. Here I define $Y(t;\epsilon_k)$ to be the differential photoelectron yield as a function of pump-probe (or probe-pump) delay and electron kinetic energy for the UV (or VUV) induced dynamics. In general, $Y(t;\epsilon_k)$ is globally fitted to

$$Y(t;\epsilon_k) = G(t) \otimes \sum_i S_i(\epsilon_k) e^{-t/\tau_i}, \tag{3.1}$$

where the $S_i(\epsilon_k)$ are the time independent decay related spectra and $G(t)$ represents the Gaussian cross correlation function associated with the IRF. The energy-resolved amplitudes of the fitting components have decay constants τ_i, assuming that the population of the excited states follows an exponential decay. In Equ. 3.1, a given $S_i(\epsilon_k)$ is associated with the energy-related photoionization cross-section $\sigma_i(\epsilon_k)$ of the i^{th} excited state. If the underlying dynamics involve photoinoization from more than one excited state (i.e., i = 1,2...) one can establish kinetic models in the global fitting where more than one decay constant can be extracted from the fitting. The total electron yield is then convolved with $G(t)$, the Gaussian cross-correlation function that represents the IRF. In the case of cc-COD, we fit to only one exponential decay for the UV driven dynamics signals, since we are focusing on dynamics involving a single excited state. Thus, Equ. 3.1 can be simplified as:

$$Y(t;\epsilon_k) = G(t) \otimes S(\epsilon_k) e^{-t/\tau}. \tag{3.2}$$

This type of analysis of the 2D global fitting is based upon the assumption that the spectrum $S_1(\epsilon_k)$ is time-independent, and only the overall amplitude varies with time. In other words, the different portions of the photoelectron spectrum are fitted with the same decay constant, which means that spectral components associated with the dynamics of the relevant state remain *frozen* at the Franck-Condon (FC) point. Under this assumption, the molecule does not experience large amplitude motion away from the FC region before the decay of the excited state, and such an analysis provides a reasonable estimation of the excited state life time [121, 122]. Often there is large amplitude motion of the wave packet moving away from the initial FC region which can be due to the large slope of the PESs, and the 2D fit can fail which may be indicated by the systematic structures in the residuals between the fitted and raw spectra.

In order to eliminate the VUV driven dynamics, I subtracted the fitted negative time signal from the total TRPES measurements [52, 120]. In this

way, I obtained the UV driven signal alone. This is important for the interpretation around zero time delay, where the pump and probe pulses overlap. We assumed a single exponential model for the VUV driven dynamics (negative time signal), leading to the following fitting function, which includes both positive and negative delay:

$$Y(t;\epsilon_k) = G(t) \otimes (S(\epsilon_k^{vuv}) e^{t/\tau_{vuv}}|_{t<0} + S(\epsilon_k^{uv}) e^{-t/\tau_{uv}}|_{t>0}), \tag{3.3}$$

Fig. 3.2 panels B and C show the UV driven (pump-probe) and VUV driven (probe-pump) dynamics contributions to the TRPES respectively, obtained by subtracting the fitted VUV and UV driven spectra from the measured spectra. In addition to allowing for the subtraction of the VUV driven dynamics, performing a global 2D fit can serve as a test of whether or not there is significant motion on the excited state before internal conversion [52]. If there is no significant structure in the residuals associated with the fit, then this suggests that the excited state wave packet does not experience much displacement before internal conversion. On the other hand, systematic structure in the residuals can serve as an indication or corroboration of motion on the excited state which is viewed via the changes in the photoelectron spectrum as the wave packet moves away from the FC point. A typical feature one can see from the photoelectron spectra related to the large motion of the wave packet is the time-dependent energy change which shows up as spectral shifting. Fig. 3.2 panel D plots the UV-pump VUV-probe spectrum from panel B with a logarithmic intensity scale. Panel E shows the energy integrated photonelectron yield from the measured and fitted spectra. It is clear that the signal from the VUV driven dynamics is stronger than the signal from the UV driven dynamics, and contributes even for positive time delays out to $\sim$ 50 fs. By subtracting the fitted spectra from the total spectra, I plot the residual spectra in panel F. One can see there is systematic structure of the residual spectra and I will discussed these features in the next sections.

3.3 Measured and simulated TRPES of cc-COD

Panel A of Fig. 3.3 shows the TRPES (UV-pump alone) as a function of pump-probe delay and kinetic energy (KE) after the decomposition of the

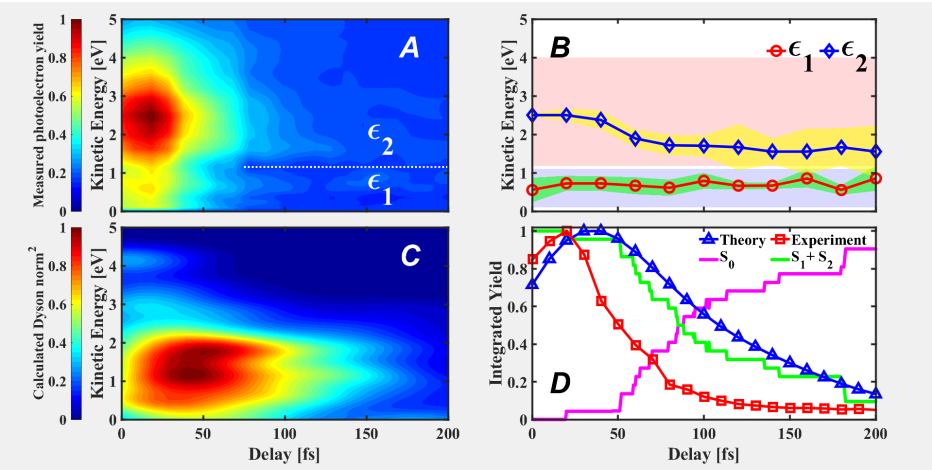

Figure 3.3: **TRPES of cc-COD with UV-pump and VUV probe.**Panels **A** and **C** show the measured and calculated TRPES respectively. The low and high KE peak regions of panel **A** are labeled as ϵ_1 and ϵ_2. Panel **B** shows the peak locations as a function of pump probe delay. The low and high KE regions are highlighted by different background colors. The yellow and green shading in panel **B** indicate the uncertainty in the peak locations obtained from a bootstrapping analysis. Panel **D** shows the state populations, the calculated ionization yield, and the experimental ionization yield (energy integrated TRPES measurement).

VUV driven TRPES signal from the total signal. As one can see, the TRPES shows two main peaks near time-zero. One broad peak has high KE between 1.2 and 4 eV, and a narrower peak has lower KE below $\sim$ 1 eV. As discussed in more detail below, these two peaks can be interpreted in terms of ionization to two different states of the cation. In the longer positive delay, The higher kinetic energy peak shows a systematic shift towards to lower energy, while the position of the lower kinetic energy peak stays relatively constant. Fig. 3.3 panel C plots the calculated TRPES for each pump-probe delay and panel D shows the total ionization yield (energy integrated TRPES) for both the measurements and the calculations as a function of pump-probe delay, as well as the ground (S_0) and excited states (S_1 + S_2) populations.

In order to extract the photoelectron peak positions as a function of pump-probe delay, I carried out two approaches to follow the evolution of the peak locations. These approaches are based on finding the maximum

for both peaks, and finding the center of mass (CoM) - from both the raw spectra (UV-pump alone, panel A of Fig. 3.3) and Gaussian fitted spectra The results are shown in Fig. 3.4. For the fitting method, I fit each of the two peaks shown in panel A of Fig. 3.3 to a single Gaussian function, which does not capture each peak perfectly, but allows for a simple analysis of the time dependent location for each peak. In Fig. 3.4, panels A and B show the time-dependent peak locations and CoM values from the raw spectra, while panels C and D plot the results from the fitted spectra. I first discuss the results from finding the locations of peak maxima. As shown in panel A and C, the higher kinetic energy peak shifts towards to lower energy monotonically, with a shift of $\sim$0.9 eV over 100 fs. In contrast, the lower kinetic energy peak oscillates and shifts less than 0.4 eV. Panels B and D plot the CoM values from both the raw and fitted spectra. The CoM of the higher energy peak also shows a monotonic shift towards to the lower energy, although the shift is only about 0.4 eV. On the other hand, the CoM of the lower energy peak is roughly constant. The extracted photoelectron peak maxima positions from the raw data at each delay are replotted in Fig. 3.3 panel B. In order to validate the statistical significance of time dependent shift of the kinetic energy, I employed a standard bootstrapping analysis to estimate the uncertainties. I extracted the peak positions of the lower and higher energy peaks from the bootstrapped datasets, and calculated the standard deviations as the error bar, which is shown in the in Fig. 3.3 panel B. It is clear that the energy shift (from about 2.5 eV to about 1.7 eV) of the higher kinetic energy peak is still larger than the standard deviation at delay $>$ 150 fs. This is in contrast with the lower energy peak, which does not shift significantly with pump-probe delay, staying around 0.7 eV.

In order to interpret the features in the experimental spectra, our theory collaborators simulated the TRPES signal using information from our previously published trajectory surface hopping calculations which can be found from Ref. [119]. Time-dependent Dyson norms were calculated for each trajectory with a time-step of 10 fs. Only those trajectories at the lower edge of the absorption spectrum (corresponding to the 4.75 eV pump pulse) are used in the simulating of the TRPES. For calculating the electron kinetic energies (KE), specific shifts were introduced to the KE of electrons from D_0, D_1 and D_2, since CASSCF overestimates the neutral excited state energies and underestimates the cationic state energies near the FC region. Shifts of 3.0 eV, 2.8 eV and 2.3 eV were introduced to the KE due to photoelectrons coming from ionization to D_0, D_1 and D_2, respectively. D_3 and D_4 are quite

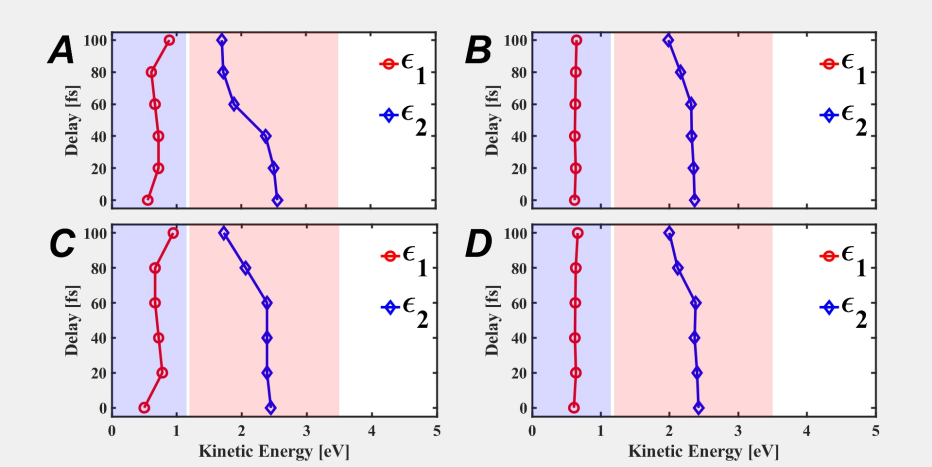

Figure 3.4: **Time evolution of peaks in the photoelectron spectrum.** Panel **A:** Time-dependent locations of peak maxima for both low and high kinetic energy peaks based on the raw spectra. Panel **B:** Time-dependent CoM values of both low and high kinetic energy peaks from raw spectra. Panel **C:** Time-dependent peak locations of both low and high kinetic energy peaks from fitted spectra. Panel **D:** Time-dependent CoM values of both low and high kinetic energy peaks from fitted spectra. Panels **A** and **B** are calculated based on the raw spectra, while Panels **C** and **D** are from the fitted spectra.

high in energy at the CASSCF level, and hence are not accessible and were neglected for the calculation of photoelectron spectrum. The energies of the photoelectrons at each delay step for each trajectory are convolved with a Gaussian function having a 0.5 eV FWHM along the energy axis and 80 fs FWHM along the delay axis in order to account for the finite energy resolution of the apparatus. For a more in depth understanding of which states are involved in the TRPES, and how they influence the dynamics, TRPES signal were also evaluated along linear interpolation paths. In order to generate the TRPES signal, the Dyson norms from S_1 and S_2 states to all of the 5 cationic states were calculated along the aforementioned LIICs. Care was taken to ensure the calculation of correct Dyson norms for each point of the LIICs as the neutral excited states switch character near the FC region at the CASSCF level. More details of the calculation can be view from Ref. [119] and Appendix A.1.

3.4 Ionization from excited state to different states in the cation

From the measured TRPES in Fig. 3.3, the feature we observed for positive delays are two peaks with different kinetic energies. And their different behaviours can be explained by the ionization from the neutral excited state, S_1, to different cationic states as the wave packet moves from the FC to the CIs. According to the calculations, there are three types of CIs between the ground and excited states, characterized by structural deformations around the two double bonds. Twisting and pyramidalization of a single double bond leads to two types of conical intersections, depending on whether the carbon adjacent to the other double bond or the carbon adjacent to the single bonds is pyramidalized. A third type of conical intersection involves twisting of both double bonds. The role of these conical intersections in the dynamics can be viewed from Ref. [119]. Here I discuss how the Dyson norms along pathways connecting them to the initial FC point vary, as they determine the photoelectron yield as the wave packet evolves on the excited state.

Figure 3.5 shows which ionic states are produced when ionization from S_1 occurs based on Koopmans' theorem: D_0 and D_3. These two states have a large Dyson norm with S_1, which can be explained by the fact that removing a single electron from either the highest occupied molecular orbital (HOMO)

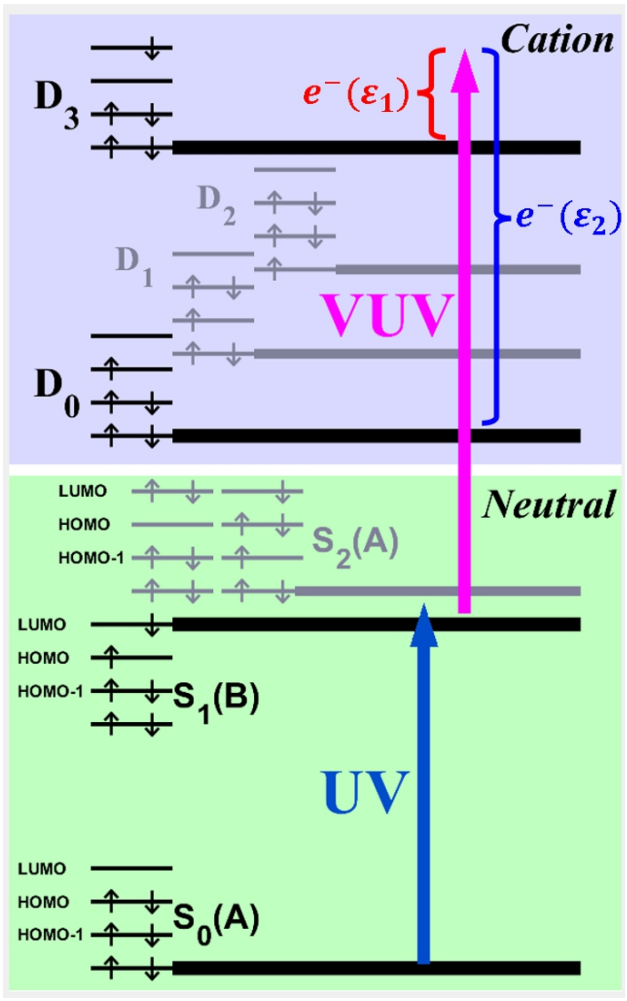

Figure 3.5: **A cartoon depiction of low lying neutral and cationic states, electron orbital occupancies, and Koopmans' correlations in the pump-probe measurements.**.

or lowest unoccupied molecular orbital (LUMO) leads to the dominant configuration in these two states. As also shown in the figure, ionization to D_3 and D_0 is energetically allowed, and thus, one expects ionization from S_1 to lead to both D_3 and D_0, at least near the FC point. In order to see how the energies of photoelectrons associated with ionization to these Dyson correlated states proceeds as the wave packet evolves on S_1, the energies of the neutral and ionic states between the FC point and the three different groups of CIs need to be checked. Fig. 3.6 shows the calculated electronic energies of the lowest lying neutral and ionic states at several points interpolated between the FC point and the three different CIs. Three important states are highlighted - the optically bright first excited state of the neutral, S_1 (red), the ground cationic state D_0 (green) and the third excited state of the cation at FC, D_3 (cyan). I note that since D_3 crosses a number of ionic states en route to the third CI, it is of mixed character and is therefore labelled D_{mix}. In Fig. 3.6, the x-axis is the fraction from FC to the CI region.

It is clear from the Fig. 3.6 that while the cyan and red lines are roughly parallel for all three panels as one moves away from the FC point, the green and red lines diverge. This means that one expects the low energy peak to remain roughly in the same place, while the high energy peak should shift to lower energies as the wave packet moves away from the FC point. This is consistent with our observation of a shifting high energy peak and a steady low energy peak in the photoelectron spectrum shown in Fig. 3.3. This also explains the systematic residuals in multiple regions from the 2D global fit analysis as shown in Fig. 3.2 panel F.

It is useful to discuss more details of the features in the residual and I focus the discussion on two key regions. One is a positive peak for early times over a broad range of energies (between $\sim$ 10 - 40 fs and from 0 - 5 eV). This feature can be interpreted in terms of an imperfect subtraction of the the contributions from VUV driven dynamics, which can contribute while there is still some overlap of pump and probe pulses. The other is a narrow positive peak just below 2 eV between 50 fs and 150 fs, together with a broad negative peak between 2 eV and 4 eV over the same range of delays. This is consistent with a shift of the high energy peak in the spectrum to lower energy over these delays. The positive residuals for energies above 4 eV do not vary significantly with time delay are likely due to stray electrons, which may also contribute to the positive residuals over all energies after 150 fs. Based upon the structures in the residuals, we conclude that the global 2D fit is consistent with the peak shift analysis above, indicating that our

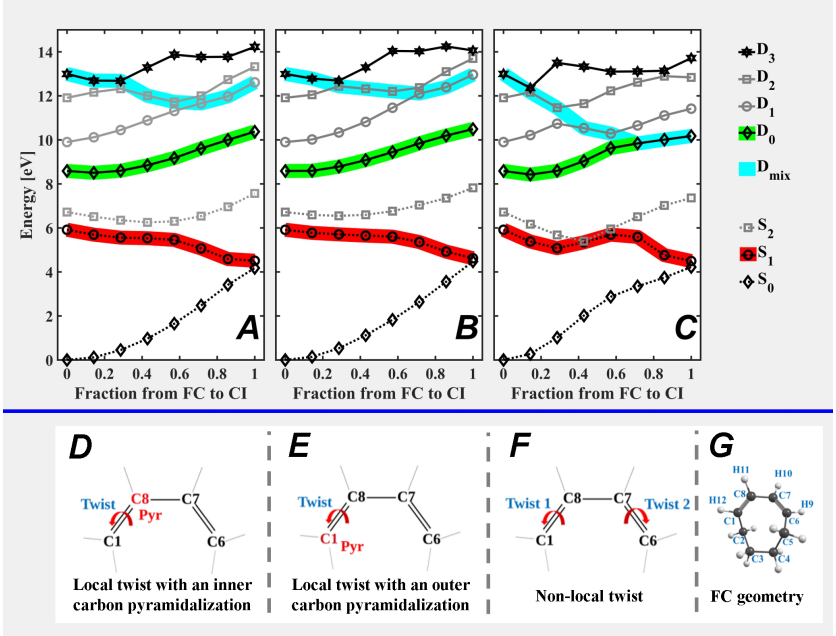

Figure 3.6: **Energies along paths to different CIs with cartoon diagrams illustrating the associated geometry changes.** The top three panels show the neutral and cationic electronic states calculated from the FC region to different CIs. **A**: Neutral and cation states from FC to the local CI with inner carbon pyramidalization. **B**: Neutral and cation states from FC to the local CI with outer carbon pyramidalization. **C**: Neutral and cation states from FC to a non-local CI (both double bonds twisted). Neutral states are plotted in dashed lines and cation states are plotted in solid lines. Four important states, including S_0, S_1, D_0, and D_3, are shown in black, while the other states are plotted in gray. Three thick colored lines highlight the states involved in the dynamics. The red, green and cyan highlights indicate S_1, D_0 and D_{mix}, respectively. Panels **D, E**, and **F** illustrate the structural changes corresponding to paths shown in panels **A**, **B**, and **C**, respectively. In addition, a cartoon depiction of the molecule in the Franck-Condon geometry is shown in panel **G**.

TRPES measurements provide evidence of significant motion along S_1 before internal conversion.

3.5 Comparison betweem measured and calculated TRPES

Figure 3.7 shows calculated photoelectron spectra along the LIICs by evaluating the Dyson norms between the neutral state S_1 and cation states along the paths to different CIs as shown in Fig. 3.6. In the calculation, the phototoelectron kinetic energy is obtained by subtracting the energy difference between D_0/D_3 and S_1 from the VUV probe photon energy in the experiment, which is 7.92 eV. The yield as a function of energy is then given by the norm of the Dyson orbital calculated by projecting each ionic state onto the neutral. In Fig. 3.7, one can see the calculated photoelectron spectrum shows two bands from the FC point towards to all three CIs, with the higher energy band decreasing in KE as a function of the fraction from FC to CI. In contrast, the lower KE band maintains a relatively constant energy around 1 eV. The behaviour of these two bands with position along the LIIC is consistent with the calculated and measured time evolution of our photoelectron spectrum, showing two main peaks - one at higher energy which shifts with position/delay, and one at lower energy which does not shift with position/delay.

The calculated energy for ionization to D_0 differs from the measured peak in the photoelectron spectrum for two main reasons. One is the error/uncertainty in the calculations, which is about 0.5 eV. The other is the fact that in the experiment, the pump laser excites the molecules on the red side of the absorption spectrum, meaning that the excitation is from the edges or tail of the ground state vibrational wave function on S_0 to lower vibrational levels on S_1. Since S_1 and D_0 diverge as one moves away from FC, the photoelectron spectrum is shifted to lower energies than one would calculate at FC. This leads to a lower measured photoelectron energy for ionization to D_0 than the calculations, although we note that the high energy shoulder of the measured high energy peak extends to roughly 5 eV (the calculated value), as one would expect based upon the explanation given above. Also, we note that the measurements and calculations roughly agree on the location of the low energy peak (for ionization to D_3), consistent with the fact that D_3 is

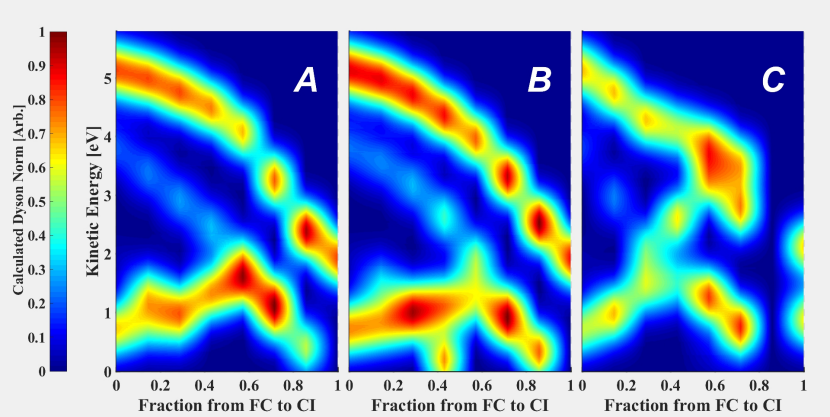

Figure 3.7: **Calculated photoelectron spectra by evaluating Dyson norms between the neutral S_1 state and low lying cationic states along paths connecting FC to different types of CIs.** The panels in the figure are correlated to the panels in Fig. 3.6. **A**: Dyson norms along the path between FC to the CI with inner carbon pyramidalization. **B**: Dyson norms along the path between FC to the CI with outer carbon pyramidalization. **C**: Dyson norms along the path between FC to a non-local CI.

roughly parallel to S_1 near the FC point, in contrast to the divergence of D_0 and D_1. The fact that the positions of the two peaks in the photoelectron spectrum vary differently with time delay, while the amplitudes of the peaks vary similarly with delay is consistent with the fact that they both arise from lifting the *same neutral* wave packet on S_1 to *different cationic states*.

The measured and calculated photoelectron spectra shown in panels A and C of Fig. 3.3 agree on a number of features, but also have significant differences. They both contain two peaks in the spectrum near zero time delay (at ∼2.5 eV and ∼0.5 eV for the measurements, and ∼4 eV and ∼1.5 eV for the calculations), with the high energy one shifting with delay, and the low energy peak not shifting with delay. Both peaks decay on a 50-100 fs timescale. However, the measurements and calculations disagree on the relative weightings of the two peaks, and the exact timescale for the decay in the yield. Also, the shift of the high energy peak in the calculations is such that the two peaks merge and appear as one for delays of 50 fs and greater. The shift of the high energy peak in the calculations is obscured to some extent by the convolutions with the experimental response function. The unconvolved calculation results show a clearer shift of the high energy peak,

which is consistent with the results shown in Fig. 3.7. This level of agreement between calculations is consistent with other TRPES studies which compare measurements and calculations [123, 124, 125]. The disagreement on the relative positions of the peaks as a function of time is likely because we have introduced a constant shift for the gap between neutral and ionic states, assuming that the error in this gap is constant across the potential energy surfaces. This however is not correct, as we have shown by detailed comparisons in our previous work [119], with the shifts becoming smaller as a function of time. It is, however, not possible to introduce a variable energy shift in our calculations.

As noted above, while the calculations and measurements agree on the qualitative features in the TRPES, they disagree on the decay times for the peaks. The experimental decay time agrees well with previous studies [116, 69], but it is about a factor of two faster than the theoretical decay time. Similar discrepancies have been observed before in ethylene [126]. In the earlier work, the discrepancy between the calculations and measurements was determined to be a result of windowing, since the probe pulse was not energetic enough to ionize the wave packet from everywhere on the excited state. While our probe photon energy is much larger than the ionization potential to D_0 everywhere on the excited state, ionization to higher lying states may be restricted as the wave packet evolves on S_1. In order to test the sensitivity of the calculations to the energies of the neutral and ionic states, and the extent of windowing effects that limit the experiments but are not captured by the calculations, I calculated the total ionization yield for different limits of integration in the photoelectron spectrum. This is shown in Fig. 3.8, which shows the calculated photoionization yield, integrating the calculated photoelectron spectrum between different energetic limits, together with the measured photoelectron yield. It is clear from the figure that one can produce calculated results that decay on timescales longer than or comparable to the experimental measurements, depending on what range of energies one integrates the photoelectron yield over. This highlights the sensitivity of the agreement to errors in the energies of neutral and ionic states, as well as the ability to determine how much energy goes into the photoelectron vs vibrations during the photoionization process.

Finally, I note that the calculations of the TRPES do not account for any of the probe photon energy going into vibrations. This has been accounted for in previous work [98, 99], and would have the effect of lowering the energies of the peaks in the spectrum, which can impact the possible windowing effects.

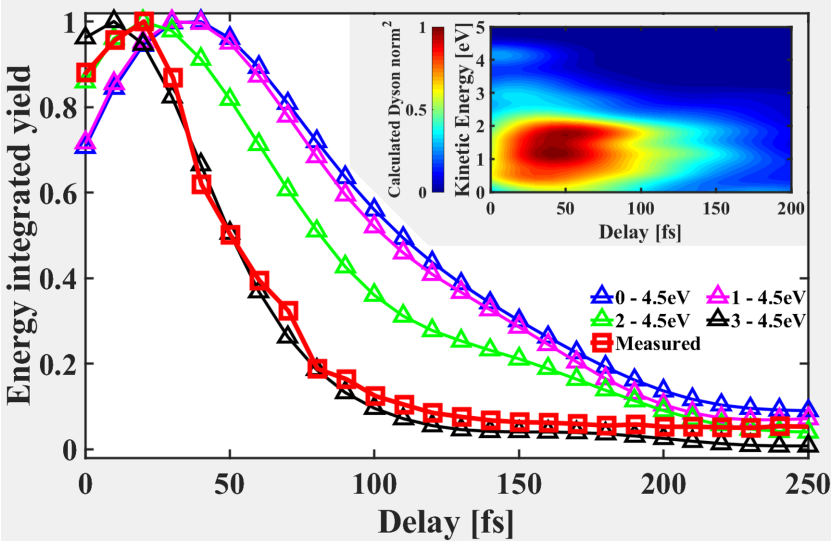

Figure 3.8: **Calculated and measured total ionization yield for different limits of integration.** Calculated total ionization yields for different ranges of photoelectron energies together with the measured yield integrated over all photoelectron energies. A calculated photoelectron spectra is plotted as an inset of the figure.

Before concluding, I note that calculations that our collaborators have carried out for a similar molecule, 1,3-cyclohexadiene, are in much better agreement with measurements reported in the literature [124], and measurements that we have performed. This suggests that the issues which lead to the differences between calculations and measurements for cc-COD are not systematic, but specific to cc-COD.

3.6 Conclusion

In conclusion, we have performed UV pump VUV probe measurements of cc-COD, using TRPES. The measurements are interpreted with the help of electronic structure and trajectory surface hopping dynamics calculations. The calculations allow us to assign the features in the TRPES and understand their behavior in terms of both the neutral and ionic state variations along the reaction coordinate. The calculations predict a slower decay than that measured by the experiment. Future work aims to address this discrepancy.

Chapter 4

Time-resolved photoelectron spectroscopy as a test of electronic structure and nonadiabatic dynamics

4.1 Introduction and motivation

As we have seen from Chap. 3, with the aid of the high-level dynamics calculations, the time-resolved photoelectron spectroscopy (TRPES) measurement can be used to interpreted the photoinduced wave packet dynamics in the excited state(s) of *cis,cis*-1,3-cyclooctadiene (cc-COD). According to the calculated electronic structures, the features in the TRPES can be viewed as ionization from the neutral excited state (S_1) to multiple cationic states. The fast and large amplitude wave packet motion was captured by the dynamics calculation, particularly the directly calculated measurement observable (photoelectron spectra). However, there are some discrepancies between the measured and calculated TRPES signal, such as the time-scales in predicted by the theory is much longer than that of the measurement, and it prevent us drawing some qualitative conclusions. While there have been many studies combining theory and experiment, theory is typically used to interpret experimental measurements [127, 128]. If the theory is not very accurate, then qualitative features are used to interpret the measurements. It is usually nontrivial to tell how accurate a theory is by comparing with the experi-

mental measurement. However, more insights can be gained by comparing calculation from different levels of theory to the measurements.

In this chapter, my goal is to investigate how experiment can be used to benchmark theory with more quantitative comparisons. In order to achieve a meaningful study, dynamics calculations from three levels of theory are chosen and I performed a TRPES measurement in order to directly compare the measured photoelectron spectra with the calculated ones and benchmark the theory. It is important to select a proper molecular system such that the benchmarking is insightful and quantitative conclusion can be drawn. Uracil is selected for this study because, although it has been studied extensively over many years [129, 130, 131, 132, 133, 134, 135, 136, 137, 138, 139, 140, 141, 142, 143, 144, 145, 146, 147, 148, 149, 150, 151, 152, 153, 154, 155, 156, 157, 158, 159, 160, 161, 162, 163, 55, 164], there are still some uncertainties regarding the dynamics [145, 148, 149, 150, 153, 160, 156]. Fig. 4.1 shows a cartoon that displays the main features of the excited state surfaces. The bright state is the second excited state with $\pi\pi^*$ character, while the first excited state is dark, with $n\pi^*$ character. Conical intersections (CIs) between S_2 and S_1 and between S_1 and S_0 have been located, and they facilitate radiationless decay to the ground state [147, 133].

The crucial uncertainty in the dynamics has been how fast the decay from S_2 to S_1 occurs. Most of the dynamics were propagated employing the complete active space self-consistent field (CASSCF) theory [165] (or other low levels of theory), and they predicted a somewhat long decay ($>$ 500 fs) [148, 149, 150, 152, 153]. However, electronic structure calculations have pointed out that CASSCF predicts a higher barrier on the S_2 surface compared with more accurate methods [161, 145, 148, 163]. The barrier is a consequence of the character of the $\pi\pi^*$ excited state subtly changing along the path, with the π density concentrating on the C=C or C=O bond [153, 161]. A higher barrier on S_2 between the Franck-Condon (FC) point and the nearest CI with S_1 leads to a longer S_2 decay time in dynamics calculations.Specifically, electronic structure methods including dynamic correlation have predicted a small or non-existent barrier [161, 163]. In a recent study, two correlated methods: multi-reference configuration interaction with single excitations [166] (MRCIS) and extended multi-state complete active space second-order perturbation [167, 168, 169] (XMS-CASPT2) were employed for the first time by our theory collaborators, in order to simulate photoexcited dynamics of uracil and predicted a much faster S_2 decay compared to CASSCF [163]. As shown in Fig. 4.1, CASSCF predicts a significantly

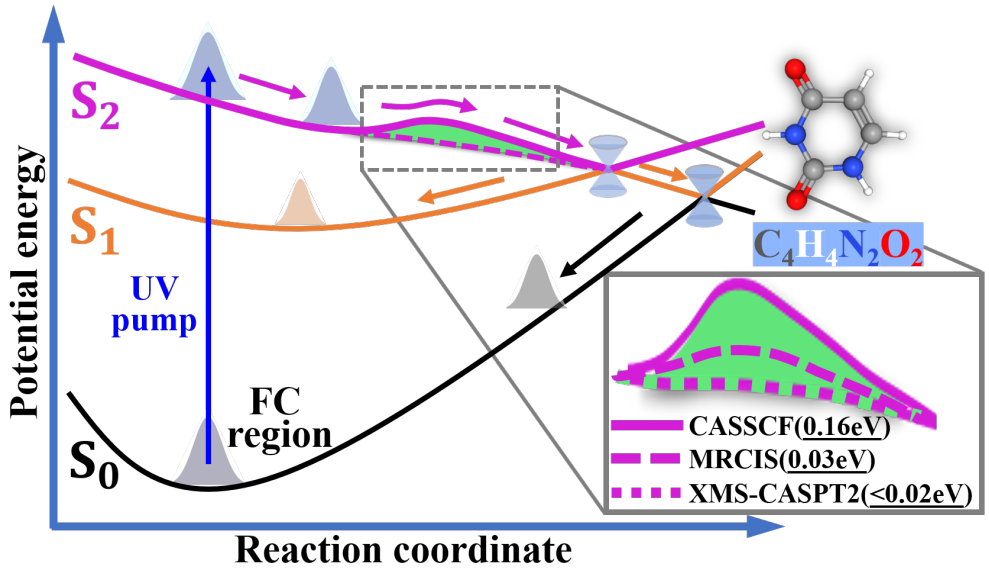

Figure 4.1: **A cartoon diagram of uracil relaxation after deep UV excitation.** Uracil is excited to the optically bright state S_2 ($\pi\pi^*$), generating a wave packet. Radiationless decay to S_1 or back down to the ground state, S_0, is facilitated by conical intersections (CIs). S_1 is an optically dark state and the population is trapped there for several picoseconds. Calculations at different levels of electronic structure theory predict different heights for a barrier on S_2 between the FC region and the S_2/S_1 CI (highlighted by the dashed box which is enlarged in the inset).

higher barrier between the FC point and the S_2/S_1 CI than XMS-CASPT2 and MRCIS. Apparently, the size of the barrier will possibly affect the wave packet dynamics, such that the population in S_2 can be trapped with a larger barrier and the internal conversion dynamics are slowed down.

The ultimate test of a theory, however, is in predicting the experimental observables accurately. Thus choosing the proper experimental method and measurement observables is essential. The more differential the measurement (i.e. spectrally and temporally resolved), the more rigorous the test. While earlier comparisons between experiment and theory of the total ionization yield versus time (without resolving the photoelectron energy) showed qualitative agreement [158], TRPES measurements are more differential, and with

sufficient time and energy resolution, can be used to discriminate between different levels of theory. Here I performed a TRPES measurement on gaseous uracil with high temporal resolution (with an instrument response function (IRF) of < 90 fs) and make use of an energetic probe (7.9 eV) in order to avoid energy windowing (insufficient probe photon energy to ionize from everywhere on the excited state potential energy surface). The measured TRPES signals are directly compared with the simulated TRPES signals using trajectories from three levels of theory. Three levels of theory (CASSCF, MRCIS and XMS-CASPT2) are considered in order to understand the role of dynamical correlation in determining the excited state dynamics, with a focus on the coupling between different electronic states and internal conversion back to the ground state. These dynamics calculations are used to simulate the time resolved photoelectron spectra. In the rest of the chapter, I will describe the experiment measurement, data analysis, and compassion between the measured TRPES and the simulated ones from all the three levels of theory.

4.2 Experimental measurements and data analysis

The TRPES experiment I performed uses the UV/VUV velocity map imaging apparatus that is described in Chap. 2. Uracil (>99.0%) sample is purchased from Sigma-Aldrich without further purification. Due to its low vapor pressure at room temperature, the solid sample manifold with heating ability is employed to deliver uracil. In the measurement, uracil is exited from ground state to the first optical bright state, S_2, by the pump UV with photon energy of 4.75 eV, followed by 7.95 eV VUV probe, ionizing the molecule to the cationic states. The VMI images from the generated photoelectrons were recorded as a function of pump-probe delays. In order to make the data acquisition efficient, I implemented different pump-probe step sizes for different pump-probe delay regions in order to catch both the short and longer delay range dynamics. A 20 fs step size was used from -600 fs to 1.2 ps in order to catch the rapid dynamics near zero delay, and a 100 fs delay step size was applied up to 10 ps which is sufficient for capturing the long time scale dynamics.

The recorded photoelectron VMI images are inverse Abel transformed

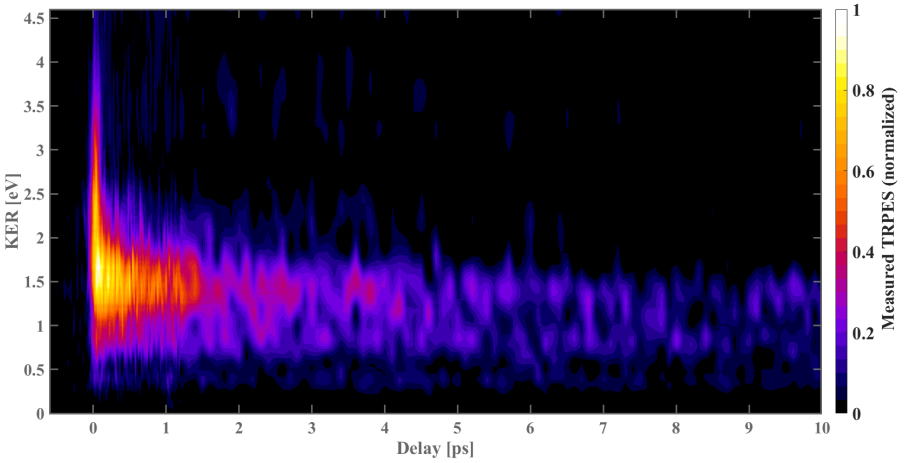

Figure 4.2: **Measured TRPES of uracil.** Uracil TRPES spectrum from the entire window is plotted as a function of pump-probe delays and kinetic energy. The spectra is plotted with a linear intensity scale.

and the kinetic energy distribution is obtained. The measured TPRES signal from the entire pump-probe window can be found in Fig. 4.2. Similar with the TRPES measurement of cc-COD described in Chap. 3, the precise pump-probe time-zero is located from an ethylene TRPES measurement under the same conditions with uracil. However, different from the data analysis of cc-COD TRPES in Chap. 3, the 2D global fitting analysis for signal decomposition between the UV/VUV driven dynamics is not necessary, since uracil has no absorption band in VUV photon energy [170]. Therefore, the signal in Fig. 4.2 only shows in the positive pump-probe delays in which UV pulse performs as pump and VUV is being as the probe. As shown in the figure, the measurement was carried out from -600 fs to about 10 ps, and one can see a higher KE peak shortly after time-zero and this signal decays very fast, less than 100 fs, followed by a low energy photoelectron band that lasts much longer time (several picosecond). This is consistent with earlier results made with longer pulses and a lower probe photon energy [138, 159]. More details related to the measurement can be view in Appendix B.1. In this work, I focus on the short time dynamics for which the calculation results are available.

Let us switch gears to the simulations. The calculated TRPES are provided from our theory collaborators, Praip Chakraborty and Spiridoula Mat-

sika. Trajectory surface hopping calculation at all three levels of theory were performed. For each individual trajectory, time-dependent Dyson norms were calculated at each time step, and all the trajectories used were propagated for the initial conditions corresponding to the experimental pump pulse wavelength range. The calculation method, including the electronic structures, trajectory surface hopping calculations, and kinetic energy shift of different cationic state, can be found in Appendix B and Ref. [163]. The calculated raw TRPES data is obtained by adding up the discrete Dyson norms contribution from all the individual trajectories. In order to account for finite energy resolution of the experimental measurement, the calculated raw TRPES data was convolved with a Gaussian function having a 0.5 eV FWHM according to the Xe photoelectron measurement that discribed in Chap. 2. Along the pump-probe delay axis, the calculated TRPES spectra were also convolved with a 90 fs FWHM Gaussian function, which is treated as IRF.

Given the computation cost associated with each method, there are 70, 70, 50 trajectories that were propagated for 1000, 500, 300 fs at the CASSCF, MRCIS, XMS-CASPT2 levels of theory, respectively, and some trajectories crash before the end of the simulation time. [1] One needs to pay extra attention in the data analysis when dealing with the crashed trajectories. Fig. 4.3 shows a detail analysis on how many trajectories crashed in each state for the different levels of theory, as well as the correction factor for averaging the calculated spectra from all of the trajectories. There are 3 different scenarios that I consider separately: crashing in the excited states (S_1 and S_2), crashing in the ground state (S_0), and trajectories that survive until the end of the simulation time window. In the figure, panels (a), (b), and (c) show the crashing information of the trajectories in the three methods, respectively. A trajectory that propagates to the end or crashes in the ground state does not affect the TRPES signal (since ionization from the ground state is not possible with our probe photon energy), and only those that crash in the excited states affect the TPRES signal. There will be more signal if no trajectories crashed in the excited states, so I need to take this into consideration and an inappropriate treatment of the crashing will induce misinterpretation of the data. For instance, without considering the crashes, the signal will decay faster, however, if considering crashes from all the neutral states, the signal may be over amplified at longer delays. Here I implement a delay-dependent

[1] 50 trajectories are launched at the XMS-CASPT2 level of theoy and 17 trajectories that start from S_2 are considered in the calculated TRPES.

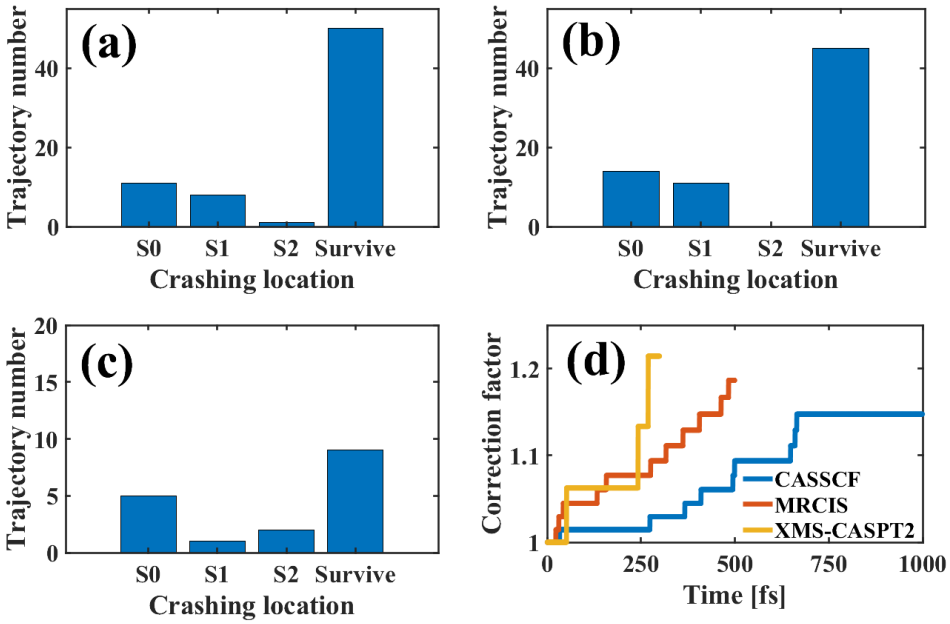

Figure 4.3: **Trajectory crashing induced normalization factor.** Panels (a), (b), and (c) show the number of trajectories that crash on S_2, S_1, and S_0, as well as those that survive until the end of the calculation time window (1000 fs for CASSCF, 500 fs for MRCIS, and 300 fs for XMS-CAPST2). Panel (d) shows the time-dependent correction factor that we apply in order to compensate for the trajectories that crash in the excited states (S_1 and S_2)

correction factor by only considering the crashes in the excited states,

$$M_{S_1+S_1}(t) = \frac{N_{S_1+S_2}(t) + C_{S_1+S_2}(t)}{N_{S_1+S_2}(t)} \tag{4.1}$$

where $N_{S_1+S_2}(t)$ is the number of trajectories surviving on S_1 and S_2 state at time t, and $C_{S_1+S_2}(t)$ the number of trajectories that have crashed. As shown in panel (d), the factor is monotonically increasing from 1 as more and more trajectories crash as a function of time. We multiply the calculated photoelectron spectra by this number, compensating for the loss of signal due to trajectories crashing in the excited states.

In order to show the influence of the correction factor, here I showcase an example of the calculated TRPES signal at XMS-CASPT2 level of theory with two different ways of dealing with the crashed trajectories. Fig. 4.4 panel (a) shows the TRPES signal by multiplying the right correction factor from Equ. 4.1, i.e., only considering the crash in the excited states, S_1 and S_2. Whereas, panel (b) showcases the TRPES in which trajectories crash at both ground and excited states are taken into consideration. Panel (c) plots the time-dependent correction factors, in which the red and the blue line-plots reflect the appropriate and inappropriate correction factors. Comparing panel (b) with panel (a), one is able to see the signal at longer time in panel (b) is strongly amplified, and according to the false-color intensity map, the signal level is even higher than that around time-zero, indicating that the results are not physical. This is consistent with the much larger value ($\sim$1.85 vs $\sim$1.15) of the correction factor if considering crash in all the states. Fig. 4.4 panel (d) reflects the energy integrated photoelectron yield between 2.0 and 4.5 eV from panels (a) and (b), and the measured TRPES, respectively. From panel (d), there is significant difference in the photoelectron yield in longer times is as twice as that from the red curve.

Figure 4.4 indicates an important point in the treatment of the calculated TRPES signal from the individual trajectories. As shown in panel (d), it is obvious that the interpretation of the time-dependence of the calculated TRPES can be dramatically changed by multiplying the inappropriate (S_0, S_1, and S_2) correction factor, and the comparison between the measurement and calculation will be meaningless. On the other hand, the calculated TRPES with the right correction factor (only including S_1 and S_2) decays much slower, which matches the experimental measurement well. The similar behaviours were also observed in the calculated TRPES from the CASSCF and MRCIS levels of theory, and I have applied the right correction factor to the

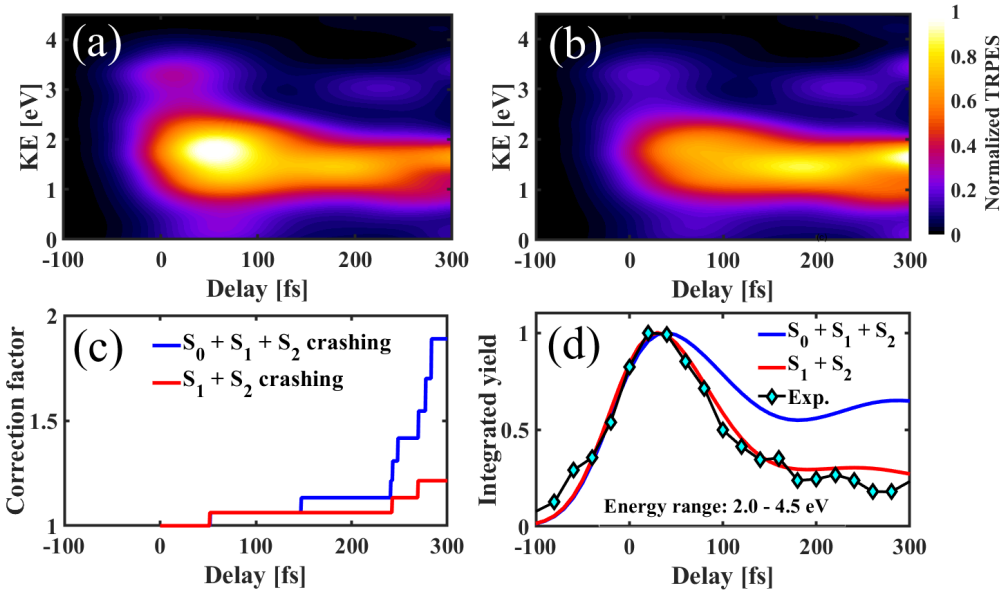

Figure 4.4: **Calculated uracil TRPES at XMS-CASPT2 level of theory with different crashing normalization factors.** Panels (a) show the TRPES signal at XMS-CAPST2 level of theory by only considering the crash of the trajectories in excited state , i.e., by multiplying Equ. 4.1. Whereas, in panel (b), the correction factor includes the crash from all the states, i.e., $M_{S_0+S_1+S_2}(t) = \frac{N_{S_0+S_1+S_2}(t)+C_{S_0+S_1+S_2}(t)}{N_{S_0+S_1+S_2}(t)}$. Panel (c) red and blue lines show the correction factors $M_{S_1+S_2}$(t) from Equ. 4.1 and $M_{S_0+S_1+S_2}$(t) above, respectively. Panel (d) reflects the energy (2.0 to 4.5 eV) integrated yield of TRPES from panels (a) and (b), as well as the experimental measurement from the same energy range, respectively.

other two levels of theory. I will discuss the comparison of the measured and calculated TRPES in next section.

4.3 Comparison between measured TRPES and simulated TRPES from three levels of theory

With careful analysis of both measurement and calculated TRPES of uracil, now I am able to interpret the results and make a meaningful test by directly comparing the measured TRPES with the simulated ones from all the three levels of theory. Fig. 4.5 panels (a), (b), and (c) plot the calculated TRPES at CASSCF, MRCIS, and XMS-CASPT2, respectively. Whereas, panel (d) reflected the results from measurement. At first glance the results look qualitatively similar, particularly in terms of the slowly decaying feature below 2 eV energy, which is present in all of the theoretical spectra, as well as the measured one. There are, however, some differences at early times and higher energies. The experimental signal shows a higher energy feature that decays very rapidly. This is also clearly evident in MRCIS, somewhat evident in XMS-CASPT2, but absent in CASSCF.

In order to compare the signals more quantitatively, and see if we can find which method agrees better with experiment, we compare the signals integrated over two energy regions: between 0.5-2 eV and between 2-4.5 eV. The integrated results are shown in Fig. 4.6. Panels (a), (b), and (c) display the measured and calculated integrated spectra for the higher kinetic energy range at CASSCF, MRCIS, and XMS-CASPT2 levels of theory, respectively. Panels (d), (e), and (f) reflects the comparison between measurement and calculation for the lower kinetic energy region. From an overall glimpse of the figure, the signals make it obvious that XMS-CASPT2 and MRCIS agree very well with experiment, whereas CASSCF predicts a much slower decay for the higher energy signal. In each panel of Fig. 4.6, a vertical black line indicates the peak locations for the higher and lower energy ranges of the measured TRPES. Here I focus more on the high energy signal, since this is more closely connected to the S_2 dynamics.

From panels (b) and (c), both the MRCIS and XMS-CASPT2 calculations capture the measured delay (relative to measurements in ethylene, for which the decay dynamics are much faster than the experimental IRF) in

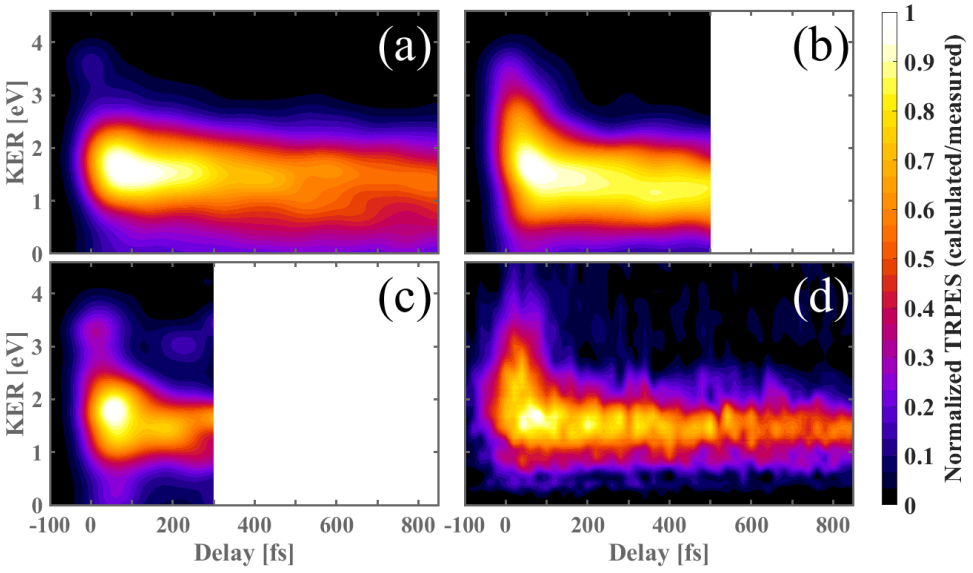

Figure 4.5: **Calculated and measured TRPES of uracil.** In this figure, the calculated and measured TRPES signals are plotted as a function of time and kinetic energy (KE). Panels (a), (b), and (c) show the calculated TPRES according to CASSCF, MRCIS, and XMS-CASPT2 levels of theory, respectively, while panel (d) shows the measured TRPES. All the TRPES signals are normalized individually.

the peak positions, whereas the CASSCF calculations shown in panel (a) do not. There is a 20 fs delay from the calculated TRPES with respect to the measured signal. I realized that the lower energy feature extends for times beyond which the XMS-CASPT2 and MRCIS calculations last, so intrinsically the calculations may not be expected to predict this signal well. Comparing among panels (d), (e), and (f) of the lower kinetic energy integration region, calculation from XMS-CASPT2 reflects the best with respect to the measurement, indicated by the overlapped peak positions. In panel (e), the MRCIS result indicates a small delay, 10 fs, with respect to the measurement. However, as shown in panel (d), this delay is largely overestimated in CASSCF, reflected by a 40 fs with respect to the measurements. While the delay between the maxima for the high and low energy electron yields is related to the S_2 decay time, it cannot be considered an actual "lifetime", because the photoelectron bands arising from S_2 and S_1 ionization are not perfectly separable and overlap, as illustrated in Fig. 4.7 below. From Fig. 4.6, CASSCF calculation cannot predict a meaningful results from either the higher and lower energy range, compared with MRCIS and XMS-CASPT2. While MRCIS and XMS-CASPT2 both agree well with the measurements, XMS-CASPT2 provides the closest agreement with experiment on the delay of the peak in the low energy electron yield. Since Fig. 4.6 reflects some important quantitative comparison between the measurement and all three levels of theory, it is important to emphasize the statistic uncertain of the experimental measurement. A standard bootstrapping analysis is employed on the measured TRPES and one standard deviation is treated as the error, as shown by the shaded region around the experimental signal in each panel of Fig. 4.6. The error bar is much smaller than the signal level, indicating good signal to noise ratio from the measurements.

Figure 4.7 shows the individual Dyson norm (squares) from different excited states that contribute to the total calculated TRPES and it provides a connection between the TRPES signal and the underlying population dynamics. Three columns represent the three levels of theory. Whereas, the spectra from S_1 and S_2 are calculated separately in the first two rows and combined in the panels in the last row. The differences between the three methods in the dynamics become apparent here. In CASSCF, the S_2 decay is slow, and for times beyond the first 50-100 fs, the signals from S_2 and S_1 are overlapped. For MRCIS and XMS-CASPT2, however, the signals from the two states are separated more temporally and spectrally. This analysis makes it clear that fitting the experimental signal and comparing the time

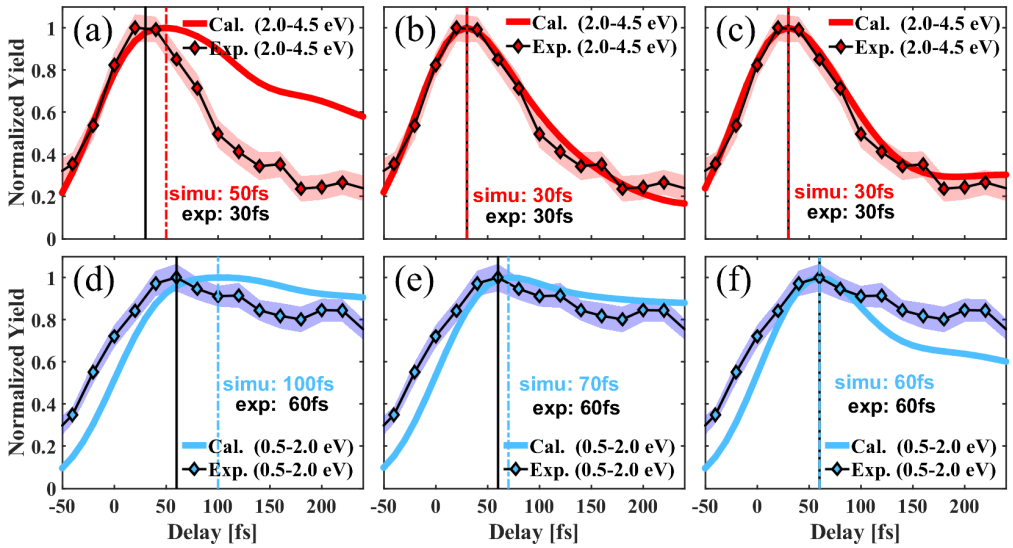

Figure 4.6: **Uracil time-dependent photoelectron yield integrated over two different energy ranges.** Panels (a), (b), and (c) show measured and simulated yields for electrons between 2.0 and 4.5 eV. Panels (d), (e), and (f) show measured and simulated yields for the lower energy range covered between 0.5 to 2.0 eV. The three columns show the calculated yields from trajectories propagated at the CASSCF (left), MRCIS (middle), and XMS-CASPT2 (right) levels. This figure focuses on the early times. The data with longer delay can be found in Fig. B.2.

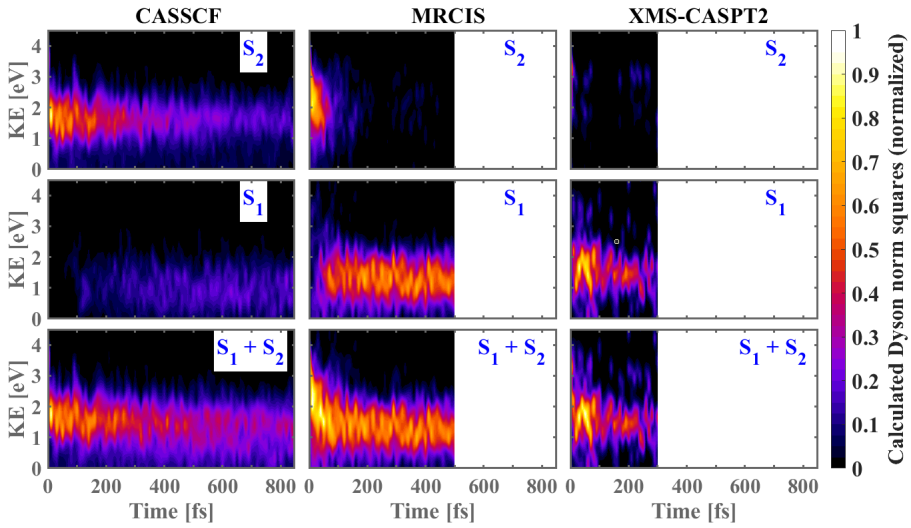

Figure 4.7: **Individual TRPES contribution from excited states of uracil.** In this figure, the Dyson norm square values of individual excited states are plotted. The three rows correspond to the contributions of S_2 (top), S_1 (middle) and S_2+S_1 (bottom), whereas the columns correspond to different levels of theory, with CASSCF on the left, MRCIS in the middle, and XMS-CASPT2 on the right. These results are not convolved with the IRF of the experiment.

constants to time constants obtained from fitting the calculated population decays is inadequate. This is because different excited states do not have unique and separate signals in the TRPES, and thus one needs to calculate the observable and compare with measurements in order to evaluate different levels of theory.

4.4 Conclusion

In this chapter, I demonstrated that quantitative comparison between theoretical calculations of excited state dynamics and pump-probe experiments can provide a tool for benchmarking electronic structure theory, particularly in cases where dynamical correlation plays a crucial role in the nonadiabatic dynamics. The experiment and the comparison between the experiment and calculation is well designed. The molecular system, uracil, provides a great

testbed such that the much debated population trapping on the first bright state S_2 is sensitive to the different levels of theory and dynamics correlation plays an important role in determining the ensuing dynamics. On the experimental side, TRPES with measured photoelectron kinetic energy, allows to spectrally choose the relevant energy range corresponding to the dynamics of interests, which is not measurement visible if only measuring the total ionization yield. Comparing the calculated and measured TRPES signals allows me to conclude that MRCIS and XMS-CASPT2 provide a better description of the excited state dynamics than CASSCF, which greatly overestimates the decay time from S_2. Distinguishing between MRCIS and XMS-CASPT2 is harder because of the very short times involved, but there is some evidence that XMS-CASPT2 compares somewhat better to the experiment.

Chapter 5

Combined spectroscopic and structural probes of CH_2I_2 dissociation dynamics

5.1 Introduction and motivation

In Chap. 3 and Chap. 4, TRPES experiments were performed in order to follow the excited state dynamics. Two organic chromophore molecules: cc-COD and uracil were investigated, focusing on the internal conversion and isomerization dynamics. The results and interpretations showcase that TRPES is not only able to probe the wave packet dynamics, but also effective to perform as a test for electronic structure and nonadiabatic dynamics calculations.

Both molecular systems show interesting dynamics, but the quantum dynamics of interest are filtered by the coordinate-dependent matrix elements of the chosen experimental observable. Thus, the TRPES measurement in the last two chapters may only provide a single view of the transient electronic energies, and several questions can be naturally raised, such as, how is the structural change as a function of time? How is the electronic energy converted into the nuclear degrees of freedom as the wave packet evolving on the excited state potentials? One can claim that some structural information may be inferred from a TRPES measurement, and TRPES can provide indirect information into the electronic and nuclear configurations, but it relies on high-level dynamics calculation and none of this information con-

tent can be directly obtained from a TRPES experiment. Alternatively, one can gain much more insight by utilizing different time-resolved techniques and looking at different measurement observables, making a combination of multiple probes. The combined methodology is advantageous since one is able to simulate multiple measurement observables in order to make a direct comparison with the measurements.

In this chapter, I demonstrate a comprehensive study on excited state dynamics with combined spectroscopic and structural probing. I discuss the experimental results and the interpretation with the aid of computer simulated measurement observerables, and end it with a discussion of the advantages of combining different probes. The molecular systems, CH_2I_2 and CH_2IBr that I chose are halogenated methanes, and the photoinduced excited state dynamics of these molecules are important for atmospheric photochemistry and understanding the concerted electron and nuclear dynamics of small polyatomic systems [171, 172, 173]. They serve as a homologous family of molecules, where one can study systematic differences in the dynamics of structurally similar molecules and understanding their excited state dynamics [174]. Fig. 5.1 shows the absorption cross section of the two molecules at the deep UV region as well the the UV spectra o the laser. A UV ($\sim$266 nm, $\sim$4.65 eV) ultrashort laser pulse launches an excited state wavepacket and the molecules undergo dissociation dynamics where the bond between the carbon and iodine atoms breaks.

Though the dynamics have been intensively studied in both theoretical and experimental perspectives [175, 176, 177, 178, 179, 180, 181, 182, 183, 184, 185, 186, 187, 188], the combined spectroscopic and structural study together with high level theory calculation have not been well developed. Fig. 5.2 shows the two molecules as well as the cartoon diagrams of the potential energy surfaces (PESs), which are plotted as a function of C-I distance along the dissociative coordinates, and each different color represents a group of states with very similar energies.

Between the two molecules, CH_2I_2 is the main object, whereas the CH_2IBr serves as a complementary contrast and they are chosen on purpose in this study with two major reasons. First reason comes from the scientific aspect. The combination of the CH_2I_2 and CH_2IBr molecules forms a good case on studying the coupled electronic and nuclear dynamics with multiple probes. These molecules, which are structural relatively simple, allow for a clear picture rather than structural complicated larger molecules. In CH_2I_2 and CH_2IBr, the dynamics I am interested in is the UV induced internal

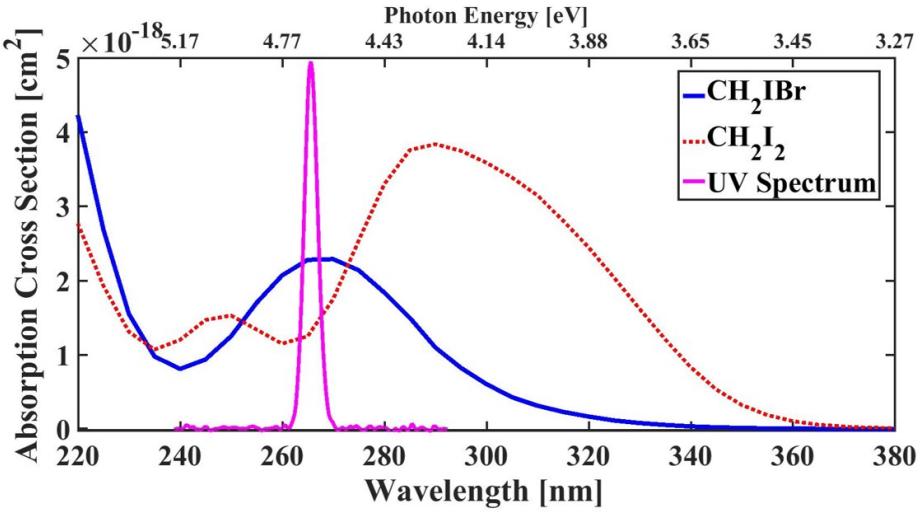

Figure 5.1: **Absorption spectra for CH_2I_2 and CH_2BrI in the UV region** The UV pump pulse spectrum from the experiment is also shown for comparison.

conversion and dissociation. Different techniques probe the same underlying dynamics from different measurement observables, such that I can compare the different measurement observables in a relative straightforward manner. As show in Fig. 5.2 both CH_2I_2 and CH_2IBr undergo dissociation with the bond breaking between the carbon and the iodine atoms, leading to the decrease of the electronic energy as well as the structural transformations. The transient electronic energy can be probed by time-resolved photoelectron spectroscopy (TRPES) and the structural transformation can be examined by ultrafast electron diffraction (UED) method. As the electronic potential energy is lost, there is a corresponding gain in nuclear kinetic energy. Neither TREPS or UED could directly measure the transient nuclear kinetic energy, but this can be directly viewed by the time-and momentum-resolved photoion spectroscopy (TRPIS).

In Fig. 5.2, the difference of the iodine and bromine substitution (two iodine atoms vs one iodine and one bromine atom) lead to the electronic structure differences. The excited states of CH_2I_2 which are able to be reached by the UV photon energy at the Franck-Condon (FC) region, consist of both bound (cyan) and dissociative state (red and blue). However, the CH_2IBr is only dominated by the direct dissociative states, which results in an in-

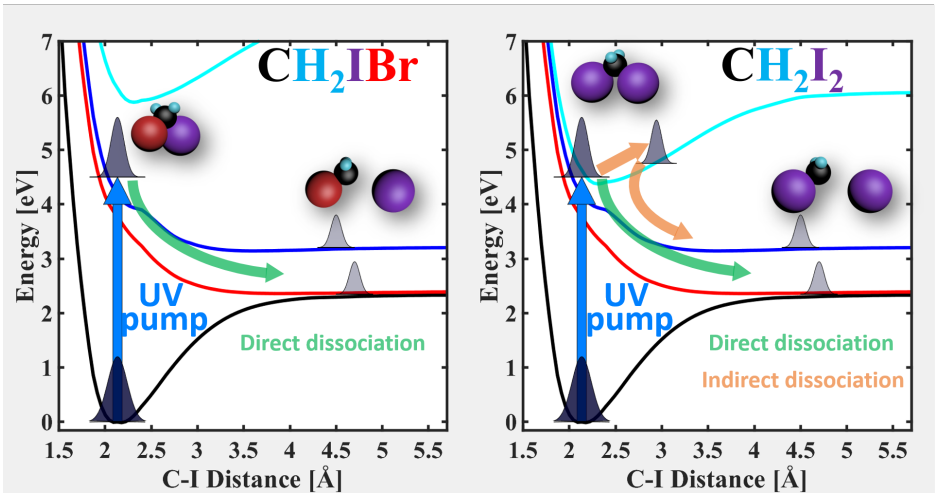

Figure 5.2: **Cartoon diagrams of UV induced dynamics of CH_2IBr and CH_2I_2.** The two panels show cartoon diagrams of potential energy surfaces of the ground and excited states as a function of C-I distance. Left is for CH_2IBr, whereas, in the right is for CH_2I_2. Several arrows, and the cartoons of wave packet and molecules illustrate the excited state dynamics.

trinsic difference of the following dynamics after the initial excitation. As the arrows shown in Fig 5.2, CH_2IBr undergoes direct dissociation, however, in the case of CH_2I_2, both the direct and indirect dissociation are involved. It is particularly interesting to examine how this difference influences the transient signal of the electronic energies, nuclear kinetic energies from the energetic probing, as well as the the pair distribution function from the structural probing. The two molecules will potentially offer an excellent testbed of examining the sensitivity of the combined methodology, as well as bench marking the methodology for the application on more complicated systems.

The other aspect comes from the experimental feasibility. The choice of CH_2I_2 and CH_2IBr allows for high signal to noise ratio in the experimental measurements. As shown in Fig. 5.2, the change of the electronic energy along the excited state is in the order of several electron volt (eV), leading to relative large amplitude motion of the wave packet, which is favorable to the electronic energy detection. On the other hand, the larger scattering cross-section of the iodine atom results in high signal level in the UED measurement, and the dissociation dynamics intrinsically leads to large structural

change which makes profound transient signal in the measured pair distribution function (PDF). Furthermore, the existence of the relatively heavier halogen atoms slows the dynamics down to the order of > 100 femtosecond (fs), in which the current experimental apparatuses offer sufficient high temporal resolutions. The spectroscopy probes allow for < 80 fs instrument response function, and the structural probe is in the order of < 150 fs.

5.2 TRPES experiment of CH_2I_2 and CH_2IBr

A TRPES experiment was carried out using the UV/VUV pump/probe scheme in conjunction with a velocity map imaging (VMI) spectrometer, measuring the kinetic energy of the photoelectrons. The experiment was firstly carried out at National Research Council (NRC) of Canada, and then was reproduced in Stony Brook, in order test the pump UV wavelength and intensity dependence. The TRPES setup in NRC shares much similarities with that from our lab in Stony Brook University. The apparatus starts with a commercial laser system, an amplified Coherent Legend Elite Duo, which delivers 35 fs pulses at 798 nm with a pulse energy of 8.0 mJ at a repetition rate of 1 kHz, and 3.25mJ is used for this experiment. The UV (3ω, $\sim$267 nm, $\sim$4.65 eV) is generated through a frequency tripling state, followed with a CaF_2 prism pair that is used for pulse compression and it gives a pulse duration with a full-width-half-maximum (FWHM) of 39 fs. The VUV (5ω, $\sim$160 nm, $\sim$7.75 eV) pulse generation mechanism is using the non-collinear Difference Frequency Four-Wave Mixing (DFFWM) scheme which is same as the setup in Stony Brook. All the details of the optical outline, and spectrum and pulse duration characterization can be found from Ref. [189].

The samples, CH_2I_2/CH_2IBr (purchased from Sigma-Aldrich (99%) without further purification), mixed with helium (typical 2% of the sample), were delivered through an Even-Lavie valve [190] into the interaction chamber, and the valve was heated to 55°C throughout the experiments, which helped to reduce the possible presence of clusters. The UV and VUV beams were weakly focused into a VMI spectrometer, using f/100 spherical reflective optics, yielding a UV pump laser intensity about 5×10^{11}W/cm^2. The VUV probe laser intensity was more than an order of magnitude weaker. The photoelectron VMI images were recorded as a function a pump and probe delays, followed by an inverse Abel transform to obtain the photoelectron kinetic energy map. Data acquisition for CH_2I_2 was conducted first, and

the whole sample manifold and the delivery line were cleaned before data acquisition of CH_2IBr, in order to prevent contamination. One thing I note here is that the CH_2I_2 measurement was reproduced in Stony Brook with multiple different pump-UV wavelength ($\sim$261 nm instead of $\sim$267 nm) and intensities ranging between 0.3 and 1.5×10^{12}W/cm^2, and the experiments reproduced all the features shown from the NRC results. The comparison of the measurements between NRC and Stony Brook can be found in Appendix C.1.2.

In this chapter, One thing different from the TRPES measurement in Chap. 3 and Chap. 4 is the determination of the real time-zero. For cc-COD and uracil TRPES experiments, the real time-zero between the pump and probe was located by running a pump-probe measurement of ethylene. Whereas, here I determine the time-zero by looking at the non-resonant UV+VUV $1 + 1'$ photonionization of Xe. By applying a single Gaussian fit of the energy integrated photoelectron yield, I was able to determine the time-zero (center of the retrieved Gaussian function), and extract an impulse response function (IRF) with 73 fs FWHM which is the cross correlation between the UV and VUV pulses. The experimental conditions of Xe were kept the same as those of CH_2I_2 and CH_2IBr. More details of the Xe TRPES signal can be found in Sec. 2.2.4.

5.3 Measured and calculated TRPES of CH_2I_2 and CH_2IBr

Figure 5.3 shows the measured and calculated photoelectron spectra as a function of pump probe delay for CH_2I_2 and CH_2BrI. Panels a) and b), show the measurements and calculations respectively for CH_2I_2, while panels c) and d) show measurements and calculations for CH_2IBr. The calculated results have been convolved with the IRF of the system to facilitate comparison with the experiment. From earlier results [191], we estimate that the VUV absorption cross section is about four times that of the UV absorption cross section. This means that near time-zero, where the pump and probe pulses overlap, the signal comes from a combination of both UV pumped and VUV pumped excited state dynamics. In order to highlight the UV driven dynamics that have contributions from VUV driven dynamics near time-zero, we multiply the signal level at positive pump-probe delays (i.e. outside the

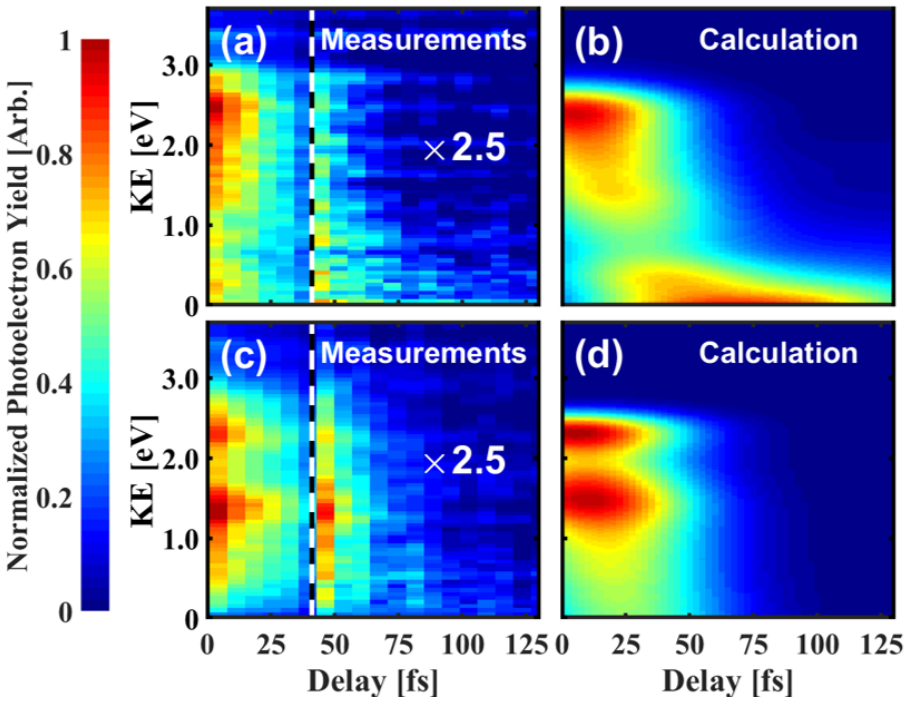

Figure 5.3: **Time resolved photoelectron spectra of CH_2I_2 and CH_2IBr.** Panels (a) and (b) showcase the measured and calculated TRPES of CH_2I_2, respectively. Whereas, the measured and calculated TRPES of CH_2IBr are plotted in panels (c) and (d), respectively. The x-axis represents the pump-probe delay (UV pump, VUV probe for positive delays). The y-axis is the electron Kinetic Energy (KE). The calculated spectra have been convolved with the IRF of the measurements and all spectra are normalized with their own peak values.

temporal overlap of the pump and probe pulses) by a factor of 2.5.

There is good agreement between the experimental and calculated TRPES. For CH_2I_2, they both have a main peak near zero delay at about 2.5 eV, corresponding to ionization from the FC region to low-lying states of the cation. As there is rapid motion of the wave packet on the excited state, and the low-lying states of the cation are close in energy, one cannot resolve the ionization to different cationic states, which one can see in the examining the calculations.[1] In both the calculated and measured spectra, the higher energy peak disappears in about 60 fs and there is a lower energy tail that persists out past 100 fs. For CH_2BrI, the calculations and measurements show two peaks at time-zero separated by $\sim$ 0.9 eV. These two peaks originate from photoionization correlating to two different final cationic states after initial photoexcitation with the UV pulse. The calculations and the experiments both show a rapid decay of the two peaks in under 60 fs without a low energy ($<$0.5 eV) tail, consistent with previous measurements of direct dissociation using core to valence extreme ultraviolet transient absorption spectroscopy that found a C-I dissociation time of about 45 fs. [192].

Since CH_2I_2 also absorbs light around our VUV spectrum [191], before interpreting the measurements with the aid of the calculations, I assessed the extent to which excited state dynamics driven by the VUV pulse contribute to the photoelectron spectrum at short positive delays. This is similar with what I have done in the signal decomposition of the cc-COD measurement. As I have discussed in Sec. 3.2, the measured TRPES yield include both UV and VUV driven signals and the overall molecular decay can be modeled by following Equ. 3.3 to Equ. C.2 with a sum of two exponential decays, i.e., one for positive and one for negative delays with decay times based on fits to the data. According to Ref. [191], the ratio of the absorption cross section from VUV is four times as that from the UV, thus I can slightly modify the fitting function such that the amplitude of the exponential function of VUV is four time as that of VU (We don't know the ionization cross sections for UV vs VUV excitation and thus we took them to be equal as the simplest approximation). Since I will focus the feature on the lower kinetic energy tail, instead of running 2D bilateral global fitting, I integrated the photoelectron spectrum at energy range from 0 - 0.5 eV, and applied a 1D bilateral

[1] As discussed in Appendix C.1.3, the VUV pumped contributions to the TRPES near zero time delay are similar to the UV pumped contributions, which is why the calculations, which include only the UV pumped contributions, agree with the experimental results, which contain both.

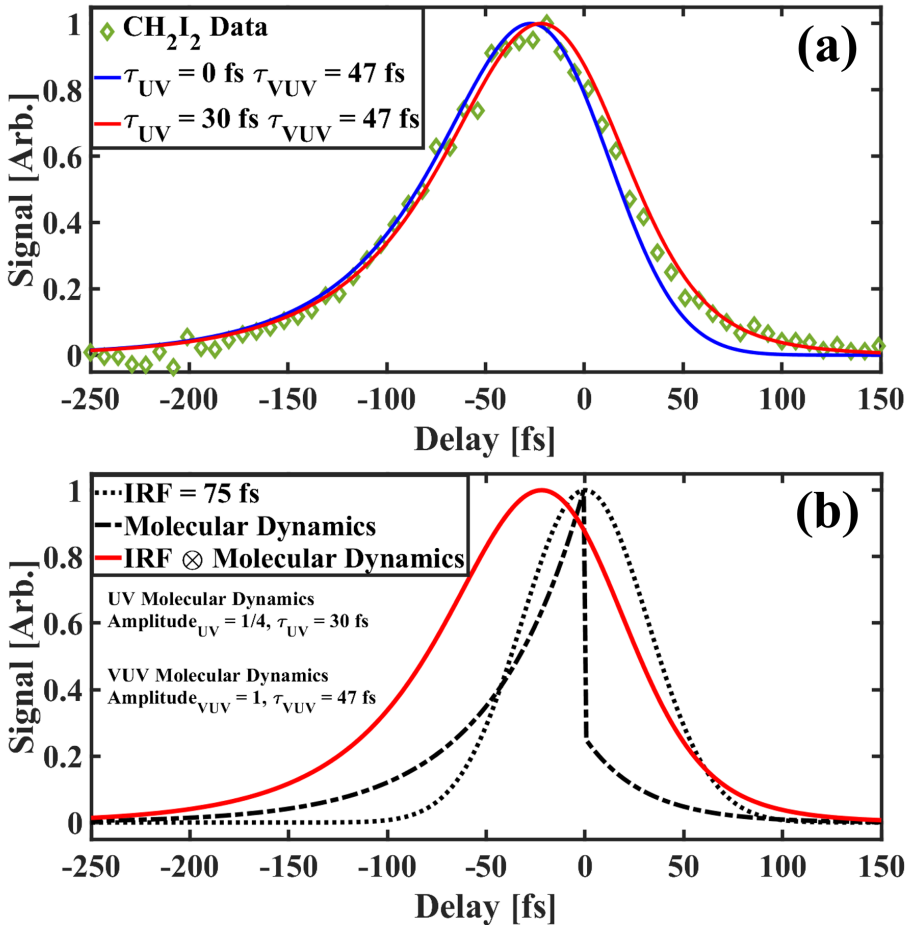

Figure 5.4: **Decomposition of the UV versus VUV driven signal of CH_2I_2** (a) The convolution of the IRF and an exponential decay model of the photoelectron yield for both UV and VUV driven dynamics (red line) and with only VUV driven dynamics (blue line) plotted alongside the experimental CH_2I_2 TRPES data integrated from 0 - 0.5 eV (open circles). (b) Decomposition of the exponential decay model shown as the solid red line in the top panel. The model consists of two exponential decays (one for positive and one for negative delays) and is represented here by the dashed black curve. The UV driven dynamics signal has an amplitude of 1/4 and a decay constant of 30 fs, and the VUV driven dynamics signal has an amplitude of 1 and a decay constant of 47 fs. The combination of these are convolved with the measured IRF (dotted black curve) to model the experiment. The model convolved with the IRF is represented by the solid red curve as it is in the top panel.

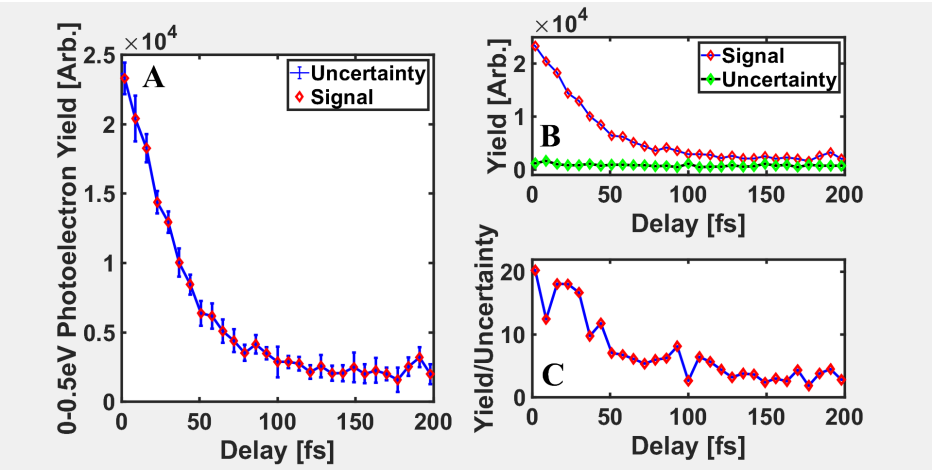

Figure 5.5: **Bootstrapping error analysis for low energy photoelectron yield in the CH_2I_2 measurement.** This figure reflects the statistic of the TRPES signal on CH_2I_2. Panel (a) plots the photoelectron yield as a function of pump-probe delay for electrons below 0.5 eV along with error bars determined by the bootstrapping analysis. Panel (b) indicates the yield and error as separate curves as a function of delay, and panel (c) showcases the ratio of the yield and uncertainty, demonstrating a signal to noise of greater than 5 over the relevant range of delays.

fitting. This energy region is also the one with the largest contribution to the dynamics at longer positive time delays.

In order to assess the importance of UV driven dynamics in the data, the model described here is compared with one that does not include UV driven dynamics - one with an exponential decay only for negative times, convolved with the IRF for the apparatus using the same decay time as before. The integrated photoelectron yield from 0 - 0.5 eV as well as the fitting results with two models afromentioned are shown in Fig. 5.4 panel (a). It is clear that the data is only consistent with the model which includes both VUV and UV driven dynamics contributing to the photoelectron yield, and not consistent with the model which contains only VUV driven dynamics, particularly for positive delays beyond 50 fs. Fig. 5.4 panel (b) shows the individual components used in this simple model of the molecular dynamics signal. Further analysis of the UV vs VUV driven dynamics contributions to the signal are given in the Appendix C.1. Another rigorous test of this low energy tail

aforementioned was provided by standard bootstrapping analysis, which allows to determine the statistical significance of the electrons measured in a given energy bin for each delay. Fig. 5.5 left panel shows the photoelectron yield as a function of pump probe delay for electrons below 0.5 eV along with error bars, which is one standard deviation determined by the bootstrapping analysis. The top right panel shows the yield and error as separate curves as a function of delay. The bottom right panel shows the ratio of the yield and uncertainty, demonstrating a signal to noise of greater than 5 over the relevant range of delays.

Before I finish the discuss of this section, it is useful to briefly mention the calculation method. For both molecule systems, the electronic structures, the dynamic calculations, and the TRPES signals presented in this chapter were performed by our theory collaborators Philipp Marquetand and Tamás Rozgonyi. The electronic structure calculations for both molecular systems were performed with MS-CASPT2(12,8)/ano-rcc-vdzp (multi-state complete active space perturbation theory second order) based on CASSCF(12,8) (complete active space self-consistent field with 12 electrons in 8 orbitals). The state-averaging included 5 singlet/4 triplet states for CH_2I_2 and 3 singlet/4 triplet states for CH_2IBr. The dynamics calculation utilized trajectory surface hopping (TSH) method, carried out by SHARC (Surface Hopping including ARbitrary Couplings) program [193, 194] interfaced with Molcas 8.0 [195]. TRPES signals were generated by calculating the Dyson norms. I analyzed the TRPES signal from each individual trajectories and interpret the experimental measurements with proper manipulation of the trajectories. The nuclear trajectories were also used to simulate the electron diffraction signal as well as the photo-fragment kinetic energy that I will discuss in the later sections. The details of TSH calculations are included in Appendix C.1.1.

5.4 Investigating features in CH_2I_2 TRPES - Direct versus Indirect dissociation

Figure 5.3 indicates several important features of the photoelectron from both the case of CH_2I_2 and CH_2IBr. Given the agreement between the measured and calculated TRPES, and having established that the measurements contain information on the UV driven dynamics, I now examine the experimental results with the aid of calculations in more detail for insights into the

dissociation dynamics. As shown in Fig. 5.3 and Fig. 5.5, one of the main features is the long lasting lower energy tail shown in the TRPES of CH_2I_2 but not in CH_2IBr.

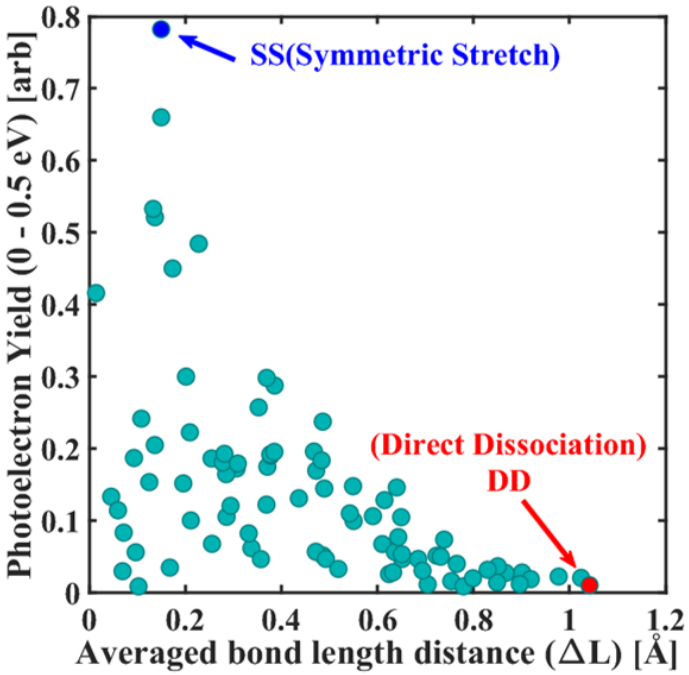

Figure 5.6: **Scatter plot illustrating the correlation between photoelectron yield and symmetric C-I stretching in CH_2I_2.** In this figure, the x-axis represents the absolute difference ($\Delta L = |L(C\text{-}I_1) - L(C\text{-}I_2)|$ and L is the pair distance between C and I atoms) between the C-I pair lengths averaged over all delays, while the y-axis represents the photoelectron yield from 0-0.5 eV averaged over all delays. Each point on the graph represents a different trajectory. Two trajectories are selected for further analysis below and marked with a red diamond and blue square. Symmetric Stretch (SS) and Direct Dissociation (DD) are used to label these two trajectories.

In order to determine whether the low energy tail in the TRPES for CH_2I_2 is associated with a particular motion of the molecule, I examined the trajectories for correlations between the low energy tail in the TRPES and motion along different degrees of freedom in the molecule. Since there is sufficient energy on the excited state for dissociation of a single C-I bond

but not both, I looked specifically at symmetric stretching of the C-I bonds and constructed a scatter plot such that one axis is the integral of the low energy tail in the TRPES, while the other axis is the absolute difference between the C-I bond lengths (which is small for symmetric stretching and large for stretching of a single C-I bond). The analysis is shown in Fig. 5.6. The values on each axis are averaged over the dynamics and each data point on the plot corresponds to a different trajectory. As is evident from the graph, trajectories which give rise to a significant tail in the photoelectron spectrum tend to have small average differences between the two C-I bond lengths (corresponding to symmetric C-I stretching). Conversely, large average differences in the C-I bond lengths, which correspond to dissociation, are associated with small yields in the photoelectron spectrum. Thus, I can associate the tail in the TRPES with the symmetric C-I stretching that does not lead directly to dissociation.

In order to illustrate the points discussed above, in Fig. 5.7 I plot the C-I distance for both bonds, along with the populated state index, and the potential energy for two complementary trajectories shown in the scatter plot - one which corresponds to the maximum low energy yield in the TRPES yield (labelled SS, Symmetric Stretch), and one which corresponds to the minimum (labelled DD, Direct Dissociation). These two trajectories show very different behaviors. For the one with the low photoelectron yield, one of the C-I bonds remains roughly constant, while the other one stretches significantly. The asymmetric C-I stretching is also associated with internal conversion and rapid potential energy loss, as illustrated in panels c) and d), while the symmetric C-I stretching is associated with less internal conversion and energy loss. The same analysis was applied to CH_2IBr TRPES signal and trajectories. However, in CH_2BrI, there is not much internal conversion (see panel d of Fig. 5.11), but rather direct dissociation which proceeds without competing stretching of both carbon halogen bonds and I will discuss the details later on.

From Fig 5.7, one is able to draw some conclusions according to the features in the measured TRPES and the motions in the calculations. However, individual trajectories cannot represent the wave packet dynamics, and only through an ensemble of trajectories with enough statistics that one can associate the behaviours in the trajectory with the wavepacket dynamics. According to the motion mentioned, i.e., direct dissociation versus symmetric stretching, I sorted the trajectories into two sup-groups viewed in the molecular geometry as a function of time. Two cartoons in the top of Fig. 5.8

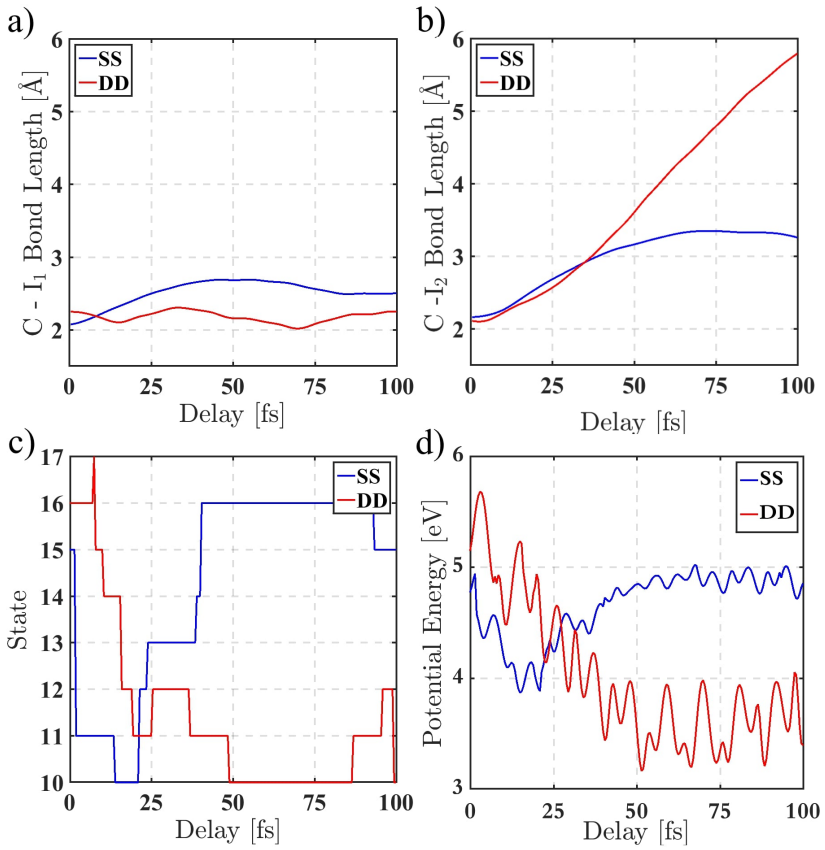

Figure 5.7: **Time-dependent C-I bond lengths, electronic states, and potential energies for two CH_2I_2 trajectories of symmetric stretch and/or direct dissociation.** The figure showcases the C-I bond lengths (panels a and b), electronic states (panel c), and potential energies (panel d) as a function of time for two trajectories chosen from the scatter plot in Fig. 5.6 - blue and red symbols in Fig. 5.6. Again, Symmetric Stretch (SS) and Direct Dissociation (DD) are used to label the two trajectories.

illustrate the quantities that are plotted, i.e. the absolute value of the difference between the C-I bond lengths, ΔL, as well as the I-C-I angle, α. Panels A and B showcase ΔL as a function of time, whereas, panels C and D plot α values. Left two panels (A and C) show the individual trajectories, whereas the right two panels (B and D) show the average for the two groups, with the standard deviation for each group indicated by the shading behind the

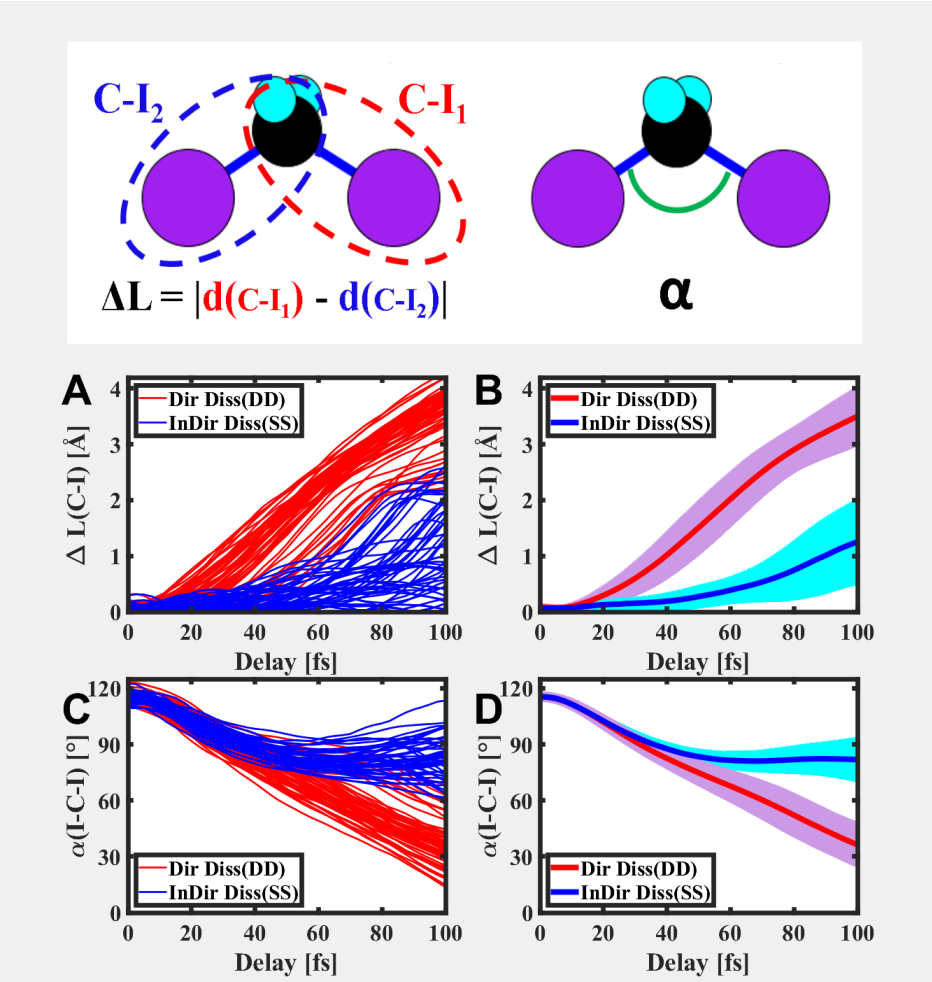

Figure 5.8: **Calculated C-I pair distances and I-C-I angles as a function of time in the first 100 fs.** Two cartoons in the top of the figure illustrate the quantities being plotted: the absolute value of the difference between C-I pair distances, ΔL, and the I-C-I angle, α. **(A)** Time evolution of ΔL from 0 to 100 fs. Each line represents a single trajectory. Lines in red and blue colors are corresponding to direct dissociation and symmetric stretching trajectories, respectively. **(B)** Time evolution of averaged ΔL from trajectories in different groups. **(C)** Time evolution of α from 0 to 100 fs. **(D)** Time evolution of averaged α from trajectories in different groups. In panels **(B)** and **(D)**, one standard deviation is treated as the error bar, which is indicated by the shaded region behind each line.

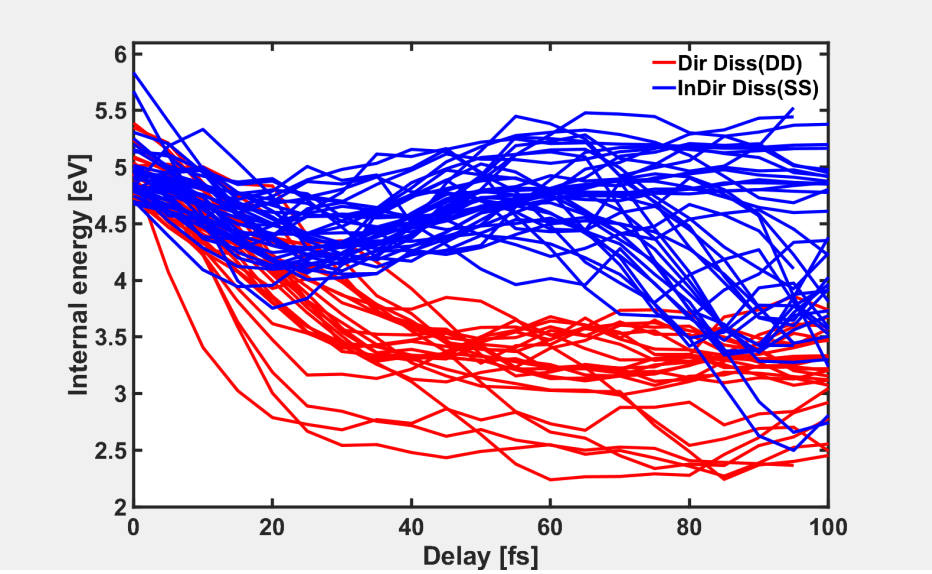

Figure 5.9: **Calculated energies as a function of time for individual trajectories in the first 100 fs.** Each individual line represents a single trajectory. Direct and indirect dissociation trajectories are plotted in red and blue colors, respectively. DD represents direct dissociation and SS represents symmetric stretch.

lines. It is clear from the graph that the two groups are well defined, as they are separated by an amount that is larger than the standard deviation for each group. Similar idea can be applied to the transient potential energies provided in each individual trajectories. Fig. 5.9 showcases the same separation of the trajectories that used in Fig. 5.8 by plotting the potential energy, where the blue and red colored lines are corresponding to the direct dissociation and symmetric stretching trajectories. Similar to Fig. 5.8, one is able to see that the trajectories naturally fall into two groups, with the direct dissociation trajectories losing energy more rapidly (in under 50 fs), and the symmetric stretching trajectories generally maintaining their energy until 100 fs or beyond. For convenience, I call trajectories with symmetric stretching motions as indirect dissociation.

From both Fig. 5.9 and Fig. 5.8, one can see the clear bifurcation in the potential energies as well as the structures. While much insight can be gain by manipulation of the trajectories on the time-dependent energy and structural changes, a ultimate test falls into the comparison between the

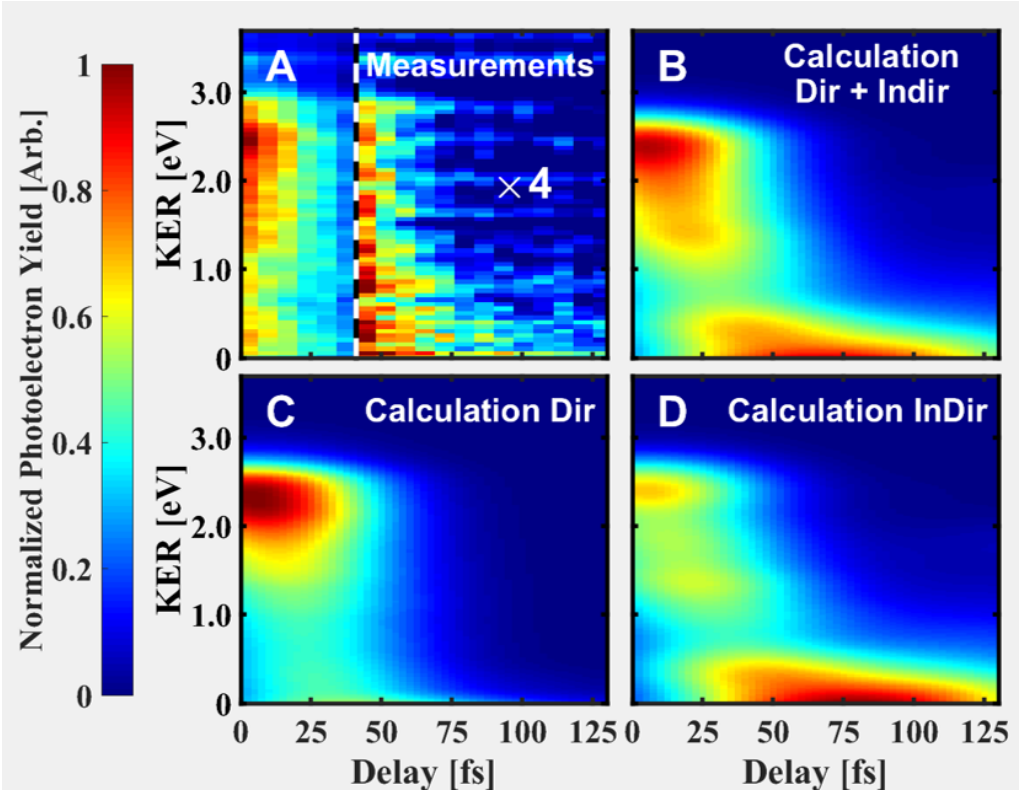

Figure 5.10: **Measured and simulated time-resolved photoelectron spectra CH_2I_2.** A: TRPES from experimental measurement. B: Simulated TRPES including all trajectories. C: Simulated TRPES for direct (Dir) dissociation trajectories. D: Simulated TRPES for indirect (InDir) dissociation trajectories.

measured and calculated TRPES signal, and a natural question is whether different trajectories in the aforementioned separation are responsible for the different features in the photoelectron spectrum. In order to address this question, the measured and calculated TRPES of CH_2I_2 from Fig. 5.3 are revisited and I plotted the calculated TRPES into two groups associated to the trajectory separation in Fig. 5.8 and Fig. 5.9, and the results are shown in Fig. 5.10. Panel A shows the experimental measurement, which is similar with that in Fig. 5.3 panel A, but the data after $\sim$40 fs is multiplied by a factor of 4 in order to to highlight the longer lasting tail. Panel B presents the calculated TRPES from all the trajectories. The interesting part is coming from panel C and D in Fig. 5.10, where the TRPES for the two groups of trajectories are showcased. Panel C shows the TRPES for the direct dissociation trajectories and panel D shows the TRPES versus delay for the indirect dissociation trajectories. If one compares between panels A and C, the higher energy peak (2.5 eV) in the measured photoelectron spectrum can be captured by the direct dissociation trajectories in which the calculated TRPES showcases a high energy peak decaying in $\sim$50 fs without a lower energy tail. Whereas, from panels A and D, it is clear that the low energy tail lasting more than 100 fs in the measured TRPES can be associated with the symmetric stretching dissociation trajectories, and thus I label these trajectories as indirect dissociation trajectories.

From Fig. 5.6 to Fig. 5.10, I have provided a series of analysis on the theoretical calculation by sorting the trajectories into two sub-groups that featured by different behaviours of the motions. I have gained very much insight into the internal dynamics that UV excited CH_2I_2 is governed by the directly and indirect dissociation dynamics, and the structural transformation and the energy changes are intrinsically correlated with each other. The direct and indirect dissociation dynamics are well shown in Fig. 5.10 from spectroscopic view, in which the features in the measured TRPES are well captured by the calculated TRPES from different sub-groups of trajectories. As I mentioned early, same analysis protocols were applied to the trajectories of CH_2IBr and only direct dissociation behaviours are observed. While some earlier work on CH_2BrI with excitation at 266 nm found evidence of C-Br bond fission as well as C-I fission [192], C-I bond fission dominated (with a ratio of about 5:1), and other work making use of excitation at 271 nm measured only C-I bond fission [196]. The calculations found evidence of C-Br fission, but only for about 5% of the trajectories, and the evolution of the TRPES was similar to that calculated for C-I fission. Thus, the

measurements are not able to separately track C-Br fission.

5.5 Non-adiabatic dynamics of CH_2I_2 and CH_2IBr

The TPRES measurements indicates clearly that the dissociation after UV excitation is more complicated in the case of CH_2I_2 than that of CH_2BrI. The energy probe by TRPRES not only showcases the non-local dynamics of CH_2I_2, but also reflects the large different structural transformations between the sub-groups of trajectories predicted from the calculation. Thus a structural measurement is necessary. Before I step into the structural probing with the UED experiment, it is important to investigate what drives the difference dynamics between the CH_2I_2 and CH_2IBr behind. In order to answer the question, I turn into the electronic structures and investigate more details of the trajectories surface hopping calculation of both CH_2I_2 and CH_2IBr.

Figure 5.11 shows the adiabatic potential energy surfaces (PESs) for several neutral and ionic states, as well as the state populations versus time after the pump pulse for both CH_2I_2 and CH_2BrI. In the upper panels (a) and (b), the calculated potential energy of the molecules are plotted as (one of) the C-I bond(s) is stretched and all of the other bonds are kept fixed. Considering the spin-orbit couplings (SOCs) effect due to the heavier iodine atom, the dissociative states yield to sets of asymptotes corresponding two the spin-orbit ground (CH_2I + I, red colored lines) and excited (CH_2I + I*, blue colored lines) state.[2] The splitting results in an energy different in the order of $\sim$ 1 eV. These PESs illustrates a number of important points. First, absorption of a pump photon with an energy about 4.65 eV leads to excitation of a cluster of excited states. In CH_2BrI, these are all directly dissociative states, whereas in CH_2I_2 it is a mixture of bound and dissociative states. As illustrated by panels (c) and (d) of the state population, in CH_2BrI,

[2]These adiabatic state are currently labeled with numbers, i.e., 1, 2, 3..., which is due to the compilation from the SOCs. These states are neither singlet nor triplet states but something in between due to the mixture by SOCs, thus labeling them as S_0, S_1 as singlets or T_1, T_2 as triplets are not proper, not even approximately. What is even more difficult, is to provide labels like $n\sigma*$ (or $\pi\pi*$ in an organic molecule with double bonds) since these characters are even difficult to assign if there is no SOC. With SOCs effect, it is doubly difficult, because the diabatic characters (like $n\sigma*$) are first mixed e.g. by the nonadiabatic couplings to give the adiabatic singlets (or triplets respectively) and then they are mixed again by SOCs.

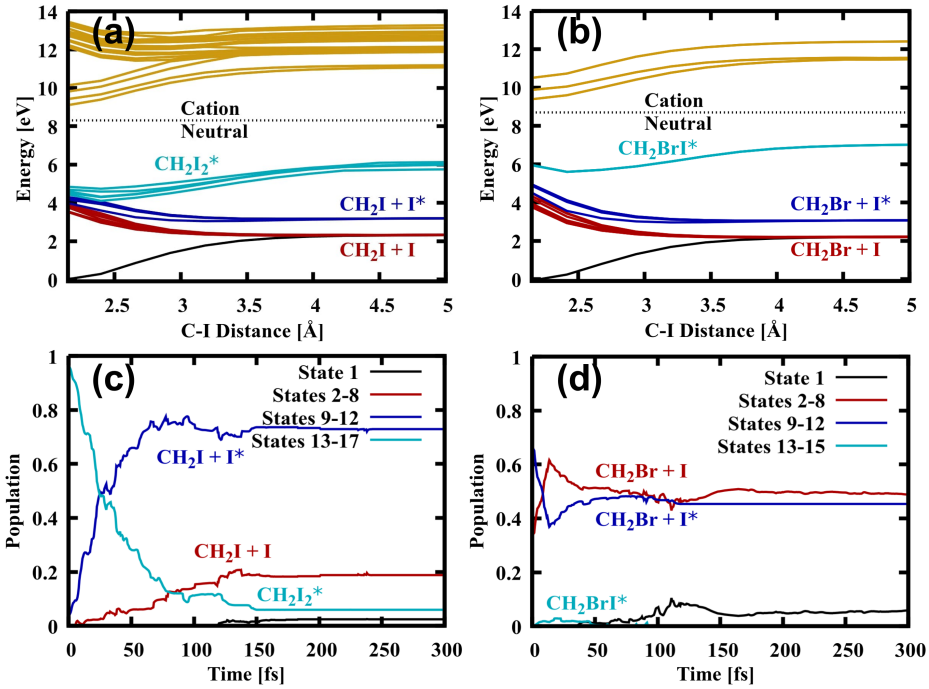

Figure 5.11: **Calculated potential energy surface and excited state populations.** In panels (a) and (b), we show the calculated spin-adiabatic potential energy curves as a function of C-I distance for several neutral and ionic states for CH_2I_2 and CH_2IBr, respectively. Different group of neutral states are highlighted with different colors. Panels (c) and (d) show the calculated neutral state populations as a function of time from the TSH calculations for CH_2I_2 and CH_2IBr respectively. The color coding for the groups of neutral states is the same for panels **(a)-(d)**. States 2–8 are maroon, states 9–12 are dark blue, and states 13–17 are light blue.

internal conversion plays little role as the molecule dissociates, whereas in CH_2I_2, there is significant internal conversion that takes place prior to dissociation. As the molecule dissociates in states 2 through 8 or 9 through 12, the ionization potential increases such that the probe pulse cannot ionize the molecule, leading to a decay of the photoelectron spectrum. The ionization potentials for I/I* and CH_2I radical are above our employed photon energy (The IP of the CH_2I radical is 8.4eV. The IP of I is 10.5 eV) [197]. CH_2I_2 molecules remaining in states 13-17 are energetically capable of being ionized and thus is responsible for the tail in the photoelectron spectrum for CH_2I_2, as I discussed from Fig. 5.6 to Fig. 5.10.

Earlier work comparing dynamics following excitation at 268 nm in CH_2BrI and CH_2ICl [198] interpreted their measurements in terms of dissociation on multiple states in conjunction with internal conversion. While they observed small differences in the measured dissociation times, they did not see evidence for simultaneous stretching of the carbon halogen bonds leading to a delayed dissociation as we observe in CH_2I_2. Future work with a slightly higher probe photon energy could allow for following of the directly dissociative portions of the wave packet in both molecules out to larger C-I bond lengths and improved time resolution would allow for following the internal conversion dynamics near the FC region in greater detail, with less contribution from VUV driven dynamics. For this current study, one way to check the significance of the internal conversion in CH_2I_2 dynamics is to compare the measurement observables with or without the non-adiabatic transitions. This step can be accomplished by simply *switch off* the hopping events as the trajectories are propagated along the excited state potentials, and I plotted measured and calculated TRPES with and without surface hopping. Fig. 5.12 compares the measurements (panel C) with calculations where the surface hopping is (panel B) and isn't (panel A) included in the calculations. From panels A to C, it is apparent that only with hopping the calculation can make a meaningful prediction for the measurement, whereas without hopping, there is significant amount of higher energy ($\sim$2 eV) signal at long delay which is not shown in the measurement. Panel D shows the energy integrated photoelectron yield from the calculations together with the experimental measurements. The results of the calculations with surface hopping agree well with the experimental measurements, while the calculations without surface hopping show significant differences. This highlights the non-adiabatic dynamics captured by the TRPES measurements.

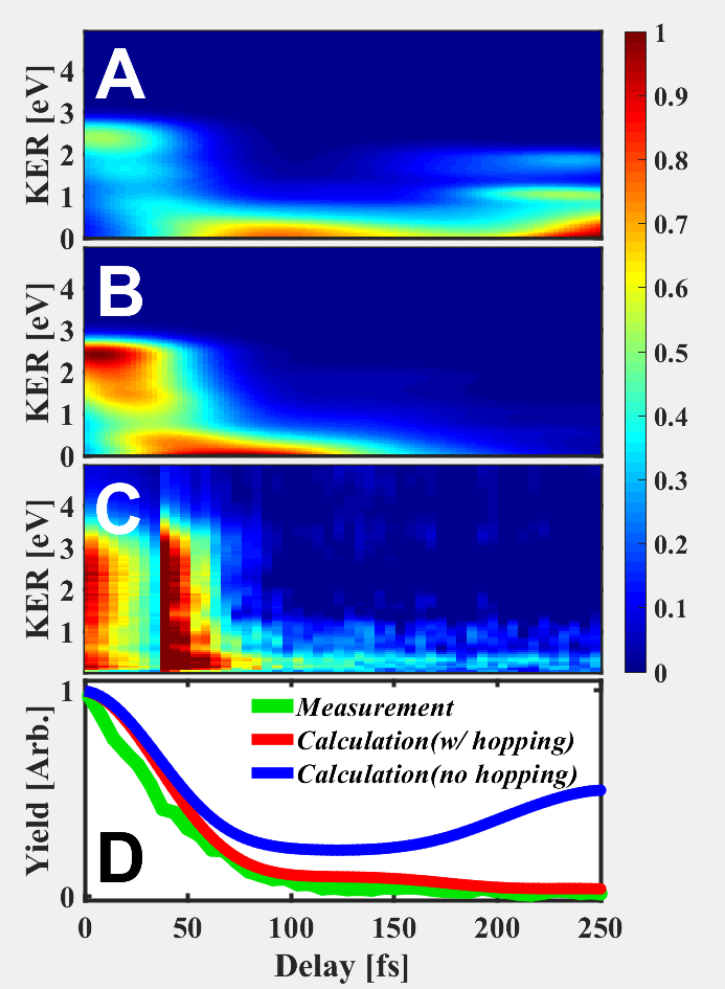

Figure 5.12: **Comparison between measured photoelectron spectra and calculations with or without surface hopping. (A)** Calculated TRPES without surface hopping between different electronic states. **(B)** Calculated TRPES including surface hopping between different electronic states. **(C)** Measured TRPES. **(D)** Measured and calculated (with and without surface hopping) energy integrated photoelectron yield as a function of pump-probe delay. Note that the measurement uses the dataset from experiment at Stony Brook.

5.6 Structural probe with ultrafast electron diffraction of CH_2I_2

Though it is true that the spectroscopic measurement by TRPES method offers great details into the ensuing dynamics of the UV excited CH_2I_2, the structure changes can be only inferred from the aid of calculation. The calculations I discussed above do indicate important structural signatures, thus an structural measurement is needed and viewing the dynamics by combined spectroscopic and structural probes is essential for understanding the dynamics. One of the main questions is that whether the direct versus indirect dissociation can be observed or not? In order to probe the transient structures, I performed an electron diffraction measurement on CH_2I_2. One point to note is that though UED measurement discussed here does not directly provide molecular structures, the directly measured pair distribution function difference (ΔPDF) can be used to directly reflect the structure change.

The UED measurement of CH_2I_2 utilized the ultrafast relativistic Mega-electron-volt (MeV) electron beam line at SLAC National Laboratory [46, 199, 200, 201]. CH_2I_2 molecules were injected with a pulsed nozzle into the interaction chamber, where they were excited by the UV-pump pulse. In contrast with the TPRES measurements, the probe pulse consisted of relativistic electrons, which were scattered [3] by the molecules and projected onto a phosphor screen in the far field. The time dependent molecular structure information was thus imprinted onto a series of diffraction patterns taken for each pump-probe delay. These patterns were recorded by a charged coupled device (CCD) camera. In order to achieve sufficient signal to noise in the measurement, I worked at pump intensities of about 10^{12}W/cm^2, which led to some two-photon absorption from the pump pulse. Based on an analysis of the angle dependent diffraction signal, a scan of the pump pulse intensity, and the strength of different features in the pair distribution function, I estimated the two-photon absorption to be about 10% of the one-photon absorption (see Appendix C.2.2). The UED measurements yielded a two dimensional projection of the three dimensional far field diffraction pattern for each pump-probe delay. This far field diffraction pattern represents the mo-

[3] In principle, the diffraction measurement includes both elastic and inelastic scattering effects. The elastic scattering electrons are mainly contributed by the charges in the nuclei and thus can give molecular structural information with relative large scattering cross section reaching to higher values in momentum transfer space.

mentum space interference pattern of the scattered electrons. The diffraction difference was first obtained by subtracting the diffraction pattern for negative time delays (averaged over four delays) [202]. The difference pattern was then Fourier transformed to produce a two dimensional position dependent distribution. Given the cylindrical symmetry of the photoexcited molecular ensemble (symmetry around the linear polarization vector of the pump laser pulse), I was able to perform an inverse Abel transform of the measured spatial distribution function to yield the three dimensional pair distribution function for each time delay. Fig. 5.13 shows the angular differentiated pair distribution function difference of the measurements. It is interesting that the angular dependence varies at different atomic pair distances, which is consistent with what we have seen in Fig. 2.21 of Chap. 2.

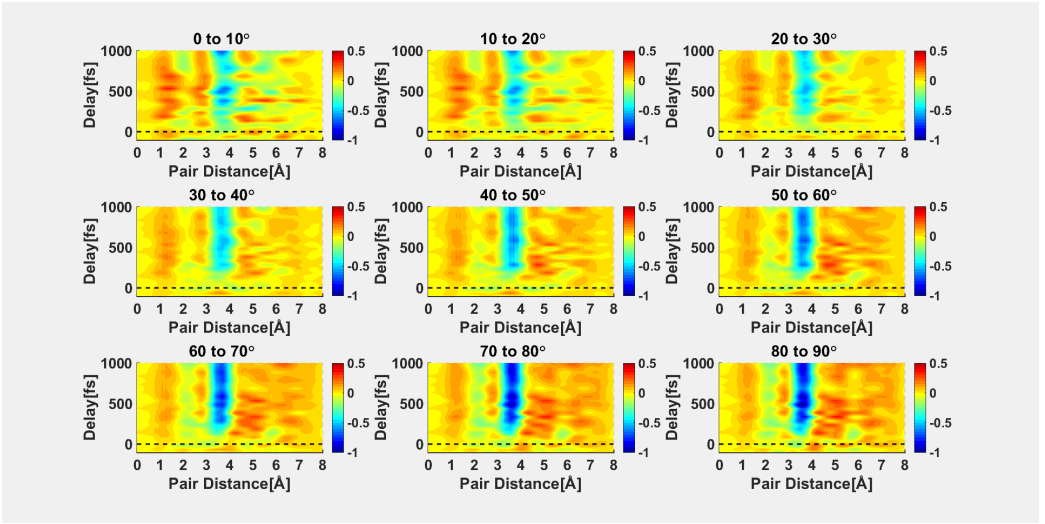

Figure 5.13: **Angle dependent ΔPDF CH_2I_2.** Each panel shows the ΔPDF within a 10° polar angle region. The depletion in the I-I initial pair distance shows the largest amplitude at 90°, consistent with the fact that the transition dipole moment is strongest along the direction perpendicular to the I-I pair. Note that the angle dependence of ΔPDF is different for different atomic pair distances.

Given the high dimensional nature of this information (three spatial dimensions + time), in order to provide a first overview of the measurements, I

integrated over both polar (with respect to the pump pulse polarization axis) and azimuthal angles to form a two dimensional distribution which shows the scattering intensity as a function of interatomic distance and pump-probe delay. This is shown in Fig. 5.14. However, analyzing the polar angle dependence of the measurements can yield valuable information, which we make use of later showed in Fig. 5.15, as well as in an analysis of multi-photon absorption from the pump pulse which can be found in Appendix C.2.2. Similar with the TRPES measurement, locating the right time-zero is essential. A pump probe measurement with a thin silicon film was performed to lock time zero within a 300 fs window. I improved the precision in the time zero determination by comparing the phase of modulations in the measured ΔPDF with those of modulations in the simulated ΔPDF at R = 2.85 Å. This can be seen in Fig. 5.15 panel B, in which both the measured and simulated ΔPDF at 2.85 Åare plotted. The simulation indicates that the first peak of the modulation occurs at around 135 fs. This a higher precision estimate of the time zero is obtained by adjusting the experimental delay axis slightly such that data and simulation agree on the position of the peak. With this adjustment, I found that all of the subsequent oscillations in the ΔPDF at R=2.85 Å agreed for simulation and experiment which I will discuss in next section.

5.7 Comparing measured and calculated pair distribution function

Fig. 5.14 shows the scattered intensity as a function of interatomic distance - the pair distribution function (PDF) - and pump-probe delay for CH_2I_2 (ground state equilibrium geometry shown in the top-left corner) from experimental measurements. The PDF for negative time delays is subtracted from the PDF for positive delays, producing the ΔPDF. This allows one to focus on the changes in the PDF due to excited state dynamics and to subtract out the ground state contributions as well as those from individual atoms, focusing on the molecular, or interference contributions arising from the excited state(s) of the molecule. Blue coloring indicates loss and red indicates gain compared with the unexcited molecules. A solid vertical magenta-colored line indicates zero time delay - i.e. where the pump laser and probe electron bunch are overlapped in time. The delay dependent PDF

shows more structure (features that vary with delay and pair distance) than the TRPES results, providing a more detailed view of the dynamics than the delay dependent photoelectron spectrum in TRPES measurements.

In order to compare the time-dependent measured ΔPDFs with the calculated ones, I simulated electron diffraction pattern for the time dependent molecular geometries extracted from the surface hopping calculation given that each trajectory includes all of the atomic positions as a function of delay. The diffraction patterns were simulated within the independent atom model (IAM) for each molecular geometry, with the elastic scattering amplitudes for C, I and H atoms calculated using the Dirac partial-wave method (ELSEPA) [84]. Experimental conditions were applied to the diffraction pattern simulation in order to compare with the measurements. I implemented a three dimensional (3D) diffraction pattern analysis same as the experimental analysis and details were provided in Sec. 2.3.3. In order to interpret the time-resolved ΔPDF, I calculated the ground state pair distribution function and plotted the geometry with relevant atomic pair distances and angles in Fig. 5.14. The ground state PDF shows two main peaks at 2.15 Å and 3.60 Å, arising from the C-I and I-I pairs respectively. Due to the relatively low electron scattering cross section of H atoms compared with C and I atoms, the contributions related to the H atoms are negligible. Compared with the ground state PDF, one can see that in the measured ΔPDF, there are several characteristic atomic pair distances that are of interest for the dynamics we follow, and we highlight a number of features in the data at these pair distances that can be interpreted in terms of specific types of motion. They are illustrated by the cartoon diagrams on the right hand side of the figure. The top cartoon illustrates I-I separation with increasing time delay. As the I atoms have the largest scattering cross section, the I-I contribution to the changing PDF is the largest. The middle cartoon illustrates I-C-I bending that takes place in an electronic state accessed by two-photon absorption from the pump pulse, and the lowest cartoon illustrates motion of the CH_2 as one of the C-I bonds is broken. These dynamics are captured by the UED measurements at different pair distances bounded by pairs of dashed lines in the main figure.

There is a deep blue stripe centered at 3.60 Å indicating a large decrease in the probability of finding I atoms separated by their equilibrium distance. Together with the decrease of the PDF at 3.60 Å, the signal shows modulated increases for distances greater than 4 Å and two narrower regions centered at 1.30 and 2.85 Å. The increase in the PDF for distances greater than 4 Å is ex-

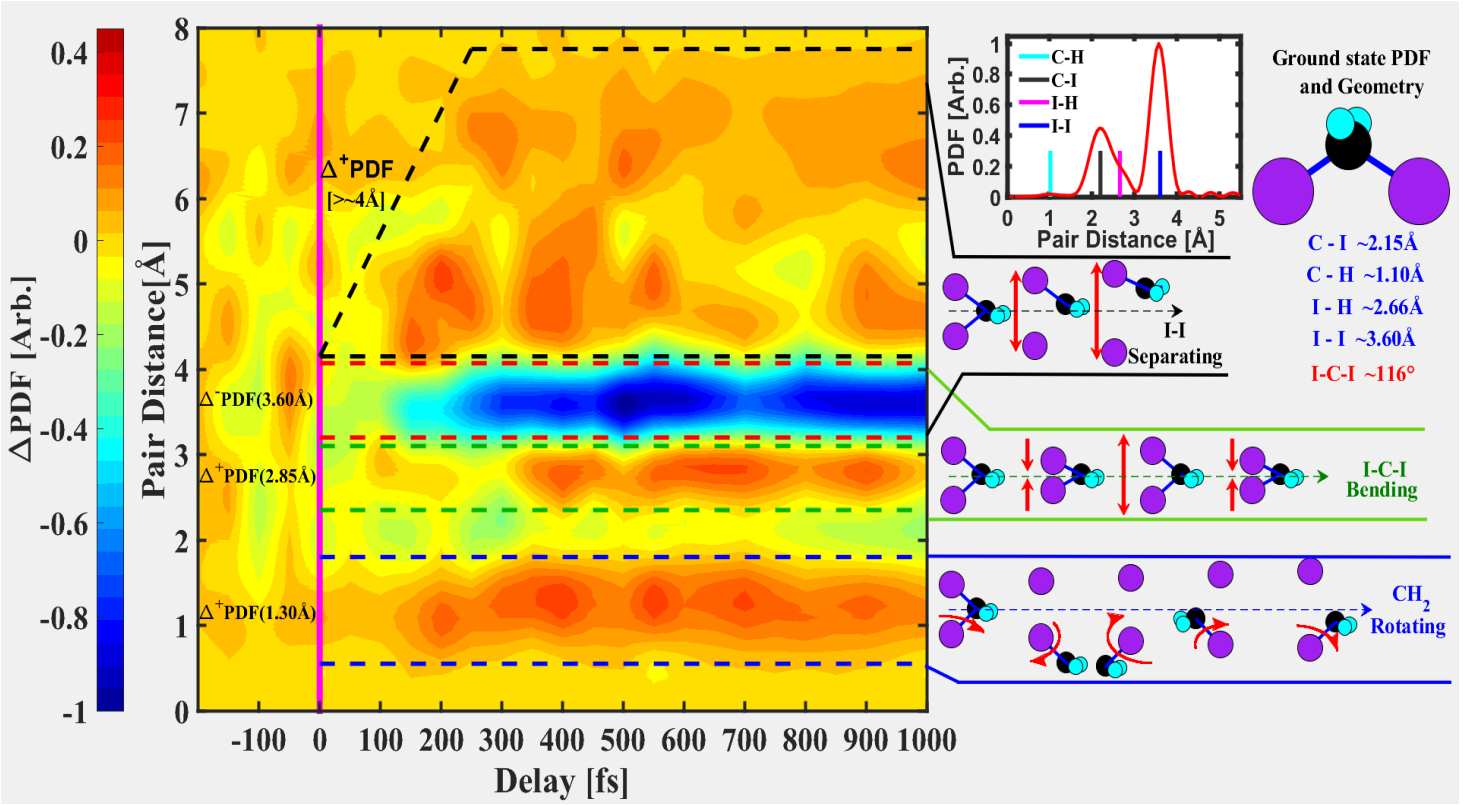

Figure 5.14: **Measured ΔPDF as a function of pump-probe delay. (A)** vertical magenta-colored line marks zero pump-probe delay. The data is normalized by the largest value of ΔPDF. Four regions corresponding to specific molecular motions are highlighted with dashed lines in different colors. Snapshots on the right side of the graph illustrate the different types of motion highlighted in the regions bounded by the dashed lines to the left. A cartoon picture on the top-right of the graph shows the ground state equilibrium geometry of CH_2I_2, with black, purple and cyan colored balls representing the carbon, iodine and hydrogen atoms, respectively. The atomic pair distances (blue color) and I-C-I angle (red color) are labeled underneath. The corresponding ground state PDF and atomic pair distances are plotted adjacently.

pected, and has contributions from both C-I and I-I pairs, with both arising directly from the dissociation of the molecule in the excited states. Given the scattering cross sections for C and I atoms, it is dominated by I-I contributions, as illustrated by the cartoon on the right hand side of the figure. While the modulations for distances greater than 4 Å have no obvious periodicity, the modulations in the PDF at 1.30 Å and 2.85 Å do. These modulations are surprising, and highlight two different kinds of motion, which are illustrated to the right hand side of the figure and discussed below.

In order to interpret the experimentally measured PDF and validate the calculations, I compare the measured and calculated PDF at the distances bordered by the dashed lines in Fig. 5.14. Motivated by the analysis of the TRPES measurements, we compare the UED measurements with calculations for the two different groups of trajectories (direct and indirect dissociation), as well as trajectories for dynamics in high-lying Rydberg states in order to account for molecular dynamics driven by two photon absorption from the pump pulse.

The modulations in the PDF at 2.85 Å are not found in our calculations of the valence state dynamics (i.e. states excited by one photon absorption), but the periodicity of the modulations corresponds to I-C-I bending motion in high-lying Rydberg states or low-lying states of the cation [203, 204]. Since these states can be accessed by two photon absorption from the pump, I performed calculations of the dynamics in high-lying Rydberg states, modeled by considering the ground state of the molecular cation, for which the potential energy surface is roughly parallel to the Rydberg states excited by two photon absorption [205]. The shapes of the potential energy surfaces for the Rydberg and ionic states are very similar, since they are both determined by the removal of a HOMO (iodine lone pair) electron, which leads to displacement along the I-C-I bending coordinate. The modulations in the ΔPDF centered at 1.30 Å are also present in our calculations as shown in Fig. 5.15, but do not correspond to periodic modulation of any atom pair distance. Rather, they are due to rotation of the CH_2 group after the bond breaks between the C and one of the two I atoms. The rotations lead to a periodic oscillation in the projection of the remaining (unbroken) C-I bond distance onto the plane of the detector with a period equal to half the rotational period since the pump laser only aligns the molecules but does not orient them. The I-C-I angle as a function of time for direct dissociation trajectories is shown in appendix B. The modulations we observe here represent to our knowledge the first direct time-resolved observation of fragment

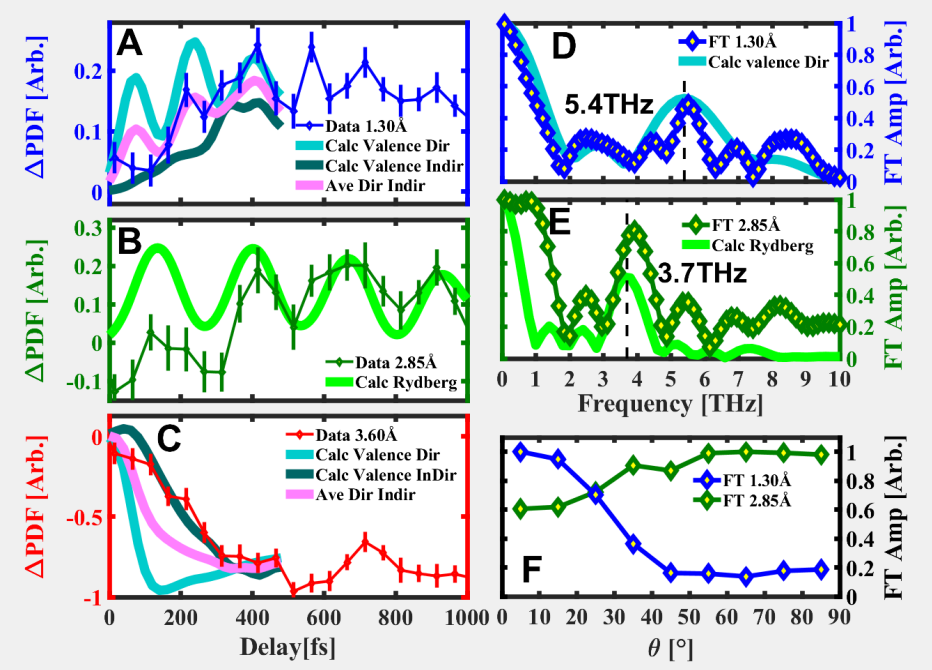

Figure 5.15: **Measured and simulated photoelectron spectra of CH_2I_2.** **(A)** Experimental and simulated time-resolved ΔPDF around 1.30 Å. The simulated ΔPDF are calculated from the groups of both direct and indirect dissociative trajectories. **(B)** Experimental and simulated time-resolved ΔPDF around 2.85 Å. The simulation is from the group of Rydberg state trajectories. **(C)** Experimental and simulated time-resolved ΔPDF around 3.60 Å. The simulations are from both direct and indirect dissociative trajectories. The pink curves in panels A and C are for an equally weighted average of direct and indirect trajectories. Fig. 5.16 contains a comparison of the data and simulation with different mixtures of direct and indirect trajectories. **(D)** Fourier analysis of ΔPDF at 1.30 Å from experimental data and simulation of direct dissociation trajectories (panel A) for a polar angle of 0°. **(E)** Fourier analysis of ΔPDF at 2.85 Å from experimental data and Rydberg state trajectories (panel B) for a polar angle of 70°. **(F)** Angle dependent Fourier analysis of the ΔPDF at 1.30 Å and 2.85 Å. θ is the angle respect to the laser polarization direction.

rotation in photodissociation.

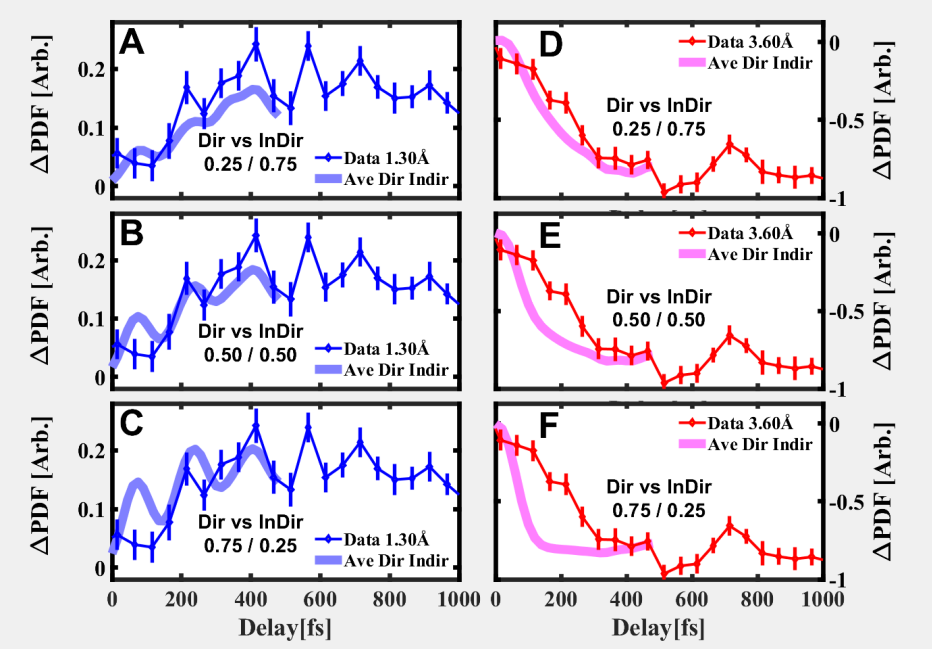

Figure 5.16: **Analysis of direct and indirect trajectory weighting.** Panels A and D show the measured and calculated ΔPDF at 1.30 Å and 3.60 Å respectively for a 0.25/0.75 weighting of direct vs indirect trajectories in the average. Panels B and E show the measured and calculated ΔPDF at 1.30 Å and 3.60 Å respectively for a 0.50/0.50 weighting of direct vs indirect trajectories in the average. Panels C and F show the measured and calculated ΔPDF at 1.30 Å and 3.60 Å respectively for a 0.75/0.25 weighting of direct vs indirect trajectories in the average.

Fig. 5.15 shows the time evolution of ΔPDF at several pair distances (panels A, B and C) and their Fourier transforms (panels D and E) for both UED measurements and simulation. Panels D and E show the absolute value of the Fourier transformed data shown in panels A and B, respectively. The thick dashed lines represent simulation results, while the thin lines with diamond markers represent the experimental measurements. In panel A, both the measurement and simulation show periodic oscillations at a frequency of 5.4 THz. In Fig. 5.15 B, both the data and simulation show a periodic oscillation at a frequency of 3.7 THz. In both panels A and B, the first period of oscillation in the experimental data have lower signal level than the

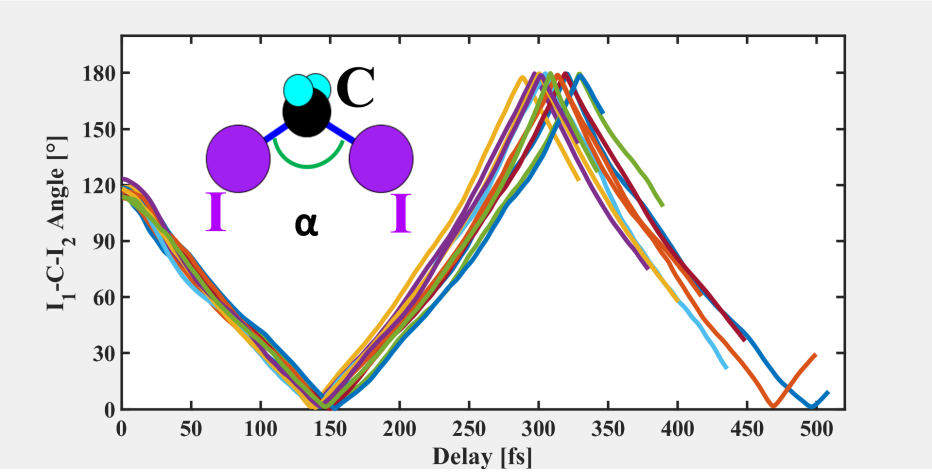

Figure 5.17: **I-C-I angle as a function of time for direct dissociation trajectories illustrating the rotation of the CH_2 group as the C-I bond is broken.** A cartoon of CH_2I_2 molecule is shown inside the figure.

calculations, due to the subtraction of the signal for negative time delays with finite pump and probe durations. Fig. 5.15 C shows the calculated and measured ΔPDF at 3.60 Å as a function of pump-probe delay. There are no modulations, but rather a rapid monotonic decrease in the signal. The analysis here makes use of the angle dependence of the measured and calculated ΔPDFs. The results shown in panel A, B and C used the angular averaged ΔPDF values. The results in panels D used ΔPDF values along a polar angle of 0°, while the results in panels E used ΔPDF values along a polar angle of 70°. Panel F highlights the angle dependence of the signal by showing the heights of the peaks in panels D and E as a function of polar angle. A quick analysis of the weighting of direct and indirect trajectories when comparing their average to the measurements is provided. Fig. 5.16 compares the measurements and calculations for different weightings of direct and indirect trajectories. The figure shows that the measurements and simulations agree best for a direct/indirect mixture between 0.25/0.75 and 0.50/0.50.

The data persists out to 1 ps, while the simulations in panel A and C only last to 500 fs. This is because the dissociative trajectories tended to crash as a result of an insufficient active space. The agreement between the measurements and calculations shown in panels A, C and D of Fig. 5.15 indicates that the structural changes associated with the groups of direct and

indirect dissociation trajectories in the lower-lying electronic states (states 8-17 in Fig. 5.18) are captured by and directly reflected in the UED measurements. The agreement between the measurements and calculations shown in panels B and E of Fig. 5.15 indicates that the dynamics in the Rydberg states are also captured by the UED measurements, and can be separated from the dynamics in the lower-lying states [21]. Note that the CH_2 rotation frequency is about 2.7 THz, corresponding to a period of 370 fs, which is half of the period shown in panel D of Fig. 5.15. This is due to the fact that the projection of the C-I bond that remains in the rotating CH_2I fragment has roughly the same value twice per rotational period, which can be better displayed by the time-dependent I-C-I angle from most of the direct dissociation trajectories shown in Fig. 5.17. This direct view of the three dimensional dynamics including wavepacket bifurcation, rotation and dissociation provides a very clear and detailed picture of the dynamics as well as a very compelling verification of the calculations.

5.8 Combined spectroscopic and structural views of CH_2I_2 dissociation dynamics

Both the TRPES and UED measurements show features which can be associated with the two different groups of trajectories - "directly dissociative" and "indirectly dissociative". This highlights both the non-local nature of the photoexcited wave packet dynamics (bifurcation of the nuclear wave packet and the exploration of multiple regions of coordinate space), as well as the non-adiabatic dynamics involved. It is interesting to note however, that trajectories within a given group show limited dispersion, facilitating the formation of two groups of trajectories.

In Fig. 5.8, the differences among trajectories inside direct or indirect dissociation groups are much smaller than the differences between the two groups, and in order to highlight the features of the direct and the indirect dissociation manner, I choose one trajectory from each group to be a representative, and explore the details from both spectroscopic and structural perspectives. Fig. 5.18 provides both a spectroscopic and structural view of representative direct and indirect dissociation trajectories. Panel A plots the relevant potential energy curves along the C-I dissociation coordinate and shows cartoon snapshots of the wavepacket for both direct and indirect dis-

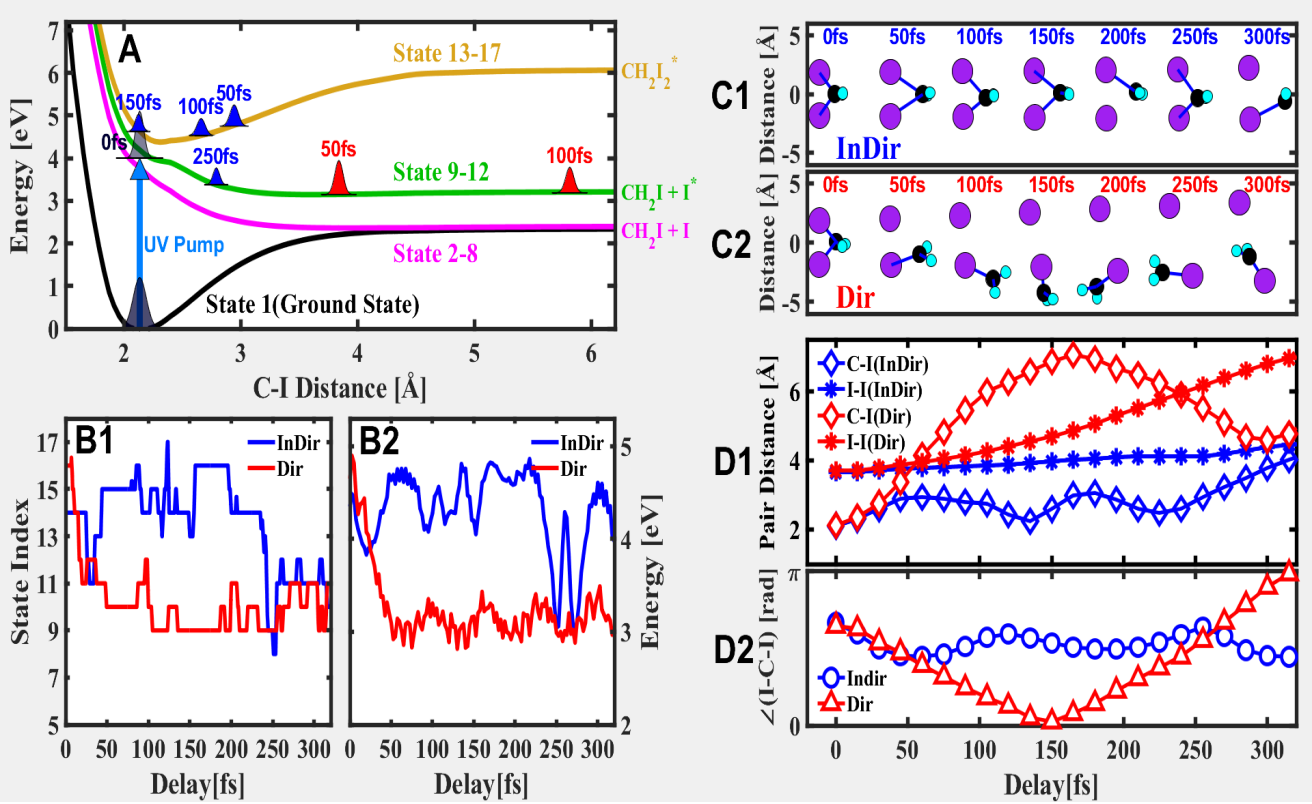

Figure 5.18: **Spectroscopic and structural views of CH_2I_2 dissociation dynamics. (A)** Potential energy curves and cartoon snapshots of the wavepacket at different time delays for indirect dissociation (blue) and direct dissociation (red) trajectories. **(B1)** Time-evolved electronic state index for indirect (blue) and direct (red) dissociation trajectories. **(B2)** Time-evolved potential energy for indirect (blue) and direct (red) dissociation trajectories. **(C1)** Snapshots of the molecular structure at different time delays for an indirect dissociation trajectory. **(C2)** Snapshots of the molecular structure at different time delays for a direct dissociation trajectory. The frames show 2D projections of the 3D molecule onto the I-C-I plane. **(D1)** Time evolution of pair distances for indirect (blue) and direct (red) dissociation trajectories. **(D2)** Time evolution of I-C-I angle from the indirect and direct dissociation trajectories.

sociation trajectories. Note that for simplicity, I grouped the excited states shown in panel a) of Fig. 5.11 into three bands and plotted them as a function of C-I bond distance. The wave packet associated with the direct dissociation trajectories moves out to large C-I distances rapidly after internal conversion from the intially photoexcited states (13-17) to the dissociative states (9-12), while the wave packet associated with the indirect trajectories remains bound in states 13-17 for ∼200 fs and then eventually internally converts followed by dissociation. Panels B1 and B2 show the electronic state index as well as the potential energy as function of delay time after the UV pump pulse. The two trajectories display very different behavior. The difference between the internal conversion rates and energy loss for the two different trajectories is reflected in panels B1 and B2.

Panels C1 and C2 of Fig. 5.18 show snapshots of time resolved geometry changes for the chosen trajectories. In panel C1, I show the structure as a function of time for the indirect dissociation trajectory. One can see that there are relatively small changes, with the initial motion dominated by symmetric stretching of the two C-I bonds. However, for the direct dissociation trajectory shown in C2, one of the C-I bonds breaks quickly, leading to rotation of the CH_2 group around the other I atom. The slow dissociation dynamics for the indirect trajectories is directly captured by the UED measurements in the I-I depletion shown in panel C of Fig. 5.15, while the rapid CH_2 rotation in the direct dissociation trajectory is directly captured by the UED measurements in the modulation of the PDF near 1.30 Å, as shown in panels A and D of Fig. 5.15. The corresponding C-I and I-I distances can be viewed in panel D1, while the I-C-I angle is shown in panel D2.

5.9 Momentum-resolved photoion spectroscopy of CH_2I_2 and CH_2IBr

As we have seen from the discussion above, the combined spectroscopic and structural probe by TRPES and UED provided very much insight into the internal conversion and dissociation dynamics in CH_2I_2 after UV excitation. Ultimately, the excess electronic energy obtained from the UV photon is converted into the nuclear degrees of freedom as the molecules dissociate into fragments. As we have seen, TRPES has the ability of probing the electronic energies and the nuclear dynamics can be inferred from the calculation.

While, UED measurements gives directly probe of the pair distribution function, yielding rich information at various pair distances, the kinetic energy of the dissociation fragments can be only inferred with the aid of the theory input. For both TRPES and UED, neither of them offers a direct probe into the nuclear degrees of freedom, i.e., measuring the nuclear kinetic energies. In order to follow the conversion of electronic energy into the nuclear degree of freedom, it is important to direct measure the transient nuclear kinetic energy. As I alluded in Chap. 2, the coincidence velocity map imaging spectrometer with UV/VUV pump-probe scheme allows the momentum resolved measurement of both photoelectrons and photoions, thus it is possible to extract the momentum of the photofragment ion momentum besides the photoelectron.

In this section, I discuss the time-and momentum-resolved photoion measurement, TRPIS, followed by the dissociation of both CH_2I_2 and CH_2IBr. Experimentally, the apparatus in this measurement is similar with that in the TRPES experiment. As laser beams intersect with the molecules (e.g., CH_2I_2 and CH_2IBr) between VMI plates, photoelectrons (e^-) and photoions (CH_2I^+, I^+ from CH_2I_2 and CH_2Br^+, I^+, Br^+ from CH_2IBr) are produced. By flipping the voltage from negative to positive polarity, photoion can be collected. Different from electrons, ion measurements need to be both energy-and-species resolved. Rather than a conventional frame based camera, this is made true by implementing the ns time resolution time-stamping camera, TimePix3 camera [75]. This fast time-stamping camera is able to record the hit position (x,y) as well as the time-of-arrival (t) for each charged particle. CH_2I_2 was measured first followed with the measurement of CH_2IBr under the same conditions with that of CH_2I_2. In the data acquisition, more than 50,000 events were collected for the parent and fragment ions, which allows to reassemble the event position information for each ion species, generating a 2D image. An inverse Abel transform was applied to the 2D image to obtain the photoion spectrum for each time delay (yield as a function of TKE and pump-probe delays). While our measurements allow for direct reconstruction of the full 3D momentum of each fragment ion based on the measured (x, y, t), we can also perform an inverse Abel transform on an ensemble of ion measurements, integrating over t values for a given ion species. This can sometimes be advantageous, producing higher momentum resolution than available from the timing information, and is the approach that we took in the measurements presented here.

Several fragment-ion species were detected including $CH_2I_2^+$, CH_2I^+ from

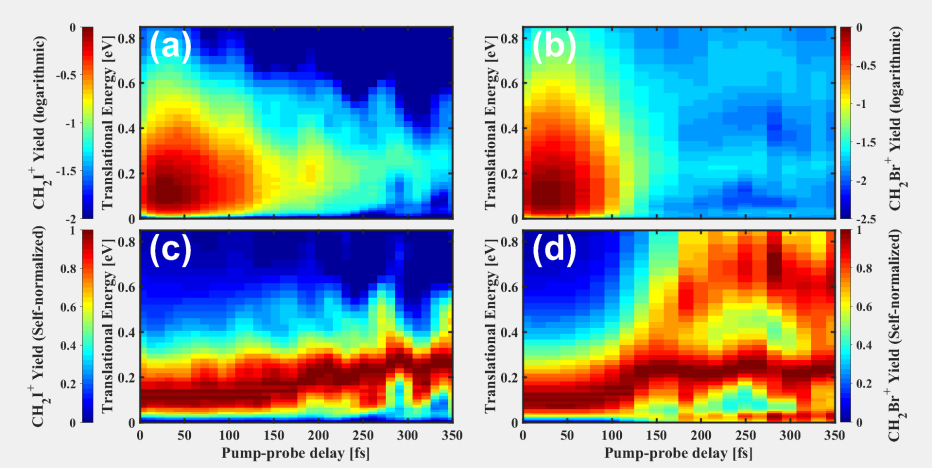

Figure 5.19: **Measured photoion spectra for both CH_2I^+ and CH_2Br^+ from CH_2I_2 and CH_2IBr respectively.** Panels **(a)** and **(b)**, show the time and energy dependent yield of CH_2I^+ and CH_2Br^+ with a logarithmic scale, respectively. Panels **c)** and **(d)** show the same spectra self normalized for each delay on a linear scale.

CH_2I_2, and CH_2IBr^+, CH_2Br^+ CH_2I^+ from CH_2IBr. I note that the interesting species are the photo-fragments, instead of the parent ions. Compared with CH_2I_2, there more species in CH_2IBr. As we have seen above in the TRPES measurements, the dissociation of a C-Br bond in CH_2IBr is much less likely than that of the C-I bond, and the CH_2I^+ observed is less than 1/5 of the CH_2I^+. Thus the focus will be the CH_2Br^+. Another issue needs care is that the measurements contain both UV and VUV driven signals since the molecules have absorption bands at both spectra regions [191]. In order to decompose the UV driven dynamics from the total signal, I applied the same 2D global fitting protocol that was used for the cc-COD TRPES analysis in Chap. 3. The analysis details is included in Appendix C.3.

Figure 5.19 showcases the measured photoion spectra of CH_2I^+ and CH_2Br^+ after removing the VUV driven signal from the 2D global fitting. Panels (a) and (b) show the measured photoion translational kinetic energy (TKE) distribution as a function of pump-probe delay for CH_2I^+ and CH_2Br^+, respectively. In order to view both the dynamics near zero time delay as well as the subtle changes to the spectrum at longer delays, panels (a) and (b) are plotted using a logarithmic color scale. In both molecules, the TRPISs

show a rapid decay in the fragment ion yield with time delay (on a $\sim$ 100 fs timescale), followed by small shifts of the TKE for the remaining peaks in the spectrum for times greater than 100 fs. However, I note that the changes in the spectra after 100 fs for the two molecules are different, with the CH_2I^+ yield displaying a single peak that increases in TKE, while the CH_2Br^+ yield shows two peaks (bands) which increase in TKE with time. As the signals beyond 100 fs are much smaller than the yields near zero time delay, I induced a self-normalization analysis, where in panels (a) and (b) the photoelectron yield at each pump-probe delay slice is normalized individually in order to better follow the TKE at pump-probe delay larger than 100 fs. The self-normalization spectra for CH_2I^+ and CH_2Br^+ are shown in panels (c) and (d), respectively. From panel (c), the single peak/band in CH_2I^+ shifts from about 0.1 eV to above 0.2 eV, whereas the peak in CH_2Br^+ splits into two peaks, which shift to about 0.25 eV and 0.6 eV at long delays, as reflected in panel (d).

A common feature in the fragment ion spectra shown in Fig. 5.19 is the increasing TKE of the peaks for both CH_2I^+ and CH_2Br^+. This is consistent with the conversion of electronic potential energy into nuclear kinetic energy as the wave packet launched by the pump pulse makes its way out on the dissociative potential. However, there is a significant difference between the two cases in that we observe two peaks in the CH_2Br^+ spectrum at he delays beyond 100 fs, whereas there is only one in the CH_2I^+ spectrum. In order to interpret the dynamics behind, it is useful to go back to Fig. 5.11 for the calculated electronic structure and state population and review the dynamics we have learned. With the absorption of a deep UV photon (4.75 eV), both molecules are excited to a cluster of excited states including both bound (cyan) and dissociative states (blue and red). Together with what we have learned from the TRPES and UED measurements, CH_2IBr undergoes direct dissociation, with dissociation taking place on two groups of states that asymptotically converge to CH_2Br^+/I and CH_2Br^+/I^*, with I^* corresponding to the spin-orbit excited state of the iodine atom. In contrast, the excitation in CH_2I_2 is mainly to bound states, and internal conversion takes place before dissociation along states that asymptotically converge to CH_2I^+/I and CH_2I^+/I^*. As I will discuss in the later sections, it is the internal conversion from initially bound states to the dissociative states that drives the differences in the fragment ion spectrum for the two molecules. However, it is straightforward to correlate the observed discrepancy between the CH_2I_2 and CH_2IBr with the profound internal conversion dynamics in

CH_2I_2, but not in CH_2IBr.

5.10 Comparing measured TRPIS with calculated fragment kinetic energy

According to Fig. 5.11, one might expect that there are two peaks in the fragment ion spectra for both molecules, since both molecules have two groups of dissociative states that asymptotically approach two different energies, separated by about more than 1 eV. For CH_2I_2, the population is dominated by the higher group of dissociative states, with a ratio of 3.75 for the populations of the higher and lower asymptotic states after 150 fs. In contrast, for CH_2IBr both states are roughly equally populated. A natural question is that whether the difference in the measurements of the two systems aforementioned is due to the different populations between the two groups of states for CH_2I_2 and CH_2IBr, respectively, or whether there is another reason.

One way to test the hypothesis is to direct calculated kinetic energy distribution of the photo-fragment, and compare with the measured ones. Ideally, the kinetic energies should be obtained from trajectories propagated in the cationic states after gaining velocity on the neutral excited-state potentials. However, such a treatment is extremely costly and I thus make use of an approximate approach instead, in which I estimated the velocities based only on the neutral excited-state trajectories. Followed by Equ. 2.26, the TKE of CH_2I/CH_2Br and I were calculated at each time step of each individual trajectories The rotational kinetic energy (RKE) of CH_2I for CH_2I_2 and CH_2Br for CH_2IBr are also calculated. However, the experiment is not able to measure the RKE and I did not include the discussion of the RKE and related analysis. In Fig. 5.20, I showed the calculated TKE of CH_2I and CH_2Br, compared with the measured TKE of CH_2I^+ and CH_2Br^+. As I discussed above, there is a significant potential energy difference between the lower and higher asymptotic groups of dissociative states ($\sim$1 eV), so one expects that higher energy states lead to lower kinetic energy while lower energy states results in higher kinetic energy. In order to check this point, I averaged the calculated TKE from each trajectory by considering the excited state index at each delay step. Figure 5.20 panels (a) and (b) show the simulated TKE of CH_2I and CH_2Br radicals as a function of time by averaging the trajectories from the lower and higher asymptotic spin-orbit coupling state.

The averaged TKE distribution from trajectories correlated to the lower and higher asymptotic are plotted in thick red and blue lines, respectively. The simulations were convolved with a 80 fs FWHM Gaussian function in order to take into account the IRF associated with the measurements. The pink and cyan shaded areas indicate the standard deviation (STD) amongst the ensemble of trajectories, and serves as a measure of the statistical uncertainty associated with the calculations.

As shown in panel (a) which is the case of CH_2I_2, the TKE of CH_2I from both groups increases as a function of time, and the two groups end up with a roughly equal amount of energy by 300 fs. In panel (b), I plot the simulated TKE for CH_2Br averaged for both lower and higher asymptotic states as a function of time. In contrast with the CH_2I results, the TKE of the two groups separate from each other, with the trajectories that come out on the lower asymptotic state having a higher amount of kinetic energy and trajectories that come out on the higher asymptotic state having lower kinetic energies as expected. Again in panel (a), the standard deviations are larger than the difference between the averaged TKEs for the two groups of trajectories. In contrast, the difference between the two groups is larger than the standard deviation in the case of CH_2IBr, leading to a clear separation. These observations are in agreement with the experimental measurements as shown in Fig. 5.19 panels (c) and (d). For CH_2I_2, both the calculated and measured TKE only show one peak, which increases in energy from about 0.1 eV to about 0.2 eV in the first few hundred fs. Comparing panels (b) and (d), one also sees that there is agreement between the measurement and calculations for CH_2IBr in that the spectrum separates into two separate peaks, whose energy increases with time in the first few hundred fs. An additional feature in panels (c) and (d) of Fig. 5.19 is the oscillation of the peak energy as a function of time, especially after 300 fs. These oscillations correspond to the halogen-carbon stretching in the CH_2Br or CH_2I fragment upon the dissociation. However, this is not the main focus on this work.

Figures. 5.11 and 5.20 illustrate several important points. The simulations capture the main features in the photoion spectra for both CH_2I_2 and CH_2IBr, and measurement and calculation agree on the time scales for the changes in the spectra. However, I note that the calculations in panel (b) of Fig. 5.20 for CH_2IBr do not perfectly agree with the measurements as shown in the panel (d). In the calculations, the TKE for both groups of trajectories are rising faster during the early times (< 150 fs) than that in the measurements. This is also true for the case of CH_2I_2 as shown in panels

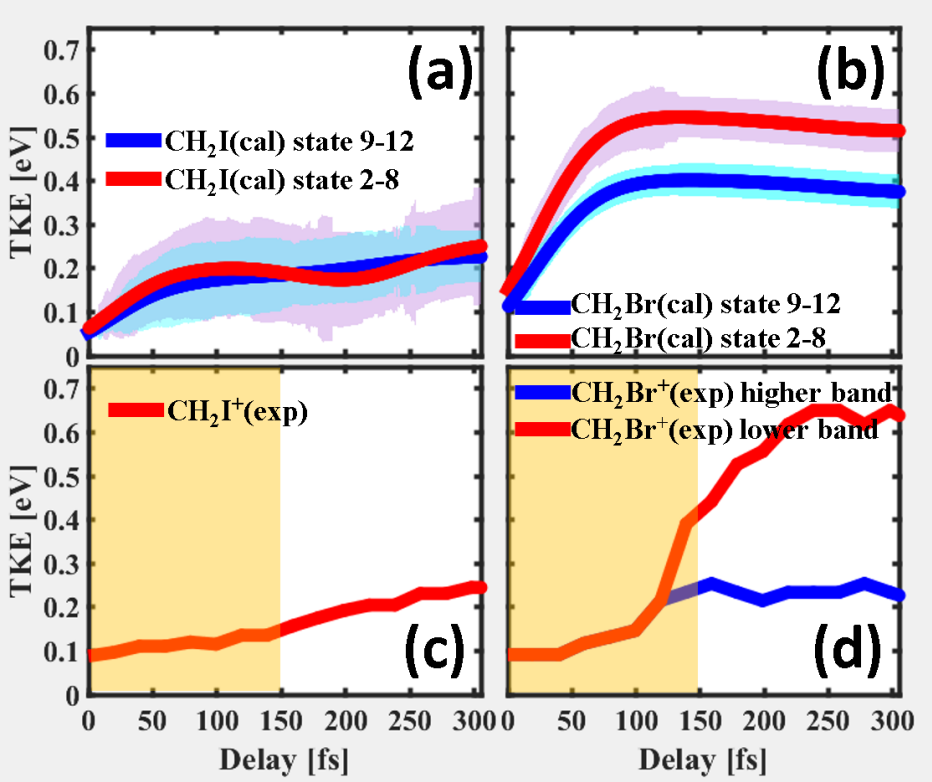

Figure 5.20: **Time-resolved translational kinetic energies from calculations and measurements for CH_2I_2 and CH_2IBr.** Panels **(a)** and **(b)**, show the calculated TKE for CH_2I and CH_2Br radicals as function of time from CH_2I_2 and CH_2IBr trajectories, respectively. Panels **(c)** and **(d)** show the measured TKE for CH_2I^+ and CH_2Br^+ respectively as a function of pump-probe delay, taken from the location of the peaks from panels **(c)** and **(d)** in Fig. 5.19. The calculated results have been convolved with a 80 fs (FWHM) Gaussian function to account for the instrument response function. In panels (c) and (d), the orange shading indicates the early pump-probe delay region affected by the changes to the TKE, which is due to the evolution in the cationic potential and the experimental signal deconvolution.

(a) and (c). This discrepancy is partially due to the fact that, upon ionization, the fragments have to climb out of the bound state well in the cation at early pump-probe delays - see panels (a) and (c) of Fig. 5.11. Thus, the experimentally measured TKE does not increase substantially until the wave packet on the neutral state moves out to distances at which the cationic potential becomes flat - around 3.5 Å. This results in a decrease of the kinetic energy of the fragment ions gain from neutral states. This is not taken into account in the calculations, and thus, one expects the calculation to show the TKE rising faster than in the measurements, as we observe in Fig. 5.20. A quickly estimation of how evolution in the cationic potential affects the TKE for different pump-probe delays is provide in Appendix C.3.2.

I also note that the TKE of the two peaks in the CH_2Br spectrum are further apart than those from the calculation, and this is due to the fact that the energy difference of the averaged cationic spin-orbit channels increases. The lower asymptotic states (states 2-8, red curves in panel (b) of Fig. 5.11) in the neutral are mostly Koopmans' or Dyson correlated with the lower states of the cation. Accordingly, the higher asymptotic states (states 9-12, blue curves) are mostly correlated with the higher states in the cation. Considering the energy difference between the higher branch of the lower cationic channel and the higher cationic channel (but also the energy difference of the average channels), one can see that this energy difference increases. This effect is not considered in the calculations and leads to the peak separations shown in Fig. 5.20 being underestimated in comparison with experiment. Another contribution to the discrepancy between experiment and theory in Fig. 5.20 is imperfections in the subtraction of the VUV pump UV probe contribution to the yield near zero time delay. As the VUV absorption cross section is significantly larger than the UV absorption cross section, there are many ions generated by first VUV absorption followed by UV ionization in the region where there is some overlap between pump and probe pulses. This contribution is subtracted from our data, but leads to some systematic error in the measured TKE for delays less than 100 fs. A detailed discussion of the subtraction is provided in Appendix C.3.1

Before turning to detailed analysis of what drives the differences in the dynamics for the two molecules, I compare the calculated and measured branching ratio, $\Phi^* = [CH_2Br/I^*]/([CH_2Br/I^*] + [CH_2Br/I])$ for the two spin orbit channels ($[CH_2Br/I^*]$ and $[CH_2Br/I]$) in CH_2IBr. In the CH_2IBr calculation, the ratio is evaluated from the number of trajectories that live on the lower and higher asymptotic states. The calculated ratio is about

0.47, while the measured ratio is about 0.48, demonstrating excellent agreement. Earlier measurements which used multiphoton ionization as a probe found a ratio of about 0.41, which is in reasonable agreement with our measurements and calculations [198]. In the case of CH_2I_2, while the measurements could not resolve the two kinetic energies peaks, the branching ratio can be extracted from the calculations by checking the time-dependent state populations. As shown in Fig. 5.11 panel (c), the branching ratio, $\Phi^* = [CH_2I/I^*]/([CH_2I/I^*] + [CH_2I/I])$, is about 0.78 after 150 fs when the populations are stable. However, I note that the branching ratio is likely overestimated due to trajectories crashing at slightly different rates on the different groups of states.

5.11 Quantitative characterization of the non-adiabatic dynamics of CH_2I_2 and CH_2IBr

In order to understand what drives the difference between the two molecules in more detail, I examined the hopping statistics from the TSH calculations. The trajectories include hundreds of hops between different electronic states, and I sorted these hops into two different types based on their initial and final state indices. As shown in Fig. 5.11 panels (a) and (b), there are 3 different groups of excited states for both CH_2I_2 and CH_2IBr, including dissociative ones which asymptotically approach the spin-orbit ground and excited states of I (I/I*) for large C-I distances, as well as a group of bound states. It is the hops between different groups of states that result in significant changes of energy or electronic state character, whereas the hops within each group of states do not involve such substantial differences. Thus the hops across groups play the essential role on the determination of the undergoing dynamics. Here in Fig. 5.21, I show the hopping statistics between groups for both CH_2I_2 and CH_2IBr. The hops were binned into 20 fs windows, and the number of hops were divided by the total number of trajectories in order to obtain the hopping rate per trajectory.

Figure 5.21 panels (a) and (b) show the hopping rate for CH_2I_2 and CH_2IBr as a function of time. For CH_2I_2, the hopping rate stays relatively high out to about 100 fs, whereas for CH_2IBr, the hops are concentrated in the first 20 fs. The extended hopping in CH_2I_2 leads to the overlap of the TKE for fragments dissociating on the two spin-orbit asymptotes for I

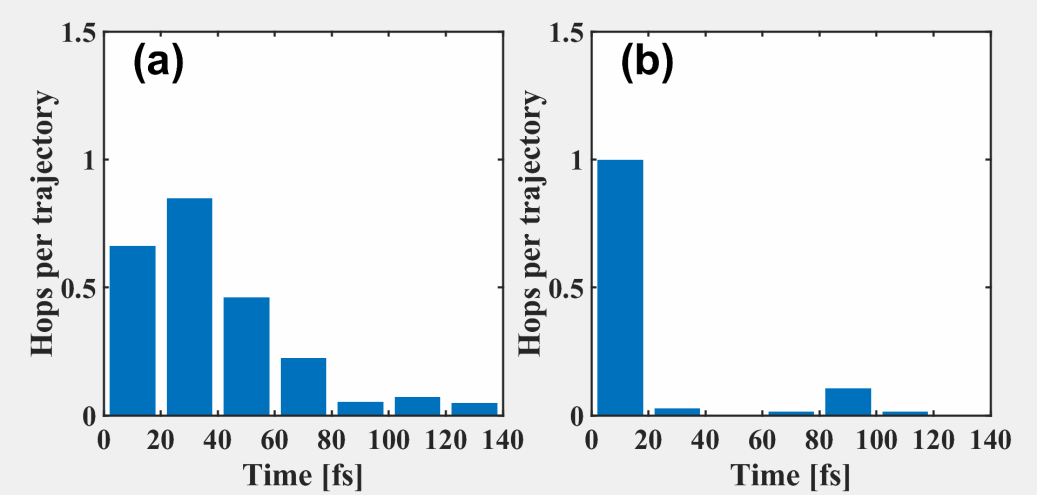

Figure 5.21: **Hopping rates for CH_2I_2 and CH_2IBr from the TSH calculation.** In this figure, panel (a) shows the hopping rate for CH_2I_2, whereas panel (b) illustrates the hopping rate for CH_2IBr. Only the hops between different groups of states are included, whereas the hops between states in the same group are excluded. The number of hops is divided by the number of trajectories in each 20 fs time window in order to obtain the hops per trajectory as a function a time.

(I and I*), since molecules do not dissociate on one group of states or the other, but rather on a mixture of the two groups. In contrast, for CH_2IBr, the asymptotic state on which the molecule dissociates is determined early in the dissociation dynamics, leading to a well defined separation in the TKE for the two I/I* asymptotes. Thus it is clear that it is the different non-adiabatic dynamics during dissociation which lead to the differences in the measured TKE for the two different molecules.

5.12 Conclusion

In conclusion, I have compared the information available from two experimental (spectroscopic vs structural) approaches with three different experiments (TRPES, UED, and TRPIS).

The TRPES experiment was performed and together with the trajectory surface hopping calculation had yielded very much insight into the internal dynamics of both CH_2I_2 and CH_2IBr after deep UV excitation around 4.65 eV. Especially the two molecules constructed a complementary comparison. It allows one to investigate the different role of the non-adiabatic effect which is induced from the electronic potentials and/or the structure difference from the two molecular systems. However, one is not able to claim that the dynamics were fully viewed from the TRPES measurement, such that one could make a making a "molecular movie". For example, while the TRPES measurements illuminate the internal conversion and dissociation of the molecule and suggest that the dissociation dynamics are non-local (multiple wave packets), the directly viewing of the nuclear degrees of freedom is missing. Apparently, an interesting point that needs further study is the dynamics related to the different asymptotic dissociative states of both systems as shown in Fig. 5.11. Since the lack of direct sensitivity from the photoelectron, one can ask whether there are experimental signatures indicated from the photoions if the wave packet undergoes the lower and higher asymptotes by gaining different amount of kinetic energy? These questions can be answered from a TRPIS measruement, such that the electronic energy conversion into the nuclear degrees of freedom can be directly monitored by examining the kinetic energy of the photo-fragment ions. With the sensitivity to the different asymptotes of the dissociative states, one can even easily obtained the ratio of the population by looking at the quantum yields associated with different kinetic energies of the photofragment ions.

TRPES and TPRIS provide energetic probes, there is still information missing. A simple question can be raised, such as how is the structural change as a function of time? One can claim that the spectroscopic to structural inversion may be also achieved, but high-level theoretical calculations is needed. And from the CH_2I_2, we clearly see that neither TRPES nor TRPIS provides any information about the rotational dynamics and the complicated structural changes accompanying dissociation. This is of broad significance, as chemical reactivity and molecular function depend not only on the distance between two different functional groups of the molecule, but also their relative orientation (as in e.g. protein folding). These can be accomplished from a diffraction measurement, such as what has been done with the relativistic UED measurement. On the other hand, the relativistic UED measurements do not provide direct information on the internal conversion (non-adiabatic coupling between electronic states) and energy conversion of the molecule as it dissociates. By combining the two approaches, one can find direct experimental evidence for non-adiabatic coupled nuclear-electronic dynamics, non-local evolution of the nuclear wave function (different groups of trajectories that have very different structural and energetic evolution as a function of time) and rotational motion of the molecule during dissociation, which highlights the three dimensional information available from diffractive imaging measurements.

Experimentally, TRPES and TRPIS measurements can rather easily be carried out in the limit of one photon absorption from the pump pulse, with built in verification via the kinetic energy of the photoelectrons and/or photoions , while UED requires higher pump pulse fluences and thus tends to contain contributions from dynamics driven by multiphoton absorption from the pump pulse, which need to be considered in the analysis. While the time resolution of the two approaches is similar, it is easier to characterize the IRF for TRPES/TRPIS via cooperative non-resonant 1+1' photon absorption. The rate at which the UED observable changes depends primarily on how fast the structure changes with time ($\frac{d\mathbf{R_i}}{dt}$, where $\mathbf{R_i}$ represents the position of the i^{th} nucleus), whereas the TRPES/TRPIS observable depends on both the rate of structural change with time as well as how rapidly the energy changes/transfer with structure - i.e. $\frac{d\mathbf{R_i}}{dt}$ and $\frac{dV(\mathbf{R_i})}{dR_i}$. This leads to the TRPES/TRPIS observable changing more rapidly than UED for some time delays (e.g. < 100 fs) and less rapidly than UED for others e.g. (> 100 fs). Generally TRPES and TRPIS are rather easy to carried out and can rely on a tabletop ultrafast laser system. The relativistic UED measurement

is more complex in the experimental apparatus such that experiments may be only preformed in national lab type of facilities.

Chapter 6

General conclusion and prospects

6.1 General conclusion

In this dissertation, I have studied excited state dynamics of several molecular systems with multiple ultrafast time-resolved experimental techniques. Especially, the combination of spectroscopic and structural probes offered a unprecedented view of how a photo-excited molecule breaks apart, illuminating the subtle interplay between electronic and nuclear dynamics underlying many fundamental processes in nature.

In Chap. 3 and Chap. 4, two important organic chromophore molecules, *cis,cis*-1,3-cyclooctadiene (cc-COD) and uracil, were experimental studied, focusing on their internal conversion and isomerization from electronic excited state back to the ground state *via* conical intersections (CIs) after exposure to UV light. TRPES measurements were carried out with UV/VUV pump/probe scheme for both molecular systems. TRPES method is sensitive to coupled electronic and nuclear dynamics, providing with an energetic probe, and may be advantageous over the structural measurement of UED method in these systems. One of the reasons behind is simply due to the smaller geometric changes in the isomerization and internal conversion, compared with dissociation process. With excessive energy obtained from the optical pump pulse (∼5 eV), the wave packet falls into rapid motions away from the Franck-Condon (FC) region to the CIs, though the structural changes may be not obvious, it often induces larger changes in the potential

energies, where TRPES can showcase higher sensitivities. It is very much advantageous by using laser pulses in the VUV region (5^{th} harmonic of a Ti:sapphire laser) as a probe of molecular dynamics because the photon energy can be chosen to lie just below the ionization potential of the ground state (typically between 8-12 eV), but above the ionization potential for the majority of excited states (typically less than 8 eV). This enables one to probe the neutral excited state dynamics over a broad range of energies without windowing effects (probe photon energy insufficient to ionize the evolving excited state wave packet), while remaining blind to the ground state.

In Chap. 3, I performed UV pump VUV probe measurements of cc-COD after an excitation to the first bright state S_1, using TRPES. The measurements reflected two main features, a lower kinetic energy band with constant kinetic energy, as well as a higher kinetic energy band with energy decreasing as function of time. The measurements were interpreted with the aid of electronic structure and trajectory surface hopping (TSH) dynamics calculations. The two bands were interpreted as the ionization from the neutral excited to different states in the cation according to the Koopmann's correlation. Three types of CIs were located and the potential energies of the several lowest neutral and cationic states at several points interpolated between the FC region and the three different CIs. As the the wave packet evolves along the potential, two cationic states, D_0 and D_3 are energetic allowed. Since D_3 crosses a number of ionic states en route to the third CI, it is of mixed character and parallel with the S_1 in the neutral, one would expect a constant photoelectron kinetic energy which corresponds to the lower energy band in the TRPES. Whereas, the potential energy of the ground state of cation, D_0, increases from the FC to the CIs, thus the high energy peak should shift to lower energies as the wave packet moves away from the FC point. The question that has not been answered is that the calculations predict a slower decay of the TRPES than measured by the experiment, in which future work aims to address this discrepancy.

In Chap. 3, theoretical inputs were mainly used to interpret the measurement results. Whereas, in Chap. 4, I demonstrated that quantitative comparison between theoretical calculations of excited state dynamics and pump-probe experiments could provide a tool for benchmarking the electronic structure theory, particularly in cases where dynamical correlation plays a crucial role in the non-adiabatic dynamics. Uracil was chosen as a testbed, focusing on the much debated population trapping of the first bright state S_2. The electronic structure were calculated at three different levels

of theory, CASSCF, MRCIS, and XMS-CASPT2. The calculations suggest that there is no trapping of population on the S_2 state at higher-level multi-reference methods which are MRCIS and XMS-CASPT2, whereas there is substantial trapping of population on the S_2 state at the CASSCF level, as is suggested by the size of the barrier on S_2 at different levels of theory (MRCIS$\sim$0.03 eV, and XMS-CASPT2$<$0.02 eV, CASSCF$\sim$0.16 eV). In order to test the accuracy of the theory by directly viewing the measured and calculated observables, TSH calculations at three different levels of theory were carried out. These dynamic calculation were then used to simulate the TRPES using the Dyson norms. On the other hand, an experimental TR-PES measurement (UV pump and VUV probe) is constructed in order to directly compare with the calculated TPRES signal. The comparison evidenced that MRCIS and XMS-CASPT2 provide a better description of the excited state dynamics than CASSCF, which greatly overestimates the decay time from S_2. However, distinguishing between MRCIS and XMS-CASPT2 is harder because of the very short times involved which is beyond the experimental temporal resolution, but there is some evidence that XMS-CASPT2 compares somewhat better to the experiment.

In Chap. 3 and Chap. 4, the coupled electronic and nuclear dynamics were studied from a spectroscopic view with TRPES method. In Chap. 5, I turned to explore combined spectroscopic and structural probes on the excited state dynamics. The molecular systems, CH_2I_2 and CH_2IBr, were chosen with care in this study. CH_2I_2 was the main object, whereas the CH_2IBr was serving as a complementary contrast. The two systems share similarities from both structure and atomic species, except one of the two iodine atoms in CH_2I_2 is substituted by bromine in the case of CH_2IBr. The study was designed by using the same excitation process, i.e., an ultrashort pulse in deep UV regime ($\sim$ 260 nm). The time-resolved photoelectron and photoion measurements on both CH_2I_2 and CH_2IBr mapped out a clear energy flow along the wave packet evolution, in which the electronic potential energy obtained from the initial optical excitation was transferred into the nuclear degrees of freedom.

The features in the TRPES signals showcased that the non-adiabatic dynamics were essential in determination of the following dynamics between the two systems, highlighted by whether or not presenting a lower kinetic energy tail of the photoelectron yield in longer delays ($\sim$150 fs). In CH_2I_2, the photoelectron started from a strong signal around time-zero correspondent to ionization to a manifold of lower lying states in the cation, followed with the lower energy tail in longer delays. In CH_2IBr, two peaks of photoelectron

yields showcased around time-zero arising from the ionization to two lower cationic states, but without the presence of a lower energy tail at longer delays. The lower kinetic feature in CH_2I_2 was interpreted by the presence of the higher energy bound states (besides the dissociative states), which can be reached by the pump UV at the FC region, such that in the longer delays the probe VUV photon energy was still high enough and ionization was possible as some of the wave packet population in the bound state. Whereas, the bound states in CH_2IBr were not able to be reached from the UV, and only dissociative states were mainly involved. In this case, ionization was not allowed as the wave packet only evolved on the dissociative ones, thus, without a lower kinetic energy tail. With a detailed analysis of the calculated trajectories, a "direct" and an "indirect" dissociation pathways were proposed for the case of CH_2I_2, and only "direct" dissociation was suggested in CH_2IBr.

The TRPES measurements reflected that CH_2I_2 dynamics was more complicated. A further analysis was carried out in order to estimate the non-adiabatic effect in CH_2I_2, by specifically turning off the non-adiabatic transition, the "hops" in each trajectories. The lower energy tail in the simulated TRPES was completely missing as shown in Fig. 5.12, and the calculated TRPES matched with the measurement only when non-adiabatic transitions were included. By grouping the trajectories into different sub-groups according to the different geometric behaviours (direct dissociation vs symmetric stretch), the TRPES indicated clear two pathways, and structural measurement appeared necessary. The TRPES highlighted non-adiabatic dynamics in CH_2I_2 and the comparison from CH_2IBr helped make this clear.

The structural measurements from the relativistic ultrafast electron diffraction (UED) experiment of CH_2I_2 yielded rich information contents regarding multiple features of the measured pair distribution function difference (ΔPDF). The direct and indirect dissociation manners were revealed and differentiated at different atomic distances in the ΔPDF, as shown in Fig. 5.14. The lost (negative value) at the original I-I distance (3.60 Å) and the increase (positive value) beyond this distance in a slower time-scale ($\sim$300 fs) highlighted the indirect dissociation dynamics, whereas, the direct dissociation behaviour was captured by a fast time-scale ($\sim$185 fs) periodic oscillation below the initial C-I_1/I_2 bond distance (<2.1 Å) regarding to the quickly rotation motion of CH_2 after dissociation. The observation of the rotation is an unique feature and may be only accessible from diffraction measurements. On the other hand, some subtle features observed from the calcula-

tions, were missing, such as the C-I stretching motions, which may be limited by the current temporal resolution due to the electron bunch length and a shorter electron bunch is necessary. Recently, two different methods of electron bunch compression have been reported from Qi *et al*, and Snively *et al*, respectively. They applied either an ultrashort pulse in THz regime or used a double-bend-achromat to compress the bunch and they reported the shortest pules duration as sub-40 fs in root-min-square (RMS) [206] and sub-30 fs FWHM [207].

The TRPES and UED measurement gave profound electronic energetic ans structural signatures of the non-local ("direct" versus "indirect" dissociation) dynamics manner involved with the competition between the internal conversion and dissociation, but neither of them gives direct probing sensitivity into the nuclear degrees of freedom. For instance, a characteristic feature in the CH_2I_2 and CH_2IBr is the two sets of spin-orbit coupling effect induced asymptotic dissociative states. With different internal energies, wave packet(s) undergoing the higher and lower asymptotes gain(s) lower and higher nuclear kinetic energies, respectively. However, these information contents are missing in either TRPES or UED measurements. The variant of TRPES, TRPIS, provided valuable information contents into the nuclear degrees of freedom which were not directly accessible from the TRPES measurements. By directly measuring the time-dependent translational kinetic energy (TKE) of photo-fragment ions (CH_2I^+ and $CH2Br^+$ for CH_2I_2 and CH_2IBr), I resolved two bands of CH_2Br^+ with different amount of TKE as expected, whereas, only one single TKE band of CH_2I^+ reflected in the measurement. With the aid of the trajectory TSH calculation, the unexpected behaviours of CH_2I_2 were interpreted by the much higher and longer lasting non-adiabatic transitions across different dissociative asymptotes as well as the bound states, which was not reflected from the calculations for CH_2IBr. It indicated that the competition between the internal conversion and dissociation will determine the ensuing dynamics.

In a more fundamental perspective, compared with spectroscopic method, diffraction techniques are so called the "passive" probes such that the measurements do not reply on the presence of a final state(s), such as the cationic state(s) in the ionization spectroscopy. Diffraction probes take the advantage that the system only involves the state(s) with the initial excitation , whereas the measurements is rather accomplished by examining an external medium with the amount of momentum transfer, such as elastic or inelastic scattering of electrons. This makes the interpretation of the diffraction mea-

surement independent from a final state(s), in which no further approximation is needed. On the other hand, spectroscopies can be named as "active" probing, such that the system is interrogated beyond the initial excitation process and the measurement observables is a correlation between the initial and the final state(s), such as the charged particles generated from an ionization process in the state(s) of the cation. Thus extra care may needed in the interpretation of the measurements. However, with the presence of a final state(s), spectroscopies provide high sensitivities which rises from the correlation/selectivity between the initial and final states, such as Koopmanns' correlations. The measurement may be very much highlighted and amplified at specific electronic and/or nuclear coordinates.

6.2 Prospects: spectroscopic and structural probing towards to X-ray regime

To conclude this dissertation, I have conducted experiments and demonstrated both spectroscopic and structural probes on the coupled electronic and nuclear dynamics in the molecular excited states initiated from an ultrashort UV pulse. TRPES and/or TRPIS were used as spectroscopic probe, and relativistic UED was applied as the structural probe. All of the experimental results were interpreted by quantum dynamics calculations, with directly comparison between the measured and calculated observables.

One of the possible directions beyond the current energetic probing is to expend the ionization from valence electrons into more deeply bounded inner shell electrons by photons in soft X-ray regime (50 to 1000 eV). Valence electrons often directly participate in chemical bonds and they can be delocalized across the whole molecule. Time-resolved valence ionization spectroscopic methods, such as TRPES, in principle allow for following coupled electronic and nuclear dynamics on their natural time scale, but they lack direct sensitivity to changes in specific nuclear distances due to the delocalized character of valence orbitals [208, 50]. Compared with an electron in the valence orbitals, one of the major advantages of using soft X-rays being as the probe ionizing an inner-shell electron is *element-and-cite-specificity*, which is due to the fact that the ionization energies of the deeply bound core-shell electron from different species of atoms usually lie several hundreds electron volts (eVs) apart [209]. Although the inner-shell electrons are more local-

ized to the atomic centers, the changes of bonding environment (covalent bonds) with valence electrons will affect the bonding energy of the electron in the inner-shell orbital [210]. A change in bonding environment, therefore, lead to a site-specific change in the time-resolved photoelectron spectrum. Thus probing the inner-shell electrons will allow for sensitivity to a specific site/atom/bond in a molecule, which is not allowed in valence ionization spectroscopy. For example, the dissociation of a C-I bond in CH_2I_2 and CH_2IBr is very much likely induced a transient changing of binding energy from a inner shell electron at either carbon or iodine inner-shell electrons. Time-resolved X-ray photoelectron spectroscopy (TR-XPS) have been proposed and several remarkable works have been reported for a similar molecule, CH_3I, after UV excitation [211, 212, 213, 214]. A recent theoretical work also reported profound signatures of XPS at carbon, nitrogen, and oxygen atoms in different geometries of lower lying molecular excited states (S_2 and S_1) of uracil ($C_4H_4N_2O_2$) [215]. One thing to note is that proper interpretation of the experimental results typically requires the modeling of the core-shell spectrum as a function of time in the relevant reaction coordinates.

For the structural probing, besides utilizing electron scattering, the diffraction measurements can be performed with an ultrashort hard X-ray (8.3 KeV, 1.5 Å, LCLS at SLAC) pulse as well [216, 217, 218, 219]. In comparing electrons to X-rays, electrons suffer from Coulomb force that tends to stretch an electron pulse in time. X-ray photons do not repel each other, and are easier to bunch together in a short pulse. Thus the time-resolution from a time-resolved X-ray diffraction measurement can be achieved in the sub-50 fs [220]. X-ray travels with the same speed of light, therefore the velocity mismatch between the X-ray and the optical pump pulse is forbidden. Therefore, a longer integration length between the X-ray pulse and the sample is possible, leading to more scattering signals. Electron scattering contains an uniform background which is mostly from an incoherent sum of the scattering from different molecules, due to a smaller transverse coherence width than the intermolecular spacing. A typical hard X-ray beam usually provides much larger transverse coherence width (usually the whole beam size) than that of an electron beam, which makes a significant point in gas phase experiment [220].

Given the fact that several X-ray free electron laser (FELs) are already in running [221, 222], plus several more are under construction [223, 224], it appears reasonable and promising to propose that the continued research of the current combined spectroscopy and structural probes will be in both

time-resolved soft X-ray core-level ionization spectroscopy and hard X-ray diffraction experiments.

Appendix A

Supporting information for Chap. 3

In this appendix, I provide some details of the theoretical calculations regarding the trajectory surface hopping calculation of *cis,cis*-1,3-cyclooctadiene (cc-COD) that are related to the experimental measurement presented in Chap. 3. The electronic structures as well as the dynamics calculations were carried out by Pratip Chakraborty and Spiridoula Matsika, published in Ref. [119].

A.1 Computational methods

Energies and Dyson norms were calculated along pathways leading to conical intersections between S_1 and S_0. The structures of conical intersections are obtained from our previous theoretical study on cc-COD. [119] Using three important conical intersection geometries (as described below) we constructed linear interpolations in internal coordinates (LIIC) from the Franck-Condon (FC) geometry to the CIs using the extended multi-state complete active space with second order perturbation (XMS-CASPT2) method [225, 226, 227] and the cc-pVDZ basis set. [228] For neutral states, a (6,6) active space was used whilst a (5,6) active space was used for cationic states. The XMS-CASPT2 calculations were performed using the corresponding CASSCF [165] reference wavefunction with an imaginary shift of 0.2 au and the single-state single-reference (SS-SR) [229] contraction scheme. The energies of three states for the neutral and five states for the cation were calculated. The XMS-

CASPT2 calculations were performed using the Bagel package. [230, 231]

The ground state of all conformers of cc-COD was optimized at the DFT level using the B3LYP functional and 6-31G(d) basis set using the Gaussian09 package. The frequencies and normal modes were calculated at the same level of theory. Sampling was performed using a harmonic oscillator Wigner distribution in Newton-X [232, 233] to generate initial conditions (nuclear coordinates and velocities) based on the optimized geometry and the normal modes from the previous calculation. 200 initial conditions were generated for each of the conformers of cc-COD at 298 K. Vertical excitation energies and oscillator strengths were calculated for all initial conditions at the CASSCF level using cc-pVDZ basis set. An active space of 4 electrons in 3 orbitals was employed and three states were averaged. Excitation energies and oscillator strengths of the initial conditions were used to calculate the absorption cross section and simulate the first absorption band of cc-COD. A Lorentzian line shape, temperature of 298 K and a phenomenological broadening value of 0.2 eV were employed.

Non-adiabatic excited state dynamics simulations were performed using trajectory surface hopping (TSH) in Newton-X on CASSCF(4,3)/cc-pVDZ full-dimensional potential energy surfaces (Ref [234, 235, 236, 237, 238]) (PES) calculated on-the-fly using the Columbus 7.0 package. The trajectories were propagated starting from the S_1 state which is the brighter of the two states (S_1 and S_2) in the Franck-Condon (FC) region with the active space chosen for this study. The fewest switches surface hopping (FSSH) [53] algorithm was employed to take into account non-adiabatic coupling between the S_2, S_1, and S_0 states. The velocity verlet algorithm was used to integrate Newton's equations of motion with a time step of 0.5 fs. The semiclassical Schrödinger equation was integrated using the fifth-order Butcher's algorithm with a time step of 0.005 fs. The simulations for both conformers were performed for 500 fs using XSEDE's computational resources. [239]. More details of the electronic structure calculation can be found in Ref. [119].

Figure A.1 shows the population of the three states for cc-COD for 500 fs from the TSH calculation. The population plot is a weighted average of the results from the two conformers for all valid trajectories. An important problem in TSH using multireference methods is that sometimes (especially after hopping to the S_0 state) trajectories fail because the active space does not converge. This can happen if the proper anti-bonding orbitals are not present in the active space or if the molecule distorts significantly. This can engender a change in the orbitals in the active space leading to energy

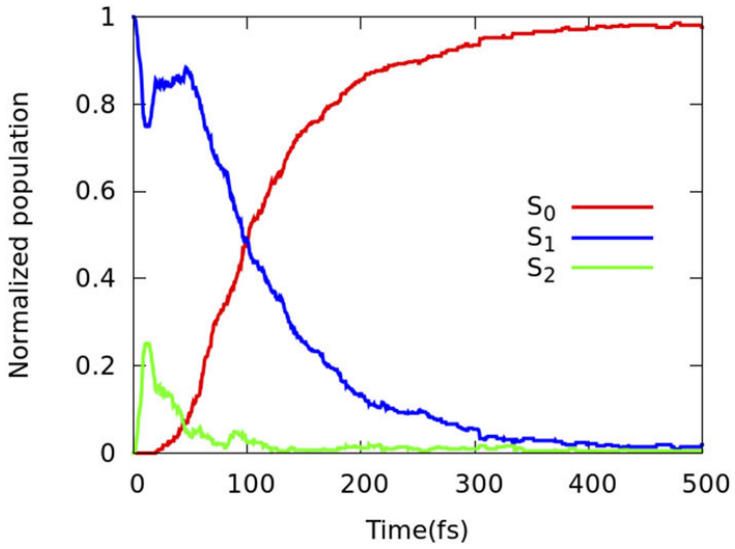

Figure A.1: **Calculated state population of cc-COD.** Calculated population dynamics of S_2, S_1 and S_0 states of cc-COD at the SA3-CASSCF(4,3)/cc-pVDZ level for a simulation window of 500 fs. The populations from the two conformers were combined using the weighted average of their Boltzmann probabilities.

conservation failure for a particular trajectory. Trajectories typically fail more often when an unbalanced active space is employed. Since we are working with a very flexible molecule and have employed a (4,3) active space which does not have an anti-bonding π^* orbital corresponding to its bonding π orbital, a portion of the trajectories failed before the end of the calculation (500 fs), mostly after reaching S_0. It is crucial to deal with this issue since the fraction of trajectories in each state depends sensitively on the fraction of trajectories that crash in each state. The default choice is that trajectories are excluded from the counting once they fail. However, in this case, when a significant portion of trajectories on the ground state fail, the excited state decay will appear to be slower than it is. Furthermore, after hopping to the S_0 state, the potential energy surfaces S_1 and S_0 typically separate in energy by a substantial amount, rendering the probability of a back-hop low. So, it is reasonable to expect that a failed trajectory will remain on S_0 and include it in the population count as such. This is the approach we used in Fig. A.1. A small percentage of trajectories also failed while propagating on S_1 (and S_2) due to failure of energy conservation. Since it is not possible to establish with confidence the fate of these trajectories, we exclude them from the population count after their failure.

A.2 Details of the theoretical calculations

A.2.1 Details of the Dyson Norm calculation

A more careful examination of the calculated Dyson norms shows information about the changes in the character of both the neutral and cationic states. The neutral S_1 state initially corresponds mainly to a HOMO $\rightarrow$ LUMO excitation, but the character becomes more mixed along the relaxation pathways. In particular, mixing with the character of S_2 can occur, which corresponds to two different configurations as illustrated in Fig. 3.5. Furthermore, the cationic states can become mixed and non-adiabatically change character along the pathways. A signature of these mixings is present in the third pathway involving the non-local CI. This is apparent when calculating the Dyson norms based only on the initial characters, as shown in Fig. 3.5. Using the simple correlations based on Koopmans' theorem shown in that figure, it is predicted that the HOMO $\rightarrow$ LUMO excitation will lead to either a hole in HOMO or a hole in LUMO. The Dyson norms to those states only are

shown in the bottom panels of Fig. A.2. Comparing the top panels of that figure, which include all Dyson norms, to the bottom panels which only include the two Koopman correlated Dyson norms, we see that the first two paths generally agree, but there is a larger discrepancy for the third path, especially in the second half. This is a signature of increased mixing. The additional features come from ionization to the D_2 state, which has a mixed character, including the configurations (HOMO-1)^1(HOMO)^1(LUMO)^1, (HOMO-1)^1(HOMO)^2 and (HOMO-1)^1(LUMO)^2. The first configuration can be produced by ionization from HOMO $\rightarrow$ LUMO (initial S_1 state) while the other two can be produced by ionizing from S_2. The non-local pathway distinguishes itself from the other two in more than one way. It has a stronger signature of mixing, as discussed above. This is similar to dynamics in butadiene, where the non-local CI is described as having more doubly excited character. [112] In addition, both the pathways as shown in Fig. 3.6, and the calculated photoelectron spectra, shown in Fig. 3.7 C, are somewhat different from the other pathways. A barrier on the S_1 surface predicts that this pathway may be less dominant in the dynamics, and the trajectory surface calculations in our theoretical study[119] indicate that indeed it only plays a role in about 16% of the trajectories.

A.2.2 Calculation at different level of theory

From Chap. 3, Fig. 3.3 shows some discrepancy between the calculation and the measurement, especially the dynamics time scales. One possibility that we explored is that the underlying electronic structure theory is not accurate enough. There are many points where the electronic structure theory can lead to slower dynamics. These include inaccurate energy gaps, slopes, and non-adiabatic couplings. In order to assess the influence of the level of theory on the decay dynamics, we compared our original CASSCF calculations with calculations at the XMS-CASPT2(4,4)/cc-pVDZ level to investigate if the level of theory is responsible for the discrepancy between the measured ionization yield and the calculated excited state population (and ionization yield). The same initial conditions (those used in the CASSCF TSH calculations) were used to simulate the absorption spectrum (with a Lorentzian line shape and a phenomenological broadening of 0.3 eV) and propagate the dynamics from the bright S_1 state. The XMS-CASPT2 absorption spectrum was plotted using an in-house code SArCASM, [240] whilst the dynamics was performed using Newton-X [241]. On-the-fly energies, gra-

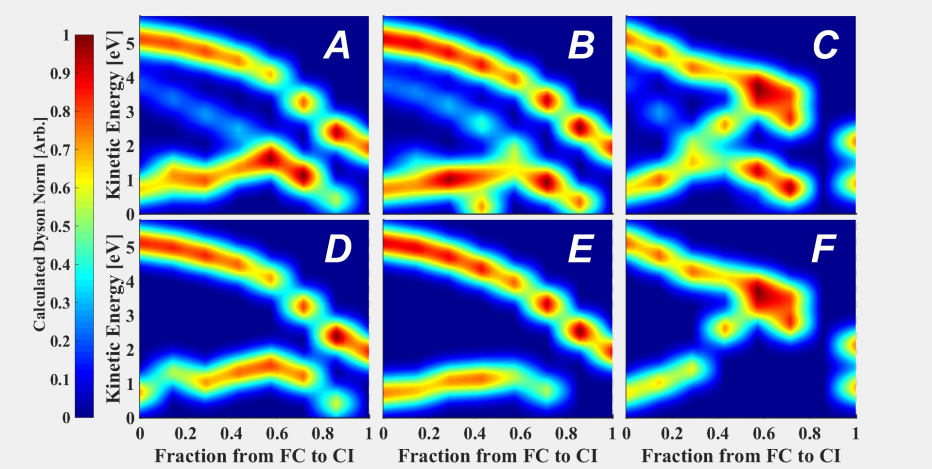

Figure A.2: **Calculated Dyson norm values related to different conical intersections.** Panels **A**, **B**, and **C** in the top row are as same as the 3 panels in Fig. 3.7, which are the Dyson norm values between S_1 and all the cationic states. Panels **D**, **E**, and **F** are the Dyson norm values only from S_1 to D_0 and D_{mix}. In the figure, panel **A** and panel **D**, panel **B** and panel **E**, panel **C** and panel **F** are corresponding to the same types of CIs, respectively.

dients and non-adiabatic couplings were generated using the Bagel package for XMS-CASPT2 level. [242, 243, 244]

Since both conformers showed similar dynamics and similar timescales at the CASSCF level, TSH at the XMS-CASPT2 level was performed for only the lowest energy conformer of cc-COD. The trajectories at the XMS-CASPT2 level were propagated starting from the S_1 state as it is the bright state in the FC region with the active space chosen for this study. [119] The fewest switches surface hopping (FSSH) [53] algorithm was employed to take into account non-adiabatic coupling (NAC) between the S_2, S_1, and S_0 states. Decoherence corrections were taken into account using the approach of non-linear decay of mixing by Granucci and Persico [245] with the recommended value of the empirical parameter, $\alpha = 0.1$ hartree. [246] The velocity verlet algorithm was used to integrate Newton's equations of motion with a time step of 0.5 fs. The semiclassical time-dependent Schrödinger equation was integrated using fifth-order Butcher's algorithm with a time step of 0.005 fs. The simulations was performed for 400 fs using XSEDE's computational resources. [239]

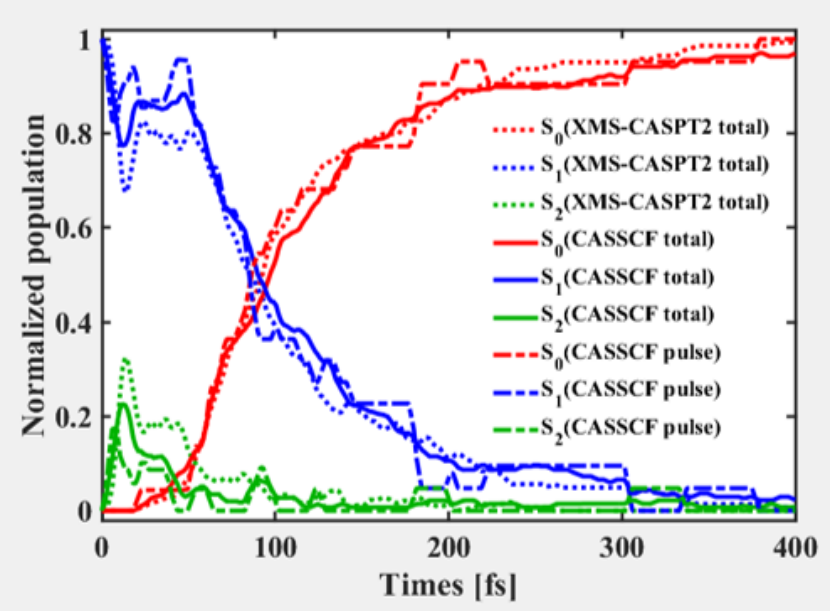

Figure A.3: **Neutral state populations estimated with different levels of theory.** Calculated populations of S_0, S_1, and S_2 with XMS-CASPT2 and CASSCF levels of theory, along with state populations from only those CASSCF trajectories that correspond to the pulse excitation energy.

Appendix B

Supporting information for Chap. 4

In this appendix, I provide some information of the theoretical method on the calculated photoelectron spectra of uracil as well as more details of the experimental data analysis. The electronic structure and the dynamics calculations were carried out by Pratip Chakraborty and Spridoula Matsika and some of the contents in this appendix can be found in Ref. [163].

B.1 Experimental details of uracil TRPES

The experiment was using exactly the same apparatus for the measurement of *cis,cis*-1,3-cyclooctadiene. The only difference is the sample delivery. It is no trivial to deliver uracil powers into the interaction chamber due to the low vapor pressure at room temperature. A solid sample manifold with heating ability was added to the vacuum chamber. The manifold consists of a sample oven and a molecular nozzle. The sample was heated up to 200 °C. A continuous molecular beam of the sample vapor was diffused into the vacuum chamber that houses the VMI spectrometer. A skimmer with a 1 mm slit is located in front of the nozzle, limiting the vertical angle of the molecular beam to avoid coating the sample onto the VMI plates. The intensity of the UV and VUV beam were lower enough such that ionization events were hardly observed from single UV or VUV beam. The instrument response function (IRF) and the real time-zero of the TRPES measurements were determined by performing probe-pump measurement with ethylene under

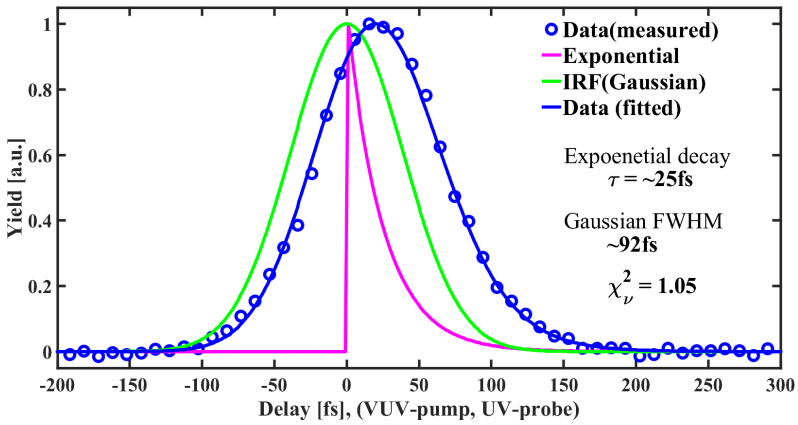

Figure B.1: **Ethylene pump-probe signal and the fit for instrument response function.** In this figure, the measured probe-pump ethylene time-of-flight ion ($C_2H_4^+$) signal is fitted by an exponential function convolved with a Gaussian, where the Gaussian function is treated as the IRF, and the real time-zero is determined by the peak of the exponential function.

the same running conditions as for uracil (intensity of UV and VUV beams and pump-probe delay setting). Fig. B.1 shows the ethylene signal and the fit. Pay attention that the delay axis is flipped compared with the uracil measurement and the fitting gives a Gaussian with ∼90 fs full-width-at-half-maximum (FWHM) which is treated as the IRF. The retrieved decay constant of ethylene (∼ 25 fs) is consistent with the value reported from literature. [78, 79, 13]. The peak position of the exponential decay is treated as the real time-zero and is used to correct the delay axis for the uracil measurements.

In each individual pump-probe scan, one photoelectron VMI image was accumulated by averaging 300 laser shots, and the pump-probe scans were repeated 150 times. For each pump-probe scan, a separate VMI image was recorded for delay of -1.5 ps. This is treated as a reference signal accounting for stray electrons and signals from the pump and probe beams individually. I estimated that about 12 electrons are detected from each laser shot. In order to validate the statistical significance of features in the experimental measurements, a standard bootstrapping analysis is employed to estimate the uncertainties. For each pump-probe delay, the photoelectron kinetic energy distribution was calculated from the averaging of 150 velocity-mapped images

of the measurement. This data set was re-sampled 100 times, with 150 images randomly selected each time, using the standard bootstrapping method. Each bootstrapped photoelectron kinetic energy distribution was analyzed using the full data analysis routine. We monitored the standard deviation (STD) as a function of the number of bootstrapped data sets used. The STD stops increasing after running about 60 times. We then treated this STD as the error bar of the measurement, and the results are shown in the shading plots in Fig. 4.6 of in Chap. 4. A similar analysis was also carried out for estimating the statistics of the calculations, and the results were included in the supplementary materials of the previous publication from Ref. [163].

B.2 Computational method

On the theory side, the TRPES signals were simulated using trajectories from all three levels of theory. The trajectories from the previously reported trajectory surface hopping (TSH) simulations at the CASSCF(12,9)/cc-pVDZ, MRCIS/CAS(12,9)/cc-pVDZ and XMS-CASPT2/CAS(12,9)/cc-pVDZ levels of theory were considered [163]. The CASSCF and MRCIS simulations were performed using an interface of Columbus[247, 248, 249] and Newton-X 2.0[232, 233] packages, whilst the XMS-CASPT2 simulations were performed using an interface of Bagel[250, 251] and Newton-X 2.2.[241]

Since we were interested in the lowest two singlet states, an active space of 12 electrons in 9 orbitals were considered, which consists of 3 pairs of π and π^* orbitals, both out-of-plane lone-pairs of the N atoms, and the in-plane lone pair of the O attached to the C adjacent to the C=C bond in uracil. The chosen active space can correctly characterize the S_1 and S_2 states of uracil. An energy conservation criterion of 0.5 eV was used for all the simulations. Since the trajectories were propagated for only the initial conditions corresponding to our experimental pump pulse, all of them can be considered for simulating a TRPES. Given the computation cost associated with each method, we had 70/70/50 trajectories that were propagated for 1000/500/300 fs at the CASSCF/MRCIS/XMS-CASPT2 level of theory. Quantum corrections to the trajectory calculations (e.g. tunneling or interference) are not expected to play an important role given the energetics and the fact that hydrogen transfer is not involved.

Time-dependent Dyson norms were calculated for each trajectory, for each level of theory with a time-step of 10 fs using the CASSCF level of

theory [112, 252]. Neutral wavefunctions and energies were calculated at the SA3-CASSCF(12,9)/cc-pVDZ level, and cationic wavefunctions and energies were calculated at the SA5-CASSCF(11,9)/cc-pVDZ level. For calculating the electron kinetic energies (KE), we introduced specific shifts to the KE of photoelectrons coming from D_0, D_1, D_2, D_3 and D_4, since CASSCF overestimates the neutral excited state energies and underestimates the cationic state energies near the Franck-Condon (FC) region. The CASSCF neutral excited state energies at the FC geometry were compared to the best theoretical estimates at the CR-EOM-CCSD(T)/aug-cc-pVTZ level of theory [253], and shifts of -0.04 and -1.42 eV were introduced to S_1 and S_2 states, respectively. On the other hand, shifts of $+1.10$, $+0.76$, $+1.02$, $+1.21$ and $+1.21$ eV were introduced to the D_0, D_1, D_2, D_3 and D_4 states by comparing the CASSCF cationic energies at the FC geometry to the EOM-IP-CCSD/6-311+G(d) values, which are extremely accurate when compared to experimental ionization potentials (IP) [254, 255]. The total shifts were calculated by combining the shifts coming from the neutral state and the cationic state. Hence, depending on which state a trajectory is on at a particular time-step, different shifts were introduced to the KE due to photoelectrons coming from ionization to D_0, D_1, D_2, D_3 and D_4. Since the active space used here does not include the second n_o orbital, CASSCF cannot recover the correct D_3 state at the FC geometry, and hence we used the D_4 state at the EOM-IP-CCSD level to calculate shifts for both the D_3 and D_4 states. However, these states are not accessible by the experimental probe laser. In the case of the XMS-CASPT2 trajectories, initially trajectories were on both the S_1 and S_2 states, as the neutral states at the FC region are in close proximity to each other at the XMS-CASPT2 level [163]. However, that is not the case at the CASSCF level of theory. Since we calculated all the Dyson norms at the CASSCF level, where the bright state switches to S_2 for all the XMS-CASPT2 trajectories starting on S_1, only the subset of trajectories (17 from total 50) which were initiated on S_2 state were used for simulating the photoelectron spectrum in the case of the XMS-CASPT2 trajectories. The calculated spectra have been convolved with a Gaussian function with 90 fs FWHM along the delay axis in order to account for the IRF.

B.3 Measured and calculated TRPES in longer times

Here I discuss some extent of the measurement and calculation in larger delay dynamics. Fig. 4.6 in Chap. 4 shows the comparison of the calculation between the measured and calculated TRPES in a small time window, focusing on the short time dynamics. Fig. B.2 panels (a), (b), and (c) show the signals for the higher KE region. There are significant discrepancies between the calculated and measured TRPES for CASSCF, whereas signals from MRCIS and XMS-CAPST agree well with the measurement over full simulation time windows. Panels (d), (e), and (f) show the signals of the lower KE region. All three levels of theory show relatively long decay time for this signal, although XMS-CASPT2 shows a slightly more rapid decay than the experiment, whereas MRCIS and CASSCF show a slighly slower decay than experiment. As mentioned in chap. 4, because of the short simulations I do not expect them to be able to reproduce the low energy long lived signal as accurately.

B.4 Investigation of the barrier on S_2 potential energy surface

There have been many studies that investigated the potential energy surface (PES) of uracil after photoexcitation to the bright S_2 state. It has been found that the S_2 PES of uracil can be quite different depending on the level of theory being employed. Previous results from the literature, together with our current results are presented together in Table B.1. Negative barriers (negative barriers are obtained when a transition state geometry that has been optimized at a lower level of theory is used to calculate the energy of the barrier at a higher level of theory) mean the pathway is essentially barrierless. It can be seen from Table B.1 that the barrier on S_2 ranges from <0.02 to 0.88 eV. This has become a contentious topic since the excited population on the S_2 surface might decay faster or slower depending on the size of the barrier. The size of the barrier on the S_2 state typically decreases substantially in going from CASSCF to higher level multi-reference and single reference theories. The barrier changes significantly even when the state averaging, active space, and basis set are changed at the CASSCF level. It

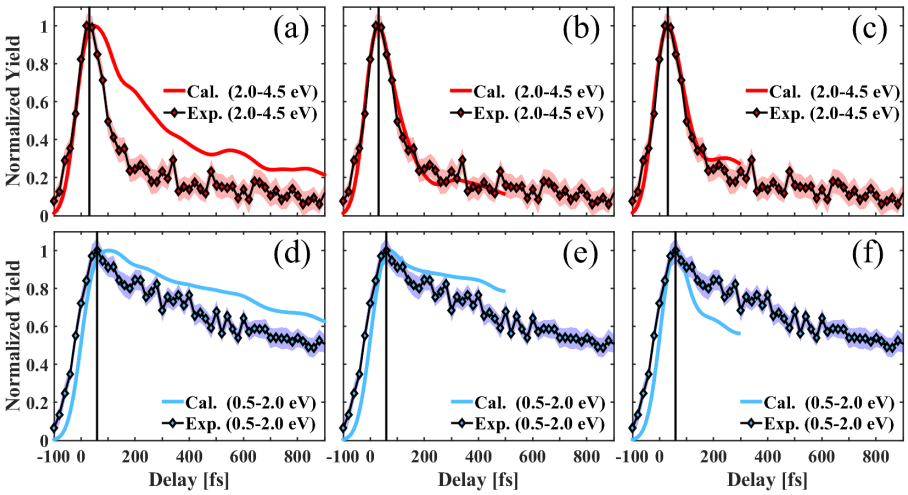

Figure B.2: **Uracil experimental time-dependent photoelectron yield integrated over two different energy ranges.** Compared with Fig. 3 in the main text, this figure shows the time-dependent yields of the complete simulated time window, in order to view the overall features between the calculation and measurements. Panels (a), (b), and (c) show measured and simulated (three levels of theory) yields of the time-and-energy resolved photoelectron of the higher KE region from 2.0 to 4.5 eV, whereas panels (d), (e), and (f) show the signals at the lower energy range, from 0.5 to 2.0 eV. The three columns show the calculated yields at the CASSCF (left), MRCIS (middle), and XMS-CASPT2 (right) levels of theory respectively. In each panel, the vertical black lines indicate the peak locations of the lineouts from the measurement.

has been claimed that this barrier will be insignificant in dynamics, given the amount of energy the system acquires during excitation [153]. However, there has been no dynamics study on uracil using a PES at a higher level of electronic structure theory than CASSCF, to the best of our knowledge.

Table B.1: **Barrier on the S_2 state of uracil at different levels of theory.** These values are taken from literature or calculated by us using 3 state averaging and cc-pVDZ basis sets for the multi-reference methods, and 6-31G(d) basis set for the TD-DFT method. Negative barriers may be obtained when a geometry that has been optimized at a lower level of theory (see ref. [256]) is used to calculate the barrier at a higher level of theory.

Methods	Barrier on S_2/eV
SA-3-CASSCF(12,9)/6-311+G(d) ref. [256]	-0.09
MRCI/CAS(12,9)/6-311+G(d) ref. [256]	-0.13
EOM-CCSD/6-311+G(d) ref. [256]	0.26
SA-3-CASSCF(8,6)/6-31G(d) ref. [148]	0.88
SA-5-CASSCF(8,7)/6-31G(d) ref. [148]	0.17
SA-5-MSPT2/CAS(8,7)/6-31G(d) ref. [148]	<0.02
MS-CASPT2(12,9)/DZP ref. 33	0.03
CASSCF(12,9)	0.16
XMS-CASPT2/CAS(12,9)	<0.02
TD-DFT/B3LYP	<0.03

As we will see later in Sec. B.5, the barrier definitely has a distinctive effect on the S_2 decay. The barrier has also been provided for the level of theories that we have used for our dynamics simulations. It can be seen from Table B.1 that MRCIS and XMS-CASPT2 have almost negligible barriers, while CASSCF does not. Hence, it is expected that a population trapped on the S_2 state will slow the decay of that state for the CASSCF method, while that will not occur for the other methods. Fig. B.3 shows all the (linear-interpolated-internal-coordinates) LIICs that have been performed to give a simple representation of the PES of uracil on the S_2 surface from the Franck-Condon (FC) geometry to the S_2/S_1 ethylenic CI.

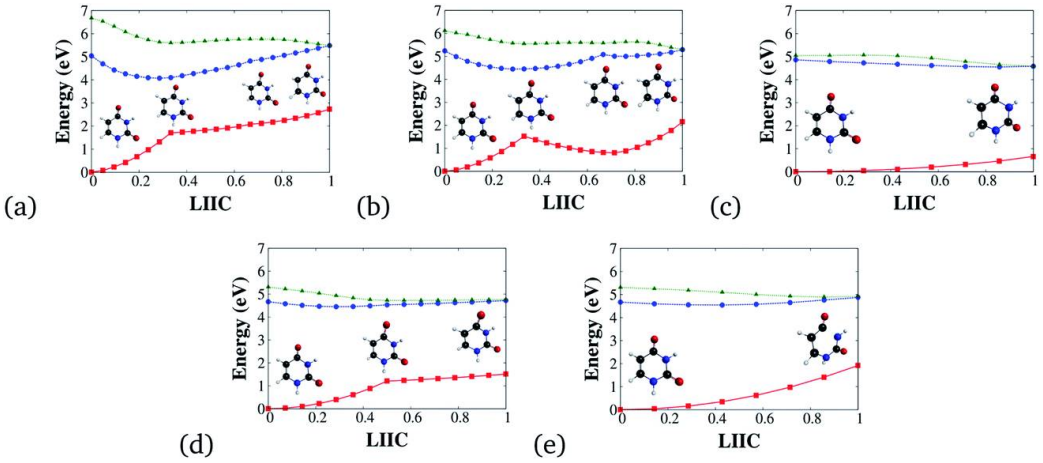

Figure B.3: **Linear interpolation from the FC geometry to the ethylenic conical intersection.** Linear interpolation from the FC geometry to the ethylenic CI21 at the (a) CASSCF (b) MRCIS (c) XMS-CASPT2, and (d) TD-DFT levels. (e) Represents LIIC to the ring-opening S_2/S_1 CI at the TD-DFT level. In all the panels, the red-solid line, the blue-dashed line and the green-dotted line represent the S_0, S_1 and S_2 states, respectively. The x axis is unitless with x = 0 being the FC geometry and x = 1 being the CI21. Panels (a) and (b) used intermediate geometries S_2 minimum at x = 0.33 and S_2 TS at x = 0.66, while panel (d) used intermediate geometry S_2 minimum at $x = 0.5$.

B.5 Time-dependent state population

Figure B.4 shows the normalized population dynamics of uracil for S_2, S_1 and S_0 states at all levels of theory. It is relatively easy to recognize that the dynamics are quite distinctive for each level of theory, especially for the multireference levels. The S_2 state population decays, completely, quite rapidly for MRCIS and XMS-CASPT2 levels, while ∼20% population remains in the S_2 state at 1000 fs for the CASSCF level. S_2 decay at the TD-DFT level is also quite fast, but not as rapid as the decays at the MRCIS and XMS-CASPT2 levels. It is known that in uracil, as S_2 decays, the population on the S_1 surface either relaxes via the $\pi\pi^*$/closed shell pathway rapidly to reach the S_1/S_0 CI directly, or gets trapped in the dark $n\pi^*$ state and relaxes to the ground state via the $n\pi^*$/closed shell pathway. A signature of this can be observed very clearly for the MRCIS and XMS-CASPT2 dynamics. In MRCIS dynamics, the population on the S_1 and S_0 state both start to increase rapidly with S_2 decay, S_1 more than S_0. That rapid gain of population ceases somewhere between 100–150 fs, evidenced by the sudden change of the slope of the population on both surfaces, and henceforth, the S_0 state gains population very slowly from the S_1 state. A very similar situation is visible for XMS-CASPT2 dynamics too. Only in this case, the population is on both S_1 and S_2 states, initially. Hence, the S_1 state gains population rapidly from S_2 and then starts losing population to S_0 rapidly till ∼150 fs. After 150 fs, the population exchange between S_1 and S_0 becomes very slow. For both of these methods, the relaxation is dominated by the $\pi\pi^*$/closed shell pathway for the first ∼150 fs, and then the population gets trapped on the dark S_1 state. The MRCIS and XMS-CASPT2 dynamics show no trapping at all on the S_2 surface, as is expected from the barrier height on S_2. However, in the case of CASSCF dynamics, the increase in the S_0 population is very gradual, as is the decay in S_2, for the whole simulation window. This is probably due to trapping of a significant portion of the population on the S_2 state, since there is a substantial barrier on S_2 at the CASSCF level on the way to the ethylenic conical intersection S_2/S_1 (CI21), compared to the higher level multireference methods. As a consequence, the S_2 decay becomes much slower at the CASSCF level. At the TD-DFT level, population decay looks very similar to the MRCIS population decay, i.e., it shows very little to no evidence of S_2 trapping. However, it is somewhat slower than MRCIS, but much faster than CASSCF. Also, the decay of the S_1 state after about 300 fs is much faster in the case of TD-DFT than MRCIS. Nonetheless, the

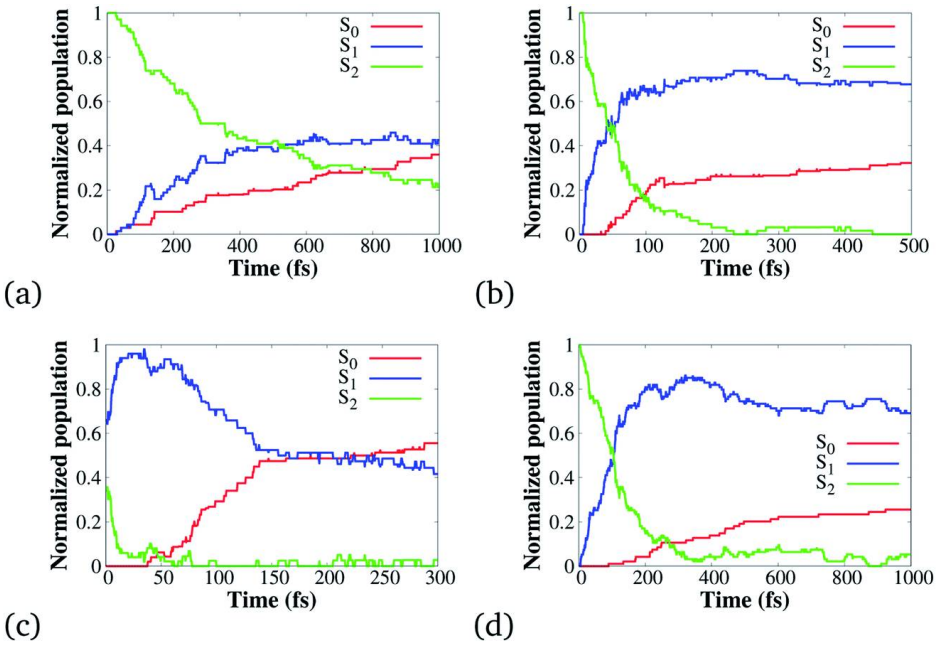

Figure B.4: **Normalized population dynamics for the lowest three singlet states (S_2, S_1 and S_0) of uracil.** Normalized population dynamics for the lowest three singlet states (S_2, S_1 and S_0) of uracil at the (a) CASSCF, (b) MRCIS, (c) XMS-CASPT2, and (d) TD-DFT level.

TD-DFT dynamics pathway has been found to be completely different to the multireference levels, since all the trajectories that are considered to be on the ground state, are there due to ring-opening via N3–C4 bond cleavage.

Appendix C

Supporting information for Chap. 5

In this appendix, I provide some details that are not covered in Chapter 3 regarding the work of combined spectroscopic and structural probes on excited state dynamics of CH_2I_2 and CH_2IBr. All the contents in this appendix are published in Ref. [257, 24, 258].

C.1 Details of CH_2I_2 and CH_2IBr time-resolved photoelectron spectroscopy

C.1.1 Trajectory surface hopping calculation and simulated TRPES of CH_2I_2 and CH_2IBr

In order to interpret the experimental results and gain insights into the energetic and structural evolution of the molecules following photoexcitation, we carried out trajectory surface hopping (TSH) [53] calculations of the excited state molecular dynamics. We used the results of these calculations to produce the same observables as obtained in the TRPES measurements in this section. The TSH calculations in this chapter were carried out by our theory collaborators, Philipp Marquetand and Tamás Rozgonyi.

The SHARC (Surface Hopping including ARbitrary Couplings) program [193, 194] was used for the TSH calculations, interfaced with Molcas 8.0 [195]. The electronic structure calculations for both molecular systems were performed with MS-CASPT2(12,8)/ano-rcc-vdzp (multi-state complete active space per-

turbation theory second order) based on CASSCF(12,8) (complete active space self-consistent field with 12 electrons in 8 orbitals). The state-averaging included 5 singlet/4 triplet states for CH_2I_2 and 3 singlet/4 triplet states for CH_2IBr. Further, we employed an IPEA shift of zero [259], an imaginary shift of 0.3 Hartree [260], the second-order Douglas-Kroll-Hess (DKH) Hamiltonian [261], and spin-orbit couplings (SOCs) from RASSI [262] and AMFI [263] formalisms. Gradients were evaluated numerically with a displacement of 0.005 a.u.. The dynamics was carried out using the velocity-Verlet algorithm with a time step of 0.5 fs for the nuclear dynamics and a time step of 0.02 fs for the propagation of the electronic wavefunction, using the local diabatization formalism [264]. Energy was conserved during a hop by scaling of the complete velocity vectors (not along the non-adiabatic coupling vectors, since the latter were not available). Wavefunction overlaps [265] were employed to compute the transition probabilities between states of the same multiplicity. An energy-based decoherence correction with a parameter of 0.1 Hartree was used [266]. The initial geometries and velocities for the trajectories were sampled from a Wigner distribution of the harmonic ground state potential. In this way, 10000 geometries were produced for each molecule, and a single-point calculation at the MS-CASPT2(12,8) level of theory was performed at each of these to obtain the state energies and oscillator strengths. The initial excited states were selected stochastically [267] restricting the excitation energy window to energies around our pump pulse (between 4.62 eV and 4.67 eV).

In order to compare with the measured TRPES signal, the energy resolved ionization probability along the trajectories was obtained in an approximate manner from Dyson norm calculations [123] using WFOverlap code [265] in a post-processing step. The necessary wavefunctions for the neutral and ionized molecule were obtained at steps of 2.5 fs along the pre-computed trajectories from MS-CASPT2(12,8)/ano-rcc-vdzp or MS-CASPT2(11,8)/ano-rcc-vdzp calculations including altogether 5 singlets, 9 doublets, 4 triplets and 4 quartets as well as all possible SOCs for CH_2I_2 and 3 singlets, 4 doublets and 4 triplets as well as all SOCs for CH_2BrI. A single time step of the neutral molecule's dynamics took about 1h on a single core (Intel Xeon E5-2650 v3). The ionization simulation was carried out as post-processing for every fifth time step, requiring approx. 5 min per point. Since initial wavefunctions were taken from the previous time step, intermittent points were recalculated with CASSCF requiring approximately 2 min, respectively.

As a test of the accuracy of the calculated TRPES, particularly given

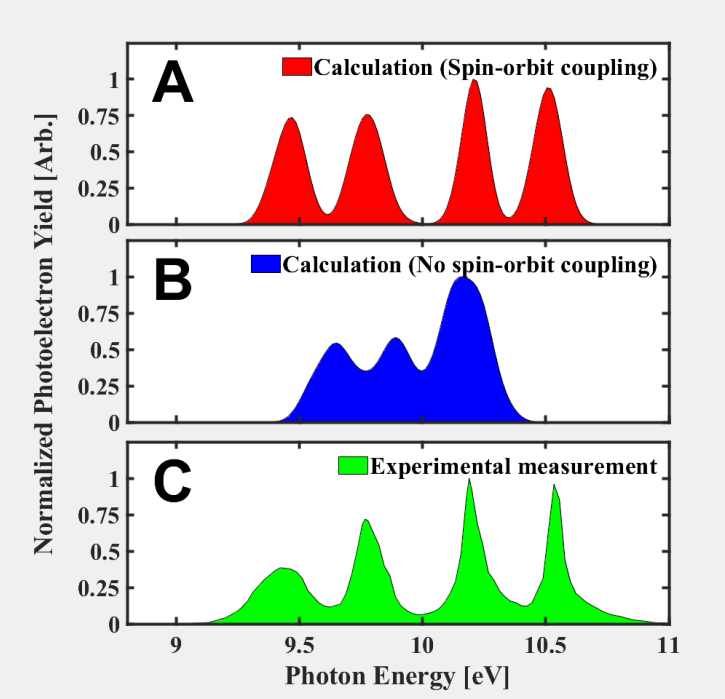

Figure C.1: **Comparison between measured and calculated static photoelectron spectra.** **(A)** Calculated ground state photoelectron spectrum including spin-orbit coupling. **(B)** Calculated ground state photoelectron spectrum without spin-orbit coupling. **(C)** Replotted version of the measured photoelectron spectra from reference [268].

the important role that spin-orbit coupling plays, we calculated the ground state photoelectron spectrum both with and without spin-orbit coupling, and compare the calculated results with the measured spectrum [268] in Fig. C.1. The calculation results are shifted by about 0.3 eV before plotting in order to compensate for the roughly 3% error in the ionization potential. As one can see, aside from a small shift in the overall energy, the calculation with spin-orbit coupling agrees with the measurements quite well (correct number of peaks, appropriate spacing and relative heights), while the calculation without spin-orbit coupling does not even produce the correct number of peaks or spacing between peaks. Our results are consistent with an extensive body of prior work which makes use of the Dyson method for calculating photoelectron spectra [97, 269, 270, 271]. The Dyson approach has also been used to calculate photoelectron spectra away from the Franck-Condon point in several earlier time-resolved photoelectron spectroscopy studies [13, 123, 272, 98, 273, 274].

C.1.2 UV pump central wavelength and intensity dependence in CH_2I_2 TRPES measurements

Before we step into the detailed interpretation of the measured diffraction signals, we investigate the sensitivity of the measurements to the details of the pump pulse. This step is essential since the pump UV parameters from the UED facility is slightly different from those in the TRPES and TRPIS measurements discribed in Sec. 5.2 and 5.9, mainly from the aspects of spectrum and intensity. In order to assess the sensitivity of the TRPES measurements to the pump pulse central frequency, bandwidth and intensity, we performed a number of experiments where these parameters were varied. Particularly, we tuned the UV parameter from the setup in Stony Brook University (SBU) to be the same as that in SLAC UED beamline facility and performed another TRPES measurement. The UV spectra from different locations as well as the CH_2I_2 absorption spectrum can be found in Fig. C.2.

A representative measurement from those performed at Stony Brook University is shown together with a measurement performed at the National Research Council (NRC) of Canada in Fig. C.3. Panels A and B showcase the measured TRPES signal from the setups from NRC and SBU, respectively. We found that the main features in the measurement were not sensitive to these variations within the range of parameters we considered (central wave-

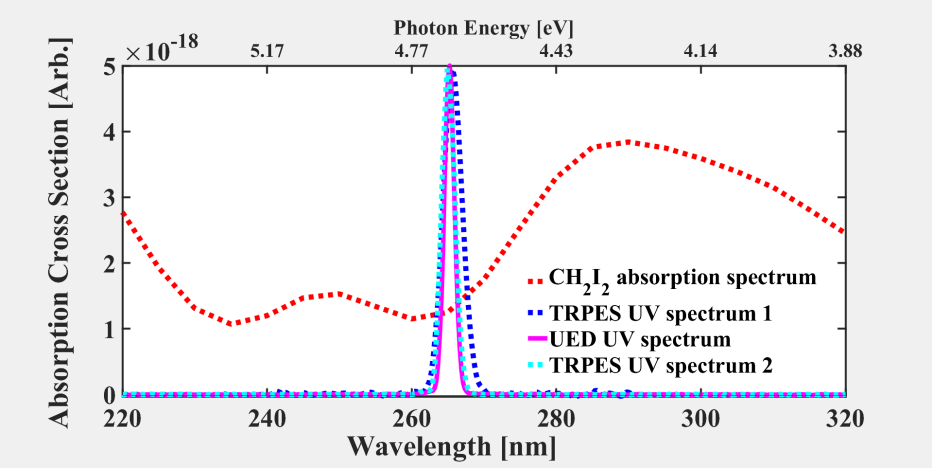

Figure C.2: **CH_2I_2 absorption spectrum together with the spectra for the pump pulses in the two experiments at NRC and Stony Brook.** The UV spectrum in the TRPES measurement is centered at 265.6 nm, while the UV spectrum of UED measurement is centered at 265.3 nm. As the TRPES measurements were repeated with two different apparatuses, the spectrum for each of these pump pulses is shown separately.

length between 266 nm and 262 nm, bandwidth between 1.5 nm and 2.0 nm and intensity between 0.3 TW/cm^2 and 1.5 TW/cm^2). The two measurements yielded slightly different time-dependence of the energy integrated yield as shown in panel c, which is due to the slighly different time resolution from the two setups.

C.1.3 VUV driven dynamics at short positive time delays

As our interpretation of the measurements relies heavily on the low energy tail observed in the CH_2I_2 TRPES, we provide additional evidence for the significance of this feature in our measurements. The first is simply a slightly different view of the TRPES, where we allow the color axis to saturate. This is shown in Fig. C.4. The presence of electrons between 0 and 0.5 eV for positive delays beyond 40 fs is clearer here than in Fig. 5.3 in Chap. 5. Again, in Chap. 5, I showcased a standard bootstrapping analysis was carried out in order to verify the significance of the lower kinetic energy electron beyond 40

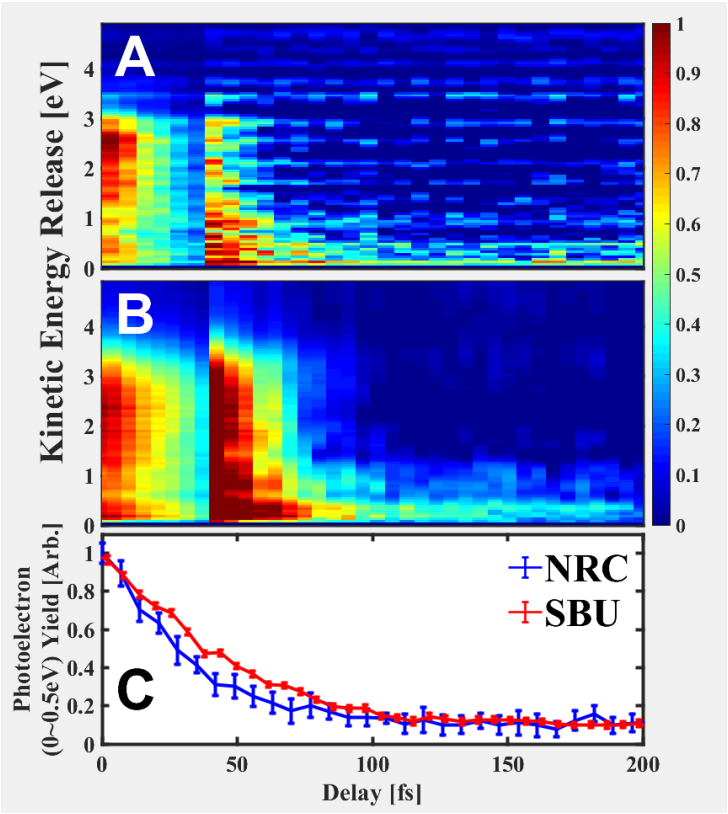

Figure C.3: **Comparison of TRPES measurements carried out at two different locations with different pump pulse parameters. (A)** RPES measurements carried out at the National Research Council in Canada (NRC) with a pump pulse intensity of 0.5 TW/cm^2 and a bandwidth of 2 nm FWHM. **(B)** TRPES measurements carried in Stony Brook University (SBU) with a pump pulse intensity of 1.0 TW/cm^2 and a bandwidth of 1.5 nm FWHM. **(C)** Yield of low energy electrons for the two measurements. In panels **A** and **B**, both spectra are multiplied by a factor of 4 after 40 fs as in Fig. 5.3.

fs, which is due to the wave packet evolved in the bound state before internal conversion to the lower lying dissociative states.

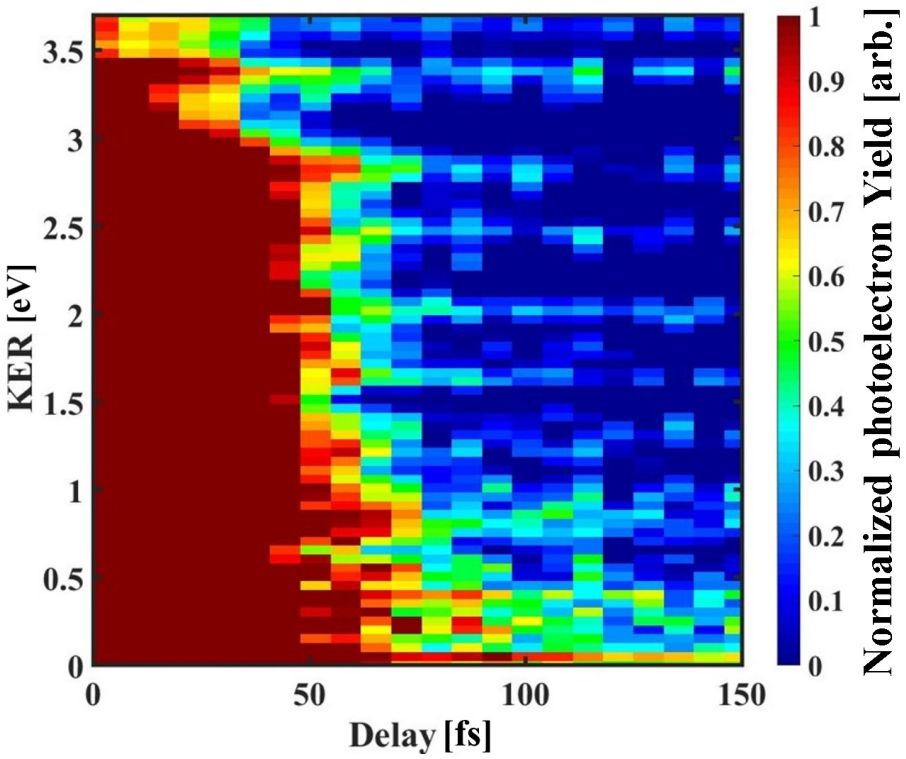

Figure C.4: TRPES for CH_2I_2 with saturated colormap in order to highlight low energy electrons for positive time delays.

In order to further evaluate the contribution of the VUV driven dynamics to the TRPES near zero time delay, we consider the evolution of the TRPES as a function of delay near time-zero. Figure C.5 shows the photoelectron spectrum for a few time delays near zero. The spectra for small negative and positive delays (e.g. -26 fs and +23 fs) show some similarities and differences, consistent with static calculations of the photoelectron spectrum that we carried out for VUV+UV and UV+VUV. They all show a broad distribution of photoelectrons between 0 and 3 eV, with a relatively sharp cutoff around 3eV, as one would expected based on the difference between the sum of the UV and VUV photon energies ($\sim$ 12.5 eV) and the ground state ionization potential ($\sim$ 9.5 eV). The broad distribution from 0-3 eV is a result of ionizing

to a mixture of low lying ionic states, and conversion of potential energy to vibrational kinetic energy on the excited state.

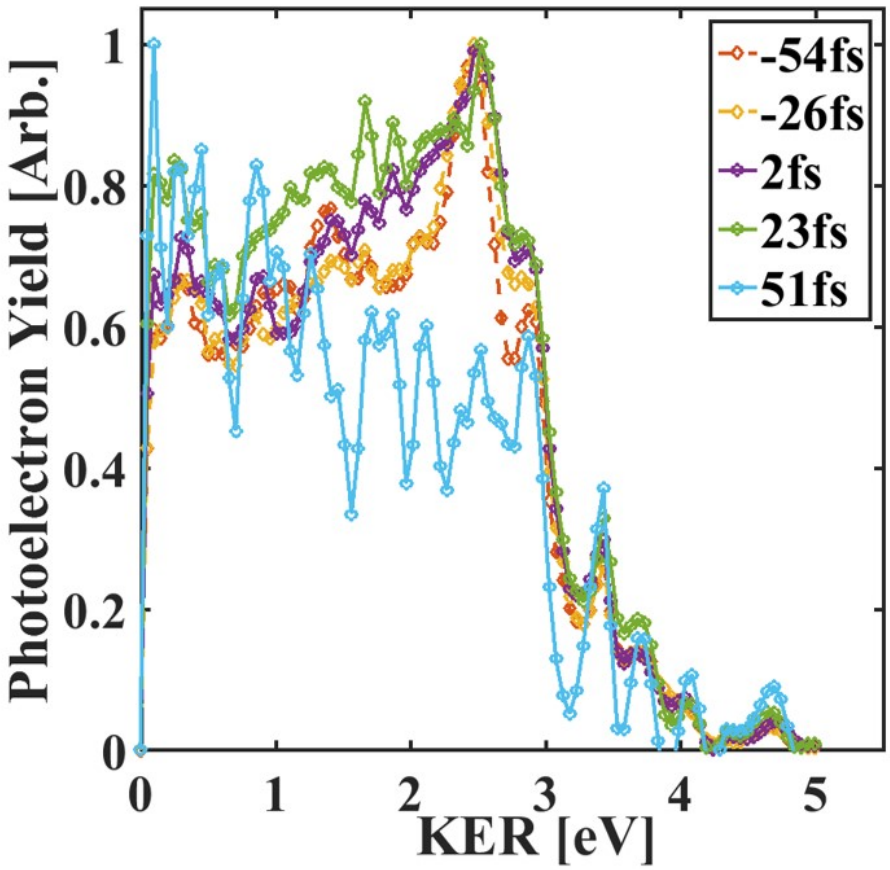

Figure C.5: Photoelectron spectra for several different delays near zero time delay.

While there are clearly differences in the spectra for positive and negative delays, the similarities provide some rationale for the agreement of the calculations including only UV driven dynamics with the measurements which include both UV and VUV driven dynamics near time-zero. The similarities in the photoelectron spectra for VUV+UV vs UV+VUV can be understood in terms of the fact that at our photon energies, the VUV absorption spectrum is dominated by Rydberg states that are correlated with the same four lowest states of the cation that contribute to the spectrum produced in our

calculations which include UV excitation (see figure 3 in reference [191]). The differences in the spectrum for positive and negative delays can be attributed to some dynamics on the excited neutral states as well as different weightings of the ionic states involved for UV vs VUV pumping.

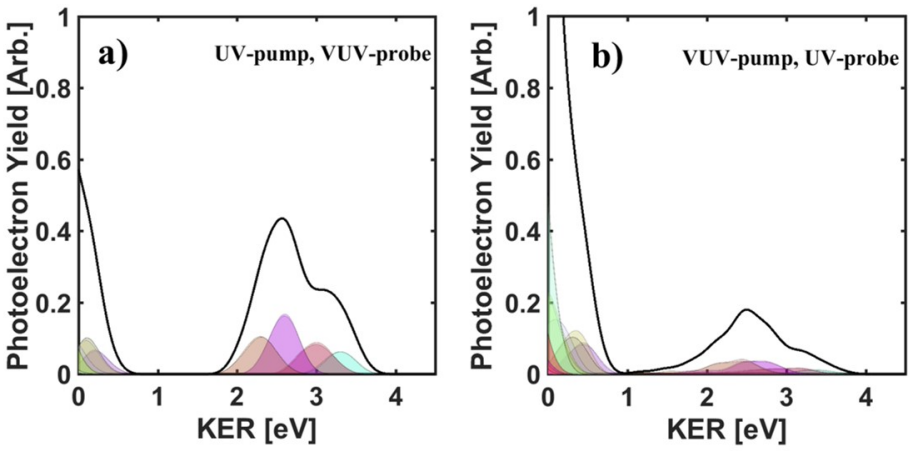

Figure C.6: The two panels show the photoelectron spectrum as calculated for a δ function pulse. The left panel shows ionization from state 16, i.e. the most highly populated state after UV excitation (4.65 eV), to different ionic channels (blue to pink peaks correspond to D0,D1,. . . , while their sum is plotted as black line). The right panel shows ionization from state 40, i.e., excitation with the VUV-photon energy of 7.75 eV. Note that less structure than in the experimental spectra is visible due to the limited number of geometries (here 99) and the artificial Gaussian broadening of 0.3 eV.

In addition to examining the TRPES for both sides of time-zero, we calculated the photoelectron spectrum due to VUV pump, UV probe.The spectra were calculated with MS-CASPT2(12,10) for 14 singlets and 12 triplets and MS-CASPT2(11,10) for 9 doublets and 4 quartets with MOLCAS 8.0. We used an ano-rcc-vdzp basis set augmented with diffuse functions for Rydberg orbitals according to the scheme proposed by Kaufmann et al. [275] The single point calculations including Dyson norm computations for the 84 states were carried out for 99 geometries from the afore-mentioned Wigner distribution. For the UV+VUV spectrum, we considered the Dyson norms between the neutral state 16 (which is the most populated state in the UV excitation with 4.65 eV) and all possible ionic states. The VUV+UV spectrum

stems from the Dyson norms between the neutral state 40 (most populated in VUV excitation with 7.7 eV) and all possible ionic states. The resulting stick spectra were convoluted with Gaussians (FWHM 0.3 eV), respectively. The results of these calculations are shown in the figure C.6. They show that the photoelectron spectra for VUV+UV and UV+VUV both populate a combination of the four lowest ionic states (D0, D1, D2, D3). Ionization to states higher than D3 (leading to the peak near zero energy) is likely due to a slight redshift in the calculations. Features between 0.5 and 2 eV are absent in the static calculated spectra but are present in figure 2 of the manuscript as a result of dynamics and temporal broadening (mimicking the finite duration of the laser pulses). These calculations indicate that the VUV+UV and the UV+VUV pathways produce similar features in the TRPES.

C.2 Details of CH_2I_2 ultrafast electron diffraction measurements

C.2.1 Azimuthally averaged diffraction pattern analysis

In Chap. 2, I have discussed a 2D based diffraction pattern analysis, by applying a 2D Fourier transform followed by an Abel inverse transform. Here I discussed the details of some diffraction pre-analysis and the conventional 1D based Azimuthally averaged diffraction pattern analysis. There are often several procedures in the per-analysis of the raw diffraction patterns discussed below:

- Background removal. Background diffraction images are usually collected before measuring the signal with sample, and they are subtracted from the diffraction pattern with molecules. This background usually accounts for the electrons from the gun or photons from the laser that are not related to the pump-probe measurement, such as some electrons induced by the dark current (electrons not driven from the UV pulse in the gun cathode), and the pump UV beam that is not full blocked to the detector, etc. Fig. C.7 top left panel shows the electron diffraction signal of a single image (20 s, $\sim$ 3600 shots, CH_2I_2 molecule), and top right panel reflects a typical background signal in the detector which are mostly distributed closed to the hole region. The background signal is fairly stable during the data acquisition.

- Hot pixel removal and median filter. As reflected in Fig. C.7 top left panel, one is able to identify some spikes or stripes with high values that are distributed around the diffraction pattern, so called "hot pixel". These hot pixel signals are mostly due to the possible X-ray that induced from the high energy electrons leaking into the surface of the apparatus before the detector. A proper hit removal algorithm can be employed and any pixel that is obviously saturated or brighter (>several times higher than the mean value) than other pixels in the peripheral region is removed. Due to the fact that the diffraction signal are mostly concentric circles/rings that slowly vary along the S space, the diffraction pattern is locally smoothed with a window of n$\times$n (n$<$10) pixel, in which some sharp features can be removed, but

still keeping the signal related to the molecular structure. In addition, this smoothed images is good for the diffraction center finding algorithm. Fig. C.7 bottom left panel shows the signal after background and hot pixel removal, followed by a median filter with a 10×10 pixel size window.

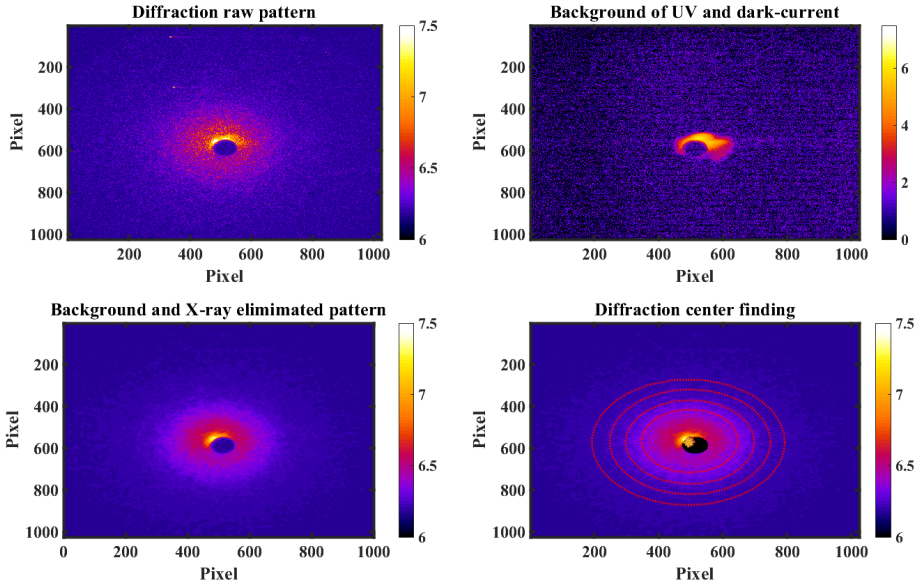

Figure C.7: **Diffraction pattern pre-analysis: raw data "clean-up".** This figure gives an example of the single-image based "clean-up" step. Top left panel is a raw diffraction image from the CH_2I_2 measurement. The top right panel reflects an image for the background signal unrelated to the main electron beam, which often come from the residual pump UV and electrons generated from dark current in the gun. Bottom right panel displayed a processed raw image after the background and hot pixel removal as well as a locally smoothing. Finally the bottom right panel showcases the image with a mask applied, such that the signal at the edge of the detector hole can be cleaned, as well the diffraction center finding method, indicated by the concentric circles. All the panels are plotted using logarithm color scale in order to highlight a number of features in the analysis.

- Detector hole mask. As discussed in the former section, the phosphor screen is drilled with a hole on the center, allowing the main electron

beam traveling thought to avoid saturation and potential damaging. The main electron beam is often set at the very edge of the hole in order to partially reach the signal in small S range. Whereas, the signal around the edge of the hole usually include some artifacts which are possibly induced by the main beam peeking onto the detector. A commonly used method is to manually apply a mask, covering the hole region, which is in Fig. C.7 bottom right panel.

- Diffraction center finding. One essential procedure is to carefully locate the diffraction center which is the key to correctly implementing the azimuthal integration of the two-dimensional (2D) diffraction pattern into one-dimensional (1D) lineout. Due to the possible changing of the experimental environment conditions, such as temperature, the electron beam may systematically drift from its original position, inducing the diffraction pattern drifting. Usually this drifting is slower than the data acquisition period (10 to 20 s) of a signal image. Another type of drifting is due to the pump UV beam, which causes ionization/-plasma effect such that the main electron beam will be deflected by the charges. Both types of drifting can be corrected using a single image-based center finding protocol. Fig. C.7 bottom right panel shows the diffraction pattern center finding algorithm. Often, it is started from an initial guess according to the main electron beam position. Several concentric circles with different radii are fitted according to diffraction signal intensity inside a smaller range (around the chosen radii) of one or several tens of pixels, ($\sim$0.2 Å^{-1}), and the centers of these circles are then retrieved and averaged. The fitted center can be used to corrected the drifting of the diffraction pattern among the images.

After the single image based "clean up", the images of the diffraction patterns for the same pump-probe delay are averaged. If one is not interested the angular distribution, the 2D diffraction patterns then are azimuthally integrated at each s (radii) in order to obtain the 1D diffraction lineout signal, which is widely used in electron diffraction measurement. Fig. 2.18 shows an averaged diffraction pattern at far negative time delay (<-10 ps) with the molecules populated in ground state. A "static" diffraction pattern analysis can be employed with the aid of the simulation in order to evaluate the experimental data quality. As discussed in Sec. 2.3.1, the atomic scattering is a monotonically decreasing curve as a function of s, and the total diffraction signal is an incoherent sum of the atomic and molecular scattering. In

the experiment, except the molecular scattering portion, one may assume the atomic scattering signal as well as other contributions ("incoherent background"), such as the inelastic scattering, with an exponential function as below:

$$I(s) = Ae^{\alpha+\beta s^{\gamma}} + C, \tag{C.1}$$

As shown in Fig. 2.16, one piece of useful information is the so called *diffraction zeros* from the simulated sM(s) of the ground state geometry, which are often easy to acquire. These points are fixed at known S values regardless of the absolute diffraction signals. With an initially guessed "incoherent background" profile, the sM(s) curve then can be obtained by Equ. 2.20. Therefor, the coefficients of the polynomials aforementioned can be optimized from fitting the sM(s) according to these *zeros*, such that the "incoherent background" can be removed from the total diffraction signal, only leaving the molecular coherent component. One of the precondition of an accurate "static" pattern analysis is the good s calibration of the measured diffraction pattern. This step can be accomplished by using a thin film of single/poly crystal sample, in which one can use the well-known orders of Bragg peaks/rings to calibrate from pixels to S.

Fig. C.8 panel (a) shows the experimental measured total signal (azimutally averaged of the diffraction pattern in Fig. 2.18 and the fitted "incoherent background" signal. As one can see, the background is fit with a smooth exponential function and the measured signal has very small modulations. By subtracting the fit background from the measurement signal, the sM(s) and PDF(r) obtained from a Fourier transform are calculated and shown in panel (b). The measured and simulated sM(s) match well up to 10 Å^{-1}, indicating the diffraction patterns own high quantity. Except some artifacts induced by the signal missing in the center, the PDFs agree well between the measurement and simulation. However, the positive delay signal which consists unknown structural changes is not applicable with the "static" diffraction pattern analysis. It is more useful to obtain the diffraction difference signal by subtracting the pattern at far negative pump-probe delays.

C.2.2 Separation of one and two photon absorption driven dynamics

Here I provide details on how we separated one and two photon contributions to the UED measurements. In all the experiments of TRPES or TRPIS,

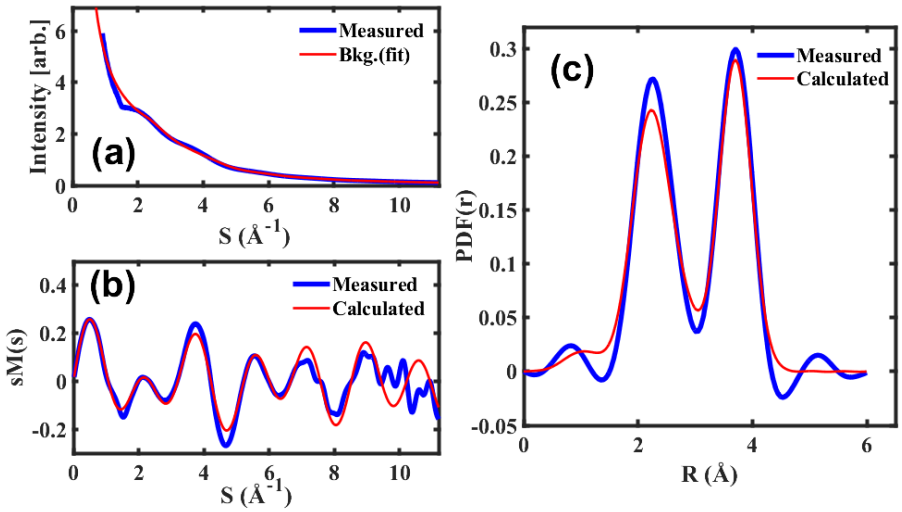

Figure C.8: **UED experimental "static" diffraction pattern analysis.** Panel (a) shows the measured diffraction signal and the fitted background signal. Panel (b) and (c) then reflect the simulated and measured sM and PDF signal, respectively.

we worked at the lowest pump pulse fluence where we could measure the dynamics with sufficient signal to noise to extract meaningful information from the measurements. The energy of the measured photoelectrons and photoions in the TRPES and TRPIS measurements were consistent with the absorption of only one pump and one probe photon, assuming ionization to low lying states of the molecular cation. While one could in principle produce similar energy photoelectrons from the TRPES measurement by absorbing two pump photons and ionizing to higher lying states of the molecular cation, this is less likely and was ruled out by performing several measurements with different pump pulse fluence.

The situation is more complicated for the UED measurements. UED has relatively low sensitivity compared to most spectroscopic techniques. Lower pumping fluence leads to low signal to noise ratio (SNR) of the signal, low scattering range in momentum transfer space, inability to transform to real-space, etc. These aspects can be significantly improved with higher pump fluence. However, higher pump fluence can lead to multiphoton absorption. In our case, it is more difficult to detect excited state dynamics without pumping hard enough to induce some two photon absorption.

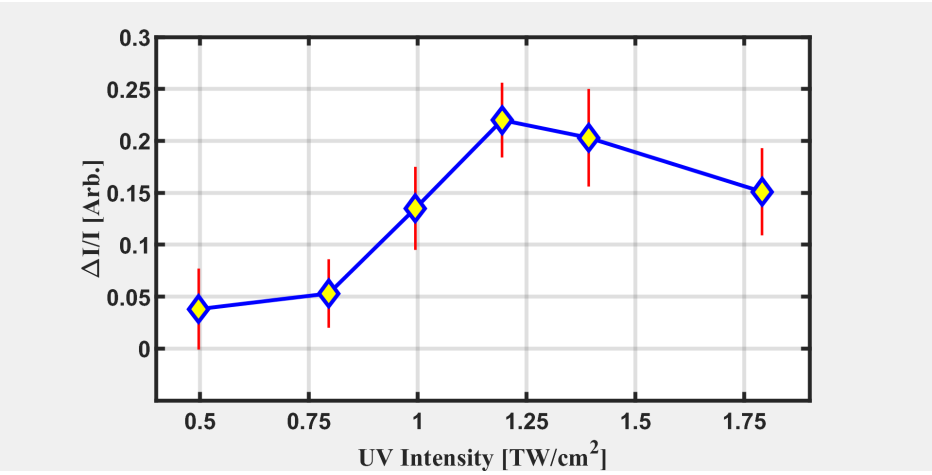

Figure C.9: **UV Pump pulse intensity dependence.** The ratio of the diffraction pattern difference, ΔI/I, between 1.1 and 2.8 Å^{-1} is plotted as a function of UV pump pulse intensity. The delay was chosen between 250 and 300 fs. All data shown in the main text were taken at an intensity around 1 TW/cm^2.

In order to check that the measurements were not dominated by multi-photon absorption from the pump pulse, we performed measurements of the diffraction signal as a function of the pump pulse intensity. Fig. C.9 shows the strongest feature in the momentum space diffraction pattern, i.e., the difference signal between 1.1 and 2.8 Å^{-1}, as a function of pump pulse intensity. The measurements described in the main text were performed for a pump pulse intensity of about 1 TW/cm^2, which corresponds to the linear portion of the graph shown in Fig. C.9. In order to further evaluate the relative contributions of multi-photon vs one-photon absorption to the measured dynamics, we performed two additional analyses.

The first approach is that I compared the modulations in the signal at 2.85 Å with the depletion at 3.60 Å in order to evaluate the two-photon driven dynamics. The simulations of the two-photon driven dynamics indicate that the wave packet is compact and oscillates, leading to a minimum I-I distance of 2.85 Å, and the simulations of the one-photon driven dynamics do not make any contribution to the ΔPDF at 2.85 Å. Given that both dynamics lead to a decrease in the PDF at a pair distance of 3.60 Å, while only the two-photon driven dynamics contribute to the modulations at 2.85 Å, we made

use the of ratio of the ΔPDF at these two distances to estimate the fraction of molecules absorbing two pump photons vs those absorbing one. According to Fig. 5.15 panels B and C n Chap. 5, the oscillation amplitude at 2.85 Å is about 12 % of the total depletion of ΔPDF at 3.60 Å a few hundred fs after the pump pulse. This indicates that the two photon absorption contribution to the dynamics is about an order of magnitude lower than the one photon absorption contribution, consistent with the linear response to the pump pulse shown in Fig. C.9 .

A second approach makes use of the angular dependence of the measured diffraction signal [100, 208]. I fit the angle dependent three dimensional ΔPDF to a series of Legendre polynomials in order to obtain the coefficients for each even order (the "so called" β parameters). One photon absorption should only contribute to 2^{nd} and 0^{th} order Legendre polynomials (β_0 and β_2), while two photon absorption contributes to 4^{th}, 2^{nd}, and 0^{th} order Legendre polynomials (β_4, β_2 and β_0). In general, an M-photon process will contribute to all the even orders from β_0 up to β_{2M}, and thus determining β_M places a limit on the contribution of M-photon absorption. Such a β parameter analysis is attractive because one can have a model independent check of the data to determine quantitatively how much 1, 2 and 3 photon processes contribute to the signal. Applying this analysis to our simulations confirmed that two photon absorption driven Rydberg dynamics contribute to β_0, β_2 and β_4, while one photon absorption driven valence dynamics contributed to only β_0 and β_2.

As with the simulations, we applied the β parameter analysis to the measured ΔPDF up to 6^{th} order. While the time and R dependent β_0 and β_2 parameters match the overall features with those from the simulated results of one photon dynamics, β_4 and β_6 are large and fluctuate. This could be due to higher order (M>1) photon absorption driven dynamics, or it could be due to the noise in the data [276], as simulated data that we analyzed led to large β_4 and β_6 parameters in the fitting if we introduced noise into the simulated data set. In order to determine whether the large β_4 and β_6 parameters were due to noise or multiphoton absorption, we compared the β_4 and β_6 parameters for positive and negative delays. For negative delays, the β_4 and β_6 values should be noise driven, whereas for positive delays, they could contain contributions from multiphoton absorption driven dynamics. Thus, the ratio of their values for positive and negative delays provides some measure of whether multiphoton absorption plays a role in the measured dynamics. A ratio greater than one indicates that there are pump pulse induced dynamics

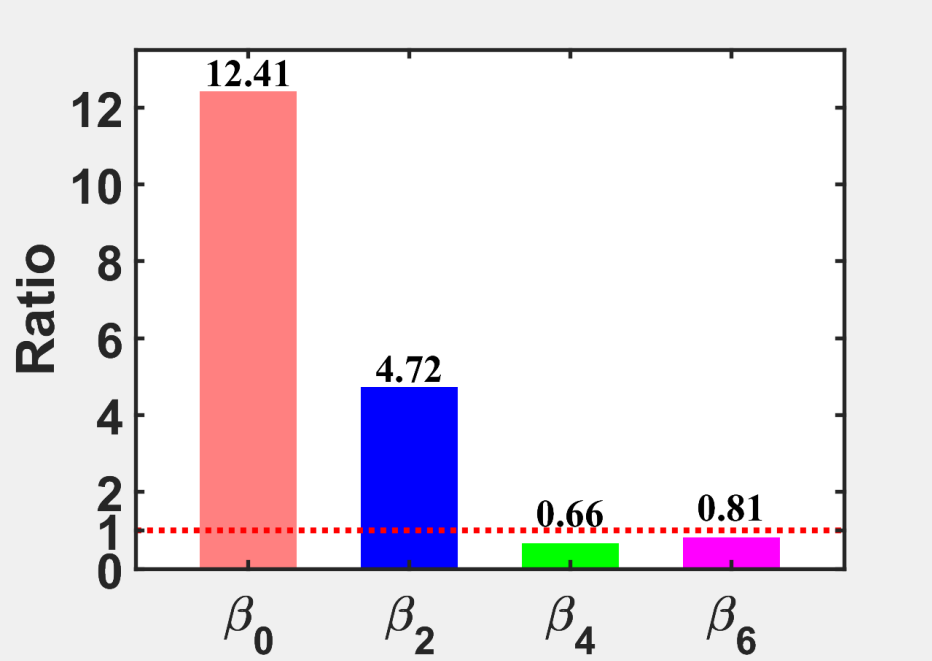

Figure C.10: β **parameter analysis of measured ΔPDF.** Ratio of integrated β parameter values for positive and negative time delays are plotted in the figure with β order of 0, 2, 4, and 6. Each β parameter is obtained by integration between 3.2 Å and 4.0 Å. A red dotted line indicates a ratio of 1.

which lead to a given β parameter order, whereas a low ratio (≤ 1) means that the β parameter is largely noise driven.

We focus our analysis on the R region of the ΔPDF associated with I-I depletion, since all orders of multiphoton absorption should contribute if there are any dynamics that involve motion of the I atoms. Fig. C.10 shows the positive/negative delay ratio for the β parameters as a function of order. Both β_0 and β_2 show values of ratio much larger than 1, while the ratios for β_4 and β_6 show very low values. This analysis confirms that our measurements are dominated by one photon absorption driven dynamics.

C.3 Details of CH_2I_2 and CH_2IBr momentum-resolved photoion spectroscopy

C.3.1 Data analysis details of the experimental measurement

In many molecules, the absorption cross section in the VUV can be stronger than in the VUV, complicating the measurements near zero time delay. As both the pump and probe pulses have finite pulse durations, there can be overlapping contributions from dynamics driven by the pump pulse (pump-probe) and dynamics driven by the probe pulse (probe-pump) when the two pulses overlap. As seen from our early TRPES measurements with the same pump and probe photons wavelengths [22], the VUV driven signal dominates over the UV driven signal for both CH_2I_2 and CH_2IBr. This issue needs to also be addressed for the photoion measurements. Fig. C.11 panels (a) and (b) plot the measured photoion spectra for fragments, CH_2I^+ and CH_2Br^+, respectively. Note that the maximum ion yields occur for slightly negative delay times, consistent with the fact that the VUV absorption cross section is larger than the UV absorption cross section. In order to isolate the UV induced dynamics, it is useful to decompose the signal into UV and VUV driven dynamics by performing a global 2D fit.

We applied a two-dimensional bilateral global least-squares fit to the measured photoion spectra [52, 277], in order to extract the UV driven contribution from the measured signal. Here, we briefly describe the process. We define $Y(t;\epsilon_k)$ to be the differential photoion yield as a function of pump-probe (or probe-pump) delay and ion kinetic energy for the UV (or VUV)

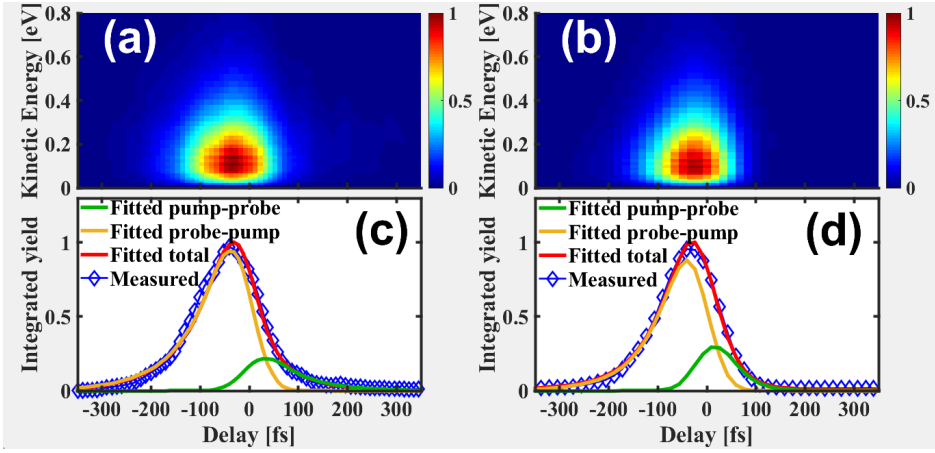

Figure C.11: **Time-resolved CH_2I_2 and CH_2IBr photoion spectra and global fitting analysis.** Panels (a) and (b) show the measured photoion spectra as a function pump-probe delay and translational kinetic energy (TKE) of CH_2I^+ and CH_2Br^+, respectively. A 2D global fitting analysis was applied in order to decompose the measurements into UV and VUV driven components. Panels (c) and (d) show measured and fitted energy integrated yields for CH_2I^+ and CH_2Br^+, respectively.

driven dynamics. In general, $Y(t;\epsilon_k)$ is globally fitted to

$$Y(t;\epsilon_k) = G(t) \otimes \sum_i S_i(\epsilon_k) e^{-t/\tau_i}, \tag{C.2}$$

where the $S_i(\epsilon_k)$ are the time independent decay related spectra and $G(t)$ represents the Gaussian cross correlation function associated with the IRF. The energy-resolved amplitudes of the fitting components have decay constants τ_i, assuming that the population of the excited states follows an exponential decay. If the underlying dynamics involve photoinoization from more than one excited state (e.g., i = 1,2...) one can establish kinetic models in the global fitting where more than one decay constant could be extracted from the fitting. The total ion yield is then convolved with $G(t)$, the Gaussian cross-correlation function that represents the instrument response function (IRF) for the apparatus. In the case of CH_2I_2 and CH_2IBr, we fit the measured signal towards both positive and negative delays, corresponding to the UV and VUV driven dynamics respectively. As in our previous work on CH_2I_2 using TRPES [22], we fit the data with a single exponential function

for each side of zero delay. Both the exponential functions start from the time-zero, but decay in opposite directions. The sum of the two functions is then convolved with the IRF. Thus equation C.2 can be simplified and rewritten as,

$$Y(t;\epsilon_k) = G(t) \otimes (S(\epsilon_k^{vuv})e^{t/\tau_{vuv}}|_{t<0} + S(\epsilon_k^{uv})e^{-t/\tau_{uv}}|_{t>0}), \tag{C.3}$$

Since the bilateral fitting is very sensitive to both the time-zero position and the IRF, we made use of pump-probe measurements with ethylene (for which the decay dynamics are very rapid) in order to locate the time zero and determine the IRF of the experiment. The ethylene pump-probe measurements were conducted with the same running conditions as for CH_2I_2 and CH_2IBr.

The fit returns the amplitudes of the time-independent spectra as well as the decay constants of both UV and VUV driven signal, which allows us to reconstruct the fitted 2D spectra for both UV or VUV driven dynamics. Figure 5.19 panels (a) and (b) in the main text show the time resolved UV driven spectra for CH_2I^+ and CH_2Br^+ with the VUV driven dynamics subtracted using the fitting approach described above.

C.3.2 Details of the theoretical calculation

In this section, I provide the calculated absorption spectra, the dissociation energies, a detailed analysis of two exemplary trajectories for each molecule, and an analysis of the effect of the cationic dynamics on the measured TKE.

Figure C.12 shows the comparison between the calculated absorption spectra from this work and the measured spectra in the literature [278, 279]. One can see that the calculations capture the main features of the absorption spectrum below 5.5 eV relevant to the experiments. There is some disagreement between the measured and calculated spectra in terms of the relative peak heights for CH_2I_2, but the number of peaks and their locations are in good agreement for both molecules. The agreement for CH_2I_2 can be improved, when including more states in the calculation (see gray line in panel (a) of Fig. C.12) but the important states in this study – states 1-12 (dark red and dark blue channels in Fig. 5.11) – remain unaffected by such a change.

In addition to calculating the absorption spectra, we estimated the dissociation limit for different dissociative channels (CH_2X+I, CH_2X+I^*, CH_2X^*+I, where X represents I or Br) for both CH_2I_2 and CH_2IBr, as shown in Tab. C.1. The energies were computed at the same MS-CASPT2 level of theory as

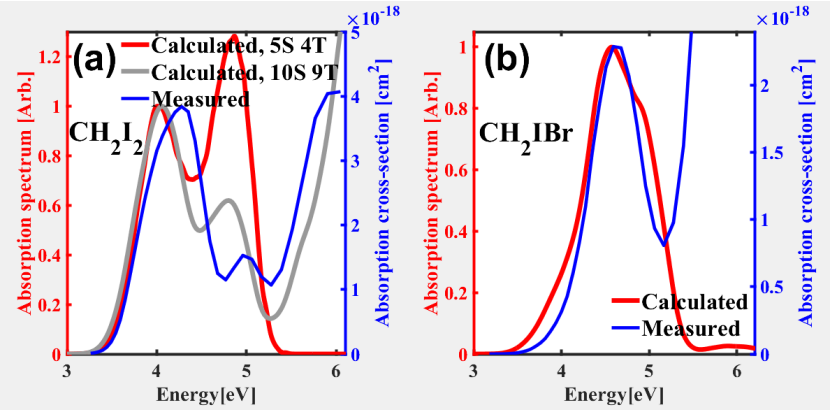

Figure C.12: **Calculated and measured absorption spectra for CH_2I_2 and CH_2IBr.** Panels (a) and (b) compare the calculated (left y-axis) and measured (right y-axis) absorption spectra in deep UV region for CH_2I_2 and CH_2IBr, respectively. The red lines indicate the calculated spectra using the same number of states used for the trajectory calculations, while the blue lines show the measured absorption cross-section with absolute values reproduced from Ref [278, 279]. For CH_2I_2, the gray line showcases the calculated spectra when more states (10 singlet, 9 triplet states, instead of 5 singlet, 4 triplet states for the red line) are included. All spectra are normalized to the peak at ~ 4 eV.

Table C.1: **Dissociation energies for different channels of CH_2IBr and CH_2I_2. FC indicates the Franck-Condon geometry**

Dissoc. Channel	Dissoc. Energy
$CH_2BrI \rightarrow CH_2Br + I$	2.091 eV
$CH_2BrI \rightarrow CH_2Br + I^*$	2.957 eV
$CH_2BrI \rightarrow CH_2Br^* + I$	6.446 eV
$CH_2I_2 \rightarrow CH_2I + I$	2.141 eV
$CH_2I_2 \rightarrow CH_2I + I^*$	3.004 eV
$CH_2I_2 \rightarrow CH_2I^* + I$	5.675 eV
CH_2BrI^+ (FC) $\rightarrow CH_2Br^+ + I$	0.964 eV
$CH_2I_2^+$ (FC) $\rightarrow CH_2I^+ + I$	1.100 eV

used for the dynamics simulations (see section III). The geometries of the parent and fragments were determined by density functional theory at the B3LYP/aug-cc-pVTZ-PP level of theory. Zero-point energies are neglected. For the $CH_2X^* + I$ channels, the geometries of the ground state CH_2X species were used, and thus the dissociation energies for these channels are somewhat overestimated. They are, however, so much higher than the available energy after photoexcitation that dissociation into these channels can be excluded.

Figure C.13 shows the total energy, translational kinetic energy (TKE), potential energy and state index as a function of time for two exemplary trajectories from each molecule. Panel (a) plots the time-dependent total energy (kinetic, T + potential, V) and potential energy (denoted V), whereas panel (c) underneath shows the state indices and TKE for CH_2I_2. Panels (b) and (d) show the same for CH_2IBr. As the legends show, one trajectory ends up in the spin-orbit coupling ground state channel ($CH_2X + I$, states 2-8) and another trajectory ends up in the excited state channel ($CH_2X + I^*$, states 9-12). While the two trajectories for CH_2I_2 end up on states with different potential energy, they lead to very similar TKE because of hopping between potentials as the molecule dissociates, redistributing kinetic energy also to rotation and vibrations of the molecular fragment. This is in contrast with CH_2IBr, for which the TKE for the two trajectories is quite different because the trajectories do not hop between groups of states that lead to different potential energy after about 20 fs.

For both CH_2I_2 and CH_2IBr, the lower-lying cationic states are bound

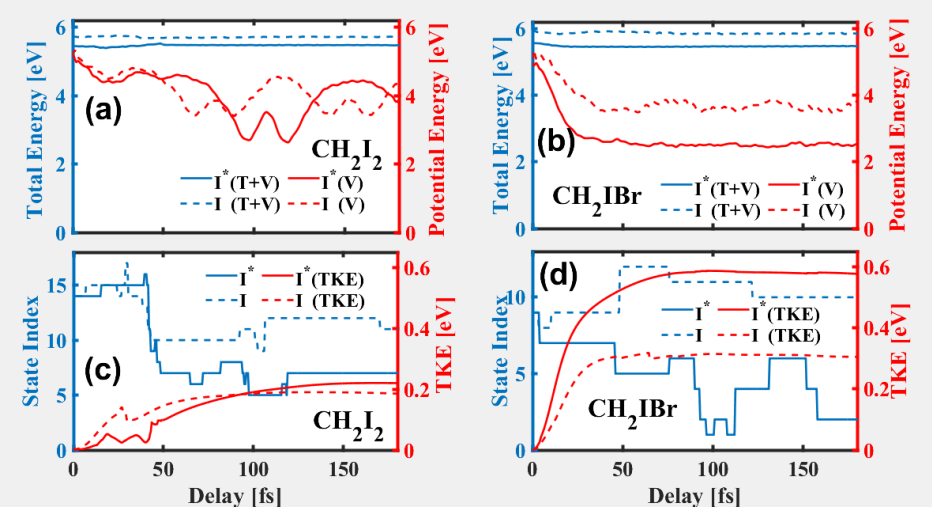

Figure C.13: **Surface hopping trajectories for CH_2I_2 and CH_2IBr.** Energies and state indices for two representative trajectories of CH_2I_2 and CH_2IBr. Panel (a) plots the time-dependent total energy and potential energy (V in the legend), whereas panel (c) underneath shares the same x-axis with panel (a), showing the state indices and TKEs. Panels (a) and (c) showcase the trajectories for CH_2I_2, whereas panels (b) and (d) are for CH_2IBr. In the legend, T represents kinetic energy, and V represents potential energy.

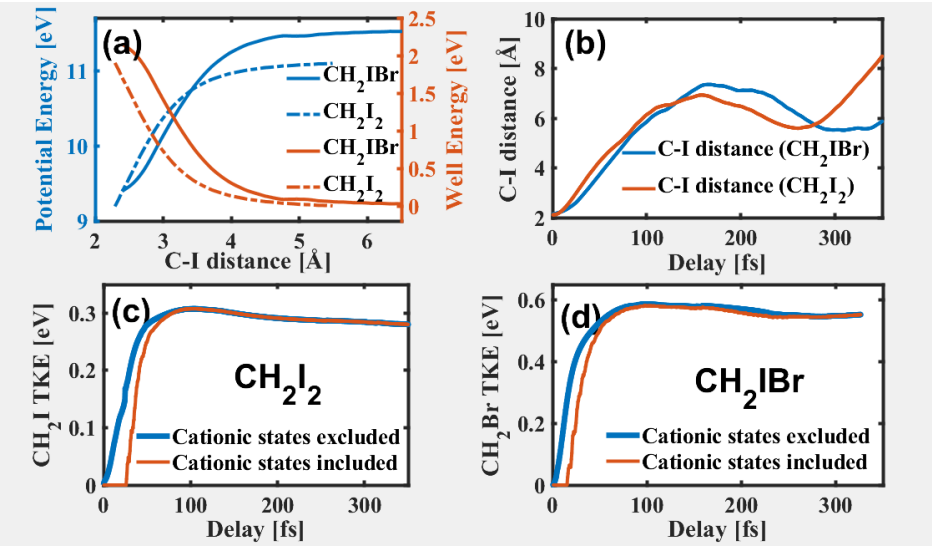

Figure C.14: **Kinetic energy of CH_2I^+ and CH_2Br^+ with and without compensation for dynamics in the cation.** Panel (a) blue colored lines (using left hand y-axis) showcase the averaged potential energies of cationic bound state of CH_2I_2 and CH_2IBr shown in Fig. 3 panels (c) and (d), respectively. By the right hand y-axis, the red colored lines show the well depth of the cationic state potential which is the energy difference from the FC region to where the potential becoming flat. Panel (b) depicts the the dissociating C-I bond length as function of time for a trajectory of CH_2I_2 and CH_2IBr. Panels (c) and (d) show a comparison of the TKE for CH_2I_2 and CH_2IBr with and without accounting for the cationic potential.

states. A natural question is how these bound-state potential wells affect the kinetic energy release upon the ionization. Fig. C.14 panel (a) shows the cationic state potential when averaged over the lower states that can be accessed by the pump and probe pulse energies as well as the well depth for both CH_2I_2 and CH_2IBr. One can see that the depth is on the order of 2 eV, which can have a significant effect on the kinetic energy after ionization (if ionization happens at a location within the well).

In order to evaluate this effect, we examine the (dissociative) C-I distance as function of time from the trajectories, as shown in panel (b). With this information, we are able to calculate the net kinetic energy, including the energy gained on the neutral states and lost in the cationic states as a

function a C-I distance or time. Panels (c) and (d) show a comparison of the translational kinetic energy (TKE) for CH_2I and CH_2Br with or without consideration of dynamics in the cation, respectively. It is clear that in the first 50 fs, the cationic bound states do have a significant effect on the final kinetic energy: The TKE changes quite a bit when one includes the cationic dynamics. However, after about 50 fs, the wave packet on the neutral states reaches a point where the cationic potential is almost flat and the molecule barely loses energy on the cationic state after ionization. Thus, the TKE is roughly the same as if one only considers the neutral state dynamics, i.e., the molecule does not lose a significant amount of kinetic energy in the cation.

Bibliography

[1] Dario Polli, Piero Altoè, Oliver Weingart, Katelyn M Spillane, Cristian Manzoni, Daniele Brida, Gaia Tomasello, Giorgio Orlandi, Philipp Kukura, Richard A Mathies, Marco Garavelli, and Giulio Cerullo. Conical intersection dynamics of the primary photoisomerization event in vision. *Nature*, 467:440, sep 2010.

[2] Yuan-Chung Cheng and Graham R. Fleming. Dynamics of light harvesting in photosynthesis. *Annual Review of Physical Chemistry*, 60(1):241–262, 2009.

[3] Jean-Marc L Pecourt, Jorge Peon, and Bern Kohler. Ultrafast internal conversion of electronically excited rna and dna nucleosides in water. *Journal of the American Chemical Society*, 122(38):9348–9349, 2000.

[4] Carlos E. Crespo-Hernández, Boiko Cohen, Patrick M. Hare, and Bern Kohler. Ultrafast excited-state dynamics in nucleic acids. *Chemical Reviews*, 104(4):1977–2020, 2004.

[5] Clélia Canuel, Michel Mons, François Piuzzi, Benjamin Tardivel, Iliana Dimicoli, and Mohamed Elhanine. Excited states dynamics of dna and rna bases: Characterization of a stepwise deactivation pathway in the gas phase. *The Journal of chemical physics*, 122(7):074316, 2005.

[6] Thomas Gustavsson, Roberto Improta, and Dimitra Markovitsi. Dna/rna: building blocks of life under uv irradiation. *The Journal of Physical Chemistry Letters*, 1(13):2025–2030, 2010.

[7] Ho-Jin Son, Shengye Jin, Sameer Patwardhan, Sander J. Wezenberg, Nak Cheon Jeong, Monica So, Christopher E. Wilmer, Amy A. Sarjeant, George C. Schatz, Randall Q. Snurr, Omar K. Farha, Gary P.

Wiederrecht, and Joseph T. Hupp. Light-harvesting and ultrafast energy migration in porphyrin-based metal–organic frameworks. *Journal of the American Chemical Society*, 135(2):862–869, 2013.

[8] Xiyou Li, Louise E. Sinks, Boris Rybtchinski, and Michael R. Wasielewski. Ultrafast aggregate-to-aggregate energy transfer within self-assembled light-harvesting columns of zinc phthalocyanine tetrakis(perylenediimide). *Journal of the American Chemical Society*, 126(35):10810–10811, 2004.

[9] Rongchao Jin, YunWei Cao, Chad A Mirkin, KL Kelly, George C Schatz, and JG Zheng. Photoinduced conversion of silver nanospheres to nanoprisms. *science*, 294(5548):1901–1903, 2001.

[10] Matthias Seel and Wolfgang Domcke. Femtosecond time-resolved ionization spectroscopy of ultrafast internal-conversion dynamics in polyatomic molecules: Theory and computational studies. *The Journal of chemical physics*, 95(11):7806–7822, 1991.

[11] Susanne Ullrich, Thomas Schultz, Marek Z Zgierski, and Albert Stolow. Direct observation of electronic relaxation dynamics in adenine via time-resolved photoelectron spectroscopy. *Journal of the American Chemical Society*, 126(8):2262–2263, 2004.

[12] Takuya Horio, Takao Fuji, Yoshi-Ichi Suzuki, and Toshinori Suzuki. Probing ultrafast internal conversion through conical intersection via time-energy map of photoelectron angular anisotropy. *Journal of the American Chemical Society*, 131(30):10392–10393, 2009.

[13] H Tao, T Allison, T Wright, A Stooke, C Khurmi, J Van Tilborg, Y Liu, R Falcone, A Belkacem, and T Martinez. Ultrafast internal conversion in ethylene. i. the excited state lifetime. *The Journal of chemical physics*, 134(24):244306, 2011.

[14] TK Allison, H Tao, WJ Glover, TW Wright, AM Stooke, Champak Khurmi, J Van Tilborg, Y Liu, RW Falcone, TJ Martínez, et al. Ultrafast internal conversion in ethylene. ii. mechanisms and pathways for quenching and hydrogen elimination. *The Journal of chemical physics*, 136(12):124317, 2012.

[15] C Dugave and L Demange. Cis-trans isomerization of organic molecules and biomolecules: implications and applications. *Chem. Rev.*, 103:2475–2532, 2003.

[16] Todd J Martinez. Insights for light-driven molecular devices from ab initio multiple spawning excited-state dynamics of organic and biological chromophores. *Acc. Chem. Res.*, 39(2):119–126, 2006.

[17] Benjamin G Levine and Todd J Martínez. Isomerization through conical intersections. *Annu. Rev. Phys. Chem.*, 58:613–634, 2007.

[18] Andrei C Florean, David Cardoza, James L White, JK Lanyi, Roseanne J Sension, and Philip H Bucksbaum. Control of retinal isomerization in bacteriorhodopsin in the high-intensity regime. *Proceedings of the National Academy of Sciences*, 106(27):10896–10900, 2009.

[19] Sanghamitra Deb and Peter M Weber. The ultrafast pathway of photon-induced electrocyclic ring-opening reactions: the case of 1, 3-cyclohexadiene. *Ann. Rev. Phys. Chem.*, 62:19–39, 2011.

[20] Wim G Roeterdink and Maurice HM Janssen. Femtosecond velocity map imaging of dissociative ionization dynamics in cf 3 i. *Physical Chemistry Chemical Physics*, 4(4):601–612, 2002.

[21] Jie Yang, Xiaolei Zhu, Thomas JA Wolf, Zheng Li, J Pedro F Nunes, Ryan Coffee, James P Cryan, Markus Gühr, Kareem Hegazy, Tony F Heinz, et al. Imaging cf3i conical intersection and photodissociation dynamics with ultrafast electron diffraction. *Science*, 361(6397):64–67, 2018.

[22] Spencer L Horton, Yusong Liu, Ruaridh Forbes, Varun Makhija, Rune Lausten, Albert Stolow, Paul Hockett, Philipp Marquetand, Tamás Rozgonyi, and Thomas Weinacht. Excited state dynamics of ch2i2 and ch2bri studied with uv pump vuv probe photoelectron spectroscopy. *The Journal of chemical physics*, 150(17):174201, 2019.

[23] Elio G Champenois, Loren Greenman, Niranjan Shivaram, James P Cryan, Kirk A Larsen, Thomas N Rescigno, C William McCurdy, Ali Belkacem, and Daniel S Slaughter. Ultrafast photodissociation dynamics and nonadiabatic coupling between excited electronic states

of methanol probed by time-resolved photoelectron spectroscopy. *J. Chem. Phys.*, 150(11):114301, 2019.

[24] Yusong Liu, Spencer L Horton, Jie Yang, J Pedro F Nunes, Xiaozhe Shen, Thomas JA Wolf, Ruaridh Forbes, Chuan Cheng, Bryan Moore, Martin Centurion, et al. Spectroscopic and structural probing of excited-state molecular dynamics with time-resolved photoelectron spectroscopy and ultrafast electron diffraction. *Physical Review X*, 10(2):021016, 2020.

[25] Byungjoo Kim, Carolyn P Schick, and Peter M Weber. Time-delayed two-color photoelectron spectra of aniline, 2-aminopyridine, and 3-aminopyridine: Snapshots of the nonadiabatic curve crossings. *The Journal of chemical physics*, 103(16):6903–6913, 1995.

[26] DSN Parker, RS Minns, TJ Penfold, GA Worth, and HH Fielding. Ultrafast dynamics of the s1 excited state of benzene. *Chemical Physics Letters*, 469(1-3):43–47, 2009.

[27] RS Minns, DSN Parker, TJ Penfold, GA Worth, and HH Fielding. Competing ultrafast intersystem crossing and internal conversion in the "channel 3" region of benzene. *Physical Chemistry Chemical Physics*, 12(48):15607–15615, 2010.

[28] Ahmed H Zewail. Femtochemistry: Atomic-scale dynamics of the chemical bond. *The Journal of Physical Chemistry A*, 104(24):5660–5694, 2000.

[29] Thomas Weinacht and Brett Pearson. *Time-Resolved Spectroscopy: An Experimental Perpective*. Dec 2018.

[30] Spiridoula Matsika and Pascal Krause. Nonadiabatic events and conical intersections. *Annual review of physical chemistry*, 62:621–643, 2011.

[31] Michal Ben-Nun, Jason Quenneville, and Todd J Martínez. Ab initio multiple spawning: Photochemistry from first principles quantum molecular dynamics. *The Journal of Physical Chemistry A*, 104(22):5161–5175, 2000.

[32] David R Yarkony. Conical intersections: The new conventional wisdom. *The Journal of Physical Chemistry A*, 105(26):6277–6293, 2001.

[33] David J Tannor. *Introduction to quantum mechanics: a time-dependent perspective*. University Science Books, 2007.

[34] SA Trushin, W Fuß, T Schikarski, WE Schmid, and KL Kompa. Femtosecond photochemical ring opening of 1, 3-cyclohexadiene studied by time-resolved intense-field ionization. *The Journal of chemical physics*, 106(22):9386–9389, 1997.

[35] W Fuß, WE Schmid, and SA Trushin. Time-resolved dissociative intense-laser field ionization for probing dynamics: Femtosecond photochemical ring opening of 1, 3-cyclohexadiene. *The Journal of Chemical Physics*, 112(19):8347–8362, 2000.

[36] Marija Kotur, Thomas Weinacht, Brett J Pearson, and Spiridoula Matsika. Closed-loop learning control of isomerization using shaped ultrafast laser pulses in the deep ultraviolet. *The Journal of chemical physics*, 130(13):134311, 2009.

[37] Brenden C Arruda and Roseanne J Sension. Ultrafast polyene dynamics: the ring opening of 1, 3-cyclohexadiene derivatives. *Physical Chemistry Chemical Physics*, 16(10):4439–4455, 2014.

[38] Christine C Pemberton, Yao Zhang, Kenichiro Saita, Adam Kirrander, and Peter M Weber. From the (1b) spectroscopic state to the photochemical product of the ultrafast ring-opening of 1, 3-cyclohexadiene: a spectral observation of the complete reaction path. *The Journal of Physical Chemistry A*, 119(33):8832–8845, 2015.

[39] Shunsuke Adachi, Motoki Sato, and Toshinori Suzuki. Direct observation of ground-state product formation in a 1, 3-cyclohexadiene ring-opening reaction. *The journal of physical chemistry letters*, 6(3):343–346, 2015.

[40] Andrew R Attar, Aditi Bhattacherjee, CD Pemmaraju, Kirsten Schnorr, Kristina D Closser, David Prendergast, and Stephen R Leone. Femtosecond x-ray spectroscopy of an electrocyclic ring-opening reaction. *Science*, 356(6333):54–59, 2017.

[41] Jianming Cao, Hyotcherl Ihee, and Ahmed H Zewail. Ultrafast electron diffraction and direct observation of transient structures in a chemical

reaction. *Proceedings of the National Academy of Sciences*, 96(2):338–342, 1999.

[42] Hyotcherl Ihee, Vladimir A Lobastov, Udo M Gomez, Boyd M Goodson, Ramesh Srinivasan, Chong-Yu Ruan, and Ahmed H Zewail. Direct imaging of transient molecular structures with ultrafast diffraction. *Science*, 291(5503):458–462, 2001.

[43] J Charles Williamson and Ahmed H Zewail. Ultrafast electron diffraction. 4. molecular structures and coherent dynamics. *The Journal of Physical Chemistry*, 98(11):2766–2781, 1994.

[44] Marcos Dantus, Scott B Kim, J Charles Williamson, and Ahmed H Zewail. Ultrafast electron diffraction. 5. experimental time resolution and applications. *The Journal of Physical Chemistry*, 98(11):2782–2796, 1994.

[45] J Charles Williamson, Jianming Cao, Hyotcherl Ihee, Hans Frey, and Ahmed H Zewail. Clocking transient chemical changes by ultrafast electron diffraction. *Nature*, 386(6621):159, 1997.

[46] S. P. Weathersby, G. Brown, M. Centurion, T. F. Chase, R. Coffee, J. Corbett, J. P. Eichner, J. C. Frisch, A. R. Fry, M. Gühr, N. Hartmann, C. Hast, R. Hettel, R. K. Jobe, E. N. Jongewaard, J. R. Lewandowski, R. K. Li, A. M. Lindenberg, I. Makasyuk, J. E. May, D. McCormick, M. N. Nguyen, A. H. Reid, X. Shen, K. Sokolowski-Tinten, T. Vecchione, S. L. Vetter, J. Wu, J. Yang, H. A. Dürr, and X. J. Wang. Mega-electron-volt ultrafast electron diffraction at slac national accelerator laboratory. *Review of Scientific Instruments*, 86(7):073702, 2015.

[47] Xiaozhe Shen, JPF Nunes, J Yang, RK Jobe, RK Li, Ming-Fu Lin, B Moore, M Niebuhr, SP Weathersby, TJA Wolf, et al. Femtosecond gas-phase mega-electron-volt ultrafast electron diffraction. *Structural Dynamics*, 6(5):054305, 2019.

[48] Thomas JA Wolf, DM Sanchez, J Yang, RM Parrish, JPF Nunes, M Centurion, R Coffee, JP Cryan, M Gühr, K Hegazy, et al. The photochemical ring-opening of 1, 3-cyclohexadiene imaged by ultrafast electron diffraction. *Nature chemistry*, 11(6):504–509, 2019.

[49] Albert Stolow, Arthur E Bragg, and Daniel M Neumark. Femtosecond time-resolved photoelectron spectroscopy. *Chem. Rev.*, 104(4):1719–1758, 2004.

[50] Toshinori Suzuki. Time-resolved photoelectron spectroscopy of non-adiabatic electronic dynamics in gas and liquid phases. *International Reviews in Physical Chemistry*, 31(2):265–318, 2012.

[51] Michael S Schuurman and Albert Stolow. Dynamics at conical intersections. *Annual review of physical chemistry*, 69:427–450, 2018.

[52] Andrey E Boguslavskiy, Oliver Schalk, Niklas Gador, William J Glover, Toshifumi Mori, Thomas Schultz, Michael S Schuurman, Todd J Martínez, and Albert Stolow. Excited state non-adiabatic dynamics of the smallest polyene, trans 1, 3-butadiene. i. time-resolved photoelectron-photoion coincidence spectroscopy. *The Journal of chemical physics*, 148(16):164302, 2018.

[53] John C. Tully. Molecular dynamics with electronic transitions. *J. Chem. Phys.*, 93(2):1061–1071, 1990.

[54] John C Tully. Perspective: Nonadiabatic dynamics theory. *The Journal of chemical physics*, 137(22):22A301, 2012.

[55] Pratip Chakraborty. *Investigating Ultrafast Photoexcited Dynamics of Organic Chromophores*. PhD thesis, Temple University. Libraries, 2020.

[56] Daniel M Neumark. Time-resolved photoelectron spectroscopy of molecules and clusters. *Annual review of physical chemistry*, 52(1):255–277, 2001.

[57] Toshinori Suzuki. Femtosecond time-resolved photoelectron imaging. *Annu. Rev. Phys. Chem.*, 57:555–592, 2006.

[58] Adam D Smith, Emily M Warne, Darren Bellshaw, Daniel A Horke, Maria Tudorovskya, Emma Springate, Alfred JH Jones, Cephise Cacho, Richard T Chapman, Adam Kirrander, et al. Mapping the complete reaction path of a complex photochemical reaction. *Physical review letters*, 120(18):183003, 2018.

[59] John N Sweetser, David N Fittinghoff, and Rick Trebino. Transient-grating frequency-resolved optical gating. *Optics letters*, 22(8):519–521, 1997.

[60] Valentin Petrov, Fabian Rotermund, Frank Noack, Jens Ringling, Olaf Kittelmann, and Ryuichi Komatsu. Frequency conversion of ti: sapphire-based femtosecond laser systems to the 200-nm spectral region using nonlinear optical crystals. *IEEE Journal of selected topics in quantum electronics*, 5(6):1532–1542, 1999.

[61] Teruto Kanai, Takeshi Kanda, Taro Sekikawa, Shuntaro Watanabe, Tadashi Togashi, Chuangtian Chen, Chengqian Zhang, Zuyan Xu, and Jiyang Wang. Generation of vacuum-ultraviolet light below 160 nm in a kbbf crystal by the fifth harmonic of a single-mode ti: sapphire laser. *JOSA B*, 21(2):370–375, 2004.

[62] Valentin Petrov, Frank Noack, Dezhong Shen, Feng Pan, Guangqiu Shen, Xiaoqing Wang, Ryuichi Komatsu, and Volker Alex. Application of the nonlinear crystal srb 4 o 7 for ultrafast diagnostics converting to wavelengths as short as 125 nm. *Optics letters*, 29(4):373–375, 2004.

[63] A Börzsönyi, Zs Heiner, MP Kalashnikov, AP Kovács, and K Osvay. Dispersion measurement of inert gases and gas mixtures at 800 nm. *Applied optics*, 47(27):4856–4863, 2008.

[64] M Beutler, M Ghotbi, F Noack, and I Hertel. Generation of sub-50-fs vacuum ultraviolet pulses by four-wave mixing in argon. *Optics Letters*, 35(9):1491–1493, 2010.

[65] M Ghotbi, M Beutler, and F Noack. Generation of 2.5 μj vacuum ultraviolet pulses with sub-50 fs duration by noncollinear four-wave mixing in argon. *Optics letters*, 35(20):3492–3494, 2010.

[66] John Reintjes. *Nonlinear optical parametric processes in liquids and gases*. Elsevier, 2012.

[67] Spencer Lourdes Horton. *Photoionizaion as a Probe of Ultrafast Molecular Dynamics*. PhD thesis, State University of New York at Stony Brook, 2018.

[68] Spencer L Horton, Yusong Liu, Pratip Chakraborty, Spiridoula Matsika, and Thomas Weinacht. Ultrafast internal conversion dynamics of highly excited pyrrole studied with vuv/uv pump probe spectroscopy. *The Journal of chemical physics*, 146(6):064306, 2017.

[69] Spencer L Horton, Yusong Liu, Pratip Chakraborty, Spiridoula Matsika, and Thomas Weinacht. Vibrationally assisted below-threshold ionization. *Physical Review A*, 95(6):063413, 2017.

[70] Spencer L Horton, Yusong Liu, Pratip Chakraborty, Philipp Marquetand, Tamás Rozgonyi, Spiridoula Matsika, and Thomas Weinacht. Strong-field-versus weak-field-ionization pump-probe spectroscopy. *Physical Review A*, 98(5):053416, 2018.

[71] André TJB Eppink and David H Parker. Velocity map imaging of ions and electrons using electrostatic lenses: Application in photoelectron and photofragment ion imaging of molecular oxygen. *Review of Scientific Instruments*, 68(9):3477–3484, 1997.

[72] Arthur Zhao, Péter Sándor, and Thomas Weinacht. Coincidence velocity map imaging using a single detector. *The Journal of chemical physics*, 147(1):013922, 2017.

[73] B Winter, SJ King, M Brouard, and C Vallance. A fast microchannel plate-scintillator detector for velocity map imaging and imaging mass spectrometry. *Review of Scientific Instruments*, 85(2):023306, 2014.

[74] Hans Lomholt Skriver and NM Rosengaard. Surface energy and work function of elemental metals. *Physical Review B*, 46(11):7157, 1992.

[75] Arthur Zhao, Martin van Beuzekom, Bram Bouwens, Dmitry Byelov, Irakli Chakaberia, Chuan Cheng, Erik Maddox, Andrei Nomerotski, Peter Svihra, Jan Visser, et al. Coincidence velocity map imaging using tpx3cam, a time stamping optical camera with 1.5 ns timing resolution. *Review of Scientific Instruments*, 88(11):113104, 2017.

[76] Jørgen E Hansen and Willy Persson. Revised analysis of singly ionized xenon, xe ii. *Physica Scripta*, 36(4):602, 1987.

[77] O Hüter and F Temps. Note: Energy calibration of a femtosecond photoelectron imaging detector with correction for the ponderomotive

shift of atomic ionization energies. *Review of Scientific Instruments*, 88(4):046101, 2017.

[78] P Farmanara, O Steinkellner, M Wick, M Wittmann, G Korn, V Stert, and W Radloff. Ultrafast internal conversion and photodissociation of molecules excited by femtosecond 155 nm laser pulses. *The Journal of Chemical Physics*, 111(14):6264–6270, 1999.

[79] T Allison. *Femtosecond molecular dynamics studied with vacuum ultraviolet pulse pairs*. PhD thesis, UC Berkeley: Physics, 2010.

[80] Andrei Nomerotski, I Chakaberia, M Fisher-Levine, Z Janoska, P Takacs, and T Tsang. Characterization of timepixcam, a fast imager for the time-stamping of optical photons. *Journal of instrumentation*, 12(01):C01017, 2017.

[81] T Poikela, J Plosila, T Westerlund, M Campbell, M De Gaspari, X Llopart, V Gromov, R Kluit, M Van Beuzekom, F Zappon, et al. Timepix3: a 65k channel hybrid pixel readout chip with simultaneous toa/tot and sparse readout. *Journal of instrumentation*, 9(05):C05013, 2014.

[82] B van der Heijden, J Visser, M van Beuzekom, H Boterenbrood, S Kulis, B Munneke, and F Schreuder. Spidr, a general-purpose readout system for pixel asics. *Journal of instrumentation*, 12(02):C02040, 2017.

[83] Michael I Davis et al. *Electron diffraction in gases*. M. Dekker, 1971.

[84] Francesc Salvat, Aleksander Jablonski, and Cedric J. Powell. Elsepa—dirac partial-wave calculation of elastic scattering of electrons and positrons by atoms, positive ions and molecules. *Computer Physics Communications*, 165:157–190, 01 2005.

[85] Jie Yang, Xiaolei Zhu, J Pedro F Nunes, K Yu Jimmy, Robert M Parrish, Thomas JA Wolf, Martin Centurion, Markus Gühr, Renkai Li, Yusong Liu, et al. Simultaneous observation of nuclear and electronic dynamics by ultrafast electron diffraction. *Science*, 368(6493):885–889, 2020.

[86] Roy Glauber and Verner Schomaker. The theory of electron diffraction. *Physical Review*, 89(4):667, 1953.

[87] Peter Reckenthaeler, Martin Centurion, Werner Fuß, Sergei A Trushin, Ferenc Krausz, and Ernst E Fill. Time-resolved electron diffraction from selectively aligned molecules. *Physical Review Letters*, 102(21):213001, 2009.

[88] Jie Yang, Markus Guehr, Theodore Vecchione, Matthew S Robinson, Renkai Li, Nick Hartmann, Xiaozhe Shen, Ryan Coffee, Jeff Corbett, Alan Fry, Kelly Gaffney, Tais Gorkhover, Carsten Hast, Keith Jobe, Igor Makasyuk, Alexander Reid, Joseph Robinson, Sharon Vetter, Fenglin Wang, Stephen Weathersby, Charles Yoneda, Martin Centurion, and Xijie Wang. Diffractive imaging of a rotational wavepacket in nitrogen molecules with femtosecond megaelectronvolt electron pulses. *Nature Communications*, 7:11232, apr 2016.

[89] Jie Yang. *Ultrafast electron diffraction from laser-aligned molecules in the gas phase*. The University of Nebraska-Lincoln, 2016.

[90] Lawrence O Brockway. Electron diffraction by gas molecules. *Reviews of Modern Physics*, 8(3):231, 1936.

[91] Ramesh Srinivasan, Vladimir A Lobastov, Chong-Yu Ruan, and Ahmed H Zewail. Ultrafast electron diffraction (ued) a new development for the 4d determination of transient molecular structures. *Helvetica chimica acta*, 86(6):1761–1799, 2003.

[92] Ramesh Srinivasan, Jonathan S Feenstra, Sang Tae Park, Shoujun Xu, and Ahmed H Zewail. Dark structures in molecular radiationless transitions determined by ultrafast diffraction. *Science*, 307(5709):558–563, 2005.

[93] R Akre, D Dowell, P Emma, J Frisch, S Gilevich, G Hays, Ph Hering, R Iverson, C Limborg-Deprey, H Loos, et al. Commissioning the linac coherent light source injector. *Physical Review Special Topics-Accelerators and Beams*, 11(3):030703, 2008.

[94] Vladimir Dribinski, Alexei Ossadtchi, Vladimir A Mandelshtam, and Hanna Reisler. Reconstruction of abel-transformable images: The

gaussian basis-set expansion abel transform method. *Review of Scientific Instruments*, 73(7):2634–2642, 2002.

[95] Gustavo A Garcia, Laurent Nahon, and Ivan Powis. Two-dimensional charged particle image inversion using a polar basis function expansion. *Review of Scientific Instruments*, 75(11):4989–4996, 2004.

[96] Kyle J Wilkin, Robert M Parrish, Jie Yang, Thomas JA Wolf, J Pedro F Nunes, Markus Guehr, Renkai Li, Xiaozhe Shen, Qiang Zheng, Xijie Wang, et al. Diffractive imaging of dissociation and ground-state dynamics in a complex molecule. *Physical Review A*, 100(2):023402, 2019.

[97] C Melania Oana and Anna I Krylov. Dyson orbitals for ionization from the ground and electronically excited states within equation-of-motion coupled-cluster formalism: Theory, implementation, and examples. *The Journal of Chemical Physics*, 127(23):234106, 2007.

[98] Sebastian Mai, Abed Mohamadzade, Philipp Marquetand, Leticia González, and Susanne Ullrich. Simulated and experimental time-resolved photoelectron spectra of the intersystem crossing dynamics in 2-thiouracil. *Molecules*, 23(11):2836, 2018.

[99] Wilmer Arbelo-González, Rachel Crespo-Otero, and Mario Barbatti. Steady and time-resolved photoelectron spectra based on nuclear ensembles. *J. Chem. Theory Comput.*, 12:5037–5049, 2016.

[100] J. Spencer Baskin and Ahmed H. Zewail. Ultrafast electron diffraction: Oriented molecular structures in space and time. *ChemPhysChem*, 6(11):2261–2276, 2005.

[101] J. Spencer Baskin and Ahmed H. Zewail. Oriented ensembles in ultrafast electron diffraction. *ChemPhysChem*, 7(7):1562–1574, 2006.

[102] M Barbatti, J Paier, and H Lischka. Photochemistry of ethylene: A multireference configuration interaction investigation of the excited-state energy surfaces. *The Journal of chemical physics*, 121(23):11614–11624, 2004.

[103] Hongli Tao, Benjamin G Levine, and Todd J Martínez. Ab initio multiple spawning dynamics using multi-state second-order perturbation

theory. *The Journal of Physical Chemistry A*, 113(49):13656–13662, 2009.

[104] Toshifumi Mori, William J Glover, Michael S Schuurman, and Todd J Martinez. Role of rydberg states in the photochemical dynamics of ethylene. *The Journal of Physical Chemistry A*, 116(11):2808–2818, 2012.

[105] Elio G Champenois, Niranjan H Shivaram, Travis W Wright, Chan-Shan Yang, Ali Belkacem, and James P Cryan. Involvement of a low-lying rydberg state in the ultrafast relaxation dynamics of ethylene. *J. Chem. Phys.*, 144(1):014303, 2016.

[106] Simon P Neville, Majed Chergui, Albert Stolow, and Michael S Schuurman. Ultrafast x-ray spectroscopy of conical intersections. *Physical review letters*, 120(24):243001, 2018.

[107] Samer Gozem, Hoi Ling Luk, Igor Schapiro, and Massimo Olivucci. Theory and simulation of the ultrafast double-bond isomerization of biological chromophores. *Chem. Rev.*, 117(22):13502–13565, 2017.

[108] Yusheng Dou, Ben R Torralva, and Roland E Allen. Detailed mechanism for trans- cis photoisomerization of butadiene following a femtosecond-scale laser pulse. *The Journal of Physical Chemistry A*, 107(42):8817–8824, 2003.

[109] Benjamin G Levine and Todd J Martínez. Ab initio multiple spawning dynamics of excited butadiene: Role of charge transfer. *The Journal of Physical Chemistry A*, 113(46):12815–12824, 2009.

[110] Paul Hockett, Enrico Ripani, Andrew Rytwinski, and Albert Stolow. Probing ultrafast dynamics with time-resolved multi-dimensional coincidence imaging: Butadiene. *Journal of Modern Optics*, 60(17):1409–1425, 2013.

[111] Oliver Schalk, Andrey E Boguslavskiy, and Albert Stolow. Two-photon excited state dynamics of dark valence, rydberg, and superexcited states in 1, 3-butadiene. *The journal of physical chemistry letters*, 5(3):560–565, 2014.

[112] William J Glover, Toshifumi Mori, Michael S Schuurman, Andrey E Boguslavskiy, Oliver Schalk, Albert Stolow, and Todd J Martínez. Excited state non-adiabatic dynamics of the smallest polyene, trans 1, 3-butadiene. ii. ab initio multiple spawning simulations. *J. Chem. Phys.*, 148(16):164303, 2018.

[113] Jaehee Kim, Hongli Tao, James L White, Vladimir S Petrovic, Todd J Martinez, and Philip H Bucksbaum. Control of 1, 3-cyclohexadiene photoisomerization using light-induced conical intersections. *The Journal of Physical Chemistry A*, 116(11):2758–2763, 2012.

[114] Jaehee Kim, Hongli Tao, Todd J Martinez, and Phil Bucksbaum. Ab initio multiple spawning on laser-dressed states: a study of 1, 3-cyclohexadiene photoisomerization via light-induced conical intersections. *J. Phys. B: At. Mol. Opt. Phys.*, 48(16):164003, 2015.

[115] MP Minitti, JM Budarz, A Kirrander, JS Robinson, D Ratner, TJ Lane, D Zhu, JM Glownia, M Kozina, HT Lemke, et al. Imaging molecular motion: Femtosecond x-ray scattering of an electrocyclic chemical reaction. *Phys. Rev. Lett.*, 114(25):255501, 2015.

[116] Werner Fuß, Subhasis Panja, Wolfram E Schmid, and Sergei A Trushin. Competing ultrafast cis-trans isomerization and ring closure of cyclohepta-1, 3-diene and cyclo-octa-1, 3-diene. *Molecular Physics*, 104(5-7):1133–1143, 2006.

[117] Keiko Komori-Orisaku, Yui Hirose, and Izumi Iwakura. Pulsed nd: Yag laser-induced photoreaction of cis, cis-1, 3-cyclooctadiene at 266 nm: selective cyclization to cis-bicyclo [4.2. 0] oct-7-ene. *Photochemical & Photobiological Sciences*, 16(2):146–150, 2017.

[118] P Bischof and E Heilbronner. Photoelektron-spektren von cycloalkenen und cycloalkadienen. vorläufige mitteilung. *Helvetica Chimica Acta*, 53(7):1677–1682, 1970.

[119] Pratip Chakraborty, Yusong Liu, Thomas Weinacht, and Spiridoula Matsika. Excited state dynamics of cis,cis-1,3-cyclooctadiene: Non-adiabatic trajectory surface hopping. *The Journal of Chemical Physics*, 152(17):174302, 2020.

[120] Anja Röder. Trpes simulator, `https://github.com/AnjaTRPES/TRPES-simulator`, 2018.

[121] Oliver Schalk, Andrey E Boguslavskiy, and Albert Stolow. Substituent effects on dynamics at conical intersections: Cyclopentadienes. *The Journal of Physical Chemistry A*, 114(12):4058–4064, 2010.

[122] Oliver Schalk, Andrey E Boguslavskiy, Michael S Schuurman, Rasmus Y Brogaard, Andreas N Unterreiner, Anna Wrona-Piotrowicz, Nick H Werstiuk, and Albert Stolow. Substituent effects on dynamics at conical intersections: cycloheptatrienes. *The Journal of Physical Chemistry A*, 117(40):10239–10247, 2013.

[123] Matthias Ruckenbauer, Sebastian Mai, Philipp Marquetand, and Leticia González. Revealing deactivation pathways hidden in time-resolved photoelectron spectra. *Scientific reports*, 6:35522, 2016.

[124] Oliver Schalk, Ting Geng, Travis Thompson, Noel Baluyot, Richard D Thomas, Enrico Tapavicza, and Tony Hansson. Cyclohexadiene revisited: A time-resolved photoelectron spectroscopy and ab initio study. *The Journal of Physical Chemistry A*, 120(15):2320–2329, 2016.

[125] TJA Wolf, Thomas Scheby Kuhlman, Oliver Schalk, TJ Martínez, Klaus Braagaard Møller, A Stolow, and A-N Unterreiner. Hexamethylcyclopentadiene: time-resolved photoelectron spectroscopy and ab initio multiple spawning simulations. *Phys. Chem. Chem. Phys.*, 16(23):11770–11779, 2014.

[126] Hongli Tao. *First principles molecular dynamics and control of photochemical reactions*. PhD thesis, Stanford University, 2011.

[127] Rachel Crespo-Otero and Mario Barbatti. Recent advances and perspectives on nonadiabatic mixed quantum–classical dynamics. *Chemical reviews*, 118(15):7026–7068, 2018.

[128] Leticia González and Roland Lindh. Quantum chemistry and dynamics of excited states.

[129] Carlos E. Crespo-Hernández, Boiko Cohen, Patrick M. Hare, and Bern Kohler. Ultrafast excited-state dynamics in nucleic acids. *Chem. Rev.*, 104(4):1977–2020, 2004.

[130] Chris T. Middleton, Kimberly de La Harpe, Charlene Su, Yu Kay Law, Carlos E. Crespo-Hernández, and Bern Kohler. Dna excited-state dynamics: From single bases to the double helix. *Ann. Rev. Phys. Chem.*, 60(1):217–239, 2009.

[131] Patrick M. Hare, Carlos E. Crespo-Hernandez, and Bern Kohler. Solvent-dependent photophysics of 1-cyclohexyluracil: Ultrafast branching in the initial bright state leads nonradiatively to the electronic ground state and a long-lived $^1n\pi^*$ state. *J. Phys. Chem. B*, 110:18641–18650, 2006.

[132] Patrick M. Hare, Carlos E. Crespo-Hernandez, and Bern Kohler. Internal conversion to the electronic ground state occurs via two distinct pathways for pyrimidine bases in aqueous solution. *Proc. Natl. Acad. Sci.*, 104:435 –440, 2007.

[133] Roberto Improta, Fabrizio Santoro, and Lluís Blancafort. Quantum mechanical studies on the photophysics and the photochemistry of nucleic acids and nucleobases. *Chem. Rev.*, 116(6):3540–3593, 2016.

[134] Susanne Ullrich, Antonio C. Borin, and Mario Barbatti, editors. *Topics in Current Chemistry - Photoinduced Phenomena in Nucleic Acids I*, volume 355. Springer, Berlin - Heidelberg, 2015.

[135] Susanne Ullrich, Antonio C. Borin, and Mario Barbatti, editors. *Topics in Current Chemistry - Photoinduced Phenomena in Nucleic Acids II*, volume 356. Springer, Berlin - Heidelberg, 2015.

[136] Thomas Gustavsson, Roberto Improta, and Dimitra Markovitsi. Dna/rna: Building blocks of life under uv irradiation. *J. Phys. Chem. Lett.*, 1(13):2025–2030, 2010.

[137] Hyuk Kang, Kang Taek Lee, Boyong Jung, Yeon Jae Ko, and Seong Keun Kim. Intrinsic lifetimes of the excited state of dna and rna bases. *J. Am. Chem. Soc.*, 124(44):12958–12959, 2002.

[138] Susanne Ullrich, Thomas Schultz, Marek Z. Zgierski, and Albert Stolow. Electronic relaxation dynamics in dna and rna bases studied by time-resolved photoelectron spectroscopy. *Phys. Chem. Chem. Phys.*, 6:2796–2801, 2004.

[139] Yonggang He, Chengyin Wu, and Wei Kong. Decay pathways of thymine and methyl-substituted uracil and thymine in the gas phase. *J. Phys. Chem. A*, 107(26):5145–5148, 2003.

[140] Yonggang He, Chengyin Wu, and Wei Kong. Photophysics of methyl-substituted uracils and thymines and their water complexes in the gas phase. *J. Phys. Chem. A*, 108(6):943–949, 2004.

[141] Clélia Canuel, Michel Mons, François Piuzzi, Benjamin Tardivel, Iliana Dimicoli, and Mohamed Elhanine. Excited states dynamics of dna and rna bases: Characterization of a stepwise deactivation pathway in the gas phase. *J. Chem. Phys.*, 122(7):074316, 2005.

[142] Thomas Gustavsson, Ákos Bányász, Elodie Lazzarotto, Dimitra Markovitsi, Giovanni Scalmani, Michael J. Frisch, Vincenzo Barone, and Roberto Improta. Singlet excited-state behavior of uracil and thymine in aqueous solution: A combined experimental and computational study of 11 uracil derivatives. *J. Am. Chem. Soc.*, 128(2):607–619, 2006.

[143] Thomas Gustavsson, Nilmoni Sarkar, Elodie Lazzarotto, Dimitra Markovitsi, Vincenzo Barone, and Roberto Improta. Solvent effect on the singlet excited-state dynamics of 5-fluorouracil in acetonitrile as compared with water. *J. Phys. Chem. B*, 110(26):12843–12847, 2006.

[144] M. Kotur, T. C. Weinacht, C. Zhou, and S. Matsika. Following ultrafast radiationless relaxation dynamics with strong field dissociative ionization: A comparison between adenine, uracil, and cytosine. *IEEE J. Sel. Top. Quantum Electron.*, 18(1):187–194, 2012.

[145] Spiridoula Matsika, Michael Spanner, Marija Kotur, and Thomas C. Weinacht. Ultrafast relaxation dynamics of uracil probed via strong field dissociative ionization. *J. Phys. Chem. A*, 117(48):12796–12801, 2013.

[146] Omair Ghafur, Stuart W. Crane, Michal Ryszka, Jana Bockova, Andre Rebelo, Lisa Saalbach, Simone De Camillis, Jason B. Greenwood, Samuel Eden, and Dave Townsend. Ultraviolet relaxation dynamics in uracil: Time-resolved photoion yield studies using a laser-based thermal desorption source. *J. Chem. Phys.*, 149(3):034301, 2018.

[147] Spiridoula Matsika. Radiationless decay of excited states of uracil through conical intersections. *J. Phys. Chem. A*, 108(37):7584–7590, 2004.

[148] Hanneli R. Hudock, Benjamin G. Levine, Alexis L. Thompson, Helmut Satzger, D. Townsend, N. Gador, S. Ullrich, Albert Stolow, and Todd J. Martínez. Ab initio molecular dynamics and time-resolved photoelectron spectroscopy of electronically excited uracil and thymine. *J. Phys. Chem. A*, 111(34):8500–8508, 2007.

[149] Harald Nieber and Nikos L Doltsinis. Elucidating ultrafast nonradiative decay of photoexcited uracil in aqueous solution by ab initio molecular dynamics. *Chemical Physics*, 347(1-3):405–412, 2008.

[150] Nikos L. Doltsinis, Phineus R. L. Markwick, Harald Nieber, and Holger Langer. *Ultrafast Radiationless Decay in Nucleic Acids: Insights From Nonadiabatic Ab Initio Molecular Dynamics*, pages 265–299. Springer Netherlands, Dordrecht, 2008.

[151] Zhenggang Lan, Eduardo Fabiano, and Walter Thiel. Photoinduced nonadiabatic dynamics of pyrimidine nucleobases: On-the-fly surface-hopping study with semiempirical methods. *J. Phys. Chem. B*, 113(11):3548–3555, 2009.

[152] Mario Barbatti, Adélia J. A. Aquino, Jaroslaw J. Szymczak, Dana Nachtigallová, Pavel Hobza, and Hans Lischka. Relaxation mechanisms of uv-photoexcited dna and rna nucleobases. *Proc. Natl. Acad. Sci.*, 107(50):21453–21458, 2010.

[153] Dana Nachtigallová, Adélia J. A. Aquino, Jaroslaw J. Szymczak, Mario Barbatti, Pavel Hobza, and Hans Lischka. Nonadiabatic dynamics of uracil: Population split among different decay mechanisms. *J. Phys. Chem. A*, 115(21):5247–5255, 2011.

[154] Benjamin P. Fingerhut, Konstantin E. Dorfman, and Shaul Mukamel. Monitoring nonadiabatic dynamics of the rna base uracil by uv pump–ir probe spectroscopy. *J. Phys. Chem. Lett.*, 4(11):1933–1942, 2013.

[155] Benjamin P. Fingerhut, Konstantin E. Dorfman, and Shaul Mukamel. Probing the conical intersection dynamics of the rna base uracil by uv-

pump stimulated-raman-probe signals; ab initio simulations. *J. Chem. Theory Comput.*, 10(3):1172–1188, 2014.

[156] Martin Richter, Sebastian Mai, Philipp Marquetand, and Leticia González. Ultrafast intersystem crossing dynamics in uracil unravelled by ab initio molecular dynamics. *Phys. Chem. Chem. Phys.*, 16:24423–24436, 2014.

[157] Bing Xue, Atsushi Yabushita, and Takayoshi Kobayashi. Ultrafast dynamics of uracil and thymine studied using a sub-10 fs deep ultraviolet laser. *Phys.Chem.Chem.Phys.*, 18:17044, 2016.

[158] Spencer L. Horton, Yusong Liu, Pratip Chakraborty, Philipp Marquetand, Tamás Rozgonyi, Spiridoula Matsika, and Thomas Weinacht. Strong-field- versus weak-field-ionization pump-probe spectroscopy. *Phys. Rev. A*, 98:053416, Nov 2018.

[159] Hui Yu, Jose A. Sanchez-Rodriguez, Marvin Pollum, Carlos E. Crespo-Hernández, Sebastian Mai, Philipp Marquetand, Leticia González, and Susanne Ullrich. Internal conversion and intersystem crossing pathways in uv excited, isolated uracils and their implications in prebiotic chemistry. *Phys. Chem. Chem. Phys.*, 18:20168–20176, 2016.

[160] Mihajlo Etinski, Timo Fleig, and Christel M. Marian. Intersystem crossing and characterization of dark states in the pyrimidine nucleobases uracil, thymine, and 1-methylthymine. *J. Phys. Chem. A*, 113(43):11809–11816, 2009.

[161] Shohei Yamazaki and Tetsuya Taketsugu. Nonradiative deactivation mechanisms of uracil, thymine, and 5-fluorouracil: A comparative ab initio study. *J. Phys. Chem. A*, 116(1):491–503, 2012.

[162] Weijie Hua, Shaul Mukamel, and Yi Luo. Transient x-ray absorption spectral fingerprints of the s1 dark state in uracil. *J. Phys. Chem. Lett.*, 10(22):7172–7178, 2019.

[163] Pratip Chakraborty, Yusong Liu, Thomas Weinacht, and Spiridoula Matsika. Effect of dynamic correlation on the ultrafast relaxation of uracil in the gas phase. *Faraday Discuss.*, page DOI: 10.1039/D0FD00110D, 2021.

[164] Branislav Milovanović, Jurica Novak, Mihajlo Etinski, Wolfgang Domcke, and Naa Došlić. Simulation of uv absorption spectra and relaxation dynamics of uracil and uracil–water clusters. *Phys. Chem. Chem. Phys.*, 23:2594–2604, 2021.

[165] Björn O Roos, Peter R Taylor, and Per EM Sigbahn. A complete active space scf method (casscf) using a density matrix formulated super-ci approach. *Chemical Physics*, 48(2):157–173, 1980.

[166] Robert J. Buenker and Sigrid D. Peyerimhoff. Individualized configuration selection in ci calculations with subsequent energy extrapolation. *Theoret. chim. acta*, 35:33–58, 1974.

[167] James Finley, Per-Åke Malmqvist, Björn O. Roos, and Luis Serrano-Andrés. The multi-state caspt2 method. *Chem. Phys. Lett.*, 288(2):299 – 306, 1998.

[168] Alexander A. Granovsky. Extended multi-configuration quasi-degenerate perturbation theory: The new approach to multi-state multi-reference perturbation theory. *J. Chem. Phys.*, 134(21):214113, 2011.

[169] Toru Shiozaki, Werner Győrffy, Paolo Celani, and Hans-Joachim Werner. Communication: Extended multi-state complete active space second-order perturbation theory: Energy and nuclear gradients. *J. Chem. Phys.*, 135(8):081106, 2011.

[170] Mario Barbatti, Adelia JA Aquino, and Hans Lischka. The uv absorption of nucleobases: semi-classical ab initio spectra simulations. *Physical Chemistry Chemical Physics*, 12(19):4959–4967, 2010.

[171] Paul J Crutzen, Ivar SA Isaksen, and John R McAfee. The impact of the chlorocarbon industry on the ozone layer. *Journal of Geophysical Research: Oceans*, 83(C1):345–363, 1978.

[172] Una Marvet, Qingguo Zhang, Emily J Brown, and Marcos Dantus. Femtosecond dynamics of photoinduced molecular detachment from halogenated alkanes. I. transition state dynamics and product channel coherence. *The Journal of Chemical Physics*, 109(11):4415–4427, 1998.

[173] Femtosecond dynamics of photoinduced molecular detachment from halogenated alkanes. II. asynchronous concerted elimination of I_2 from CH_2I_2, author=Zhang, Qingguo and Marvet, Una and Dantus, Marcos, journal=The Journal of Chemical Physics, volume=109, number=11, pages=4428–4442, year=1998, publisher=American Institute of Physics.

[174] Katharine Moore Tibbetts, Xi Xing, and Herschel Rabitz. Optimal control of molecular fragmentation with homologous families of photonic reagents and chemical substrates. *Physical Chemistry Chemical Physics*, 15(41):18012–18022, 2013.

[175] Jinzhong Zhang, Eric J Heller, Daniel Huber, Dan G Imre, and David Tannor. CH_2I_2 photodissociation: Dynamical modeling. *The Journal of Chemical Physics*, 89(6):3602–3611, 1988.

[176] Haifeng Xu, Ying Guo, Shilin Liu, Xingxiao Ma, Dongxu Dai, and Guohe Sha. Photodissociation dynamics of CH_2I_2 molecules in the ultraviolet range studied by ion imaging. *The Journal of Chemical Physics*, 117(12):5722–5729, 2002.

[177] Ya-Jun Liu, Luca De Vico, Roland Lindh, and Wei-Hai Fang. Spin-orbit ab initio investigation of the ultraviolet photolysis of diiodomethane. *ChemPhysChem*, 8(6):890–898, 2007.

[178] Anuvab Mandal, Param Jeet Singh, Aparna Shastri, and B.N. Jagatap. Electronic state spectroscopy of diiodomethane (CH_2I_2): Experimental and computational studies in the 30 000–95 000 cm- 1 region. *The Journal of Chemical Physics*, 140(19):194312, 2014.

[179] Benjamin W Toulson, Jonathan P Alaniz, J Grant Hill, and Craig Murray. Near-uv photodissociation dynamics of CH_2I_2. *Physical Chemistry Chemical Physics*, 18(16):11091–11103, 2016.

[180] Tsukasa Takanashi, Kosuke Nakamura, Edwin Kukk, Koji Motomura, Hironobu Fukuzawa, Kiyonobu Nagaya, Shin-ichi Wada, Yoshiaki Kumagai, Denys Iablonskyi, Yuta Ito, et al. Ultrafast coulomb explosion of a diiodomethane molecule induced by an x-ray free-electron laser pulse. *Physical Chemistry Chemical Physics*, 19(30):19707–19721, 2017.

[181] Zhengrong Wei, Jialin Li, Huimin Zhang, Yunpeng Lu, Minghui Yang, and Zhi-Heng Loh. Ultrafast dissociative ionization and large-amplitude vibrational wave packet dynamics of strong-field-ionized diiodomethane. *The Journal of Chemical Physics*, 151(21):214308, 2019.

[182] AF Lago, James P Kercher, András Bödi, Bálint Sztáray, B Miller, D Wurzelmann, and Tomas Baer. Dissociative photoionization and thermochemistry of dihalomethane compounds studied by threshold photoelectron photoion coincidence spectroscopy. *The Journal of Physical Chemistry A*, 109(9):1802–1809, 2005.

[183] Andrew R Attar, Lorena Piticco, and Stephen R Leone. Core-to-valence spectroscopic detection of the CH_2IBr radical and element-specific femtosecond photodissociation dynamics of ch2ibr. *The Journal of Chemical Physics*, 141(16):164308, 2014.

[184] Michael Burt, Rebecca Boll, Jason WL Lee, Kasra Amini, Hansjochen Köckert, Claire Vallance, Alexander S Gentleman, Stuart R Mackenzie, Sadia Bari, Cédric Bomme, et al. Coulomb-explosion imaging of concurrent CH_2IBr photodissociation dynamics. *Physical Review A*, 96(4):043415, 2017.

[185] Merlin Fisher-Levine, Rebecca Boll, Farzaneh Ziaee, Cédric Bomme, Benjamin Erk, Dimitrios Rompotis, Tatiana Marchenko, Andrei Nomerotski, and Daniel Rolles. Time-resolved ion imaging at free-electron lasers using timepixcam. *Journal of Synchrotron Radiation*, 25(2):336–345, 2018.

[186] Sonia Marggi Poullain, David V Chicharro, Eduardo Navarro, Luis Rubio-Lago, Jesús González-Vázquez, and Luis Bañares. Photodissociation dynamics of bromoiodomethane from the first and second absorption bands. a combined velocity map and slice imaging study. *Physical Chemistry Chemical Physics*, 20(5):3490–3503, 2018.

[187] Vincent Tagliamonti, Brian Kaufman, Arthur Zhao, Tamás Rozgonyi, Philipp Marquetand, and Thomas Weinacht. Time-resolved measurement of internal conversion dynamics in strong-field molecular ionization. *Physical Review A*, 96(2):021401, 2017.

[188] Vincent Tagliamonti, Péter Sándor, Arthur Zhao, Tamás Rozgonyi, Philipp Marquetand, and Thomas Weinacht. Nonadiabatic dynamics and multiphoton resonances in strong-field molecular ionization with few-cycle laser pulses. *Physical Review A*, 93(5):051401, 2016.

[189] Ruaridh Forbes. *Molecular dynamics and photoionisation processes: from strong-fields to soft X-rays*. PhD thesis, UCL (University College London), 2018.

[190] Uzi Even. Pulsed supersonic beams from high pressure source: Simulation results and experimental measurements. *Advances in Chemistry*, 2014, 2014.

[191] Anuvab Mandal, Param Jeet Singh, Aparna Shastri, and BN Jagatap. Electronic state spectroscopy of diiodomethane (ch2i2): Experimental and computational studies in the 30 000–95 000 cm- 1 region. *The Journal of Chemical Physics*, 140(19):194312, 2014.

[192] Andrew R. Attar, Lorena Piticco, and Stephen R. Leone. Core-to-valence spectroscopic detection of the ch2br radical and element-specific femtosecond photodissociation dynamics of ch2ibr. *The Journal of Chemical Physics*, 141(16):164308, 2014.

[193] Sebastian Mai, Martin Richter, Moritz Heindl, Maximilian F. S. J. Menger, Andrew Atkins, Matthias Ruckenbauer, Felix Plasser, Markus Oppel, Philipp Marquetand, and Leticia González. Sharc2.0: Surface hopping including arbitrary couplings — program package for non-adiabatic dynamics. sharc-md.org, 2018.

[194] Martin Richter, Philipp Marquetand, Jesús González-Vázquez, Ignacio Sola, and Leticia González. SHARC: ab initio molecular dynamics with surface hopping in the adiabatic representation including arbitrary couplings. *J. Chem. Theory Comput.*, 7(5):1253–1258, 2011.

[195] Francesco Aquilante, Jochen Autschbach, Rebecca K Carlson, Liviu F Chibotaru, Mickaël G Delcey, Luca De Vico, Nicolas Ferré, Luis Manuel Frutos, Laura Gagliardi, Marco Garavelli, et al. Molcas 8: New capabilities for multiconfigurational quantum chemical calculations across the periodic table. *Journal of computational chemistry*, 37(5):506–541, 2016.

[196] Michael Burt, Rebecca Boll, Jason W. L. Lee, Kasra Amini, Hansjochen Köckert, Claire Vallance, Alexander S. Gentleman, Stuart R. Mackenzie, Sadia Bari, Cédric Bomme, Stefan Düsterer, Benjamin Erk, Bastian Manschwetus, Erland Müller, Dimitrios Rompotis, Evgeny Savelyev, Nora Schirmel, Simone Techert, Rolf Treusch, Jochen Küpper, Sebastian Trippel, Joss Wiese, Henrik Stapelfeldt, Barbara Cunha de Miranda, Renaud Guillemin, Iyas Ismail, Loïc Journel, Tatiana Marchenko, Jérôme Palaudoux, Francis Penent, Maria Novella Piancastelli, Marc Simon, Oksana Travnikova, Felix Brausse, Gildas Goldsztejn, Arnaud Rouzée, Marie Géléoc, Romain Geneaux, Thierry Ruchon, Jonathan Underwood, David M. P. Holland, Andrey S. Mereshchenko, Pavel K. Olshin, Per Johnsson, Sylvain Maclot, Jan Lahl, Artem Rudenko, Farzaneh Ziaee, Mark Brouard, and Daniel Rolles. Coulomb-explosion imaging of concurrent ch_2bri photodissociation dynamics. *Physical Review A*, 96:043415, Oct 2017.

[197] Peter J Linstrom and William G Mallard. The nist chemistry webbook: A chemical data resource on the internet. *Journal of Chemical & Engineering Data*, 46(5):1059–1063, 2001.

[198] Marta L Murillo-Sánchez, Sonia Marggi Poullain, Juan J Bajo, María E Corrales, Jesús González-Vázquez, Ignacio R Solá, and Luis Bañares. Halogen-atom effect on the ultrafast photodissociation dynamics of the dihalomethanes ch 2 icl and ch 2 bri. *Physical Chemistry Chemical Physics*, 20(32):20766–20778, 2018.

[199] Jie Yang, Markus Guehr, Theodore Vecchione, Matthew S Robinson, Renkai Li, Nick Hartmann, Xiaozhe Shen, Ryan Coffee, Jeff Corbett, Alan Fry, et al. Femtosecond gas phase electron diffraction with mev electrons. *Faraday discussions*, 194:563–581, 2016.

[200] X. Shen, R.K. Li, U. Lundström, T.J. Lane, A.H. Reid, S.P. Weathersby, and X.J. Wang. Femtosecond mega-electron-volt electron microdiffraction. *Ultramicroscopy*, 184:172 – 176, 2018.

[201] RK Li, MC Hoffmann, EA Nanni, SH Glenzer, ME Kozina, AM Lindenberg, BK Ofori-Okai, AH Reid, X Shen, SP Weathersby, et al. Terahertz-based subfemtosecond metrology of relativistic electron beams. *Physical Review Accelerators and Beams*, 22(1):012803, 2019.

[202] H Ihee, J Cao, and A.H Zewail. Ultrafast electron diffraction: structures in dissociation dynamics of fe(co)5. *Chemical Physics Letters*, 281(1):10 – 19, 1997.

[203] Dominik Geißler, Brett J. Pearson, and Thomas Weinacht. Wave packet driven dissociation and concerted elimination in ch2i2. *The Journal of Chemical Physics*, 127(20):204305, 2007.

[204] Sarah R. Nichols, Thomas C. Weinacht, Tamás Rozgonyi, and Brett J. Pearson. Strong-field phase-dependent molecular dissociation. *Physics Review A*, 79:043407, Apr 2009.

[205] Péter Sándor, Vincent Tagliamonti, Arthur Zhao, Tamás Rozgonyi, Matthias Ruckenbauer, Philipp Marquetand, and Thomas Weinacht. Strong field molecular ionization in the impulsive limit: Freezing vibrations with short pulses. *Physical Review Letters*, 116(6):063002, 2016.

[206] EC Snively, MAK Othman, M Kozina, BK Ofori-Okai, SP Weathersby, S Park, X Shen, XJ Wang, MC Hoffmann, RK Li, et al. Femtosecond compression dynamics and timing jitter suppression in a thz-driven electron bunch compressor. *Physical review letters*, 124(5):054801, 2020.

[207] Fengfeng Qi, Zhuoran Ma, Lingrong Zhao, Yun Cheng, Wenxiang Jiang, Chao Lu, Tao Jiang, Dong Qian, Zhe Wang, Wentao Zhang, et al. Breaking 50 femtosecond resolution barrier in mev ultrafast electron diffraction with a double bend achromat compressor. *Physical review letters*, 124(13):134803, 2020.

[208] Albert Stolow, Arthur E. Bragg, and Daniel M. Neumark. Femtosecond time-resolved photoelectron spectroscopy. *Chemical Reviews*, 104(4):1719–1758, 2004.

[209] Markus Drescher, Michael Hentschel, R Kienberger, Matthias Uiberacker, Vladislav Yakovlev, Armin Scrinzi, Th Westerwalbesloh, U Kleineberg, Ulrich Heinzmann, and Ferenc Krausz. Time-resolved atomic inner-shell spectroscopy. *Nature*, 419(6909):803–807, 2002.

[210] Kai Siegbahn. *ESCA Applied to Free Molecules*. North-Holland, 1969.

[211] Rebecca Boll, Benjamin Erk, Ryan Coffee, Sebastian Trippel, Thomas Kierspel, Cédric Bomme, John D Bozek, Mitchell Burkett, Sebastian Carron, Ken R Ferguson, et al. Charge transfer in dissociating iodomethane and fluoromethane molecules ionized by intense femtosecond x-ray pulses. *Struct. Dyn.*, 3(4):043207, 2016.

[212] Ludger Inhester, Zheng Li, Xiaolei Zhu, Nikita Medvedev, and Thomas J. A. Wolf. Spectroscopic signature of chemical bond dissociation revealed by calculated core-electron spectra. *J. Phys. Chem. Lett.*, 10(21):6536–6544, 2019.

[213] Ruaridh Forbes, Felix Allum, Sadia Bari, Rebecca Boll, Kurtis Borne, Mark Brouard, Philip H Bucksbaum, Nagitha Ekanayake, Benjamin Erk, Andrew J Howard, et al. Time-resolved site-selective imaging of predissociation and charge transfer dynamics: the ch3i b-band. *Journal of Physics B: Atomic, Molecular and Optical Physics*, 53(22):224001, 2020.

[214] Tatsuo Gejo, Tatsuru Nishie, Takahiro Nagayasu, Kenta Tanaka, Yoshihito Tanaka, Akinobu Niozu, Kiyonobu Nagaya, Ryosuke Yamamura, Nozomi Futamata, Taiga Suenaga, et al. Dissociation and ionization dynamics of cf3i and ch3i molecules via pump-and-probe experiments using soft x-ray free-electron laser. *Journal of Physics B: Atomic, Molecular and Optical Physics*, 2020.

[215] Marta L Vidal, Anna I Krylov, and Sonia Coriani. Dyson orbitals within the fc-cvs-eom-ccsd framework: theory and application to x-ray photoelectron spectroscopy of ground and excited states. *Physical Chemistry Chemical Physics*, 22(5):2693–2703, 2020.

[216] Jochen Küpper, Stephan Stern, Lotte Holmegaard, Frank Filsinger, Arnaud Rouzée, Artem Rudenko, Per Johnsson, Andrew V Martin, Marcus Adolph, Andrew Aquila, et al. X-ray diffraction from isolated and strongly aligned gas-phase molecules with a free-electron laser. *Physical Review Letters*, 112(8):083002, 2014.

[217] Mats Simmermacher, Andrés Moreno Carrascosa, Niels E. Henriksen, Klaus B. Møller, and Adam Kirrander. Theory of ultrafast x-ray scattering by molecules in the gas phase. *The Journal of chemical physics*, 151(17):174302, 2019.

[218] Philip H Bucksbaum, Matthew R Ware, Adi Natan, James P Cryan, and James M Glownia. Characterizing multiphoton excitation using time-resolved x-ray scattering. *Physical Review X*, 10(1):011065, 2020.

[219] Thomas Kierspel, Andrew Morgan, Joss Wiese, Terry Mullins, Andy Aquila, Anton Barty, Richard Bean, Rebecca Boll, Sébastien Boutet, Philip Bucksbaum, et al. X-ray diffractive imaging of controlled gas-phase molecules: Toward imaging of dynamics in the molecular frame. *The Journal of chemical physics*, 152(8):084307, 2020.

[220] J Amann, W Berg, V Blank, F-J Decker, Y Ding, P Emma, Y Feng, J Frisch, D Fritz, J Hastings, et al. Demonstration of self-seeding in a hard-x-ray free-electron laser. *Nature photonics*, 6(10):693–698, 2012.

[221] Patrick G O'Shea and Henry P Freund. Free-electron lasers: Status and applications. *Science*, 292(5523):1853–1858, 2001.

[222] Primoz Rebernik Ribic and G Margaritondo. Status and prospects of x-ray free-electron lasers (x-fels): a simple presentation. *Journal of Physics D: Applied Physics*, 45(21):213001, 2012.

[223] Tony Heinz, Oleg Shpyrko, Dimitri Basov, Nora Berrah, Phil Bucksbaum, Tom Devereaux, David Fritz, Kelly Gaffney, Oliver Gessner, Venkat Gopalan, et al. Basic energy sciences roundtable: Opportunities for basic research at the frontiers of xfel ultrafast science. Technical report, USDOE Office of Science (SC)(United States), 2017.

[224] Linda Young, Kiyoshi Ueda, Markus Gühr, Philip H Bucksbaum, Marc Simon, Shaul Mukamel, Nina Rohringer, Kevin C Prince, Claudio Masciovecchio, Michael Meyer, et al. Roadmap of ultrafast x-ray atomic and molecular physics. *Journal of Physics B: Atomic, Molecular and Optical Physics*, 51(3):032003, 2018.

[225] James Finley, Per-Åke Malmqvist, Björn O Roos, and Luis Serrano-Andrés. The multi-state caspt2 method. *Chemical physics letters*, 288(2-4):299–306, 1998.

[226] Alexander A Granovsky. Extended multi-configuration quasi-degenerate perturbation theory: The new approach to multi-state multi-reference perturbation theory. *The Journal of chemical physics*, 134(21):214113, 2011.

[227] Toru Shiozaki, Werner Győrffy, Paolo Celani, and Hans-Joachim Werner. Communication: Extended multi-state complete active space second-order perturbation theory: Energy and nuclear gradients, 2011.

[228] Thom H Dunning Jr. Gaussian basis sets for use in correlated molecular calculations. i. the atoms boron through neon and hydrogen. *The Journal of chemical physics*, 90(2):1007–1023, 1989.

[229] Jae Woo Park. Single-state single-reference and multistate multireference zeroth-order hamiltonians in ms-caspt2 and conical intersections. *Journal of chemical theory and computation*, 15(7):3960–3973, 2019.

[230] BAGEL, Brilliantly Advanced General Electronic-structure Library. `http://www.nubakery.org` under the GNU General Public License.

[231] Toru Shiozaki. Bagel: Brilliantly advanced general electronic-structure library. *Wiley Interdisciplinary Reviews: Computational Molecular Science*, 8(1):e1331, 2018.

[232] Mario Barbatti, Matthias Ruckenbauer, Felix Plasser, Jiri Pittner, Giovanni Granucci, Maurizio Persico, and Hans Lischka. Newton-x: a surface-hopping program for nonadiabatic molecular dynamics. *WIREs Comput. Mol. Sci.*, 4(1):26–33, 2014.

[233] M. Barbatti, G. Granucci, M. Ruckenbauer, F. Plasser, R. Crespo-Otero, J. Pittner, M. Persico, and H. Lischka. NEWTON-X: A package for Newtonian dynamics close to the crossing seam, version 2, `http://www.newtonx.org`,.

[234] Ron Shepard. Geometrical energy derivative evaluation with MRCI wave functions. *Int. J. Quantum Chem.*, 31(1):33–44, 1987.

[235] R. Shepard, H. Lischka, P. G. Szalay, T. Kovar, and M. Ernzerhof. A general multireference configuration interaction gradient program. *J. Chem. Phys.*, 96(3):2085–2098, 1992.

[236] H. Lischka, M. Dallos, and R. Shepard. Analytic mrci gradient for excited states: formalism and application to the n- valence- and n-(3s,3p) rydberg states of formaldehyde. *Mol. Phys.*, 100(11):1647–1658, 2002.

[237] Hans Lischka, Michal Dallos, Péter G. Szalay, David R. Yarkony, and Ron Shepard. Analytic evaluation of nonadiabatic coupling terms at the MR-CI level. I. Formalism. *J. Chem. Phys.*, 120(16):7322–7329, 2004.

[238] Michal Dallos, Hans Lischka, Ron Shepard, David R. Yarkony, and Péter G. Szalay. Analytic evaluation of nonadiabatic coupling terms at the MR-CI level. II. Minima on the crossing seam: Formaldehyde and the photodimerization of ethylene. *J. Chem. Phys.*, 120(16):7330–7339, 2004.

[239] J. Towns, T. Cockerill, M. Dahan, I. Foster, K. Gaither, A. Grimshaw, V. Hazlewood, S. Lathrop, D. Lifka, G. D. Peterson, R. Roskies, J. R. Scott, and N. Wilkins-Diehr. XSEDE: Accelerating Scientific Discovery. *Comput. Sci. Eng.*, 16(5):62–74, Sep. 2014.

[240] Tolga NV Karsili, Mushir Thodika, Linh Nguyen, and Spiridoula Matsika. The origin of fluorescence in dna thio-analogues. *Chemical Physics*, 515:434–440, 2018.

[241] M. Barbatti, G. Granucci, M. Ruckenbauer, F. Plasser, R. Crespo-Otero, J. Pittner, M. Persico, and H. Lischka. NEWTON-X: A package for Newtonian dynamics close to the crossing seam, version 2.2, `http://www.newtonx.org`,.

[242] Bess Vlaisavljevich and Toru Shiozaki. Nuclear energy gradients for internally contracted complete active space second-order perturbation theory: Multistate extensions. *Journal of chemical theory and computation*, 12(8):3781–3787, 2016.

[243] Jae Woo Park and Toru Shiozaki. Analytical derivative coupling for multistate caspt2 theory. *Journal of Chemical Theory and Computation*, 13(6):2561–2570, 2017.

[244] Jae Woo Park and Toru Shiozaki. On-the-fly caspt2 surface-hopping dynamics. *Journal of Chemical Theory and Computation*, 13(8):3676–3683, 2017.

[245] Giovanni Granucci and Maurizio Persico. Critical appraisal of the fewest switches algorithm for surface hopping. *J. Chem. Phys.*, 126(13):134114, 2007.

[246] Chaoyuan Zhu, Shikha Nangia, Ahren W. Jasper, and Donald G. Truhlar. Coherent switching with decay of mixing: An improved treatment of electronic coherence for non-Born–Oppenheimer trajectories. *J. Chem. Phys.*, 121(16):7658–7670, 2004.

[247] H. Lischka, R. Shepard, I. Shavitt, R. M. Pitzer, M. Dallos, Th. Müller, P. G. Szalay, F. B. Brown, R. Ahlrichs, H. J. Böhm, A. Chang, D. C. Comeau, R. Gdanitz, H. Dachsel, C. Ehrhardt, M. Ernzerhof, P. Höchtl, S. Irle, G. Kedziora, T. Kovar, V. Parasuk, M. J. M. Pepper, P. Scharf, H. Schiffer, M. Schindler, M. Schüler, M. Seth, E. A. Stahlberg, J.-G. Zhao, S. Yabushita, Z. Zhang, M. Barbatti, S. Matsika, M. Schuurmann, D. R. Yarkony, S. R. Brozell, E. V. Beck, J.-P. Blaudeau, M. Ruckenbauer, B. Sellner, F. Plasser, and J. J. Szymczak. COLUMBUS, an ab initio electronic structure program, release 7.0 (2012).

[248] Hans Lischka, Thomas Müller, Péter G. Szalay, Isaiah Shavitt, Russell M. Pitzer, and Ron Shepard. Columbus—a program system for advanced multireference theory calculations. *WIREs Comput. Mol. Sci.*, 1(2):191–199, 2011.

[249] Hans Lischka, Ron Shepard, Russell M. Pitzer, Isaiah Shavitt, Michal Dallos, Thomas Müller, Péter G. Szalay, Michael Seth, Gary S. Kedziora, Satoshi Yabushita, and Zhiyong Zhang. High-level multireference methods in the quantum-chemistry program system COLUMBUS: Analytic MR-CISD and MR-AQCC gradients and MR-AQCC-LRT for excited states, GUGA spin–orbit CI and parallel CI density. *Phys. Chem. Chem. Phys.*, 3:664–673, 2001.

[250] BAGEL, Brilliantly Advanced General Electronic-structure Library. `http://www.nubakery.org` under the GNU General Public License.

[251] Toru Shiozaki. BAGEL: Brilliantly Advanced General Electronic-structure Library. *WIREs Comput. Mol. Sci.*, 8(1):e1331, 2018.

[252] Yusong Liu, Pratip Chakraborty, Spiridoula Matsika, and Thomas Weinacht. Excited state dynamics of cis,cis-1,3-cyclooctadiene: Uv pump vuv probe time-resolved photoelectron spectroscopy. *J. Chem. Phys.*, 153(7):074301, 2020.

[253] Evgeny Epifanovsky, Karol Kowalski, Peng-Dong Fan, Marat Valiev, Spiridoula Matsika, and Anna I. Krylov. On the electronically excited states of uracil. *J. Phys. Chem. A*, 112(40):9983–9992, 2008.

[254] Mariana Assmann, Horst Köppel, and Spiridoula Matsika. Photoelectron spectrum and dynamics of the uracil cation. *The Journal of Physical Chemistry A*, 119(5):866–875, 2015.

[255] Mariana Assmann, Thomas Weinacht, and Spiridoula Matsika. Surface hopping investigation of the relaxation dynamics in radical cations. *The Journal of Chemical Physics*, 144(3):034301, 2016.

[256] Spiridoula Matsika, Michael Spanner, Marija Kotur, and Thomas C Weinacht. Ultrafast relaxation dynamics of uracil probed via strong field dissociative ionization. *The Journal of Physical Chemistry A*, 117(48):12796–12801, 2013.

[257] Spencer L. Horton, Yusong Liu, Ruaridh Forbes, Varun Makhija, Rune Lausten, Albert Stolow, Paul Hockett, Philipp Marquetand, Tamás Rozgonyi, and Thomas Weinacht. Excited state dynamics of ch2i2 and ch2bri studied with uv pump vuv probe photoelectron spectroscopy. *The Journal of Chemical Physics*, 150(17):174201, 2019.

[258] Yusong Liu, Tamás Rozgonyi, Philipp Marquetand, and Thomas Weinacht. Excited-state dynamics of ch2i2 and ch2ibr studied with uv-pump vuv-probe momentum-resolved photoion spectroscopy. *J. Chem. Phys.*, 153(18):184304, 2020.

[259] J Patrick Zobel, Juan J Nogueira, and Leticia González. The ipea dilemma in caspt2. *Chemical science*, 8(2):1482–1499, 2017.

[260] Niclas Forsberg and Per-Åke Malmqvist. Multiconfiguration perturbation theory with imaginary level shift. *Chemical Physics Letters*, 274(1-3):196–204, 1997.

[261] M Reiher. Wiley interdiscip. *Rev. Comput. Mol. Sci*, 2:139–149, 2012.

[262] Per Åke Malmqvist, Björn O Roos, and Bernd Schimmelpfennig. The restricted active space (ras) state interaction approach with spin–orbit coupling. *Chemical physics letters*, 357(3-4):230–240, 2002.

[263] B Schimmelpfennig. Amfi–an atomic mean field integral program. *Stockholm University*, 1996.

[264] Giovanni Granucci, Maurizio Persico, and Alessandro Toniolo. Direct semiclassical simulation of photochemical processes with semiempirical wave functions. *The Journal of Chemical Physics*, 114(24):10608–10615, 2001.

[265] Felix Plasser, Matthias Ruckenbauer, Sebastian Mai, Markus Oppel, Philipp Marquetand, and Leticia González. Efficient and flexible computation of many-electron wave function overlaps. *Journal of chemical theory and computation*, 12(3):1207–1219, 2016.

[266] Giovanni Granucci and Maurizio Persico. Critical appraisal of the fewest switches algorithm for surface hopping. *The Journal of chemical physics*, 126(13):134114, 2007.

[267] Mario Barbatti, Giovanni Granucci, Maurizio Persico, Matthias Ruckenbauer, Mario Vazdar, Mirjana Eckert-Maksić, and Hans Lischka. The on-the-fly surface-hopping program system newton-x: Application to ab initio simulation of the nonadiabatic photodynamics of benchmark systems. *Journal of Photochemistry and Photobiology A: Chemistry*, 190(2-3):228–240, 2007.

[268] AW Potts, HJ Lempka, DG Streets, and WC Price. Photoelectron spectra of the halides of elements in groups iii, iv, v and vi. *Philosophical Transactions for the Royal Society of London. Series A, Mathematical and Physical Sciences*, pages 59–76, 1970.

[269] Matthias Ruckenbauer, Sebastian Mai, Philipp Marquetand, and Leticia González. Photoelectron spectra of 2-thiouracil, 4-thiouracil, and 2, 4-dithiouracil. *The Journal of chemical physics*, 144(7):074303, 2016.

[270] Ekram Hossain, Shihu M Deng, Samer Gozem, Anna I Krylov, Xue-Bin Wang, and Paul G Wenthold. Photoelectron spectroscopy study of quinonimides. *Journal of the American Chemical Society*, 139(32):11138–11148, 2017.

[271] Michael A Parkes, Jonathan Crellin, Alice Henley, and Helen H Fielding. A photoelectron imaging and quantum chemistry study of the

deprotonated indole anion. *Physical Chemistry Chemical Physics*, 20(22):15543–15549, 2018.

[272] José A Sánchez-Rodríguez, Abed Mohamadzade, Sebastian Mai, Brennan Ashwood, Marvin Pollum, Philipp Marquetand, Leticia González, Carlos E Crespo-Hernández, and Susanne Ullrich. 2-thiouracil intersystem crossing photodynamics studied by wavelength-dependent photoelectron and transient absorption spectroscopies. *Physical Chemistry Chemical Physics*, 19(30):19756–19766, 2017.

[273] William J Glover, Toshifumi Mori, Michael S Schuurman, Andrey E Boguslavskiy, Oliver Schalk, Albert Stolow, and Todd J Martínez. Excited state non-adiabatic dynamics of the smallest polyene, trans 1, 3-butadiene. ii. ab initio multiple spawning simulations. *The Journal of chemical physics*, 148(16):164303, 2018.

[274] Michael R Coates, Martin AB Larsen, Ruaridh Forbes, Simon P Neville, Andrey E Boguslavskiy, Iain Wilkinson, Theis I Sølling, Rune Lausten, Albert Stolow, and Michael S Schuurman. Vacuum ultraviolet excited state dynamics of the smallest ring, cyclopropane. ii. time-resolved photoelectron spectroscopy and ab initio dynamics. *The Journal of chemical physics*, 149(14):144311, 2018.

[275] Karl Kaufmann, Werner Baumeister, and Martin Jungen. Universal gaussian basis sets for an optimum representation of rydberg and continuum wavefunctions. *Journal of Physics B: Atomic, Molecular and Optical Physics*, 22(14):2223, 1989.

[276] Katharine L Reid. Photoelectron angular distributions. *Annual review of physical chemistry*, 54(1):397–424, 2003.

[277] Yusong Liu, Pratip Chakraborty, Spiridoula Matsika, and Thomas Weinacht. Excited state dynamics of cis,cis-1,3-cyclooctadiene: Uv pump vuv probe time-resolved photoelectron spectroscopy. *The Journal of Chemical Physics*, 153(7):074301, 2020.

[278] Hannelore Keller-Rudek, GK Moortgat, Rolf Sander, and R Sörensen. The mpi-mainz uv/vis spectral atlas of gaseous molecules of atmospheric interest. *Earth System Science Data*, 5(2):365–373, 2013.

[279] Juliane C Mössinger, Dudley E Shallcross, and R Anthony Cox. Uv–vis absorption cross-sections and atmospheric lifetimes of CH_2Br_2, CH_2I_2 and CH_2BrI. *Journal of the Chemical Society, Faraday Transactions*, 94(10):1391–1396, 1998.